Role Of Structure In Ionic Conduction In Oxide Glasses.

INFORMATION TO USERS

This manuscript has been reproduced from the microfilm master. UMI films the text directly from the original or copy submitted. Thus, some thesis and dissertation copies are in typewriter face, while others may be from any type of computer printer.

The quality of this reproduction is dependent upon the quality of the copy submitted. Broken or indistinct print, colored or poor quality illustrations and photographs, print bleedthrough, substandard margins, and improper alignment can adversely affect reproduction.

In the unlikely event that the author did not send UMI a complete manuscript and there are missing pages, these will be noted. Also, if unauthorized copyright material had to be removed, a note will indicate the deletion.

Oversize materials (e.g., maps, drawings, charts) are reproduced by sectioning the original, beginning at the upper left-hand corner and continuing from left to right in equal sections with small overlaps. Each original is also photographed in one exposure and is included in reduced form at the back of the book.

Photographs included in the original manuscript have been reproduced xerographically in this copy. Higher quality 6" x 9" black and white photographic prints are available for any photographs or illustrations appearing in this copy for an additional charge. Contact UMI directly to order.

UMI

A Bell & Howell Information Company
300 North Zeeb Road, Ann Arbor MI 48106-1346 USA
313/761-4700 800/521-0600

ROLE OF STRUCTURE IN IONIC CONDUCTION IN OXIDE GLASSES

By

Wei-Che (Michael) Huang

A Dissertation
Presented to the Graduate and Research Committee
of Lehigh University
in Candidacy for the Degree of

Doctor of Philosophy
in
Materials Science and Engineering

Lehigh University
March 1996

CERTIFICATE OF APPROVAL

This is to certify that the dissertation

"Role of Structure in Ionic Conduction in Oxide Glasses"

Prepared by Wei-Che (Michael) Huang

Is approved and recommended for acceptance as a dissertation in partial fulfillment of the requirements for the degree of Doctor of Philosophy.

April 30, 1996
(Date)

(Professor in Charge).

Special committee members directing the doctoral research

March 18, 1996.
(Accepted Date)

Dr. Himanshu Jain (Chairman)

Dr. Helen M. Chan (Lehigh)

Dr. Katayun Barmak (Lehigh)

Dr. Matthew A. Marcus (AT&T)

ACKNOWLEDGEMENTS

There have been numerous people without whose help this work would have not been possibly accomplished. First, I would like to express my grateful thanks to my advisor, Dr. H. Jain, for his understanding, encouragement and guidance through this research. He introduced me to the novel world of ionic conduction in glasses. His profound and advanced knowledge in glass science is the roadmap to go through this study. His support and instruction prevented me from being lost in those baseless concepts and unrealistic models.

My appreciation is expressed to my doctoral committee members, Dr. H.M. Chan, Dr. K. Barmak (Lehigh University) and Dr. M.A. Marcus (AT&T, Bell Lab.) for their suggestions and assistance during this dissertation work. Their insights have made this research a much better work. My special thanks are to Dr. M.A. Marcus (AT&T) and Dr. G. Meitzner (Exxon), who have specifically helped me with the recording and the processing of the EXAFS spectra of germanate glasses. My thanks also go to Dr. A.C. Miller (Lehigh), who has helped with the XPS spectroscopy and to Dr. E.I. Kamitsos (National Hellenic Research Foundation, Athens, Greece), who has helped with the IR measurements.

To my friends and colleagues at Lehigh, I wish to express my appreciation for their broad range of experience and cooperation. Special thanks go to Dr. X. Lu and Dr. C.H. Hsieh for their helpful discussions and arguments during the study, without which this work could not go this far. The precious friendships during my study at Lehigh are memorable,

both intellectually and culturally: Dr. J.L. Dyllan Hong, Dr. M. Raymond, Dr. Jie Chen, Dr. P. Pen, Dr. M. Tseng, Dr. L. Ma, Mr. M. Xu, Mr. C.H. Jiang, Mr. S. Saha, Mr. L. An, Mr. Y.Z. Li, Miss D. Wang, and others with whom I have shared a wonderful experience. I also express my appreciation to the support staff at Lehigh, C. Sottosanti, J. Diclemente, G. Kozma, P. Newhart, V. Newhard, A. Pressler, A. Benscoter and J. Williams.

I would like to thank my parents, Y.L. Huang and M.C. Chen, and my sisters for their love, patience and support (financially and spiritually) through these years.

Most of all, I would like to express my deepest appreciation to my beloved wife, Chia-Ying Lin, and lovely son, Michael S. Huang, Jr., who have been a constant resource of love, affection and support through all of this work.

TABLE OF CONTENTS

LIST OF TABLES

LIST OF FIGURES

ABSTRACT

The importance of structure for the ionic conductivity of oxide glasses has been established using: (1) binary Rb and K germanate glasses; (2) mixed (Rb,Ag) and (Rb,K) germanate glasses (3) neutron irradiated high purity quartz and (4) sodium triborate glasses with different melt conditions.

The electrical conductivity is measured from 10 Hz to 100 kHz and from room temperature to 620 °C. The interatomic distances, coordination number, degree of disorder and the fractions of BOs and NBOs for the germanate glasses are obtained using EXAFS and XPS techniques. In the alkali germanates, both GeO_6 and NBO units are produced for all alkali concentration < 20 mol%. The molar volume shows a minimum with respect to alkali concentration without affecting appreciably the various interatomic distances, indicating a non-uniform spatial distribution of atoms in the glass structure. The structural disorder around alkali ions in germanate glasses is much higher than that in corresponding silicate glasses, suggesting that the modified random network model is less appropriate for the former.

The composition dependence of d.c. conductivity is explained in terms of the 'unoccupied volume' as a pathway for diffusion. The cooperative ion movement model for alkali silicates is inappropriate for describing conductivity in germanate glasses. The local structure for the mixed mobile ion glasses does not seem to be the key for the development of the mixed mobile ion effect.

The activation energy, density, and IR absorptivity of sodium borate glasses are

affected by the melt conditions, indicating extremely slow relaxations and anomalous expansion in this system.

In contrast to the literature, the present glasses do not show simple correlations between the non-ideality of electrical relaxation (Kohlrausch exponent β) and the d.c. conductivity, or the nominal cation-cation distance. Instead, β is strongly determined by the ion distribution and the Coulombic interactions between a mobile cation and its charge compensating center. A dose of 1×10^{19} (or greater) fast neutron/cm^2, which is known to create appreciable disorder in quartz, enhances the non-ideality of the electrical relaxation. It introduces a second plateau in a.c. conductivity at high frequencies and a broadening of the electric modulus peak.

CHAPTER 1 INTRODUCTION

1.1 Overview

The transport properties of oxide glasses have been of great interest for several decades because of their applications in glass technology. Recent developments include the evolution of low energy loss devices [1,2], electrical insulators [3,4], nuclear waste forms [5,6], fast ion conductors [7,8,9,10], solid electrolytes [11,12,13,14], etc. In these applications, glasses have several advantages over crystalline electrolytes: such as physical isotropy (ionic conduction in glasses is isotropic; whereas in many crystalline solids the conduction occurs only along well-defined channels or planes depending on crystal structure), absence of grain boundaries (places where high resistivity occurs), good workability (low viscosity at high temperature), and easy formation with continuously variable compositions. Thus, by systematically controlling the processing, one can easily obtain the room temperature conductivity in glasses ranging from as little as 10^{-15} to as much as 10^{-2} $\Omega^{-1}cm^{-1}$ [1]. This good workability makes glasses suitable for a wide range of electrical and dielectric applications.

It is well known that the most common species responsible for the transport properties of oxide and sulfide glasses are the most mobile alkali or silver monovalent cations (M^+). They are predominantly responsible for the dynamic response of these glasses under the application of an electric field below glass transition temperature (T_g). Glass network forming cations (NFCs) have negligible diffusivity and, therefore, do not contribute to the dynamic response directly. Nevertheless, the NFCs, along with oxygen atoms (in

oxides), form glass network and provide the framework through which an M^+ can move, thus indirectly determining the ultimate dynamic response of the glass [15,16]. Then, it appears logical that the local structure of glass, including both the network and the local environment of mobile ions, should play an important role in determining the ionic conduction.

Unlike ionic conduction in crystalline solids for which both theoretical and experimental work has been well established (for reviews, see refs [17,18]), the mechanisms for ion transport in glasses are still far from clear. This is mainly due to the fact that glasses do not possess well defined (ordered) structure as crystals do and that their disordered structure is not well understood yet, thus hindering the understanding of ionic conduction. For instance, ionic transport in crystals can be easily understood through the thermally activated defect pairs (Schottky type or Frenkel type) in the ordered structure. The activation energy for conduction is, therefore, composed of defect-pair formation energy and defect migration energy, both of which are often constant over a wide range of compositions because of the persistence of crystal structure. In contrast, glass structure changes simultaneously with the addition of doping ions, making it impossible to distinguish the formation and migration energies. Also, the lack of long-range order makes glasses difficult to investigate using conventional techniques like x-ray or neutron diffractions, etc. As a result, a clear picture of ion movements in glasses is still lacking.

In general, one needs to understand the glass structure (of an alkali silicate, borate or germanate glass) through three different aspects: (a) Physical structure which describes the geometrical configuration and the arrangement of atoms with respect to each other.

(b) Chemical structure which describes the nature of bonding (covalent, ionic, etc.) between three different species (mobile cation, network cation and oxygen anion) and (c) Bonding energy structure which describes the strength of various bonds. It is important to point out that these three aspects of structure are the different manifestations of the same overall structure. They are closely interdependent, yet are considered separately due to the limited information available from a particular experimental technique.

For over two decades, extended x-ray absorption fine structure (EXAFS) technique has been successfully used to determine the local structure of glasses (mainly silicate glasses) [19,20,21]. Unlike x-ray and neutron diffractions, where the total diffraction intensity includes several entangled correlation functions that mask the mobile ion-oxygen correlation (although some deconvoluted structural information can be obtained from materials containing isotopes), EXAFS can separate individual atomic pair radial distribution functions, which describe the local structure of network modifier as well as network forming atoms separately. For example, in sodium silicate glasses, Si-O distance is restricted to the Si EXAFS spectrum, and Na-O distance is restricted to the Na EXAFS spectrum. These two spectra are obtained independently because of separate Si and Na x-ray absorption energies. Thus, EXAFS technique is an excellent method for examining the details of physical structure of glass. In addition, IR spectroscopy, which detects vibration modes of network structural units, can be used to detect the geometry of different structural units [22,23]; and x-ray photoelectron spectroscopy (XPS) which determines the fraction of non-bridging oxygen (NBO) and the ionicity of alkali ions, is suitable for examining the chemical structure of glass [24,25]. Dielectric constant (from electrical

measurement) together with bond length information (EXAFS) can be used to examine the bonding energy structure. All these techniques have shown excellent sensitivity to the local structure.

In this dissertation, we will investigate the correlation between glass local structure and ionic conductivity, and discuss the possible mechanisms of direct current (d.c.) conductivity and alternating current (ac) conductivity.

1.2 Outline of the Dissertation

This dissertation is basically organized into four main sections: (i) Background (chapter 2), (ii) Experimental (chapter 4), (iii) Results (chapter 5), and (iv) Discussion (chapters 6 to 9). Specifically, chapter 2 gives the reader a general review of recent developments of d.c. conductivity, a.c. conductivity (electrical conductivity relaxation), and glass structure. This chapter points out the lack of understanding of ionic conduction in glasses and sets directions for the present work. It also describes the general features of EXAFS, IR and XPS which have been used for determining glass structure. Chapter 3 establishes the statement of objectives of this dissertation. It also describes the approach undertaken to answer the questions raised in chapter 2. Chapter 4 describes the detailed experimental procedures, such as the glass making processes, the wide frequency electrical measurements, and various spectroscopy measurements. Chapter 5 presents all experimental results and their analysis. It describes the analysis methods and lists the values for the d.c. conductivity parameters, the electric modulus (M*), the Kohlrausch exponent (β), the dielectric constant (ε), and all local structural parameters from EXAFS, XPS, IR. Chapters

6 to 9 present the discussion of observations in literature and new findings from the present work. In chapter 6, we first discuss the compositional dependence of local structure of oxide glasses. Then, we test the validity of a recently proposed modified random network (MRN) structure model [19,20] by using our results for germanate glasses. A new structure model which describes the atomic scale spatial inhomogeneity is then proposed. In chapter 7, we examine the applicability of a cooperative ion movement model using the structural and conductivity parameters. Then, the roles of different structural parameters in determining d.c. conductivity for various glass systems are discussed. In chapter 8, the local structural parameters are used to examine the applicability of two main models describing the a.c. relaxation: the distributions of activation energies model and Ngai's mobile ion-ion coupling model. A possible mechanism which involves the interaction between a mobile ion and its charge compensating center (CCC) is proposed. In chapter 9, the effect of melt conditions on glass structure and electrical conductivity of sodium triborate glasses is discussed. The variations of activation energy for electrical conductivity, density and IR absorptivity of the glass with annealing time are examined. Chapter 10 summarizes the contributions of this work and presents the conclusions.

CHAPTER 2 BACKGROUND

2.1 Introduction

In order for current to flow in either crystalline or amorphous solids, charge must be somehow transported. There are two ways by which charge can be transported through a material: (i) by the movement of ions, (ii) by the movement of electrons without significant displacement of ions. In alkali oxide glasses, only ionic conduction processes take place because of their large band gap which prohibits electronic conduction [26,27]. There are two kinds of conduction processes in ionic solids depending on the frequency range of the applied electric field: (a) long-range ion transport (d.c. conductivity) which occurs at low frequencies; (b) short-range ion movement (a.c. conductivity) which occurs at high frequencies.

In this chapter, we will review recent developments concerning both d.c. and a.c. conductivity. Several important theoretical and phenomenological models which describe ionic conductivity are discussed. The missing information for better understanding of the conductivity and inadequacies of conduction models are pointed out. The role of glass structure in ionic conduction is considered following the review of conductivity. The experimental techniques (EXAFS, XPS and IR) which have been used in this work for the determination of glass local structure are introduced. At the end, the importance of local structure in ionic conductivity are emphasized.

2.2 D.C. Conductivity (σ_{dc})

2.2.1 Introduction

The ionic d.c. conductivity, σ_{dc}, of a solid with only one kind of charge carrier can be written in the form of

$$\sigma_{dc} = nq\mu \tag{2.1}$$

where n is the mobile ion concentration, q is the charge on an ion, and μ is its mobility [15,26]. In crystals the conduction occurs via a defect mechanism. The concentration of ionic carriers is thermally activated, which is given by:

$$\begin{aligned} n &= N_o \exp\left(-\frac{\Delta G_c}{kT}\right) \\ &= N_o \exp\left(\frac{\Delta S_c}{k}\right)\exp\left(-\frac{\Delta H_c}{kT}\right) \\ &= n_c \exp\left(-\frac{\Delta H_c}{kT}\right) \end{aligned} \tag{2.2}$$

where N_o is the nominal ion (charge carrier) concentration, ΔG_c is the free energy for the formation of n defect pairs, ΔS_c is the associated entropy, ΔH_c is the associated enthalpy, k is the Boltzmann constant, T is the absolute temperature and n_c is the effective infinite temperature ion concentration which includes the entropy term [26,28,29]. The mobility μ in eq. (2.1) is related to diffusivity (D) via the Nernst-Einstein relation [15,26]:

$$\mu = \frac{q}{kT}D = \frac{q}{kT}fd^2\nu \tag{2.3}$$

where f is a geometric correlation factor, d is the jump distance between two ion sites and ν is the jump frequency. The jump frequency ν is also known to be thermally activated and can be expressed as [15,26]:

$$\begin{aligned} \nu &= \nu_o \exp\left(-\frac{\Delta G_m}{kT}\right) \\ &= \nu_o \exp\left(\frac{\Delta S_m}{k}\right)\exp\left(-\frac{\Delta H_m}{kT}\right) \\ &= \nu_m \exp\left(-\frac{\Delta H_m}{kT}\right) \end{aligned} \tag{2.4}$$

where ν_o is the attempt frequency, ΔG_m is the free energy for ion migration, ΔS_m is the associated entropy, ΔH_m is the associated enthalpy and ν_m is the attempt frequency including entropy term [28,29]. By combining eqs. (2.1), (2.2), (2.3) and (2.4), we can obtain ionic conductivity σ_{dc}:

$$\begin{aligned} \sigma_{dc} &= \frac{n_c q^2}{kT} f d^2 \nu_m \exp\left(-\frac{\Delta H_c + \Delta H_m}{kT}\right) \\ &= \frac{\sigma_o}{T}\exp\left(-\frac{E_{dc}}{kT}\right) \end{aligned} \tag{2.5}$$

where

$$\sigma_o = \frac{n_c q^2}{k} f d^2 \nu_m \tag{2.6}$$

is a temperature independent constant called the pre-exponential term and $E_{dc} = \Delta H_c + \Delta H_m$ is the d.c. activation energy for conductivity. The theoretically derived eq. (2.5) for d.c. conductivity is an Arrhenius type equation which describes well the experimental results in the literature (Fig. 2.1) [30] and those in the present work (Fig. 2.2) [16]. Note that the slopes of the Arrhenius plots (σ_{dc}•T vs. 1/T) in Figs. 2.1 and 2.2 represent the activation energy for d.c. conductivity, E_{dc}.

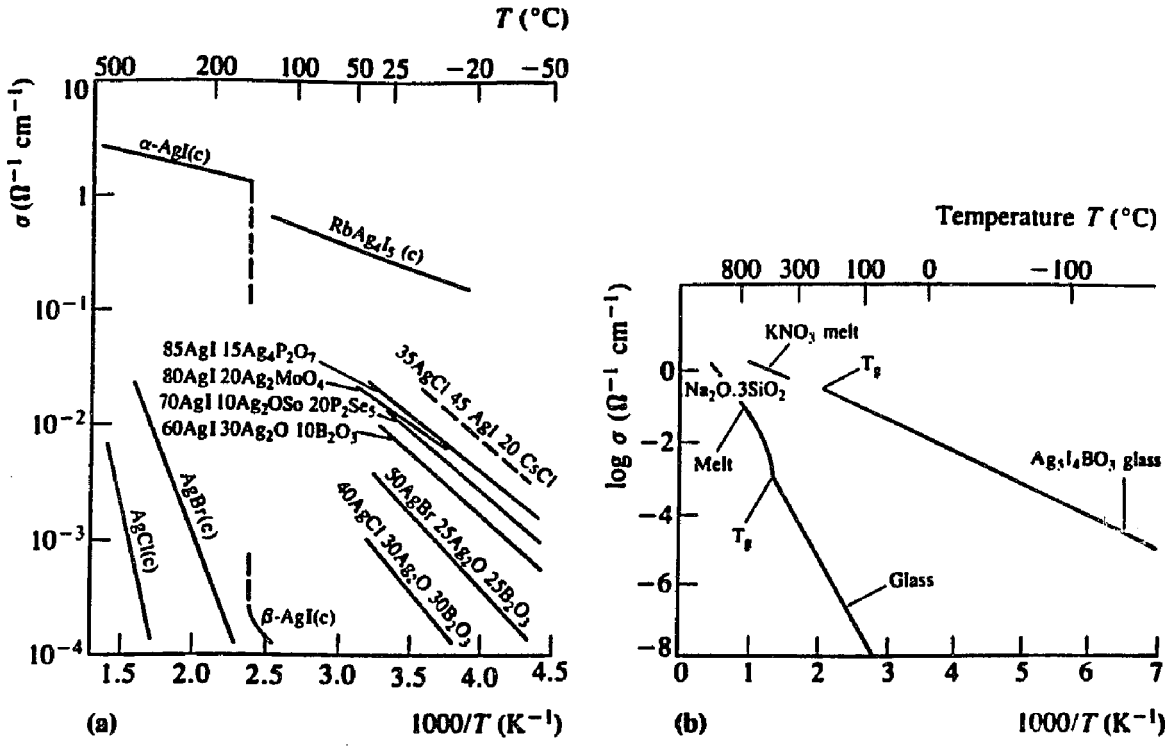

Figure 2.1 Arrhenius plots of the d.c. conductivity in ionically conducting solids: (a) Ag^+ ion conducting glasses and crystals. (b) Poorly conducting and superionic glasses.

Unlike ionic conduction in crystals where E_{dc} can be considered from two separate contributions-the concentration of charge carriers (ΔH_c) and their mobility (ΔH_m) that can be distinguished at different intrinsic and extrinsic temperature regions, the conduction in glasses is quite complicated mainly because the ΔH_c and the ΔH_m simultaneously change

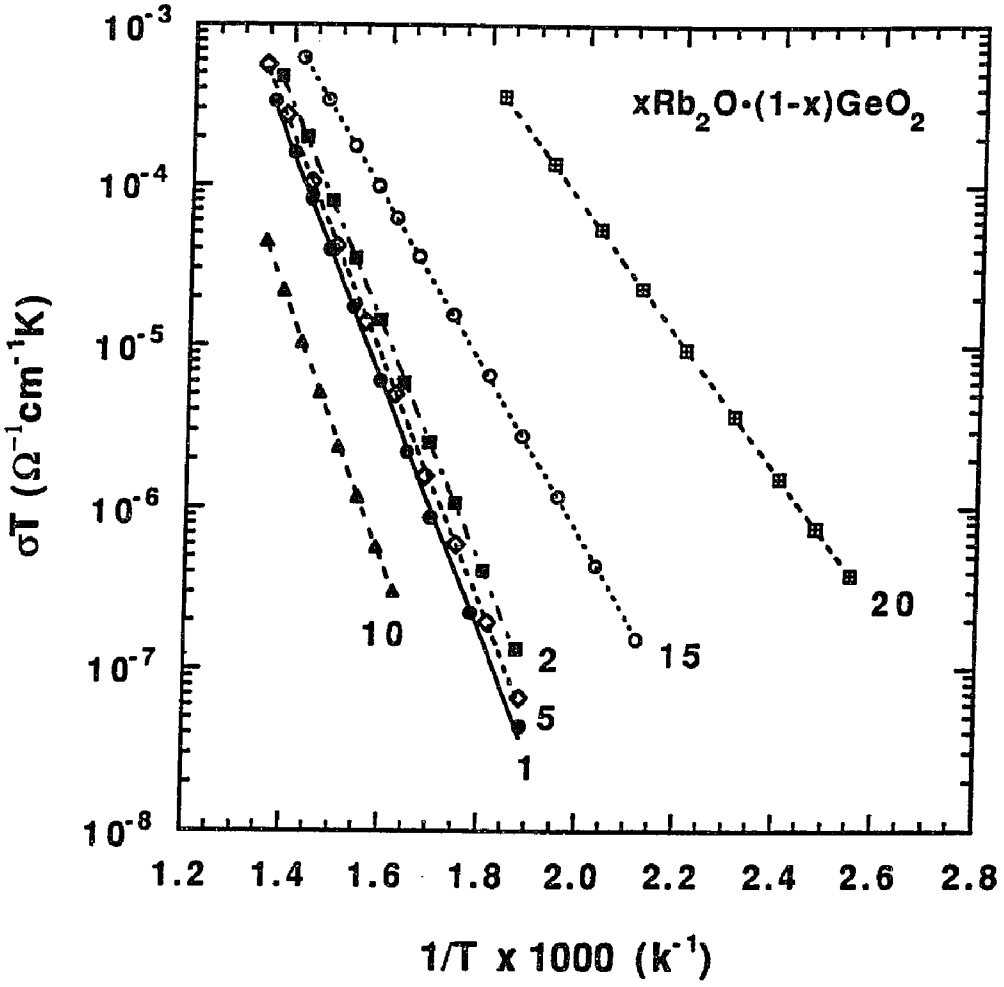

Figure 2.2 D.c. conductivity Arrhenius plots of $\sigma_{dc}T$ vs. 1/T for $xRb_2O\bullet(1-x)GeO_2$ glass series [16]. Rb_2O mol% is identified for each curve.

with varying compositions. In addition, the individual pre-exponent parameters (such as n_c, f, d and ν_m in eq. (2.6)) are all merged into one experimentally determined pre-exponential term (σ_o). This makes it difficult to understand ionic conductivity through the pre-exponential term. The mechanism of ion conduction in glasses has not yet been completely understood, especially regarding glass structure. In the following section, we

introduce the physical description of structure-based ion jumps and the role of an electric field in assisting the ion jumps. The importance of glass structure is then emphasized.

2.2.2 Physical Description of Ion Jumps

D.c. ionic conductivity involves the long range migration of ionic charge carriers through the material under the driving force of an applied electric field. When the long range movement occurs, mobile ions need to overcome the potential energy barrier (E_{dc}) around it. E_{dc} represents the highest barrier in the path of least resistance for ion jumps in the glass. The derivation of σ_{dc} in terms of E_{dc} can be found elsewhere in standard text books [15,26,27]:

$$\begin{aligned} \sigma_{dc} &= \frac{nq^2d^2}{kT} p \\ &= \frac{\alpha nq^2d^2}{h} \exp(-\frac{E_{dc}}{kT}) \end{aligned} \qquad (2.7)$$

where n is the number of mobile ions, q is the charge on the ion, d is the jump distance, k is the Boltzmann constant, p is the probability that an ion can move either to the right or to the left sites, h is the Plank constant, α is a geometric accommodation coefficient. Clearly, E_{dc} inside the exponential term is the dominant factor for σ_{dc}. It is worthwhile to mention that ionic conductivity is not affected by the electric field, the function of which is merely to direct the random diffusion of ions that occurs spontaneously at any given temperature T. The field does not pull the ions out of the wells. It only affects the configuration of the potential wells (see Fig. 2.3).

In general, E_{dc} in glasses is believed to comprise the electrostatic forces of attraction

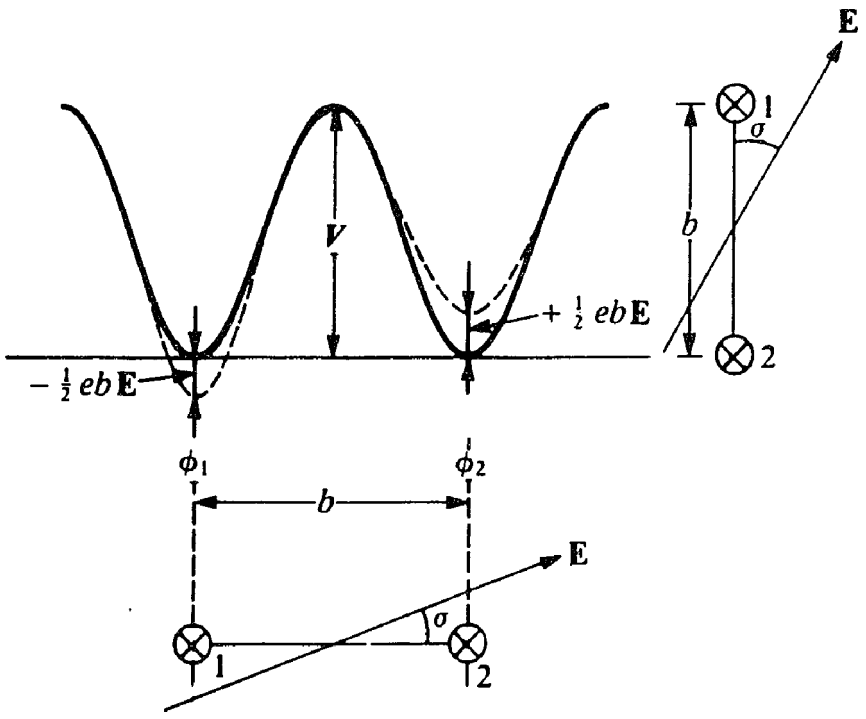

Figure 2.3 Potential well energy configuration in a glass or ceramic. Solid lines indicate energy without electric field (**E**); dashed lines indicate energy with **E** applied.

between the mobile ion and its surrounding anions and the elastic forces of constriction (strain forces) encountered by this ion when it goes through the glass matrix. E_{dc} has been investigated through d.c. conductivity for over 50 years. However, the understanding of E_{dc} is still far from complete. This is due to the fact that glass local structure which

determines E_{dc} (see Fig. 2.3) is not well understood. In this dissertation we will focus on examining E_{dc} in relation to the local structure rather than on separating E_{dc} into constituent parts. In the following section, a detailed review of the development of various mechanisms for d.c. conductivity is given.

2.2.3 Models of Ionic Transport Based on Glass Structure

A number of models have been proposed to explain various aspects of E_{dc} for d.c. ionic conductivity in glasses: they include Anderson-Stuart's 'strong-electrolyte' model [31], the 'weak-electrolyte' model [32,33], the 'defect' model [34,35] (for a review, see refs. [1,30]), and more recently the modified random network (MRN) based cooperative ion movement model [36,37]. These models have their own distinct characters as briefly discussed next:

(1) The 'strong-electrolyte' model. In this model the effective mobile ion concentration is assumed to be independent of temperature, making only the mobility term (see eq. (2.1)) responsible for E_{dc}. In this regard, E_{dc} is evaluated in terms of a specific microscopic picture as shown in Fig. 2.4: a cation is presumed to hop from an occupied site in the vicinity of a negatively charged site (such as an NBO site) to another NBO site by passing a 'gateway' formed by BOs. As a consequence, E_{dc} may be viewed as consisting of two terms, an electrostatic binding energy E_b required to remove a cation from an NBO site, and a strain energy E_s required to open the 'gateway'. By various assumptions and approximations, it was shown by Anderson and Stuart [31] that:

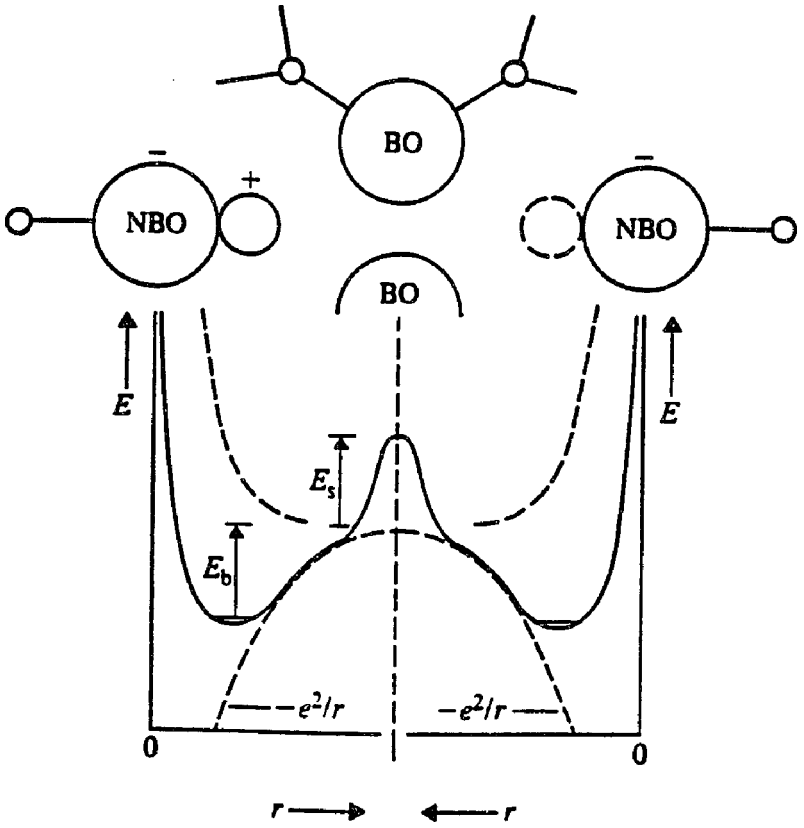

Energetics of ionic transport

Figure 2.4 A pictorial view of the Anderson-Stuart 'strong-electrolyte' model for d.c. conductivity [31].

$$E_{dc} = E_b + E_s = \frac{\Gamma Z Z_o e^2}{\gamma (r + r_o)} + 4\pi G r_d (r - r_d)^2 \qquad (2.8)$$

where G is the shear modulus; r, r_d and r_o are the radii of the cation, the 'gateway' through which it passes, and the oxygen ion, respectively; Z and Z_o are the valences of the cation

and oxygen; Γ is a 'lattice' parameter and γ is the covalency parameter approximated to the dielectric constant of the lattice.

The A&S model considers ion jumps as a single step with one energy barrier, E_{dc}, and all mobile ions participate in the conduction process. This model attempted to semi-quantitatively predict the energetics of long range ion migration and was found to work well for some amorphous materials such as Li^+ ion conducting glasses [38] and liquid electrolytes [39]. However, this model merely depends on some empirical or poorly defined parameters and ignores the details of glass structure and jump mechanism, which makes its applicability remain to be examined, especially on insulating glasses [40]. Also, it cannot explain complex behaviors such as the mixed alkali effect [41,42].

(2) The 'weak-electrolyte' model. Here μ is assumed to be independent of ion concentration and only responsible for a very small portion of E_{dc}. E_{dc} is suggested to be determined by the mobile ion concentration which is thermodynamically equilibrated at a given temperature. Ravaine and Souquet [32,33] were the first to propose the 'weak-electrolyte' model. They observed for Na_2O-SiO_2 glasses that a large increase in ionic conductivity is accompanied by a large increase in Na_2O activity (a_{Na2O}). as shown in Fig. 2.5. An empirical relation that σ_{dc} is proportional to square root of a_{Na2O} was found

$$\sigma_{dc} = C \bullet (a_{Na_2O})^{\frac{1}{2}} \qquad (2.9)$$

where C is a constant and a_{Na2O} is proportional to $[Na^+]\bullet[ONa^-]$ if there is a thermal equilibrium for the mobile ion Na^+ concentration, where

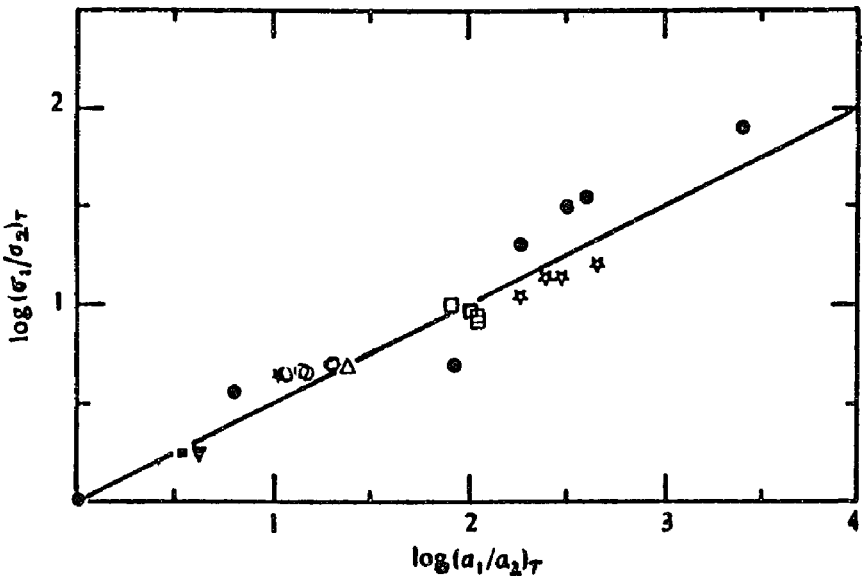

Figure 2.5 Comparison between ratio of conductivities and ratio of activities of alkali oxide [32].

$$Na_2O \rightleftharpoons Na^+ + ONa^- \qquad (2.10)$$

For conventional thermodynamics and the assumption of constant activity coefficient, $[Na^+]$ = $[ONa^-]$. Thus

$$\sigma_{dc} \propto [Na^+] \tag{2.11}$$

Clearly, eq. (2.11) shows that ionic conductivity is merely a function of Na^+ ion concentration. The 'weak-electrolyte' model considers thermodynamic equilibrium of ion concentration; whereas it ignores the effect of glass structure. An explicit implication for this model is that the mobility must remain constant over the concentration range under consideration (i.e. $\sigma_{dc} = [Na^+]eu$ and $\sigma_{dc} \propto [Na^+]$, so u stays constant). Indeed, the conductivity of many high alkali concentration silicates was well described by this model [32,33]. This may be due to the fact that ion mobility in these glasses is very small and nearly constant in the high alkali regime where glass structure is wide open. However, this is not true in highly insulating oxide glasses with low alkali concentration. For such glasses, the addition of alkali oxides dramatically changes the glass structure, and hence the mobility. The 'weak-electrolyte' behavior considers that a mobile ion must be dissociated before it can move, and the ion mobility is independent of ion concentration. However, this assumption is not generally true as both the dissociation process and the migration step itself are strongly structural dependent.

(3) The 'defect' model [34,35]. It is based on the concepts employed for crystalline ionic conductors, where ionic transport usually involves the formation and migration of particular defects (e.g. vacancies, interstitials, and interstitialcies). In this model ionic conduction for glasses occurs through either an interstitialcy or a vacancy mechanism. Only a relatively small portion of ions are mobile at any instant; resembling the 'weak-electrolyte' approach.

Since the electrical conductivity arises from a diffusion mechanism, a 'conductivity'

diffusion coefficient, D_σ, can be defined via the Nernst-Einstein relation

$$D_\sigma = \frac{kT\sigma}{nq^2} \tag{2.12}$$

However, the tracer diffusion coefficient, D* will not be equal to D_σ because it is influenced by correlation effect; the two coefficients are related by the so-called Haven ratio [35]

$$H_R = \frac{D^*}{D_\sigma} \tag{2.13}$$

where $H_R \leq 1$. The significance of the Haven ratio has been extensively discussed. Many people believed that $H_R \leq 1$ arises from the jumping correlation between two cations (in interstitialcy mechanism) or a cation and its nearby vacancy site (in vacancy mechanism) [1,15]. It has been observed that H_R is close to 1 at extremely low alkali concentration and gradually decreases toward 0.3 - 0.4 at high alkali concentration (see Fig. 2.6 [15]). A low H_R indicates that alkali movement is highly correlated in the tracer-diffusion process, where certain types of jump are precluded following a given hop. On the other hand, a high H_R (= 1) implies a direct interstitial process. Thus, in principle, measurement of H_R allows the diffusion mechanism to be identified. Jain et al. [43] proposed a structural model to account for these observations, in which they suggested that there were many equivalent alkali cation interstitial sites around a NBO, each of them being associated with one alkali. At very low alkali concentration, the diffusive motion of an alkali is mainly direct interstitial mechanism between interstitial sites at different NBO sites. As the alkali

concentration increases, the alkali cation-cation interactions become more correlated, causing H_R to decrease.

Ion jumping approach is straightforward in crystals. However, for glasses the precise value of H_R cannot be obtained without knowing the geometry of the jump process. Also

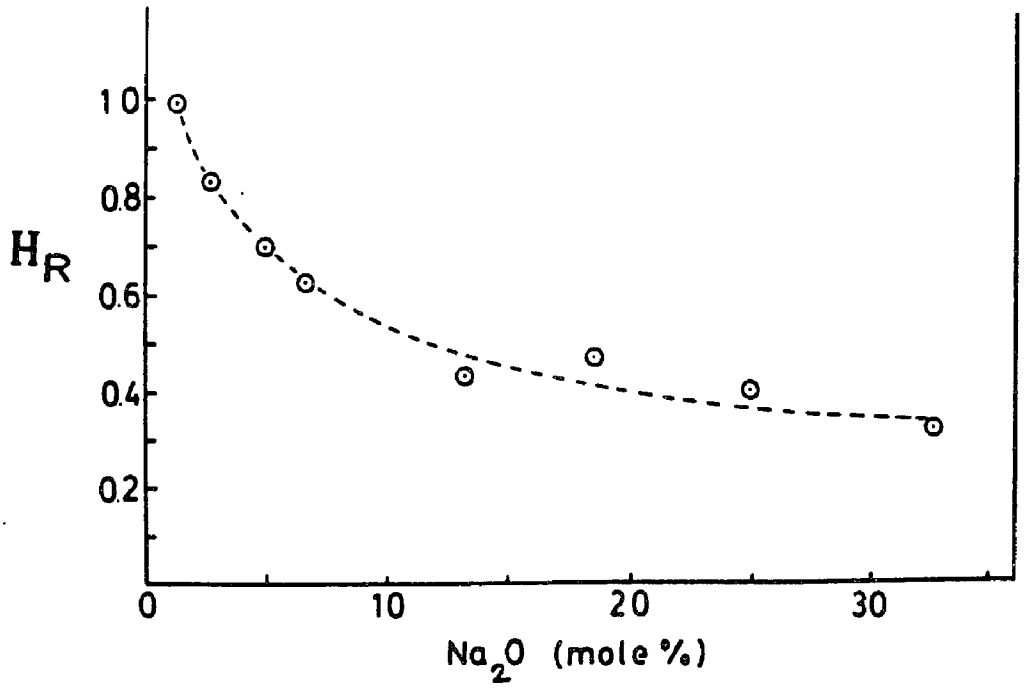

Figure 2.6 Haven ratio as a function of sodium concentration in alkali borate glasses at 300°C [15].

it is not clear how interstitial or vacancy defects are defined in a non-crystalline host. So the applicability of the 'defect' model to glasses has not been well understood due to the lack of knowledge of glass structure.

(4) The MRN based cooperative ion movement model. In this model the activation energy barrier is determined by the cooperative ion motion. Greaves and Ngai [36,37] propose this ion transport model for silicate glasses based on the modified random network (MRN) glass structure model [19,20]. According to the MRN model the glass structure is comprised of two interlacing sublattices: (a) network regions predominantly constructed from the network forming cations and oxygens and, (b) inter-network regions predominantly made of modifier cations. That is, the alkali ions are not distributed randomly and homogeneously through the structure, but segregate in the inter-network regions. When alkali concentration is small, the cooperative effect is negligible. As alkali concentration increases, modifier regions extend to form percolation 'channels' through which ion transport takes place. This makes the motion of ions highly correlated with each other. One important drawback of this model is the strain part of the activation energy is not considered. This model works well for the silicate glasses with small strain energy. However, its validity remains to be tested for other glasses, especially those with highly compact structure like germanates.

A review of the above models shows that the greatest difficulty in understanding the d.c. conductivity probably arises from the lack of knowledge of the glass local structure. Specifically, a one-to-one correspondence between local structure and ionic conductivity is yet to be established. Without local structural information of network formers and

modifiers, an understanding of the ionic conduction process in glasses cannot be obtained.

2.3 Electrical Conductivity Relaxation (ECR)

2.3.1 Introduction

The electrical conductivity relaxation (ECR) phenomenon refers to the time dependent response of charge in a sample when an electric field is applied [15,44,45,46]. Monovalent cations (M^+) such as alkali or silver ions are the most common mobile charge carriers and are predominantly responsible for this dynamic response, although other kinds of less mobile ions may also have a minor contribution [47]. It has been observed [1,46,48] that ECR generally occurs in the intermediate frequency region which may span from sub-audio to microwave or higher frequency range depending on materials and temperature. This observation is not surprising because at low frequencies, a charge carrier easily follows the applied field; and at very high frequencies, it seems relatively motionless with respect to the field, both leading to negligible electrical relaxation. Study of the physical origin of ECR in solids has been of the subject of dielectric research for the last couple of decades [1,45,49,50]. However, the understanding of ECR behavior has remained far from clear.

It has been experimentally demonstrated that the time-dependent ECR behavior after the application of an electric field is not simply exponential. This non-exponentiality of electrical relaxation in ionic glasses was first investigated by Moynihan et al. [44,45] using the following Kohlrausch-Williams-Watts (KWW) equation [51,52], which was originally applied to account for the relaxation phenomenon of many kinds of stresses in

complex systems:

$$\phi(t) = \exp[-(\frac{t}{\tau^*})^{\beta}] \qquad (2.14)$$

where τ^* is a macroscopic relaxation time (which is equivalent to τ_{dc}) and β is a value between 0 and 1, both of which are material dependent [53]. In frequency domain, many formalisms have been used to equivalently describe the ECR behavior depending on the measured electrical conductance, G, and capacitance, C [54]. These formalisms include: complex permittivity, complex admittance, complex impedance, complex modulus, etc. Among them, the frequency dependence of the real part (σ') of complex conductivity ($\sigma^* = \sigma' + i\sigma''$) and the imaginary part (M") of complex modulus ($M^* = M' + iM''$) are the two most popular forms (M^* is mathematically defined as the reciprocal of complex dielectric constant (ε^*) [1,46]).

σ' for many solids is found to follow a frequency-dependent power law as shown in Fig. 2.7 (for a review, see Jonscher [55]):

$$\sigma' = \sigma_{dc} + A\omega^s \qquad (2.15)$$

where σ_{dc} is the d.c. conductivity, A is a temperature dependent parameter, $\omega = 2\pi f$ (f is the frequency) and s is the power law exponent describing the electrical relaxation behavior of the solid, with a value between 0 and 1 (mostly 0.5 - 0.6) [29]. For an ideal leaky solid (e.g. one with low ion concentration), s approaches 0. For a real dielectric solid (one with high mobile ion concentration or at high temperatures), s increases toward 1. Here we exclude the s = 1 region in this argument, which usually occurs at high frequencies and

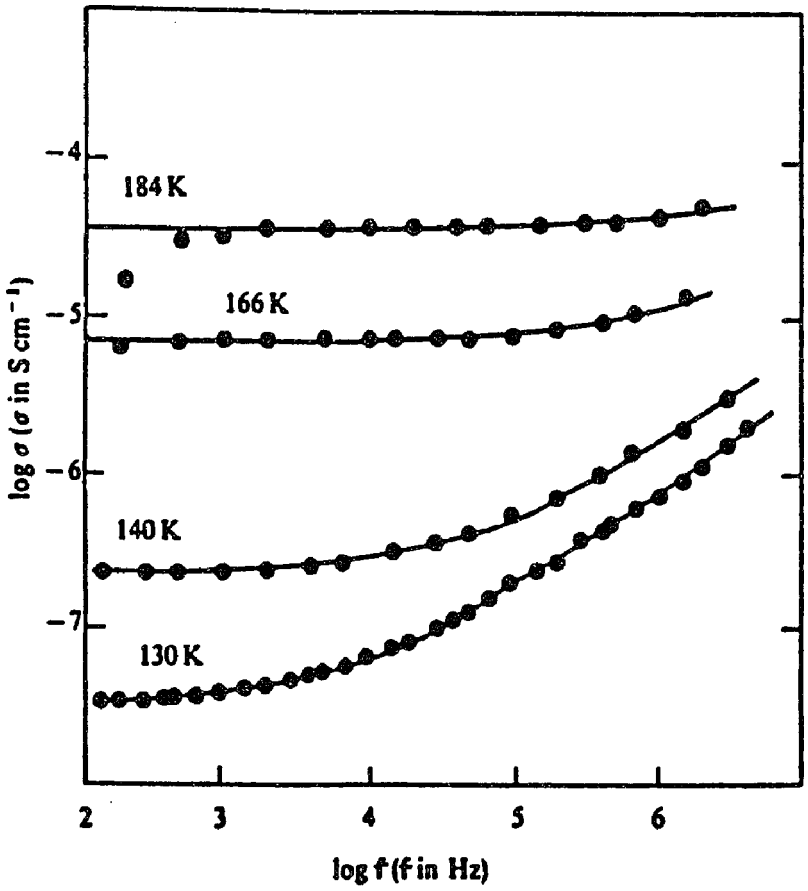

Figure 2.7 A Jonscher fit of a.c. conductivities in $Ag_7I_4AsO_4$ glass at various temperatures [29].

low temperatures regardless of the types of dielectrics investigated [56]. It was asserted by Dyre [57], Elliott [58] and Nowick et al. [59] that the power law formalism should be preferred because it describes the frequency dependent electrical response over a much wider frequency range. However, a 'window' effect [60] has been shown to exist according to which the value of the power law exponent can be altered depending on the choice of

frequency range, thus limiting the usefulness of the power law formalism.

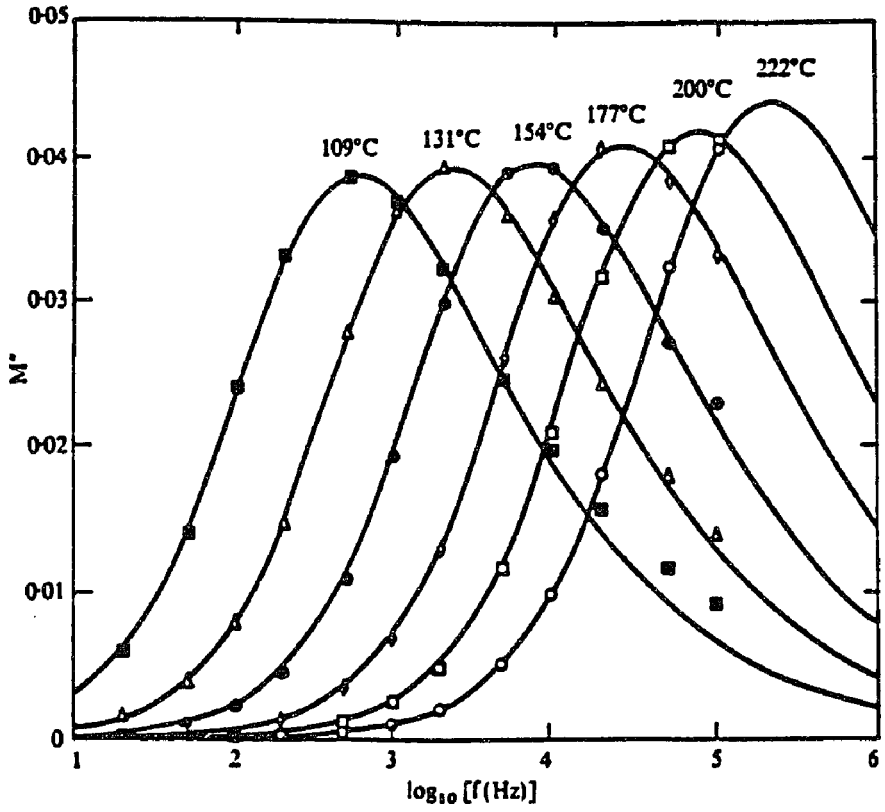

Figure 2.8 A KWW fit of conductivity relaxations (modulus spectra) in lithium triborate glass [50].

On the other hand, M" vs. ω plots show a peak near the d.c. conductivity relaxation time (τ_{dc}) (see Fig. 2.8 [50]), which is best described by the Fourier transform of the KWW function (see eq. (2.14)):

$$M^*(\omega) = \frac{1}{\varepsilon^*} = M' + iM''$$
$$= \varepsilon_\infty^{-1}\left[1 - \int_0^\infty dt \exp(-i\omega t)\left(-\frac{d\phi}{dt}\right)\right] \qquad (2.16)$$

where ε_∞ is the high frequency dielectric constant. For an ideal leaky dielectric, $\phi(t)$ is a simple exponential decay function (where $\beta = 1$) and a plot of M" vs log ω gives a Debye like peak at $\omega_{max} = 1/\tau_{dc}$, for which the full width at half maximum (FWHM), Δ = 1.14 decades. A broader, asymmetric (non-Debye) M" peak gives β a value < 1, which is usually observed in real solids [45]. The broad M" peaks seen in Fig. 2.8 ($\beta = 0.52$) indicate non-exponential decay processes.

Although the use of M" has been questioned by Elliott [58] and Nowick et al. [59] for describing the ECR behavior, especially the relaxation at high frequencies, as long as the discussion of the relaxation behavior is restricted to the vicinity of d.c. relaxation time (τ_{dc}, given by ($\varepsilon_\infty C_o/G$) [60]), M" should be suitable for describing the ECR phenomenon [9,46]. Here C_o is the vacuum capacitance. Thus, the M" formalism is appropriate for discussing the ECR behavior around τ_{dc}, but for frequencies >> $1/\tau_{dc}$, the data are better analyzed using the power law formalism.

2.3.2 Relaxation Time Distribution Model

It has been known experimentally that β in vitreous ionic conductors usually decreases from ≈ 1.0 at very dilute mobile ion concentration to ≈ 0.5 at high concentrations [61,62]. A value of $\beta < 1$ was initially attributed by Moynihan et al. [44,45] to the distribution of relaxation times, which arises from the amorphousness or structural disorder

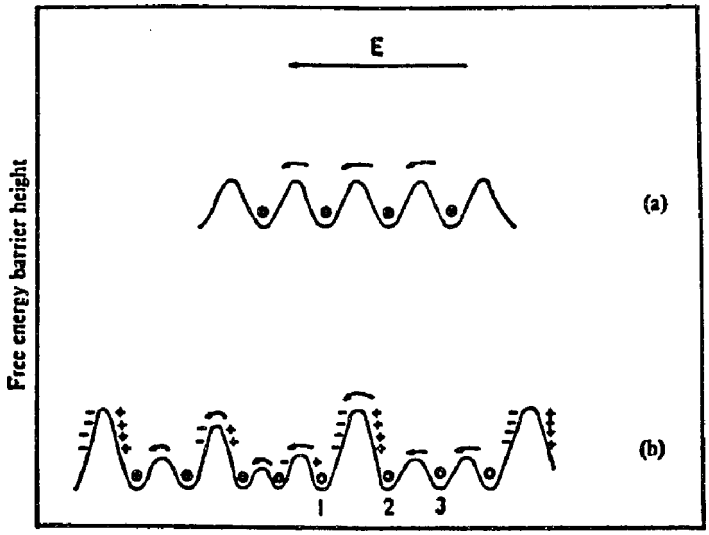

Figure 2.9 Schematic representation of energy barriers of (a) a lattice with long range order (b) a vitreous solid with short range order [44].

in the solids. They suggested that for a solid with long range order, there is a single relaxation time; whereas for a vitreous solid with short range order, there exists a distribution of relaxation times as shown in Fig. 2.9. It is the distribution of relaxation times that broadens the M" peak, causing β to decrease from 1. The approach of this distribution of relaxation time model can be understood as follows:

From eqs. (2.14) and (2.16), M* can be written as

$$M^*(\omega) = \frac{1}{\varepsilon^*} = M' + iM'' = \frac{\varepsilon'}{\varepsilon'^2 + \varepsilon''^2} + i\frac{\varepsilon''}{\varepsilon'^2 + \varepsilon''^2} \tag{2.17}$$

where $\varepsilon^* = \varepsilon' + i\varepsilon'' = \varepsilon' + i\,(\sigma'/\omega\varepsilon_0)$. And because $\tau_\sigma = \varepsilon_\infty\varepsilon_0/\sigma'$ and $M_\infty = 1/\varepsilon_\infty$, then

$$\begin{aligned} M^*(\omega) &= M' + iM'' \\ &= M_\infty\left(\frac{i\omega\tau_\sigma}{1+i\omega\tau_\sigma}\right) \\ &= M_\infty\left[\frac{(\omega\tau_\sigma)^2 + i\omega\tau_\sigma}{1+(\omega\tau_\sigma)^2}\right] \end{aligned} \tag{2.18}$$

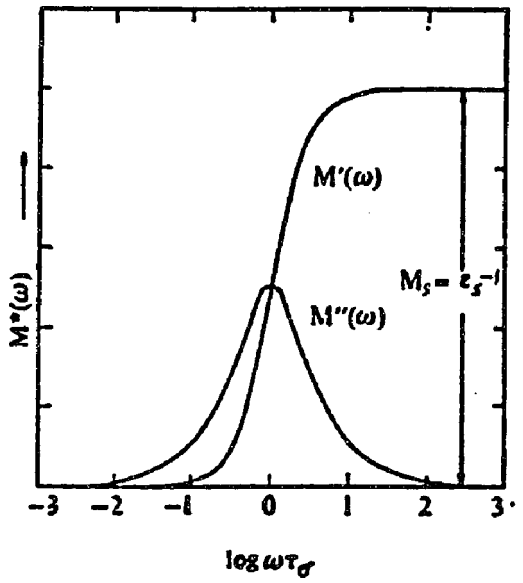

Figure 2.10 Frequency dependence of real and imaginary parts of M* for a dielectric with single conductivity relaxation time [44].

where τ_σ has units of time and is termed the 'conductivity relaxation time'. Plots of frequency dependence of real and imaginary parts of M* with single relaxation time are shown in Fig. 2.10. Note that the M" peak in this figure is an ideal Debye peak with FWHM = 1.14 decades. By introducing a distribution function, $g(\tau_\sigma)$, in eq. (2.18) for

vitreous solids with distribution of relaxation times, one obtains

$$M^* = M' + iM''$$
$$= M_\infty \int_0^\infty g(\tau_\sigma) d\tau_\sigma \left[\frac{(\omega\tau_\sigma)^2 + i\omega\tau_\sigma}{1 + (\omega\tau_\sigma)^2} \right] \qquad (2.19)$$

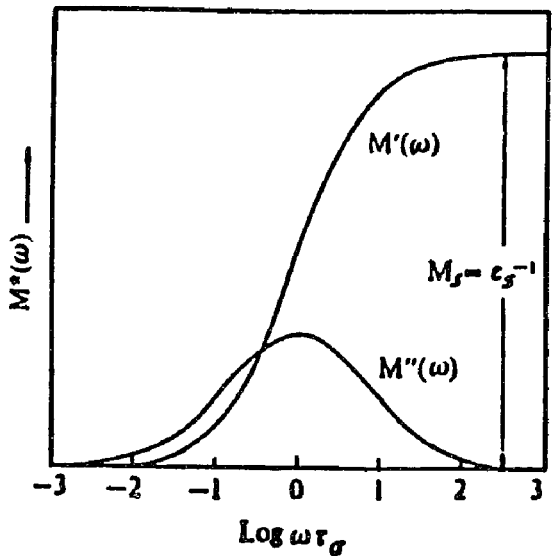

Figure 2.11 Frequency dependence of real and imaginary parts of M* for a dielectric with a distribution of conductivity relaxation times [44].

Fig. 2.11 shows the frequency dependence of real and imaginary parts of M* with a distribution of relaxation times in vitreous systems. The low and high frequency limits of M' and M" remain the same as those in the single relaxation time approach. The only effect of the distribution of relaxation times is to broaden the dispersion region for M' and to broaden and depress the maximum of the M" peak. The broadening of M" peak (the FWHM of M" peak) was then tabulated by Moynihan et al. [45] for different β values

Table 2.1 The corresponding β values for the Δ of M" peaks [45].

β	Δ
1.00	1.142
0.95	1.193
0.90	1.251
0.85	1.317
0.80	1.395
0.75	1.484
0.70	1.586
0.65	1.701
0.60	1.837
0.55	1.994
0.50	2.189
0.45	2.428
0.40	2.722
0.35	3.100
0.30	3.609

as shown in Table 2.0.

2.3.3 Ion-Ion Coupling Models

In contrast to the distribution of conductivity relaxation times model, Ngai et al. [49,50,63] proposed a very different explanation, suggesting, instead, that the broadening of M" peaks is due to the coupling between mobile ions, in which the motion of a charge carrier is greatly influenced by the relaxation of its neighborhood. They suggested that for ionic motion at time shorter than a characteristic time τ_c, there is only a single microscopic relaxation time:

$$\tau_o = \tau_\infty \exp\left(\frac{E_p}{kT}\right) \tag{2.20}$$

where E_p is the microscopic (primitive) activation energy. τ_o would be the relaxation time if there is no mobile ion-ion interaction. The broadening of modulus peak is caused by the interaction of mobile ions. They further showed that for $t > \tau_c$, there would be a macroscopic relaxation time which describes the ion-ion interaction:

$$\tau^* = \tau_\infty^* \exp\left(\frac{E_a^*}{kT}\right) \tag{2.21}$$

in which

$$E_p = \beta E_a^* \tag{2.22}$$

where β is the KWW exponent. $E_a^* > E_p$ due to the coupling effect (E_a^* is equal to E_{dc} of d.c. conductivity).

Subsequently, Kanert, Jain, Ngai and coworkers [53,64,65] successfully correlated the activation energy E_a^* to the activation energy of nuclear spin relaxation (NSR):

$$E_{NSR} = E_p = \beta E_a^* \tag{2.23}$$

implying that there indeed exists a microscopic activation energy, E_p.

The coupling model in which $\beta < 1$ is attributed to the coupling of mobile ions has been asserted by the observation that β increases with increasing E_a^* in alkali aluminogermanate glasses (Fig. 2.12) [53,64]. Here a high value of energy barrier E_a^*

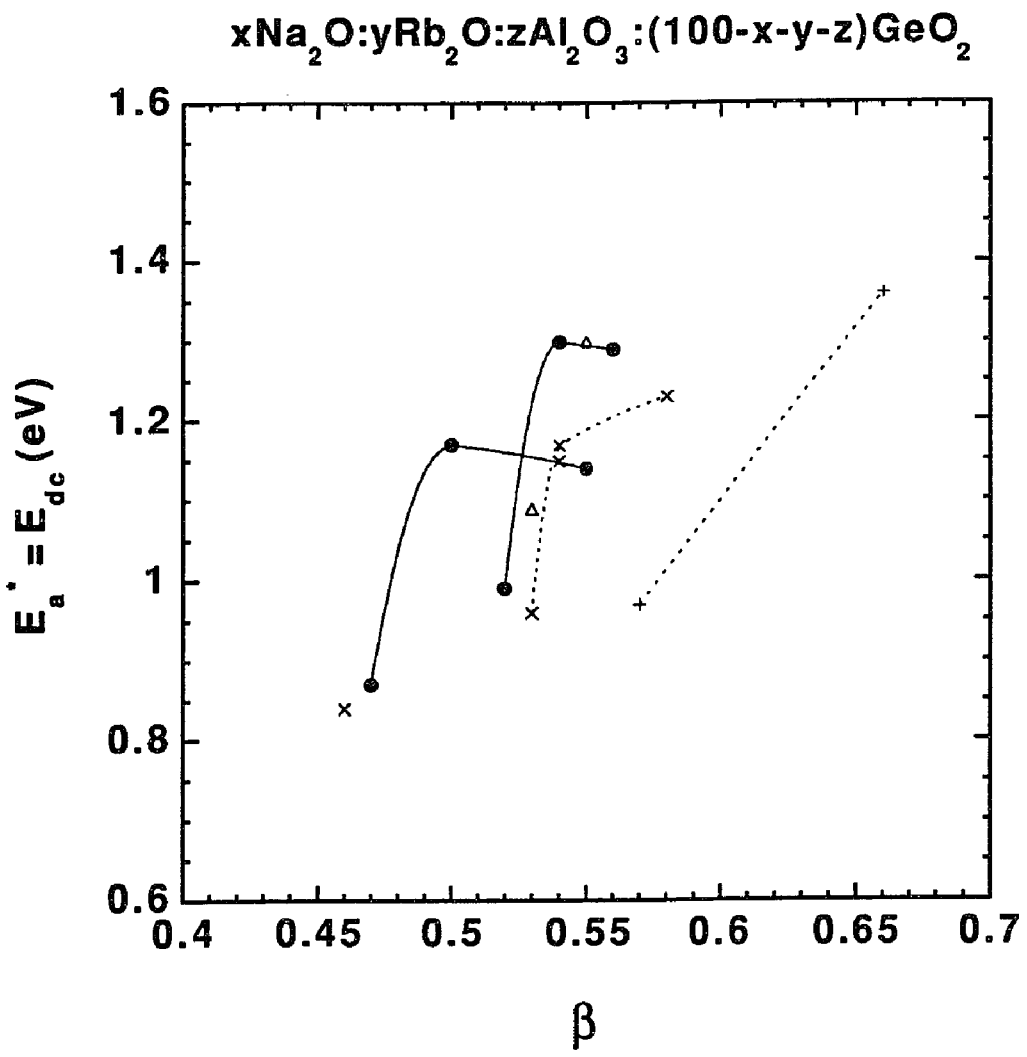

Figure 2.12 Plot of d.c. conductivity activation energy E_a* vs. β in mixed alkali aluminogermanate glasses [64].

suppresses strong coupling of mobile ions, thus increasing the β value.

Later, Elliott [66,67] proposed the 'diffusion controlled relaxation' (DCR) model in which non-ideal relaxation occurs when an ion diffuses to a site and causes the ion already residing at the site to move to another equilibrium position. Also, Funke's jump relaxation model [68,69] considers the jump of an ion to be coupled with the relaxation

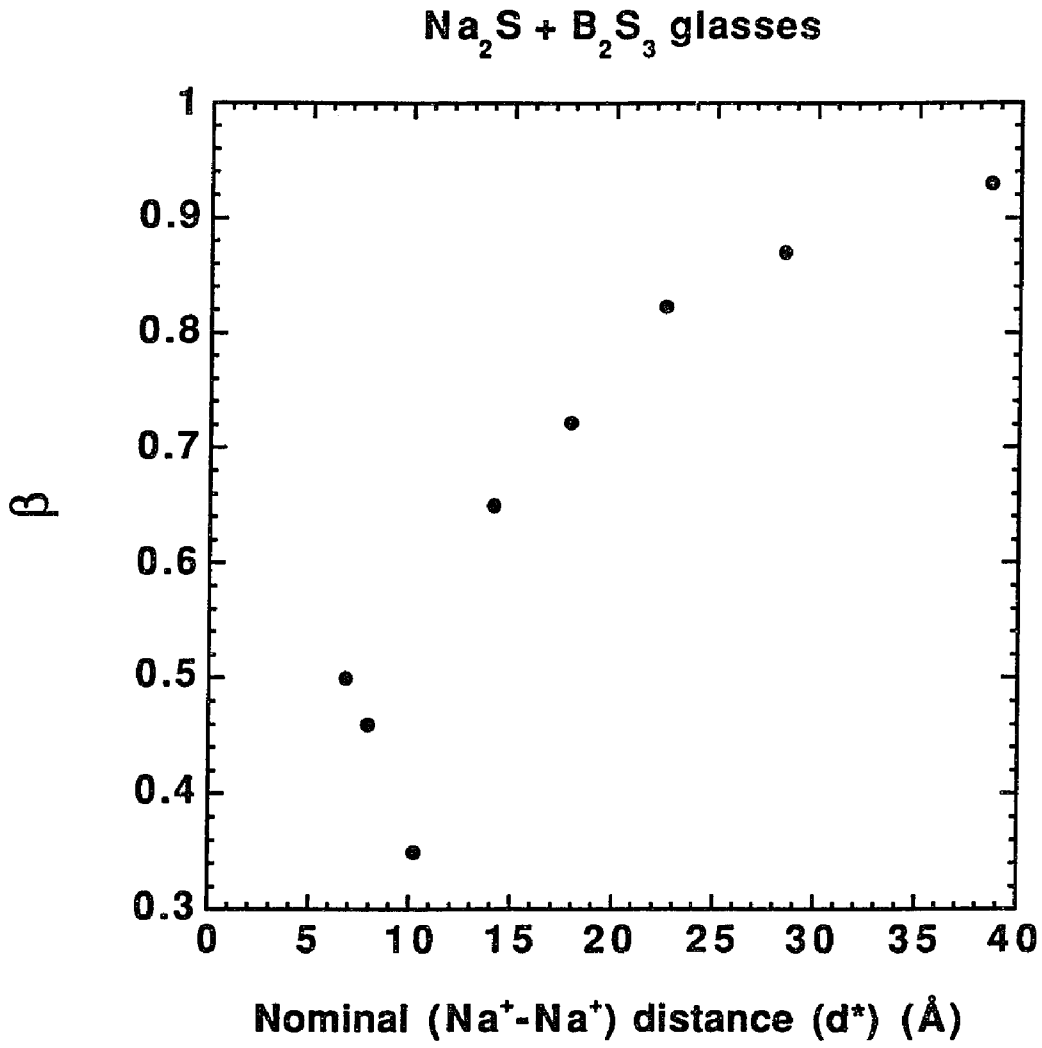

Figure 2.13 Plot of β vs. d* in $Na_2S + B_2S_3$ glass series [70].

of surrounding atoms. These mobile ion-ion coupling models have stimulated many subsequent experimental investigations. For example, Patel and Martin [70] show that nominal alkali ion-ion distance, d*, is correlated with β in view of the coupling mechanism (Fig. 2.13). This distance, d*, is one property in their glasses which shows a rapid decrease as does β with the initial increase of mobile ion concentration.

In summary, the non-Debye type electrical relaxation was attributed by Moynihan to the influence of structural disorder with distribution of hopping energy barriers. But Ngai and coworkers referred it to the strong coupling of mobile ions. Although their further NSR experiments suggested that β could be affected by the many-particle interaction, more convincing experiments are still needed to clarify this ambiguous problem. Specifically, little attention has been given in the past to establish the models for ionic conductivity relaxation based on glass structure.

2.4 Local Structure of Glasses

2.4.1 Introduction

About a decade ago, Greaves et al. [19] conducted pioneering EXAFS experiments on a few silicate glasses and determined the local structure around sodium and silicon. They found that the width of the first-neighbor peak, i.e. the Na-O distance distribution, was no more than could be expected from thermal motion (see Fig. 2.14). Therefore, they postulated that the alkali ions in silicate glasses were not distributed randomly as expected from Zachariasen's continuous random network (CRN) model [71] (Fig. 2.15). Instead, these ions were considered to have a rather well defined environment to the extent that the structure of glass may be considered to consist of regions rich in mobile ions separated by regions devoid of such ions such as shown in Fig. 2.16 [20]. If this new modified random network (MRN) model of glass is generally true, it has very far-reaching implications for our understanding of various properties, especially those dependent on the distribution and movement of alkali ions [37]. Computer simulations and molecular

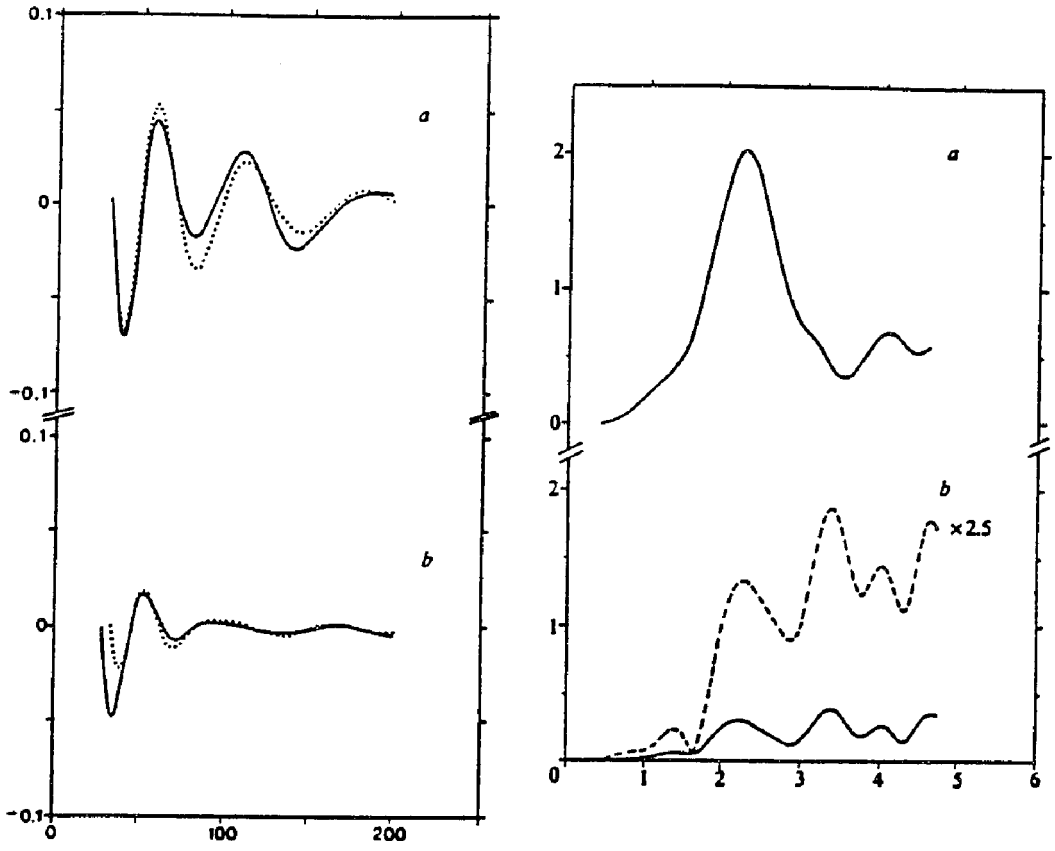

a. Sodium disilicate
b. Soda-lime-silicate

Figure 2.14 The environment of Na in various oxide glasses measured from Na K-edge EXAFS. Left: the normalized fine structure; right: the Fourier transforms [19].

dynamic calculations of the structure of silicate glass have also indicated segregation of alkali ions, which is consistent with the MRN model [72,73]. However, there is no report of direct microscopic observation of microheterogeneity on the scale postulated in the MRN structure. Also, it is not clear how universal such microsegregation is, if it does exist (e.g.

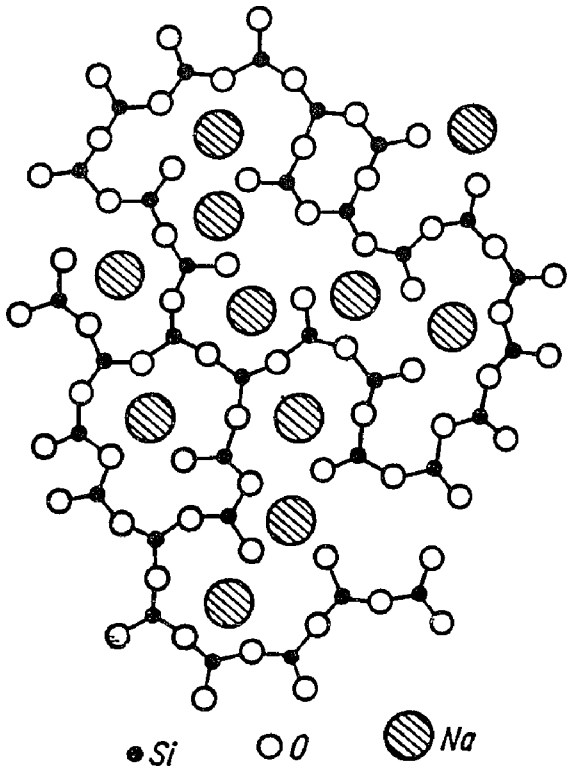

Arrangement of atoms (or ions) in a sodium silicate glass. When Na_2O is incorporated, the large sodium ions are, after rupture of oxygen bridges, located in the new, larger cavities.

Figure 2.15 Schematic representation of the continuous random network (CRN) model for a sodium silicate glass [71].

in alkali germanate glass).

2.4.2 Extended X-ray Absorption Fine Structure (EXAFS)

The EXAFS analysis has been proven to be very useful for studying the local structure of glass [19,20,74]. This technique is both atom-specific and local structure-

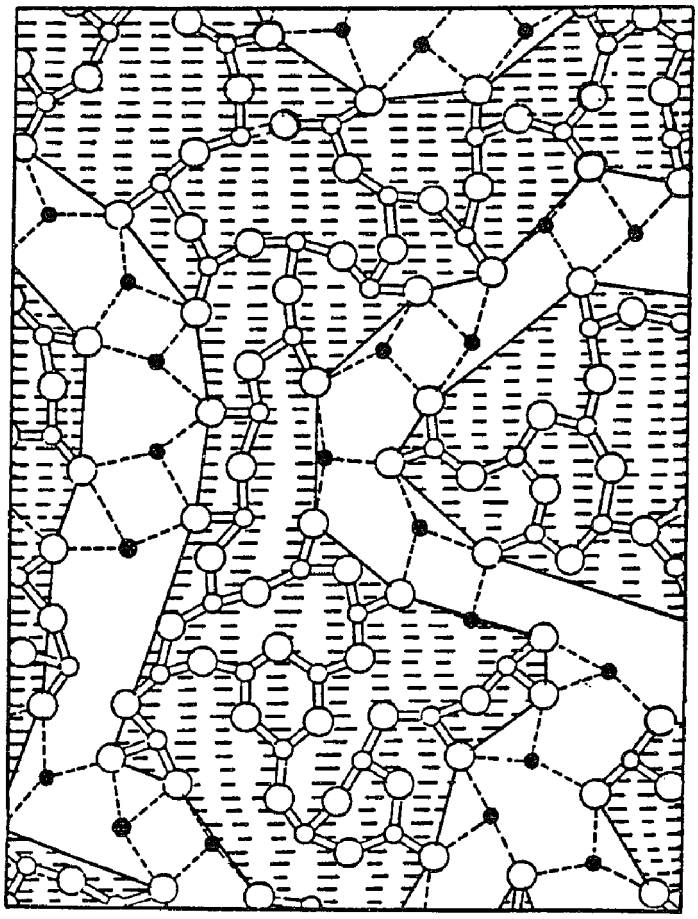

Figure 2.16 The modified random network (MRN) model for an oxide glass. Covalent bonds are shown by solid lines and ionic bonds by dotted lines. •: network modifier cation, o: network forming cation, O: oxygen.

sensitive. The EXAFS is a post-edge (post absorption edge) structure which does not arise from direct absorption process, but from what can be viewed as an 'internal diffraction' phenomenon. Consider that a photon with energy slightly higher than threshold is absorbed by an atom, and a photo-electron is ejected; the photo-electron wave will propagate outward

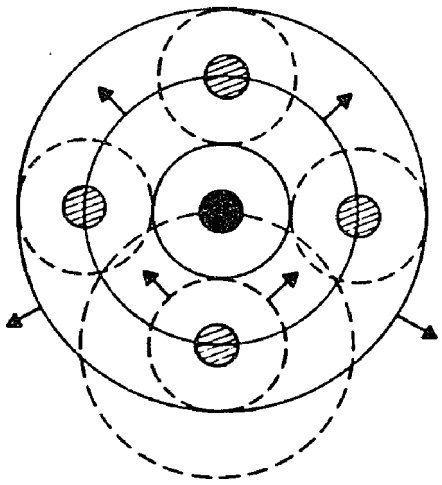

Filled circle: absorbing atom

Hatched circles: neighboring atoms

The solid circles represent the outgoing electron wave and the dashed circles represent the back-scattered electron wave; interference takes place where these waves overlap.

Figure 2.17 Schematic illustration of the EXAFS process. An atom absorbs an x-ray creating an outgoing photo-electron wave which was back-scattered off neighboring atoms [75].

to infinity if the absorbing atom is isolated (e.g. in a gas), in which case the absorption coefficient decreases smoothly from the absorption edge and then the EXAFS will be structureless. On the other hand, however, if an absorbing atom is surrounded by other atoms like in solids, the outgoing photo-electron wave will be back-scattered (diffracted),

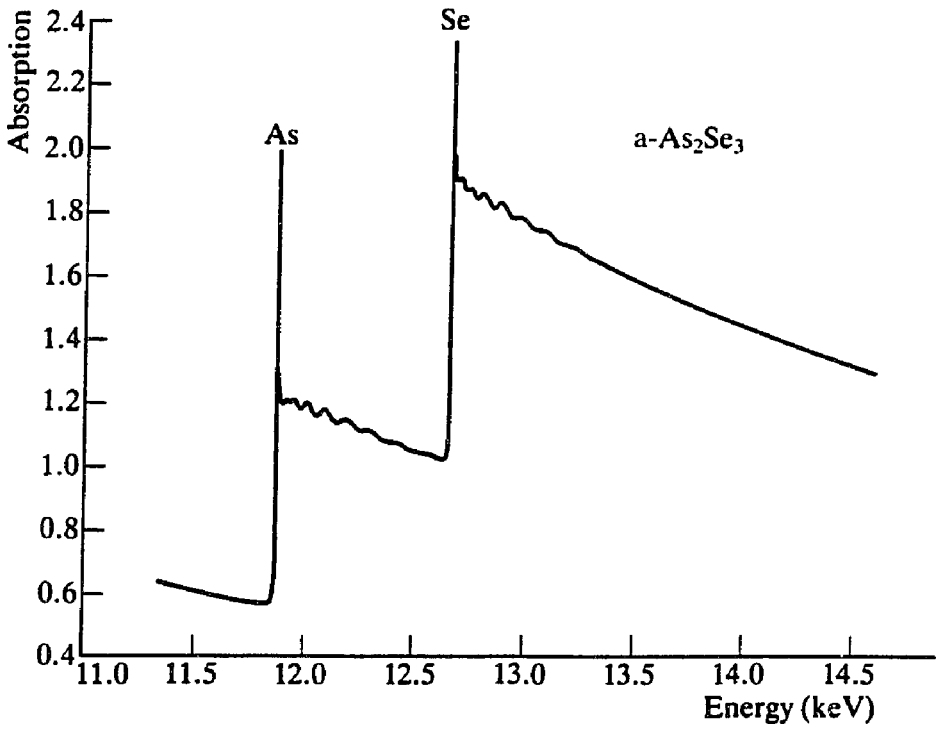

Figure 2.18 Extended x-ray absorption fine structure for a-As_2Se_3 showing the fine structure beyond the As and Se K edges [75].

and the back-scattered waves will interfere with the outgoing waves as shown in Fig. 2.17 [75]. This interference in turn influences the matrix elements for the absorption process, resulting in alternate constructive (when the interatomic spacing is an integral number of wavelengths) and destructive (half-integral number) interferences. Thus, one can expect to observe a periodic oscillation of x-ray absorption above the absorption edge - the fine

structure. It is the local bonding environment of the absorbing atom that determines the fine structure. Fig. 2.18 shows some observations of the EXAFS for amorphous As_2Se_3 glasses. Note that the As edge and the corresponding fine structure are widely separated from the Se edge and its fine structure.

The magnitude of the EXAFS signal, $\chi(E)$, is obtained from the measured value of x-ray absorption coefficient $\mu_x(E)$ by subtracting the background μ_o and normalizing:

$$\chi(E) = \frac{\mu_x(E) - \mu_o}{\mu_o} \qquad (2.24)$$

where E is the photo-electron energy. The EXAFS amplitude is calculated in the form of an analytic expression which can then be used to compare with experiment, thus providing structural information without the need for trial structures. Sayers et al. [76] have developed an analytic expression correlating the magnitude with various parameters in k space

$$\chi(k) = -\Sigma_j \frac{N_j}{R_j^2} \frac{|f_j(\pi)|}{k} \exp\left(-\frac{2R_j}{\lambda_e}\right) \exp\left(-2\sigma_j^2 k^2\right) \sin(2kR_j + 2\delta(k) + \eta_j(k)) \qquad (2.25)$$

where a sum over all shells of back scattering atoms, j. is taken, each containing N_j atoms at a distance R_j from the absorption atom. The magnitude of the EXAFS is proportional to N_j, inversely proportional to R_j^2 (since both the outgoing and back-scattered waves are assumed to be spherical, decreasing in amplitude as 1/R) and proportional to the back-scattering amplitude $|f_j(\pi)|$ from the atoms in the *j*th shell. The amplitude is attenuated because of the finite mean free path λ_e of the electrons in the material and by the Debye-

Waller factor involving mean displacements σ_j (static or thermal) about the equilibrium bond length. Finally, the amplitude is sinusoidally modulated by a function of phase shift of the electron. The structural information, R_j (interatomic distance), N_j (coordination number) and σ_j^2 (structural disorder, mean square displacement), can then be obtained by fitting eq. (2.25) to real experimental spectra for each shell surrounding respective atoms.

2.4.3 X-ray Photoelectron Spectroscopy (XPS)

In addition to EXAFS, XPS is a photoelectron technique which can be used to detect the fraction of bridging oxygen (BO: oxygen bonded with two silicon atoms) and non-bridging oxygen concentration (NBO: oxygen bonded with one silicon atom and one alkali ion) [24,77,78]. It was first shown by Gresh et al. [79] in late 1970s that XPS can distinguish between bridging oxygen and non-bridging oxygen in glasses. Later, Smets et al. [77], Onorato et al. [78] and Goldman [24] have applied this technique to evaluate the concentration of NBO in complex aluminosilicate, germanosilicate and simple silicate glasses. In their studies, the O 1s core level XPS spectrum was deconvoluted into two BO and NBO peaks with an energy separation ~ 2 eV.

In XPS, one measure the kinetic energy (E_K) of an electron ejected from a core level by an x-ray photon. The binding energy of the electron (E_B) is given as:

$$E_B = h\nu - E_K - W \qquad (2.26)$$

where $h\nu$ is the photon energy, E_K is the kinetic energy of the electron, and W is the spectrometer work function. E_B is a characteristic energy of both an element and its atomic energy level so that it can used to identify the presence of a particular element and its

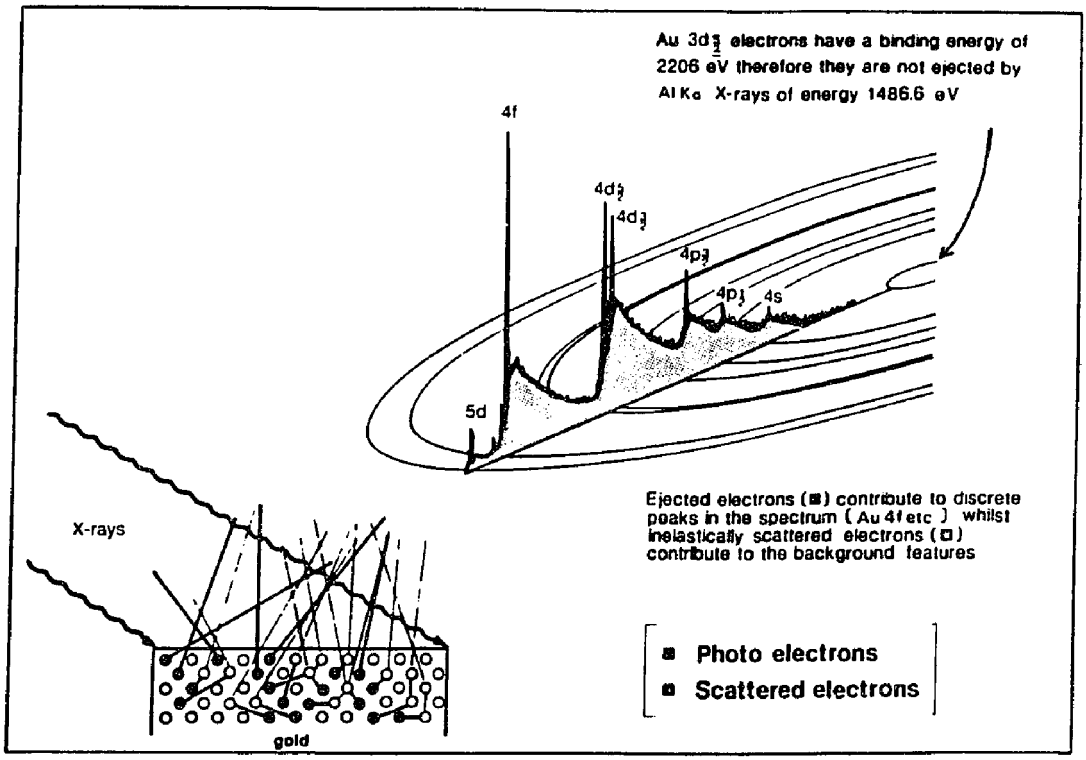

Figure 2.19 Photo-electron spectrum of gold showing the manner in which electrons escaping from the solid can contribute to the discrete peaks [80].

bonding environment. Fig. 2.19 shows the XPS spectrum of gold and how electrons escaping from the solid can contribute to the discrete peaks [80]. Fig. 2.20 shows the deconvolution of a C 1s peak, relating to the chemical shift for C atoms bonded to different environments [81].

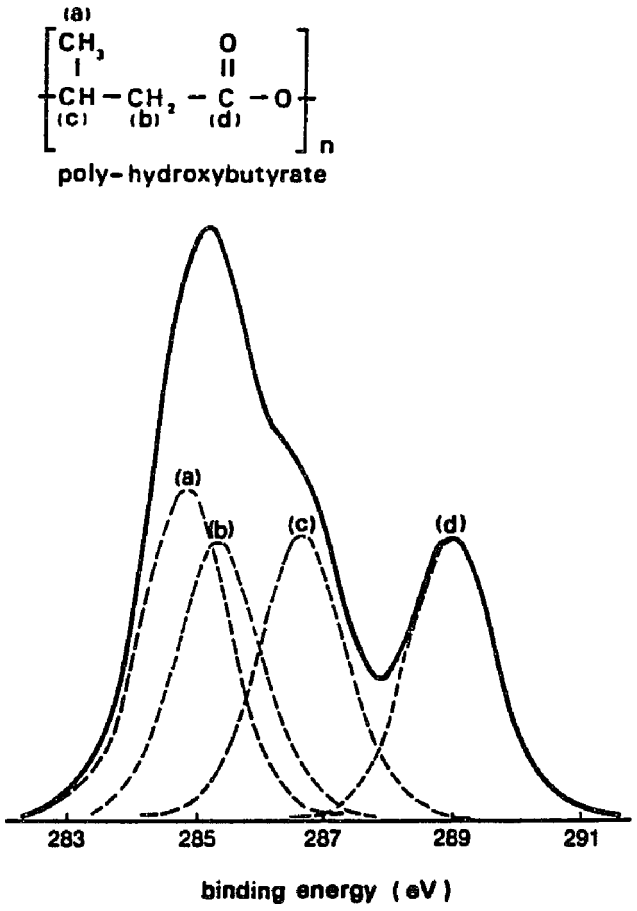

Figure 2.20 Curve synthesis of C 1s spectrum of poly-hydroxybutyrate, relating the chemical shift on the C 1s electrons to the polymer structure [81].

2.4.4 Infrared Spectroscopy (IR)

IR spectroscopy, which detects vibration modes of network structural units, has also been proved useful to distinguish the geometry of different short-range structural units [82,83,84]. For example, Kamitsos and co-workers have applied IR spectroscopy to distinguish the trigonal BO_3, tetrahedral BO_4 and pentaborate B_2O_5 structural units in

lithium borate [82,84] and sodium borate [83] glasses.

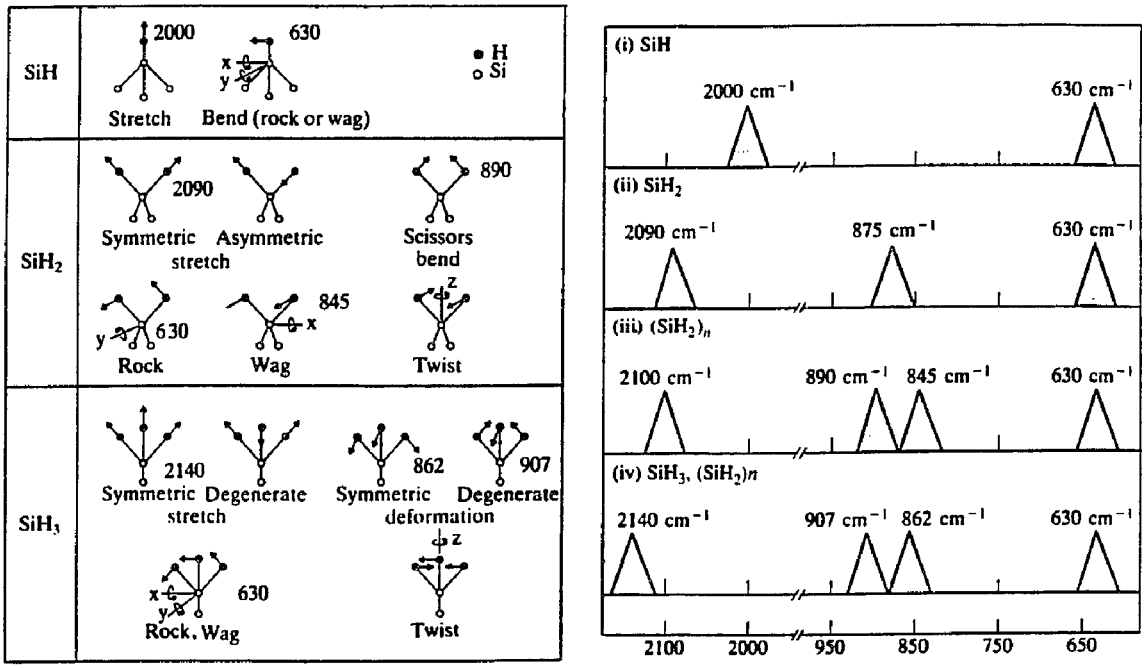

Figure 2.21 (a) Local Si:H vibrations for SiH, SiH_2 and SiH_3 groups in the a-Si:H film. (b) Schematic representation of the assignment of features for SiH_x units in IR absorption spectrum.

In an IR experiment, one measures the infrared transmission or reflectance spectra on a Fourier-transform IR vacuum spectrometer. The experimental reflectivity data are then analyzed by using the Kramers-Krönig (KK) inversion technique [85], from which

the absorption coefficient for different wavenumbers can be calculated. Fig. 2.21(a) shows some IR vibration modes for different SiH_x units in a-Si:H films [86]. Fig. 2.21(b) shows schematic representation of the corresponding IR absorption peaks.

2.5 Summary

To summarize, a review of the mechanisms for d.c. ionic conductivity shows that a microscopic understanding of the activation energy for ion transport is lacking. Also, one cannot explain the complex mixed alkali effect. One obvious difficulty with the existing models is the lack of understanding of glass local structure. Specifically, a one-to-one correspondence between the local structure and ionic conductivity has yet to be established. An investigation of electrical response in relation to microscopic structure is needed.

The non-Debye type electrical relaxation was attributed initially by Moynihan and later by Dyre, Martin, etc. to the distribution of relaxation times, arising from structural disorder. But Ngai, Funke, etc. have attributed it to the coupling of mobile ions. To choose between these two fundamentally different explanations, convincing experiments are needed relating the local structure of glass with the electrical relaxation behavior.

The MRN structure model provides some novel thoughts for the mechanisms of ionic conductivity. However, there is no direct microscopic observation of microheterogeneity on the scale postulated in the MRN structure. Also, it is not clear how universal such microsegregation is, if it does exit. An investigation of the local structure of other glass systems should be helpful for establishing this model.

CHAPTER 3 PROPOSED RESEARCH

3.1 Statement of Objectives

A review of the d.c. and a.c. conductivity shows that we have very little knowledge about how does ion transport in glass relate to glass structure which itself is poorly understood. This is due to fact that, in contrast to ionic crystals, glass network structure changes with charge carrier concentration in a poorly understood manner. So, our general objective is to establish a correlation between ion dynamics and the physical structure of glass. The specific objectives are to:

(1) Determine the physical characteristics of carefully selected model glass compositions, including geometrical configuration, bond length, structural disorder, C.N., NBO, etc.

(2) Determine the most significant electrical parameters (activation energy, Kohlrausch exponent, etc.) for the same glasses.

(3) Examine correlations between the structural characteristics and electrical parameters.

(4) Determine the significance of physical factors for the mixed mobile ion effect as manifested in the maximum/minimum in the ion movement related properties.

3.2 Approaches

To achieve our goal, we will systematically modify the structure of glass by physical treatments such as by annealing and neutron irradiation, and by composition

variation.

First, to study the effect of composition, binary germanate glass series, $xRb_2O\bullet(1-x)GeO_2$ and $xK_2O\bullet(1-x)GeO_2$ with $x \leq 0.4$, are selected for structural investigation because their network structural units undergo transformation from tetrahedrally coordinated germanium to octahedrally coordinated germanium with the addition of alkali concentration. Such structural variations should help us determine the importance of structure for the conductivity. Furthermore, germanate glasses are good candidates for investigating the applicability of the MRN structure model (microheterogeneity) and its related cooperative ion motion conductivity model, because they do not phase separate as readily as silicates. Then, by determining the electrical conductivity, we will examine the correlations between the structural characteristics and the electrical parameters.

Second, to study the effect of melt temperature, sodium triborate glasses will be investigated. In this experiment, composition will be kept constant and the structural variation is to arise from different melt conditions. A large mole fraction of Na_2O is chosen to minimize the effect of any inadvertent impurities.

Third, to study the effect of irradiation and annealing, samples of high purity quartz with a few ppm Na atoms will be subjected to neutron irradiation for different times to systematically change their amorphousness. This experiment is intended to study the effect of structural amorphousness on the ionic conduction. Jain and Nowick [87] have discovered that the activation energy for d.c. conductivity is affected by the redistribution of alkali ions from annealing of quartz crystal. So, thermal annealing will be also performed on quartz to examine the effect of charge distribution on β.

Finally, two mixed mobile ion germanate glasses, $0.2(Rb,Ag)_2O•0.8GeO_2$ and $0.2(Rb,K)_2O•0.8GeO_2$, will be prepared for studying structural origin of the mixed mobile ion (MMI) effect. A structural based model for the MMI has been proposed for alkali silicate glasses [88]. Therefore, it is useful to determine if the short-range local structure plays any role in the development of this effect in glasses.

The structure will be characterized by EXAFS, XPS and/or IR spectroscopy. The conductivity measurements will be performed in our laboratory at Department of Material Science and Engineering, Lehigh University using General Radio capacitance bridge assembly. The conductance and capacitance of a specimen are to be measured as a function of frequency (from 10 Hz to 100k Hz) as well as temperature. D.c. and a.c. conductivities will be analyzed in terms of complex impedance and complex modulus. EXAFS spectroscopy is to be performed at National Synchrotron Light Source (NSLS), Brookhaven National Laboratory. Data analysis will be carried at AT&T, Murray Hill, NJ (Dr. Marcus) and at Exxon, Annadale, NJ (Dr. Meitzner). IR absorptivity will be measured through the cooperation with Dr. Kamitsos in Greece. XPS, in addition to EXAFS and IR, will be measured at Zettlemoyer Center for Surface Studies, Lehigh University, as a supplement to determine the fraction of BOs and NBOs.

CHAPTER 4 EXPERIMENTAL METHODS

4.1 Materials

4.1.1 Sodium Borate Glasses

Sodium borate glasses with starting batch composition 0.3 Na_2O - 0.7 B_2O_3 were prepared from melt. To assess the reproducibility of results, glass samples were prepared from two independent batches of same nominal composition. Appropriate amounts of dry analytical grade Na_2CO_3 and B_2O_3 were thoroughly mixed and then melted in a platinum crucible in an electric furnace. The melt was heated to 1400°C where it became bubble free. After keeping it at 1400°C for two hours it was quickly transferred into a box furnace at 850°C for isothermal annealing. At varying intervals a small portion of the melt (at 850°C) was taken out for making glass by casting in a stainless steel mold at room temperature. Identical conditions (including the mold) were used in making glass samples for a given batch of melt. The melt annealing time (t) was considered zero when the thermocouple next to the melt indicated 850°C - it took a few seconds for the melt to cool from 1400°C. Typically, glasses were cast after annealing the melt for 0 min., 1 min., 5 min., 20 min., 1 hr., 2 hr., and 3 hr. Stresses from inhomogeneous cooling during casting were eliminated by a brief annealing at 425°C and then furnace cooling them to the room temperature.

4.1.2 Binary and Mixed Alkali Germanate Glasses

(1) $xRb_2O \cdot (1-x)GeO_2$ series

Eight glass compositions were prepared to form the glass series: $xRb_2O•(1-x)GeO_2$ with x = 0.01, 0.02, 0.05, 0.10, 0.15, 0.20, 0.30, 0.40. This series is used to examine the effect of alkali concentration on germanate structure. The samples were prepared by the melt-quench method. Appropriate amounts of puratronic grade[+] GeO_2 (99.999%) and analytical grade[+] Rb_2CO_3 (99.8%) powders were thoroughly mixed (for ~ 10 hrs) and preheated at 900 to 1000 °C for 1 hour and then melted in a platinum crucible. The liquid was equilibrated for about 1 hour at a temperature between 1200 and 1450 °C depending on composition and viscosity. Homogenized bubble free liquid was cast in a stainless steel mold and then the glass was annealed at ~ 450 - 475 °C for ~ 1/2 hour to remove internal stress before furnace cooling to room temperature. The resulting samples were cut into thin plates with dimensions ~ 1 cm^2 x 1 mm for electrical measurements, ~ 1 cm^2 x 0.5 mm for XPS and ground into fine powders for EXAFS spectroscopy.

(2) $xK_2O•(1-x)GeO_2$ series

Glass samples for the potassium germanate series, $xK_2O•(1-x)GeO_2$ with x = 0.0023, 0.02, 0.05, 0.074, 0.10, 0.15, 0.20, 0.247, were also prepared by the melt-quench method. Appropriate amounts of puratronic grade[+] GeO_2 (99.999%) and K_2CO_3 (99.999%) powders were processed to form bubble-free glass as described above. As those of the $xRb_2O•(1-x)GeO_2$ series, the resulting samples were cut into thin plates with dimensions ~ 1 cm^2 x 1 mm for electrical measurements, ~ 1 cm^2 x 0.5 mm for XPS and ground into fine powders for EXAFS spectroscopy.

(3) Mixed Alkali Germanate Glasses

[+] Johnson Matthey, Ward Hill, MA 01835, USA.

Glass samples were prepared for the two mixed mobile ion (MMI) glass series: $0.2[yAg\bullet(1\text{-}y)Rb]_2O\bullet 0.8GeO_2$ and $0.2[yK\bullet(1\text{-}y)Rb]_2O\bullet 0.8GeO$ with y = 0, 0.25, 0.50, 0.75, 1.00, respectively. These two series are prepared to investigate MMI effect with the total mobile ion concentration fixed while varying the ratio of the two mobile ions. Appropriate amounts of puratronic grade$^+$ GeO_2 (99.999%) and analytical grade$^+$ Rb_2CO_3 (99.8%), Ag_2O (99+%) powders (or puratronic grade K_2CO_3 (99.999%) depending on the series) were processed to form glass using the melt-quench method (the preheating and glass melting temperatures is determined depending on viscosity and composition). Because of the reactivity of silver with platinum, an alumina crucible was used when glasses contained silver. To prevent crystallization, homogenized bubble free liquid was quickly cast by cold pressing using two brass blocks and, then, the glass was annealed at ~ 450 °C for ~ 1/2 hour to remove internal stress before furnace cooling to room temperature. The resulting samples were cut into thin plates with dimensions ~ 1 cm^2 x 1 mm for electrical measurements and ground into fine powders for EXAFS spectroscopy. Some silver precipitated out of the Ag_2O containing liquids and settled at the bottom of crucible. So the actual Ag concentration in glass is less than the batch composition [89]. However, this loss of silver does not qualitatively change the observation of mixed alkali effect in the present samples [16].

4.1.3 High Purity Quartz Sample

Specimens approximately 1 cm × 1 cm × 1 mm size cut from a large Premium Q

Sweep grade synthetic quartz crystal* were used for both the electrical measurements and neutron irradiation experiments. The planes of the specimen were perpendicular to the optic or c-axis of the crystal. All the samples belonged to the z-growth region of the crystal, which contains relatively fewer impurities [87]. The most important trace impurities include Al and Na but smaller amounts of Fe, Li or H are also likely to be present. The concentrations of these impurities in a high quality quartz crystal such as used here range from 0.1 to 10 ppm.

Since the conductivity of quartz crystal is known to be sensitive to the concentration and distribution of the impurities [87,90], conductance G and capacitance C were measured for each specimen in the as received condition, and after heating to 525 °C. The heat treatment allowed the impurities to reach an equilibrium distribution [46]. The subsequent electrical measurements were considered suitable for comparison with those obtained on the same specimen after neutron irradiation.

The neutron irradiation of the specimens was conducted at the High Flux Beam Reactor (HFBR) of Brookhaven National Laboratory at a fast neutron (> 1 MeV) flux of 1.5×10^{14} n/cm^2-s. Three specimens, Q6, Q4 and Q2 (see chapter 5, sec. 5.5), were irradiated at 50 to 60 °C for 1.85 h, 18.5 h and 185 h, resulting in 1×10^{18}, 1×10^{19} and 1×10^{20} fast n/cm^2 total radiation dose respectively. The extent of the transformation of the specimens to the amorphous state from neutron irradiation was characterized by density, which was measured at room temperature using Archimedes method.

---

* Supplied by Sawyer Research Products, Cleveland, OH, USA.

4.2 Electrical Conductivity Measurements

4.2.1 Sample Preparation

For electrical measurements, the flat surfaces of the cut samples with dimension ~ 1 cm^2 x 1 mm were polished and cleaned. Gold electrodes were deposited by vacuum

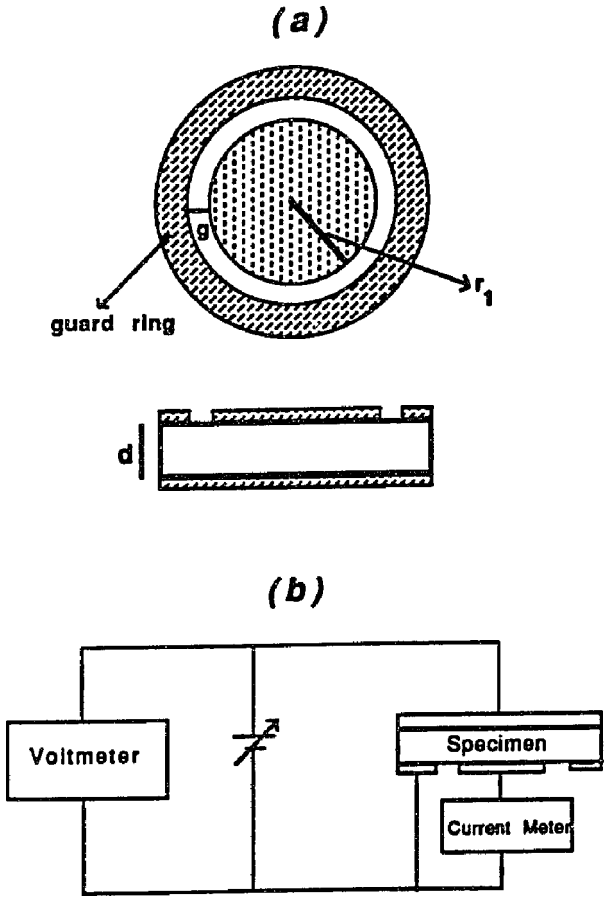

Figure 4.1 Three electrode configuration for electrical measurements (a) specimen with electrodes and (b) circuit connections [91].

evaporation and then covered with thick gold paste in a three-electrode configuration with a guard ring [91] (see Fig. 4.1). Heating of the samples did not show any deterioration of the electrodes as indicated by the capacitance measurements before and after heating.

4.2.2 Electrical Measurements

A.c conductance, G, and capacitance, C, of a sample were measured with a precision capacitance bridge (General Radio 1616) in the frequency range of 10 Hz to 100 kHz at various temperatures depending on glass series; 100 - 320 °C for sodium borate glass series, 225 - 450 °C for binary and mixed alkali germanate glass series, and 100 - 500 °C for high purity quartz before neutron irradiation and 350 - 700 °C for quartz after irradiation. The sample temperature was determined with a calibrated K-type thermocouple placed beside the sample. Fig. 4.2 shows the experimental set-up of the electrical measurement. The measurements were begun after the sample temperature had equilibrated within ± 0.25 °C. The conductivity of Ag containing glasses was measured in dark to prevent any conversion of Ag^+ ions to colloidal silver [92].

4.3 EXAFS Spectroscopy

4.3.1 Sample Preparation

To eliminate self-absorption effects, it was necessary to prepare thin glass samples for which the change in optical depth on crossing the absorption edge was ≤ 0.1 [93]. For this reason, the glass was powdered to ~ 5 μ particle size by grinding in polystyrene solution with a mortar and pestle. The powder was mixed with ~ 200 ml polystyrene-

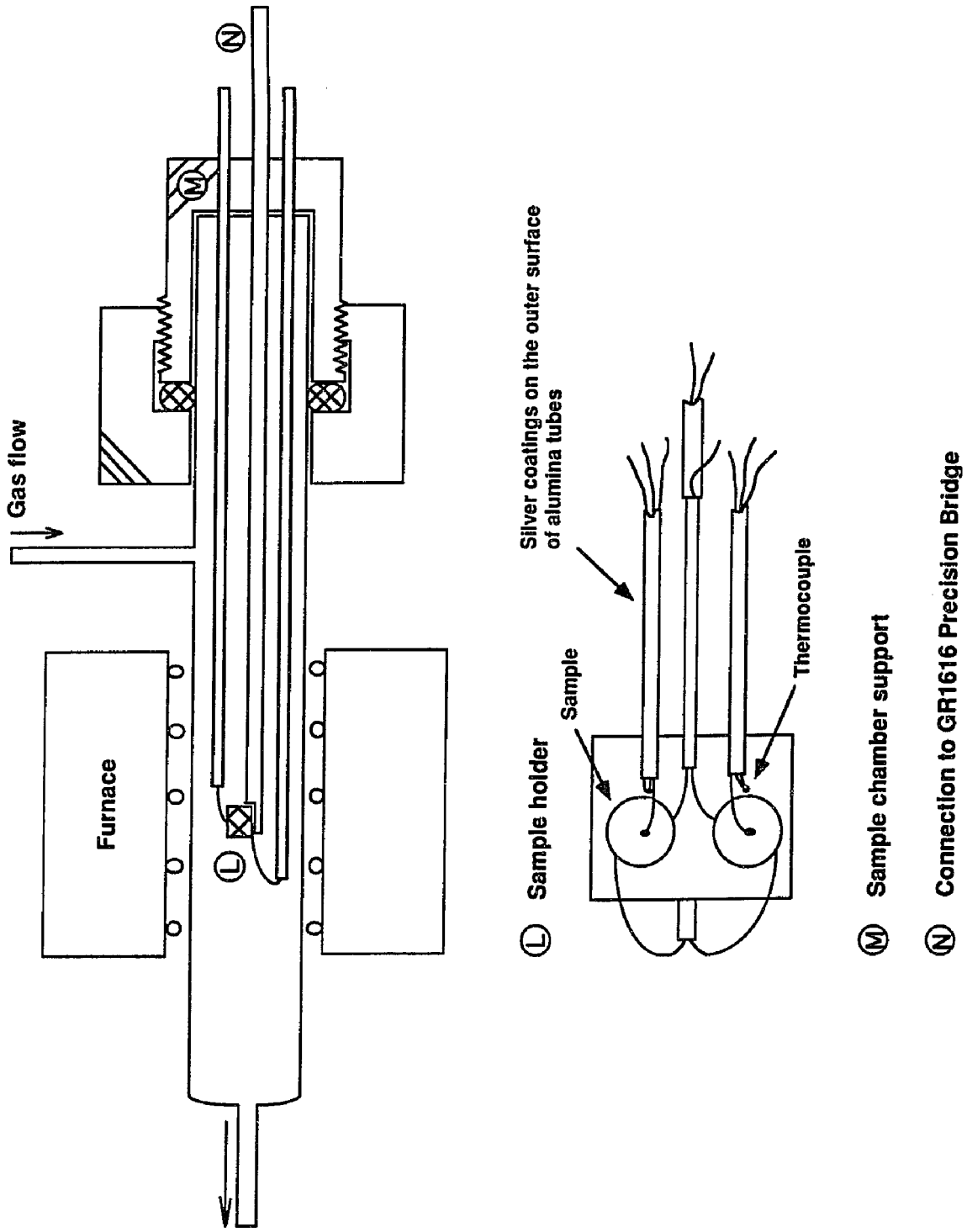

Figure 4.2 Experimental set-up for the electrical measurement.

toluene solution in a 250 ml beaker containing a closely fitting filter paper at its bottom. Next the solution was left undisturbed until the powder settled onto the filter paper and the supernatant solution became clear (about 6 hrs later). Then the clear supernatant solution was pipeted out and the powder on the filter paper was dried and protected with an adhesive tape [93].

4.3.2 Spectroscopy Measurements

The K-edge EXAFS spectra of Ge (11.10 keV), Rb (15.20 keV), and Ag (25.52 keV) in binary Rb germanate and Rb-Ag mixed mobile ion germanate glasses were recorded on the X6B beamline equipped with a Si (220) monochromator, at National Synchrotron Light Source, Brookhaven National Laboratory, Upton, NY (for details of EXAFS with synchrotron radiation, see [94]). The fluorescence x-ray intensities were measured at room temperature with a Lytle detector or plastic scintillator; while the transmitted x-ray intensity was measured with an ion chamber [95]. GeO_2 and Ag_2O were measured as model compounds for the determination of standard parameters, viz. interatomic distance ($R_{M\text{-}O}$), coordination number (CN) and Debye-Waller factor ($\Delta\sigma^2$, the mean square variation in interatomic distance).

The K-edge EXAFS spectra of K (3.61 keV), Ge (11.10 keV) and Rb (15.20 keV) in our binary K germanate glasses were recorded on the X10C beamline equipped with a Si (111) monochromator with energy resolution ($\Delta E/E$) $\simeq 2 \times 10^{-4}$, at the same laboratory. The transmission and fluorescence X-ray intensities were measured with ion chambers in which there flowed a mixture of helium and nitrogen (for K K-edge); or a mixture of

nitrogen and argon (for Ge and Rb K-edge) [95,96]. To eliminate the thermal contribution, the samples were cooled to around liquid helium temperature (~ 10 K) using a cryostat. For the measurement of K-edge (3.61 keV) soft X-ray spectra, it was necessary to use a vacuum pipe for guiding the X-ray beam from the beamline window to the sample without being scattered by the air. Puratronic grade GeO_2[+] was measured as a model compound for the determination of Ge-O amplitude and phase shift. XRD was used to verify that this model compound was in the α-SiO_2 phase.

4.4 XPS Measurements

For XPS measurements, the glass samples were cut into thin plates with dimension ~ 1 cm^2 x 1 mm. The XPS measurements were carried out on a spectrometer (Scienta ESCA-300) with Al K_α x-ray source (1486.67 eV). To avoid surface contamination the sample was fractured in situ in a vacuum better than 3.7 x 10^{-9} torr. The photoelectrons were generated from the fracture surface of area about 10 x 1 mm^2. The surface was flooded with 4 to 10 eV electrons for minimizing charging. The x-ray spot size was about 1.6 x 0.3 mm^2. The step size (referring to the internal kinetic energy of photoelectron) in the analyzer was 0.1 eV and the energy resolution was 0.4 eV, as determined at the Fermi edge of Ag metal. The photoelectron energy was determined with a hemispherical analyzer. Data analysis was carried out with ESCA-300 software package using a least square Gaussian fit and Shirley background substraction [97]. Relative XPS peak position, FWHM (Full Width at Half Maximum) and intensity (peak area) ratio were determined with this

[+] Johnson Matthey, Ward Hill, MA 01835, USA.

program.

4.5 IR Spectroscopy

4.5.1 Sample Preparation

Before spectroscopic measurements, each sample was repolished to remove partially hydrolyzed layers. Repolishing two or three times was sufficient for the infrared reflectivity to reach a constant value.

4.5.2 Spectroscopy Measurements

Specular infrared reflectance spectra of sodium borate glasses were measured at room temperature on a Fourier-transform vacuum spectrometer (Bruker 113v). The angle of incidence was 11° off-normal and a high reflectivity aluminum mirror was used as reference. A combination of sources, detectors and beam splitters was used to measure continuous reflectance spectra in the 30-4000 cm^{-1} region. Each spectrum represents the average of 200 scans of 2 cm^{-1} resolution. The experimental reflectance spectra were analyzed by Kramers-Kronig transformation to obtain the optical and dielectric properties and to calculate subsequently the absorption coefficient spectra [84].

4.6 Density Measurements

The density of glass and quartz samples was determined at room temperature using Archimedes method by weighing a sample in 0.01% BRIJ-35[#] standard solution. Repeated

[#] Fisher Scientific, Orangeburg, NY 10962.

measurements on a sample gave reproducible values within ± 0.001 g/cm^3 for sodium borate glass series. Therefore, we consider this to be the magnitude of uncertainty for intercomparison of the two batches of samples, even if uncertainty in absolute density may be larger. For germanate glass series, the uncertainty is ± 0.003 g/cm^3. For quartz samples, it is ± 0.004 g/cm^3.

CHAPTER 5 RESULTS

5.1 D.c. Conductivity

The d.c. conductivity (σ_{dc}) of the various samples is determined using the complex impedance analysis of conductance (G) and capacitance (C) [91,98] assuming that the electrical behavior of the glass can be described by an equivalent circuit, composed of parallel connection of a resistor and a capacitor (see Fig. 5.1). The real (Z') and the imaginary (Z") parts of complex impedance (Z*) are calculated from:

$$Z' = \frac{G}{G^2 + \omega^2 C^2}, \qquad Z'' = \frac{\omega C}{G^2 + \omega^2 C^2} \tag{5.1}$$

where ω (= $2\pi f$) is the angular frequency of electrical signal. The complex impedance plot (Z" vs. Z') consists of a high frequency arc of a circle whose center usually lies below the Z' axis. The d.c. resistance (R) is then given by the intersection of this arc with the Z' axis. A second low frequency arc which represents electrode-sample interface polarization is sometimes observed at high temperatures and low frequencies. Fig. 5.2 shows an example of the Z" vs. Z' plot for a rubidium germanate glass at various temperatures. The bulk d.c. conductivity (σ_{dc}) is thus obtained from

$$\sigma_{dc} = \frac{t}{A}\left(\frac{1}{R}\right) \tag{5.2}$$

where t is the sample thickness and A is the effective electrode area. The temperature dependence of σ_{dc} is analyzed using the Arrhenius equation [91]

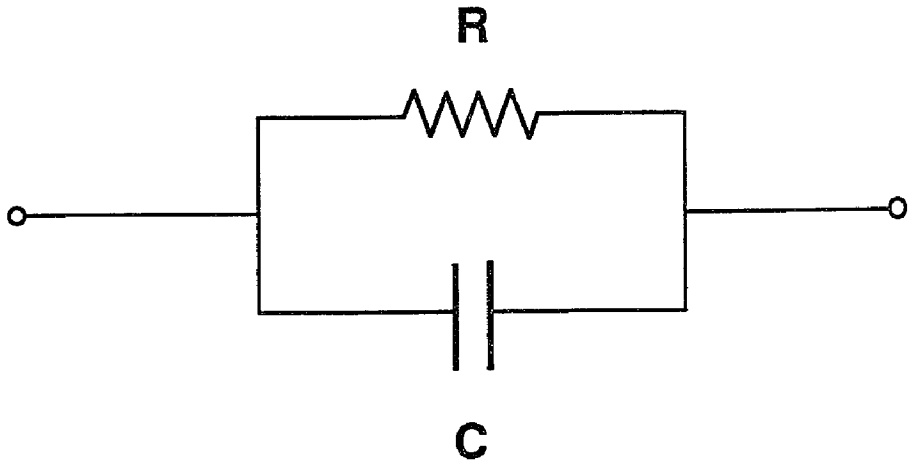

Figure 5.1 The equivalent circuit for a dielectric material: a parallel connection of a resistor and a capacitor.

$$\sigma_{dc} = \frac{\sigma_o}{T} \exp\left(-\frac{E_{dc}}{kT}\right) \tag{5.3}$$

where σ_o and E_{dc} are the best fit values of the pre-exponential factor and activation energy, k is the Boltzmann constant, and T is the absolute temperature. The pre-exponential term

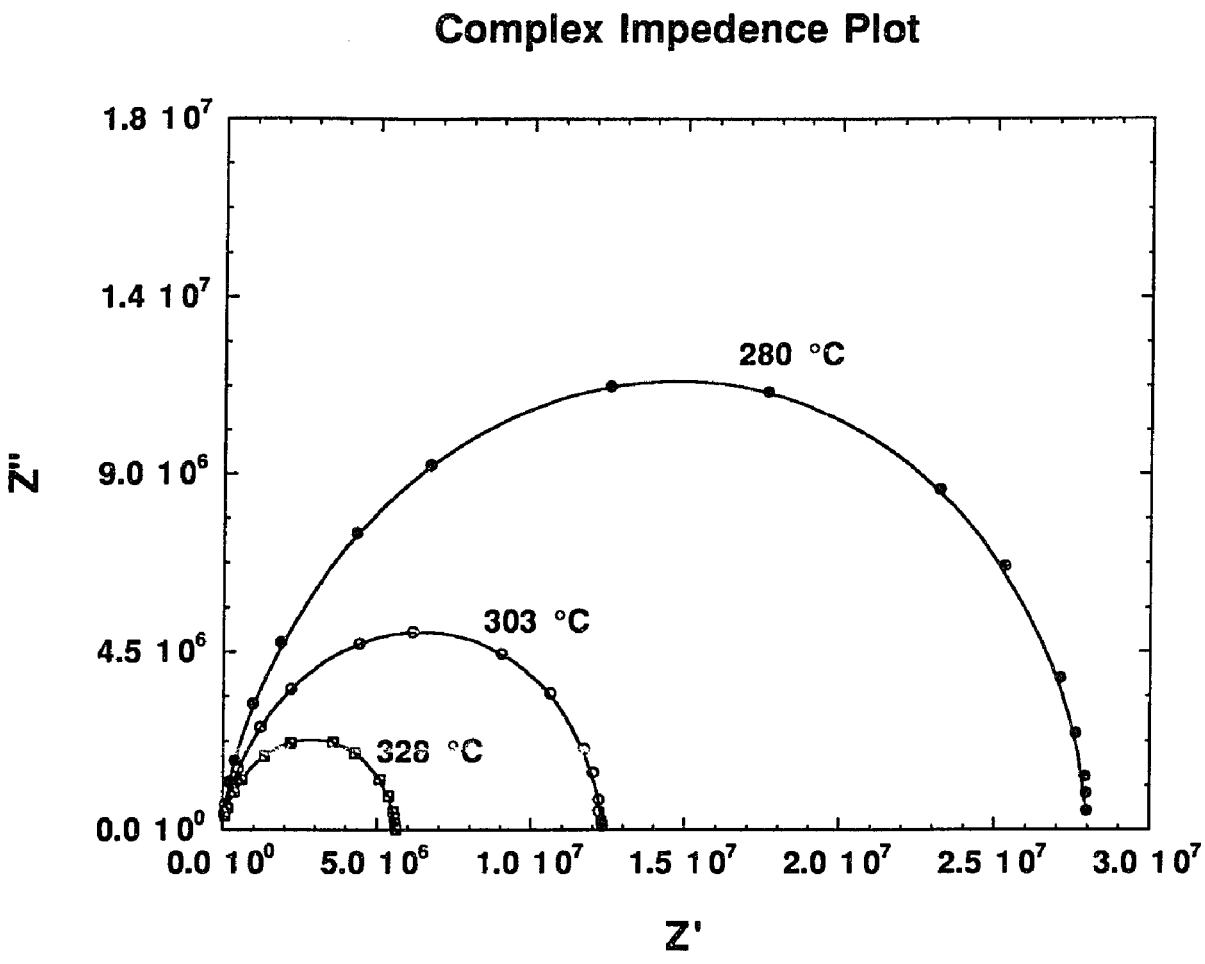

Figure 5.2 Plots of the complex impedance Z" vs Z' at various temperature for $0.15Rb_2O{\bullet}0.85GeO_2$ glass.

σ_o is a function of concentration, jump distance and vibration frequency of mobile ions. Note that the geometric factor, t/A, does not affect the value of E_{dc}. Typical Arrhenius plots of σT vs. 1/T are shown in Fig. 5.3 for binary Rb germanate glasses, where the slope of each line gives the respective value of E_{dc}. The plots of σT vs. 1/T for binary K germanate glass series are shown in Fig. 5.4. The plots of σT vs. 1/T for the mixed mobile ion

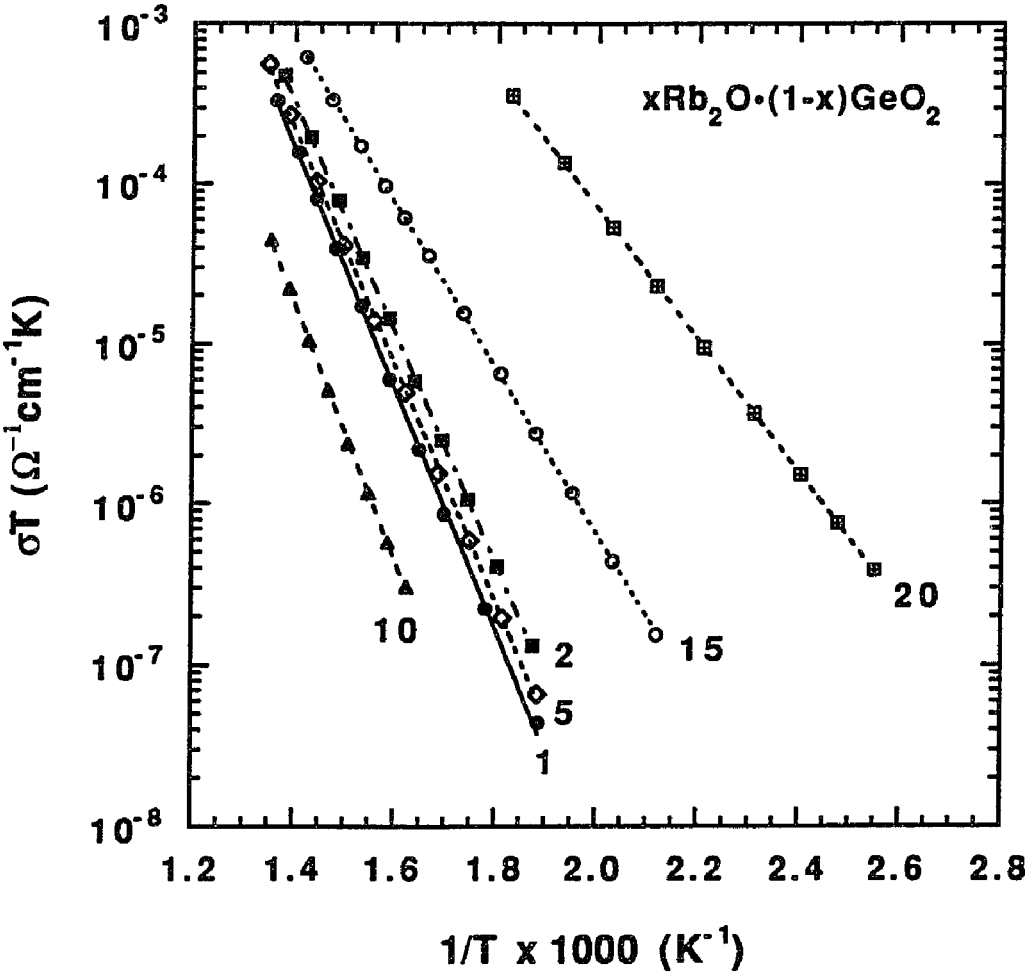

Figure 5.3 Arrhenius plot of σT vs. 1/T for $xRb_2O•(1-x)GeO_2$ glass series. Rb_2O mol% is identified for each curve. Straight lines are the least square fits to eq. (5.3).

$(Rb,Ag)_2O$-GeO_2 germanate glasses are shown in Fig. 5.5 and those for the $(Rb,K)_2O$-GeO_2 series are shown in Fig. 5.6. Similar plots for the sodium borate series are shown in Fig. 5.7. For the quartz crystal, before and after irradiation, the plots are shown in Fig. 5.8. All the corresponding values of d.c. conductivity parameters, viz. σ_o and E_{dc}, and the

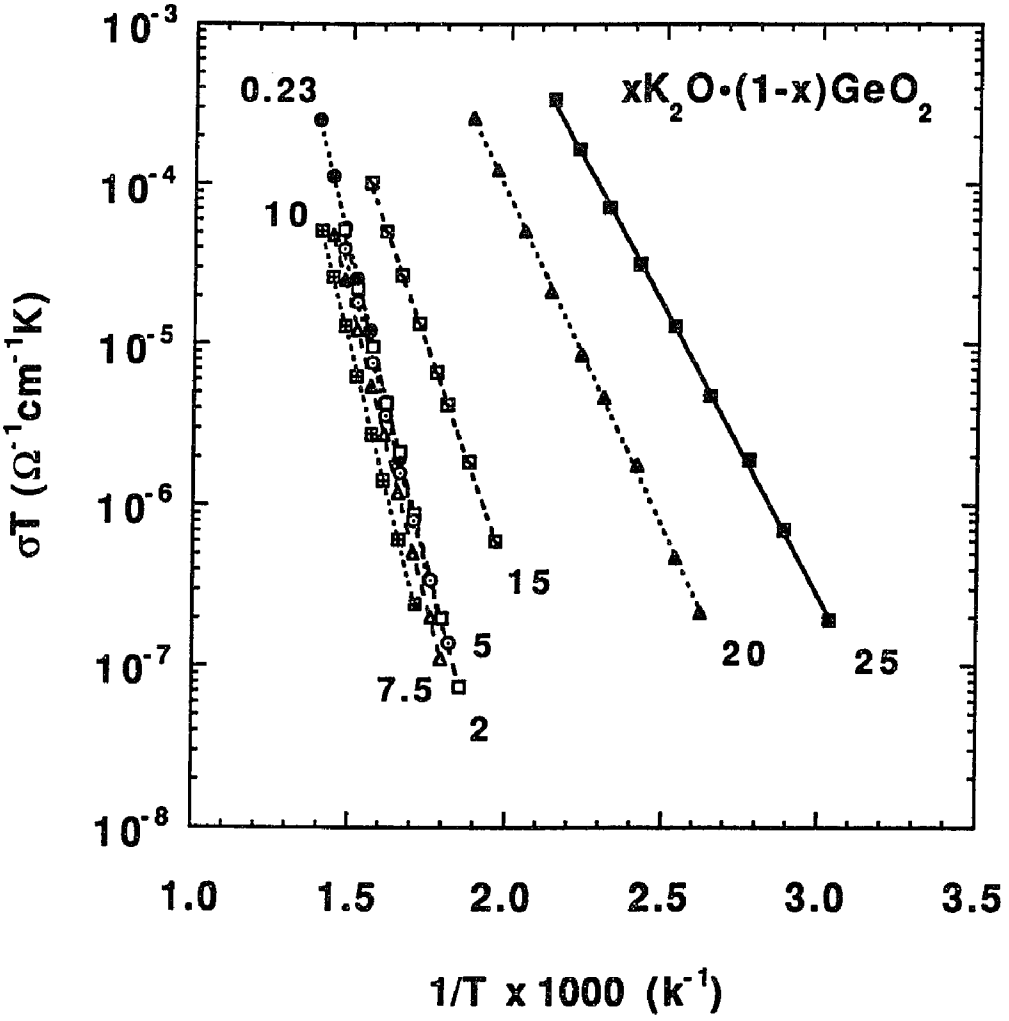

Figure 5.4 D.c. conductivity Arrhenius plot of σT vs. 1/T for $xK_2O•(1-x)GeO_2$ glass series. K_2O mol% is identified for each curve in this diagram.

corresponding standard deviation of E_{dc}, for each glass series are listed in the corresponding tables: i.e. for the Na_2O-B_2O_3 series in Table 5.1(a); for the Rb_2O-GeO_2 series in Table 5.2(a); for the K_2O-GeO_2 series in Table 5.3(a); for the $(Rb,Ag)_2O$-GeO_2 series in Table 5.4(a); for the $(Rb,K)_2O$-GeO_2 series in Table 5.5(a); and for the high purity quartz (before and after irradiation) in Tables 5.6(a) and 5.6(b).

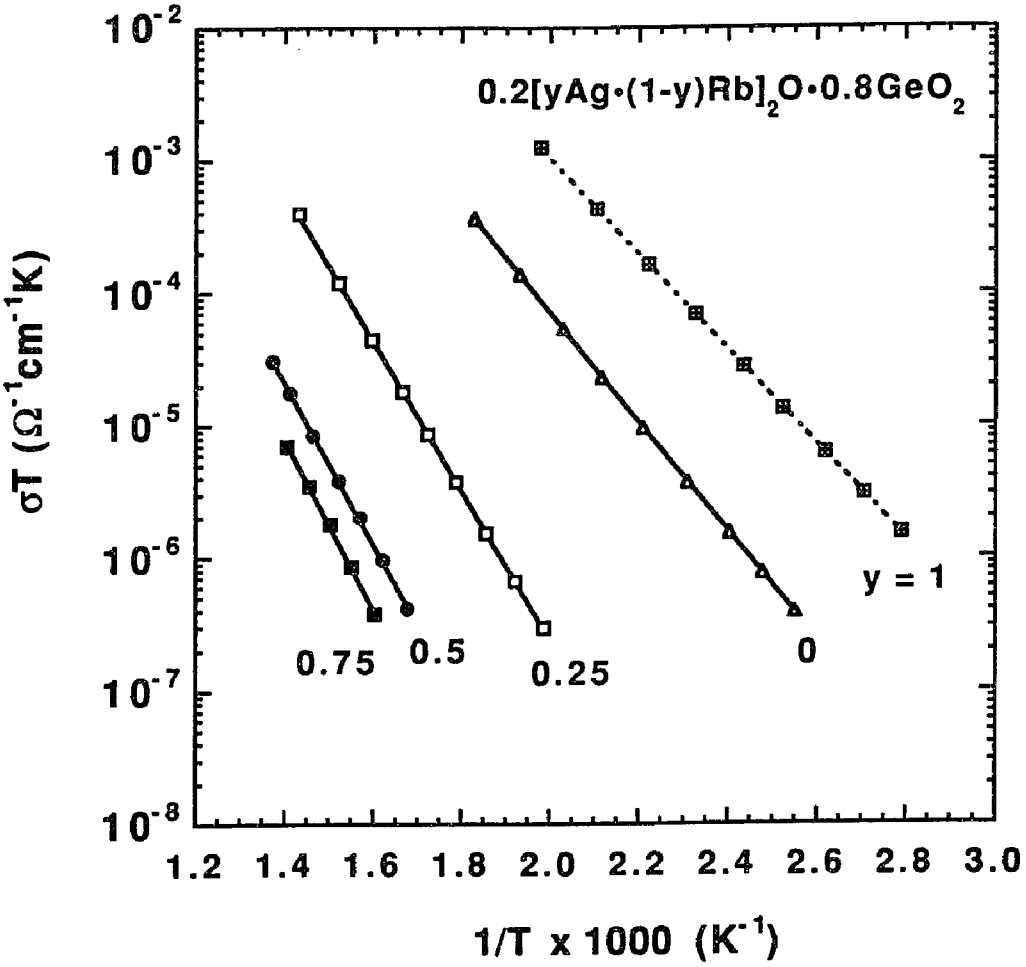

Figure 5.5 D.c. conductivity Arrhenius plot of σT vs. 1/T for 0.2[yAg•(1-y)Rb]$_2$O•0.8GeO$_2$ glass series. Ag_2O mol% is identified for each curve in the diagram.

5.2 Dielectric Constant (ε_i)

The high frequency relative dielectric constant (ε_i) for each sample is obtained by extrapolating the ε" vs. ε' plot to high frequencies, where ε" is the imaginary part and ε' is the real part of the complex dielectric constant (ε*) [99]. Fig. 5.9 shows an example

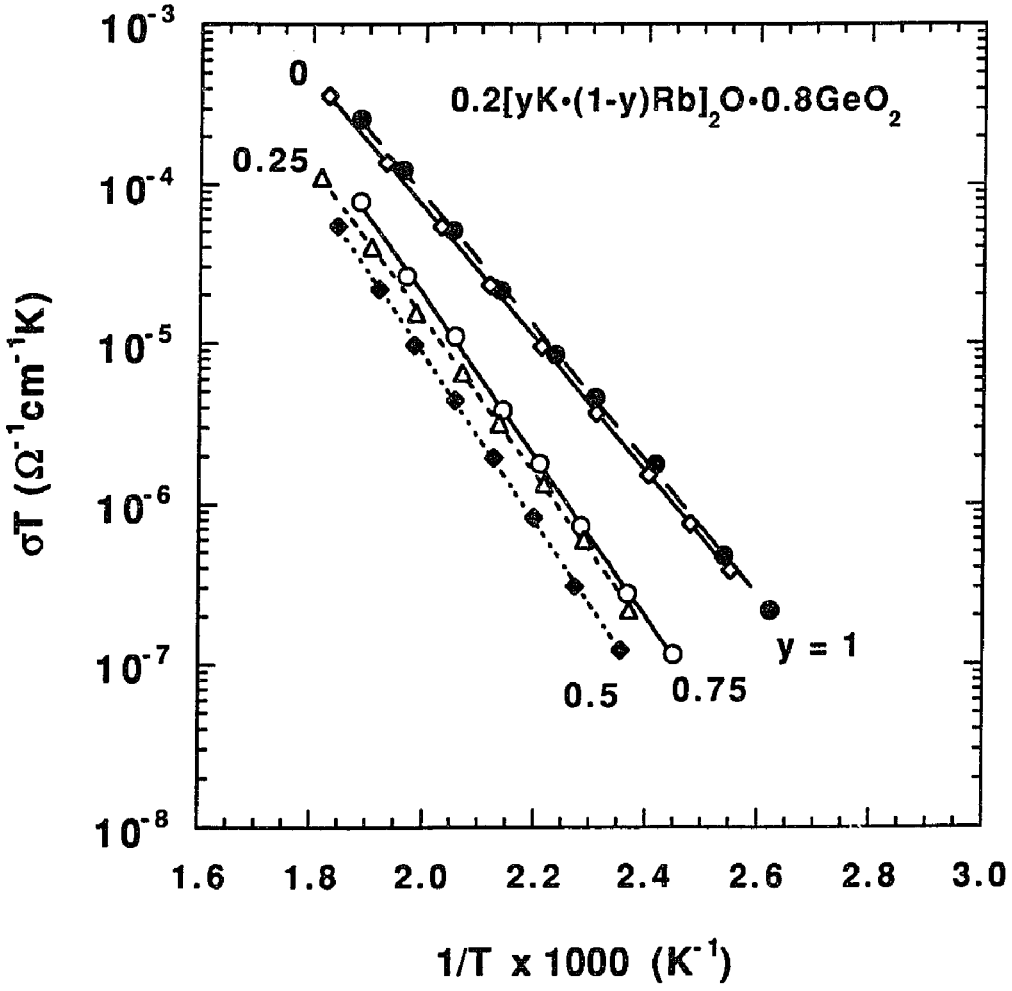

Figure 5.6 D.c. conductivity Arrhenius plot of σT vs. 1/T for 0.2[yK•(1-y)Rb]$_2$O•0.8GeO$_2$ glass series. K_2O mol% is identified for each curve in the diagram.

of the ε" vs. ε' plot for the $0.15Rb_2O•0.85GeO_2$ glass. The values of ε_i obtained from such analysis represent the bulk dielectric constant free from electrode/glass interfacial polarization. The uncertainty of ε_i from at least 3 measurements is $\leq \pm 0.5$. The values of ε_i for each glass series are listed in the corresponding Tables (see Sec. 5.5).

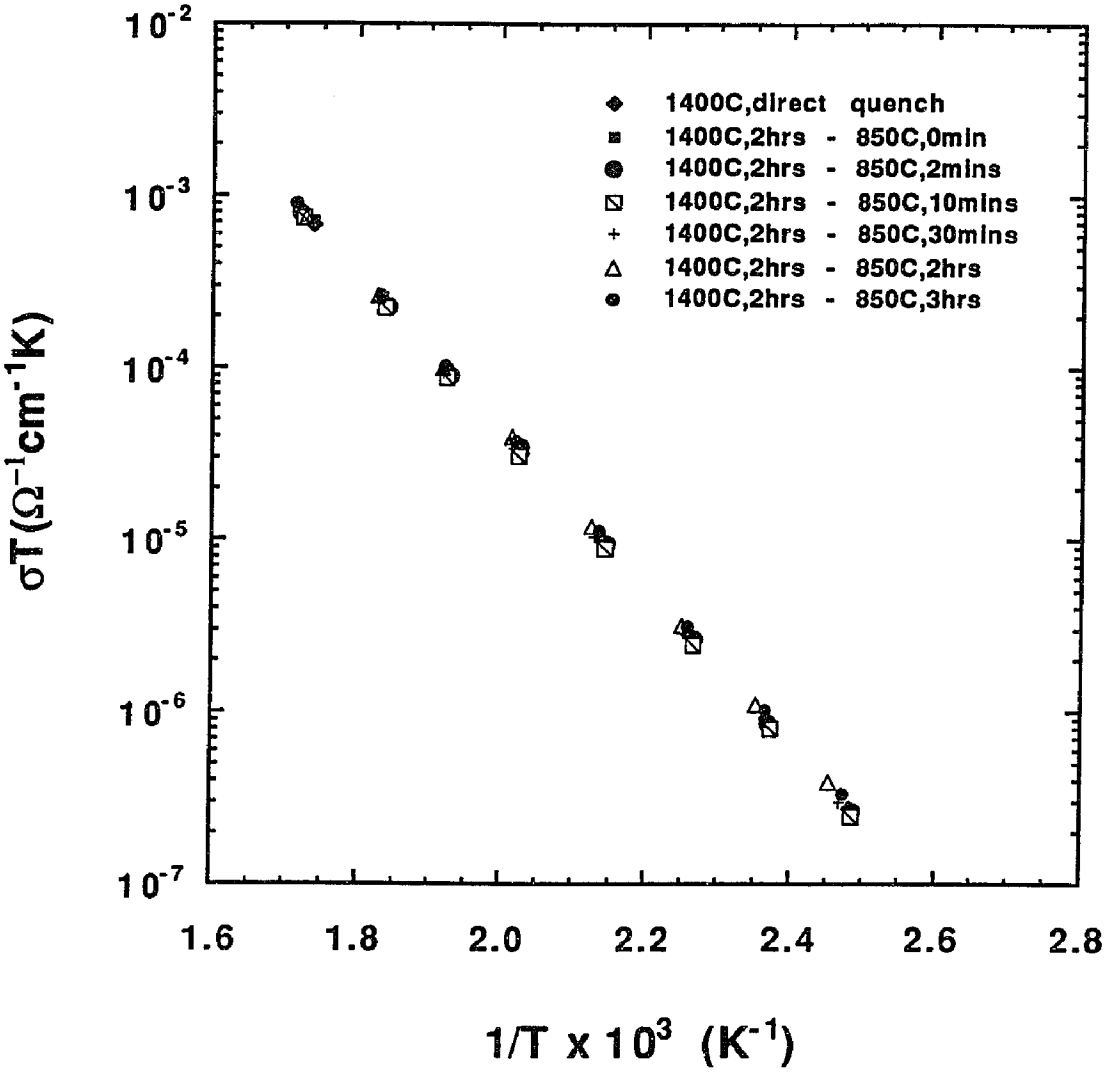

Figure 5.7 D.c. conductivity Arrhenius plot of σT vs. 1/T for sodium triborate glasses.

5.3 Electric Modulus (M") and Kohlrausch Exponent (β)

Electrical conductance (G) and capacitance (C) as a function of frequency, which contain the total electrical response, are also used to give the imaginary part of modulus for each sample using

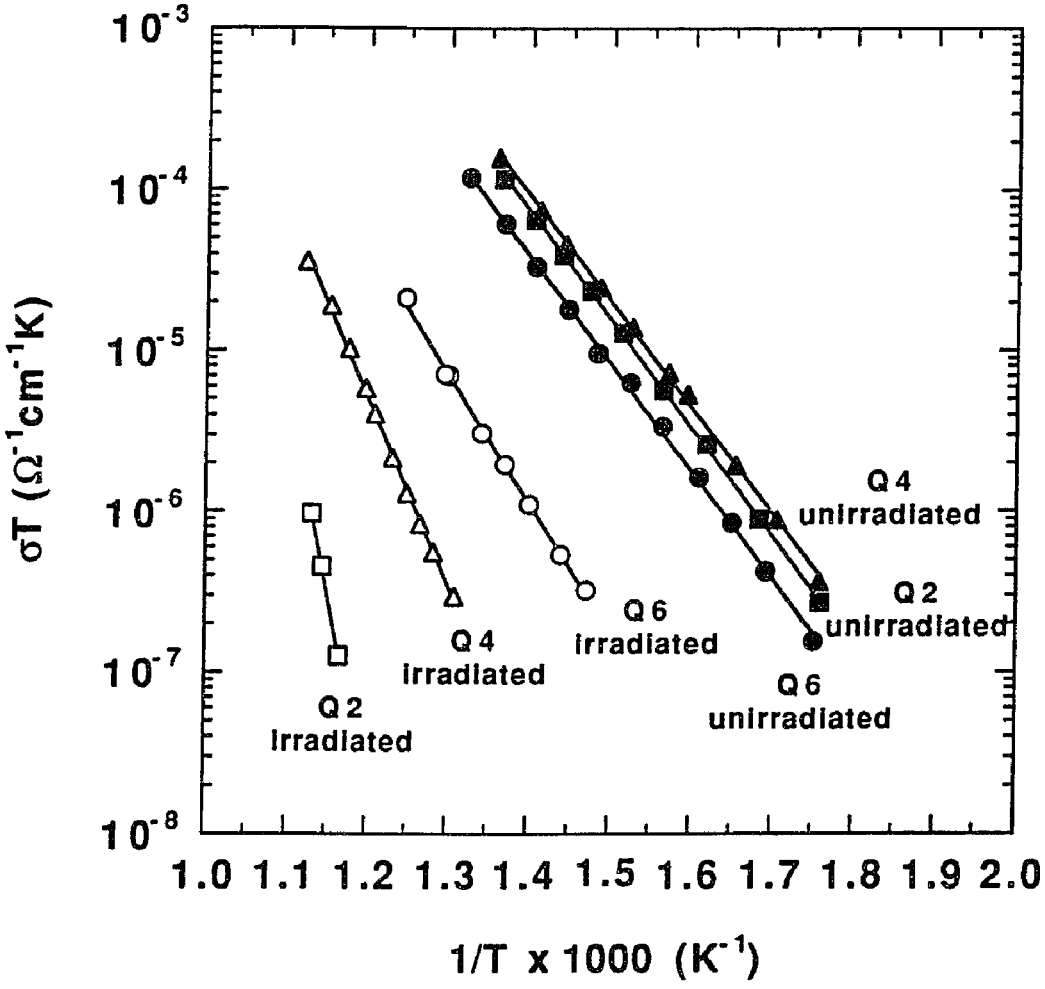

Figure 5.8 D.c. conductivity Arrhenius plot of σT vs. 1/T for quartz Q2, Q4 and Q6 before and after neutron irradiation.

$$M'' = \frac{\omega G C_o}{G^2 + \omega^2 C^2} \tag{5.4}$$

where C_o is the vacuum equivalent capacitance of the sample [44,46,47]. Fig. 5.10 shows several typical M" vs. log frequency peaks for the binary K germanate glass series, where

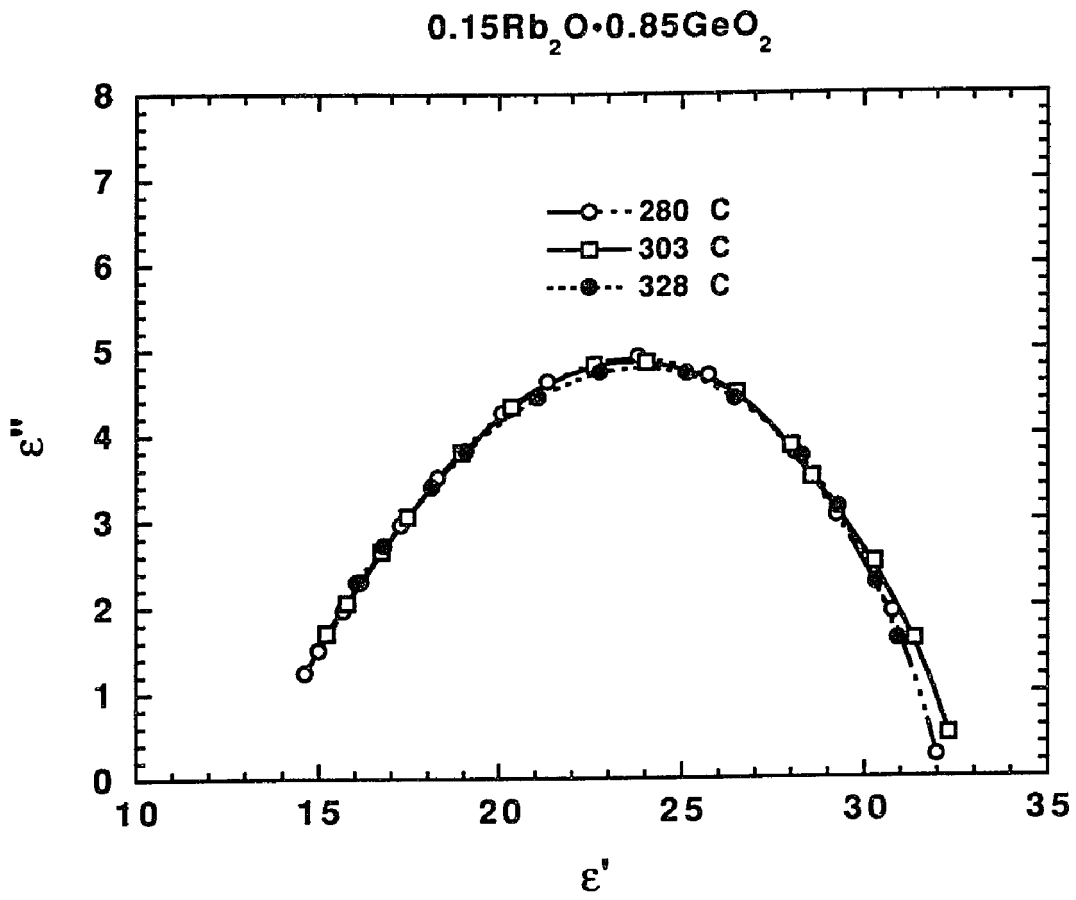

Figure 5.9 Plot of the complex dielectric constant ε" vs ε' for $0.15Rb_2O•0.85GeO_2$ glass.

the value of β for a sample can be determined from the FWHM of M" peak [45]. The uncertainty of β value from at least 3 measurements is less than ± 0.02. The broadening of M" peaks at high alkali concentration indicates a decrease in β value. The values of β as a function of composition for each glass series and quartz are listed in the corresponding Tables (Sec. 5.5).

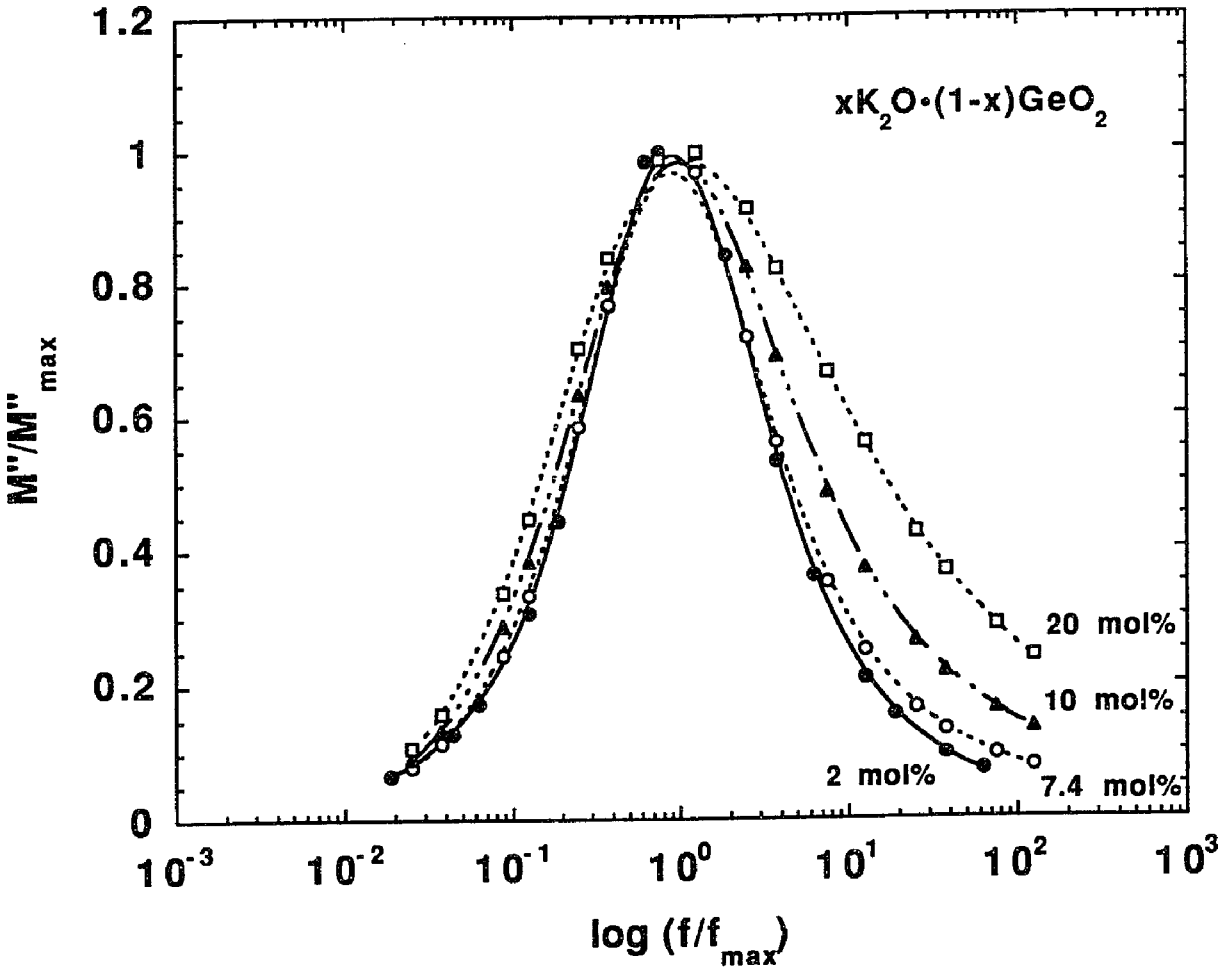

Figure 5.10 M" peaks vs. log frequency for the binary potassium germanate glasses. The lines are draw to show the broadening of M" peak at high alkali concentration.

5.4 Local Structure

5.4.1 EXAFS

EXAFS spectra have been obtained for respective elements in four glass series: namely, Ge, Rb and Ag K-absorption edges in the binary Rb germanate and mixed mobile

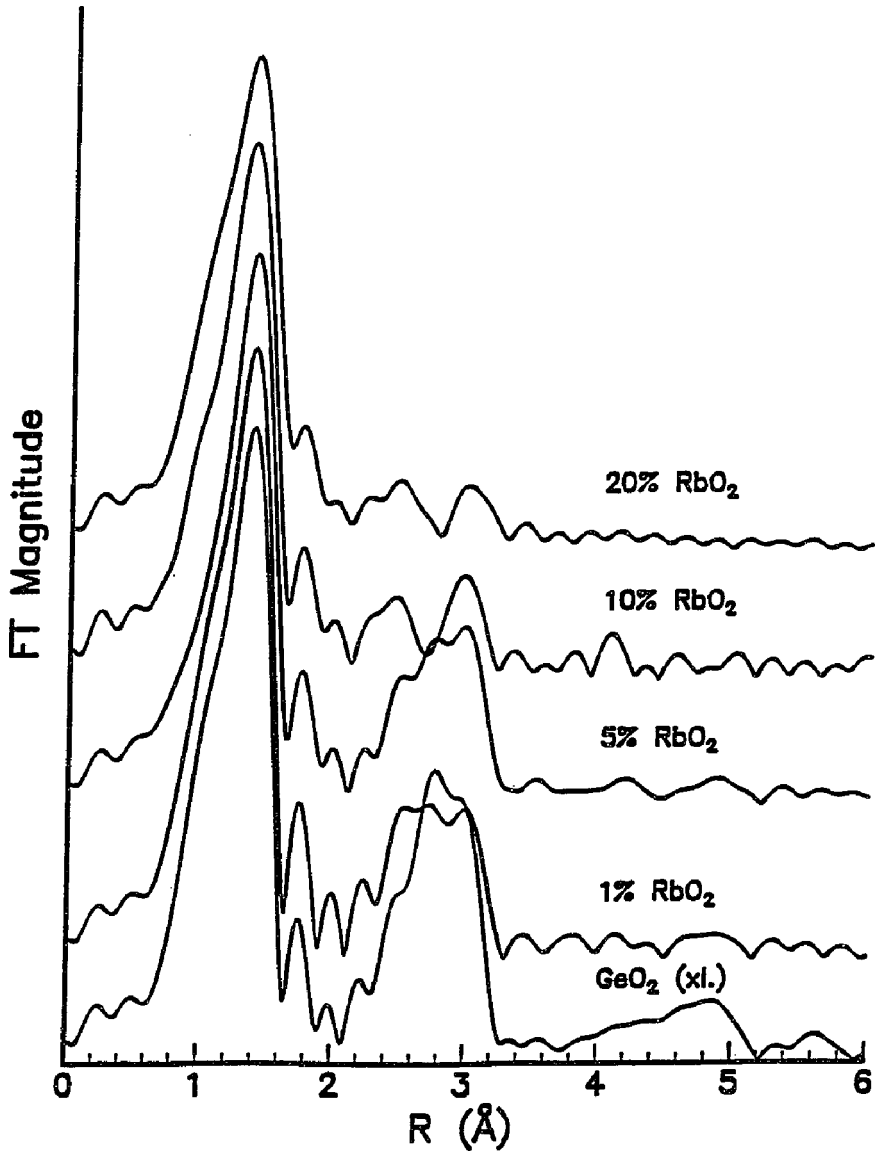

Figure 5.11 Fourier magnitudes of $k^2\chi(k)$ extracted from EXAFS spectra for Ge K-edge in $xRb_2O{\cdot}(1\text{-}x)GeO_2$ glasses.

ion Rb-Ag germanate glass series; and Ge, Rb and K K-edges in the binary K germanate and mixed alkali Rb-K germanate glass series. The basic principle of EXAFS and standard procedure for EXAFS data analysis and processing can be found elsewhere [100,101]. Data analysis for background subtraction, normalization and Fourier transformation of raw spectra was carried out using programs developed at AT&T [102] and the SEXIE program

of Rupp et al. [103] for the binary Rb germanate and mixed mobile ion Rb-Ag germanate glass series, and using the EXAPLT and EXAFIT programs developed at Exxon [104] for the binary K germanate and mixed alkali Rb-K germanate glass series. The normalized EXAFS, $\chi(k)$, was multiplied by k^2 to amplify the magnitude of EXAFS at higher k region, where k is the x-ray wave vector. Fourier magnitudes of $k^2\chi(k)$ for the Ge K-edge in $xRb_2O\bullet(1\text{-}x)GeO_2$ series for different x (up to 20 mole%) are shown in Fig. 5.11 to describe the radial pair distribution function of Ge-O and Ge-Ge bonds. Spectrum for the model compound GeO_2 is also shown in this figure, where we see a well defined peak corresponding to the first shell neighbor, which is assigned to Ge-O. Puratronic grade GeO_2 and analytical grade Ag_2O in this work were used as model compounds for the determination of amplitude and phase shift of Ge-O and Ag-O. Since the Rb-O (and K-O) distance distributions in rubidium (potassium) oxide, nitrate, carbonate, and acetate compounds are all broad and complex, we used the FEFF program of Rehr et al. [105] to model the Rb-O, K-O and Rb-Ge amplitudes and phase shifts. In some of the silver containing samples there was an indication of Ag precipitation. However, results for only those samples are included in this paper for which there was negligible contribution from Ag-Ag EXAFS.

From the $k^2\chi(k)$ of each Ge EXAFS spectrum, bond distance, CN and structural disorder $\Delta\sigma^2$ around the first neighbor have been determined with respect to GeO_2 standard. The first shell information corresponding to Ge-O is listed in Tables 5.2(b), 5.3(b), 5.4(b), and 5.5(b) for the four glass series.

Parallel analysis of Rb EXAFS gives Rb-O distance, CN and disorder around Rb

as listed in Tables 5.2(c), 5.4(c) and 5.5(c) for the respective glass series. In Rb EXAFS we also observe the second shell of atoms around Rb and obtain corresponding parameters for the Rb-Ge bond (Tables 5.2(d) and 5.4(d)). The local structure around Ag was determined for the mixed mobile ion series, $(Rb,Ag)_2O$-GeO_2 and the results for Ag-O bond are given in Table 5.4(e).

Parallel analysis of K EXAFS obtained at liquid helium temperature gives K-O distance, CN and disorder around K as listed in Tables 5.3(c) and 5.5(d).

Statistical analysis of the data indicates that the present results are relatively more accurate for Ge EXAFS than for Rb, K, or Ag EXAFS. Estimated uncertainty for Ge-O distance is ± 0.01 Å but for Rb-O distance it is ≤ ± 0.03 Å, and for K-O it is ≤ ± 0.02 Å [105]. By systematic fitting procedure (e.g. choosing the same k range for every spectrum), the statistical relative uncertainty for any two samples is within ± 0.003 Å for Rb-O distance and ± 0.008 Å for the K-O distance. In general the uncertainty in CN is high and is typically 20 - 30% [106].

5.4.2 XPS

The O_{1s} x-ray photoelectron spectra for the glasses consist of a predominant peak at E_o and a smaller component at ~ 2 eV lower binding energy; for the binary Rb germanate glasses, E_o ~ 533 eV, for the binary K germanate glasses, E_o is ~ 532 eV; the difference in E_o between the two series being due to the calibration of spectrometer work function. Fig. 5.12 shows the spectra of Rb germanate series with the same E_o as the reference energy. Fig. 5.13 shows a typical example of the deconvolution of O_{1s} spectrum

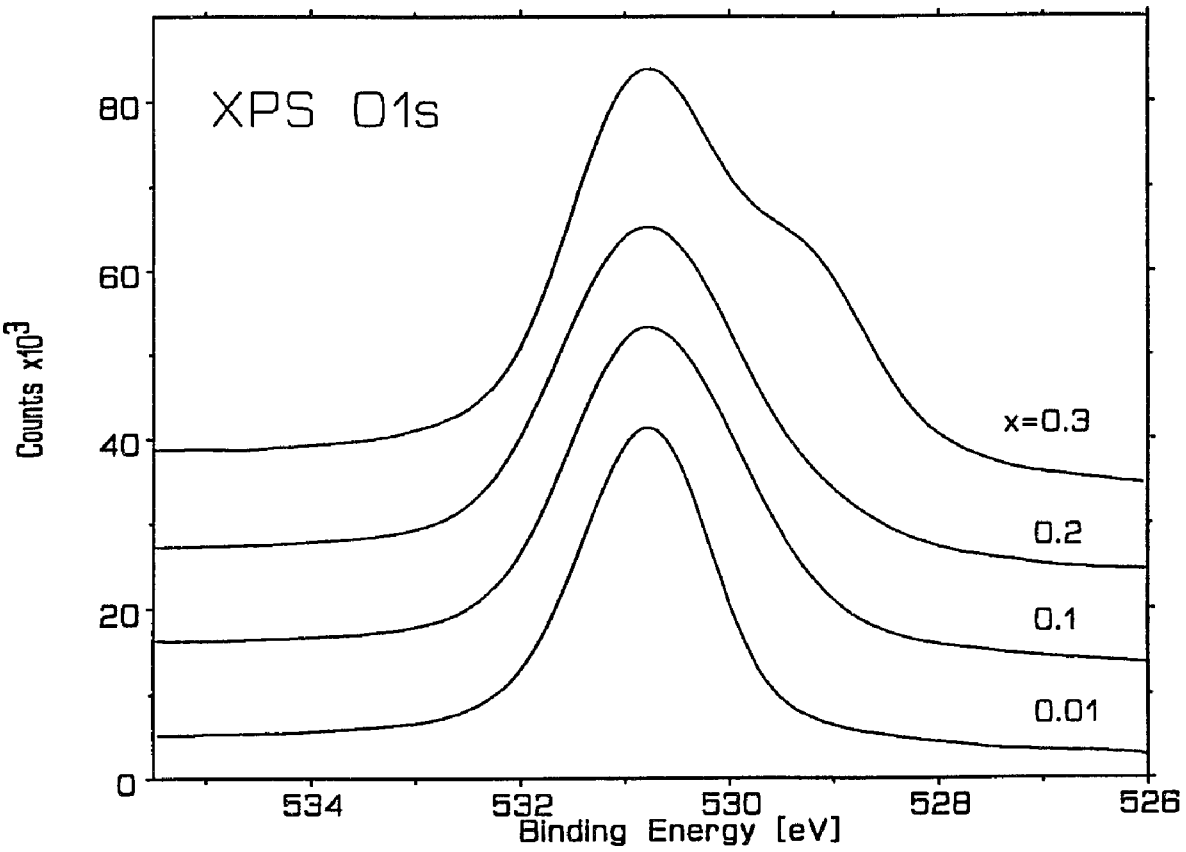

Figure 5.12 O_{1s} XPS spectra of $xRb_2O•(1-x)GeO_2$ glasses with binding energy scale relative to the binding energy of respective BOs (E_o) given in Table 5.2.

into 2 peaks for $0.3Rb_2O•0.7GeO_2$ glass using ESCA-300 software package. The lower binding energy component of the O_{1s} spectrum is attributed to NBOs and the higher binding energy component is attributed to BOs [77]. Here a shift of the photoelectron peak toward lower binding energies corresponds to an increase in electron density on the relevant atom. Thus, the difference in electron charge density between an NBO and a BO is reflected in

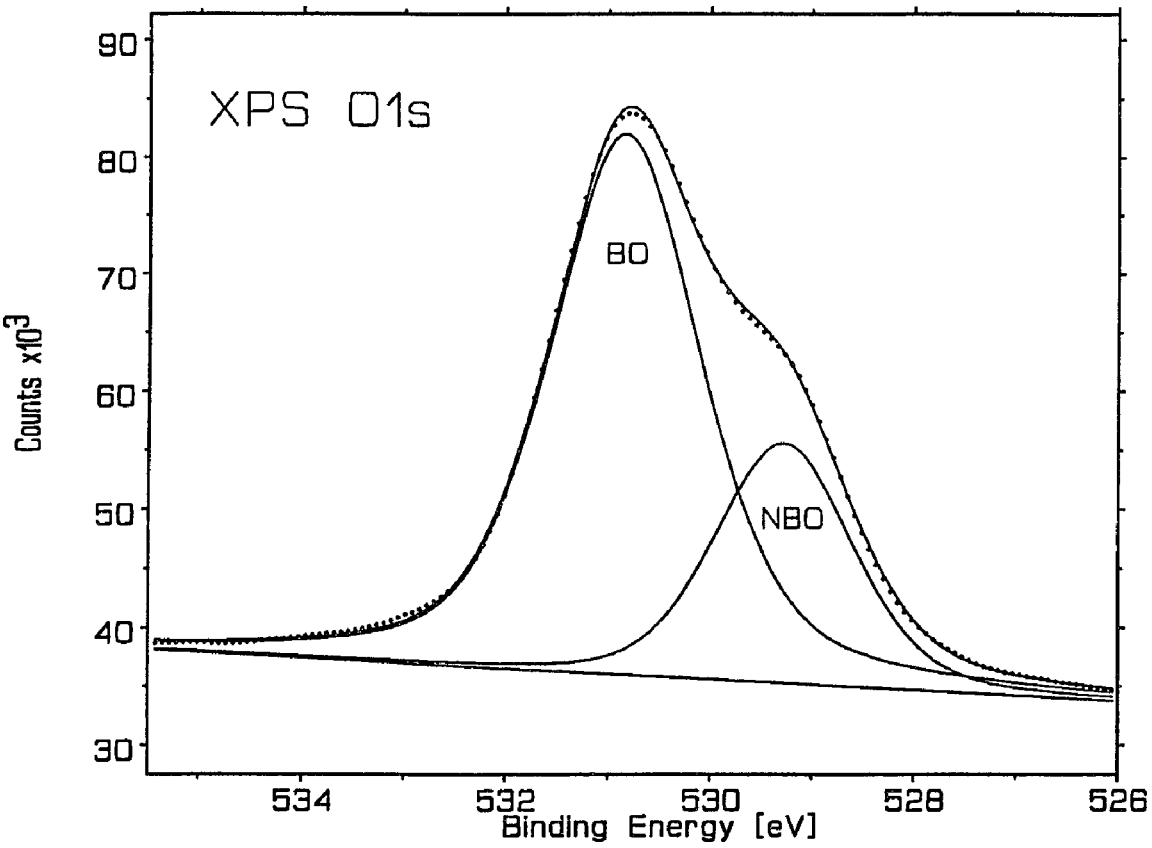

Figure 5.13 Deconvolution of O_{1s} XPS spectrum of $0.3Rb_2O{\bullet}0.7GeO_2$ glass into the BO and NBO components.

the energy difference of corresponding peaks. The corresponding values of peak energy for the NBO and BO peaks are listed in Table 5.2 for the Rb_2O-GeO_2 series and in Table 5.3 for the K_2O-GeO_2 series. Note that although the absolute values of O_{1s} binding energy may have uncertainty > 0.1 eV due to incomplete neutralization of surface charge, the relative values are expected to be accurate to better than ± 0.1 eV. The area under the

deconvoluted components represents the relative amount of the two kinds of oxygens and thus gives the fraction of NBO. From the deconvolution of O_{1s} XPS spectra, the relative ratio of non-bridging oxygen (NBO) and bridging oxygen (BO) concentration in both glass series has been determined as listed in Table 5.2 for the Rb_2O-GeO_2 series and in Table 5.3 for the K_2O-GeO_2 series.

Following the literature [106] we assume that the addition of Rb_2O to GeO_2 causes either the production of NBO or conversion of GeO_4 to GeO_6, and calculate the fraction of six-coordinated Ge, N_6, from the fraction of NBO (Table 5.2(e)):

$$\text{fraction of NBO} = 2(x-p)/(2-x) \text{ and } N_6 = p/(1-x)$$

where x is the value in $xRb_2O\bullet(1-x)GeO_2$ and p is the fraction of xRb_2O which causes the conversion of GeO_4 into GeO_6. The values of N_6 for this series are listed in Table 5.2(e). Similar approach is also applied to obtain the values of N_6 for the $xK_2O\bullet(1-x)GeO_2$ series as listed in Table 5.3(d).

5.4.3 IR

The infrared spectroscopy measurements and spectrum analysis were carried out by Dr. Kamitsos's group at Theoretical and Physical Chemistry Institute, Athens, Greece. The infrared reflectance spectra of batch 1 samples (labeled by 1a, 1b, 1c, 1d and 1e respectively) of the sodium triborate glass series have been obtained at various annealing times as shown in Fig. 5.14. While the overall spectral profile appears quite the same, the absolute reflectivity depends on annealing time. The same behavior is exhibited by the absorption coefficient spectra depicted in Fig. 5.15. It is shown that the absorption

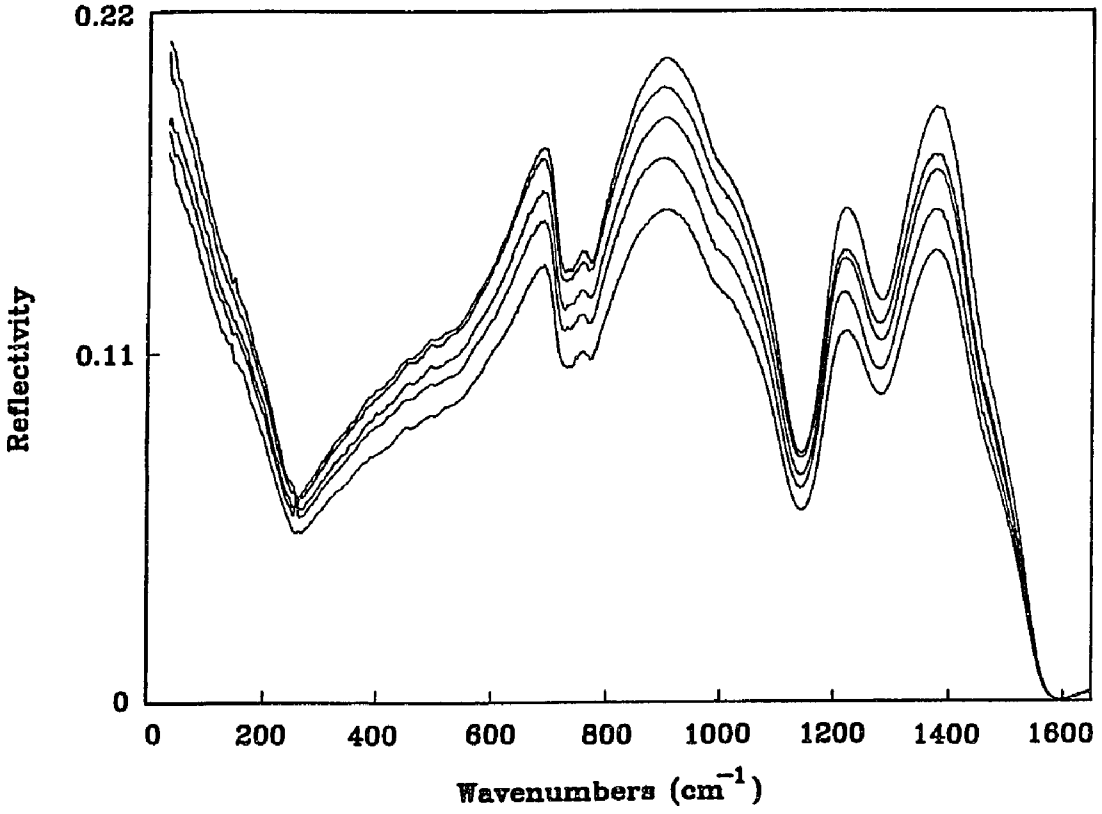

Figure 5.14 IR reflectance spectra of batch 1 samples. From top to bottom: 1c, 1b, 1a, 1d, 1e. The sequence is followed throughout the entire spectral range.

coefficient reduces in the order 1c > 1b > 1a > 1d > 1e. This sequence is followed in the mid-infrared region (400-1600 cm^{-1}) where the vibrations of the borate network are mainly active [84], as well as in the far-infrared (see inset of Fig. 5.15) where the asymmetric absorption profile originates from the rattling motion of Na^+ ions [107].

To quantify the dependence of the infrared spectra on annealing time, we have

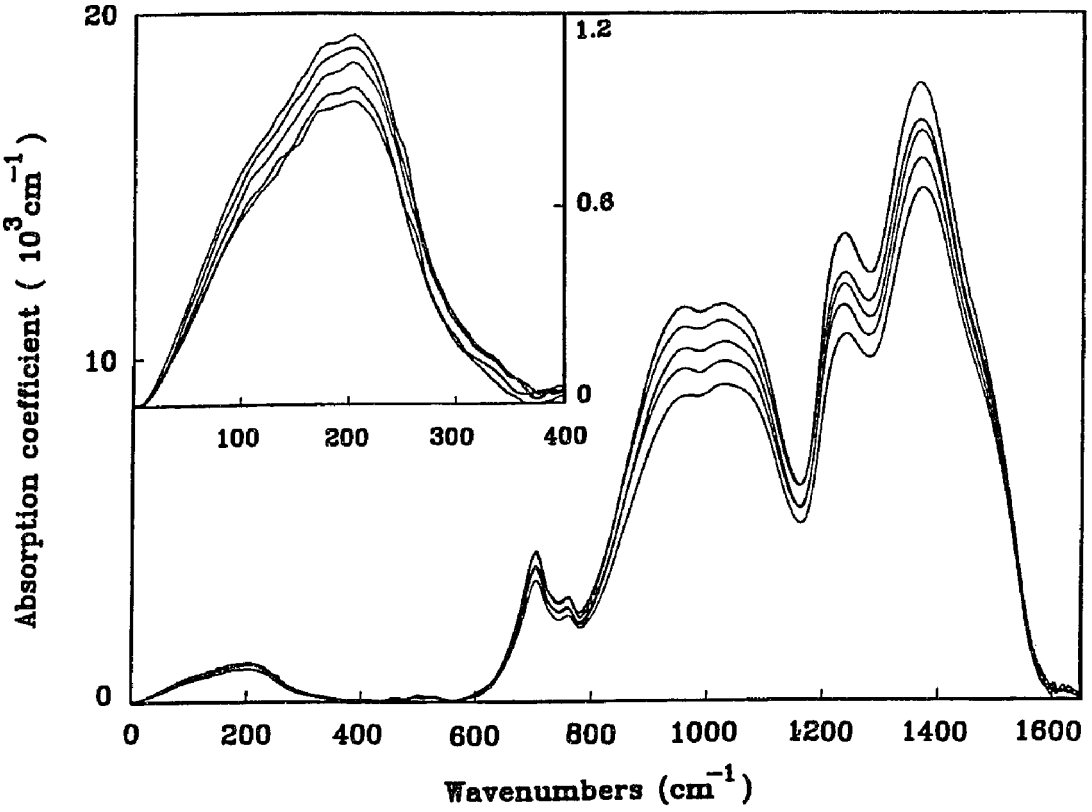

Figure 5.15 Absorption coefficient spectra of batch 1 samples. From top to bottom: 1c, 1b, 1a, 1d, 1e, in the whole spectral range. The inset shows the far-IR range in an expanded scale.

integrated the infrared absorption in the 0-1600 cm^{-1} region to obtain the total area under the spectrum, A. As shown in Fig. 5.16(a), the total IR area appears decreasing with annealing time. The same trend is followed by the average value of the refractive index n (obtained at frequencies 2500, 3300 and 3,900 cm^{-1}) (Fig. 5.16(b)).

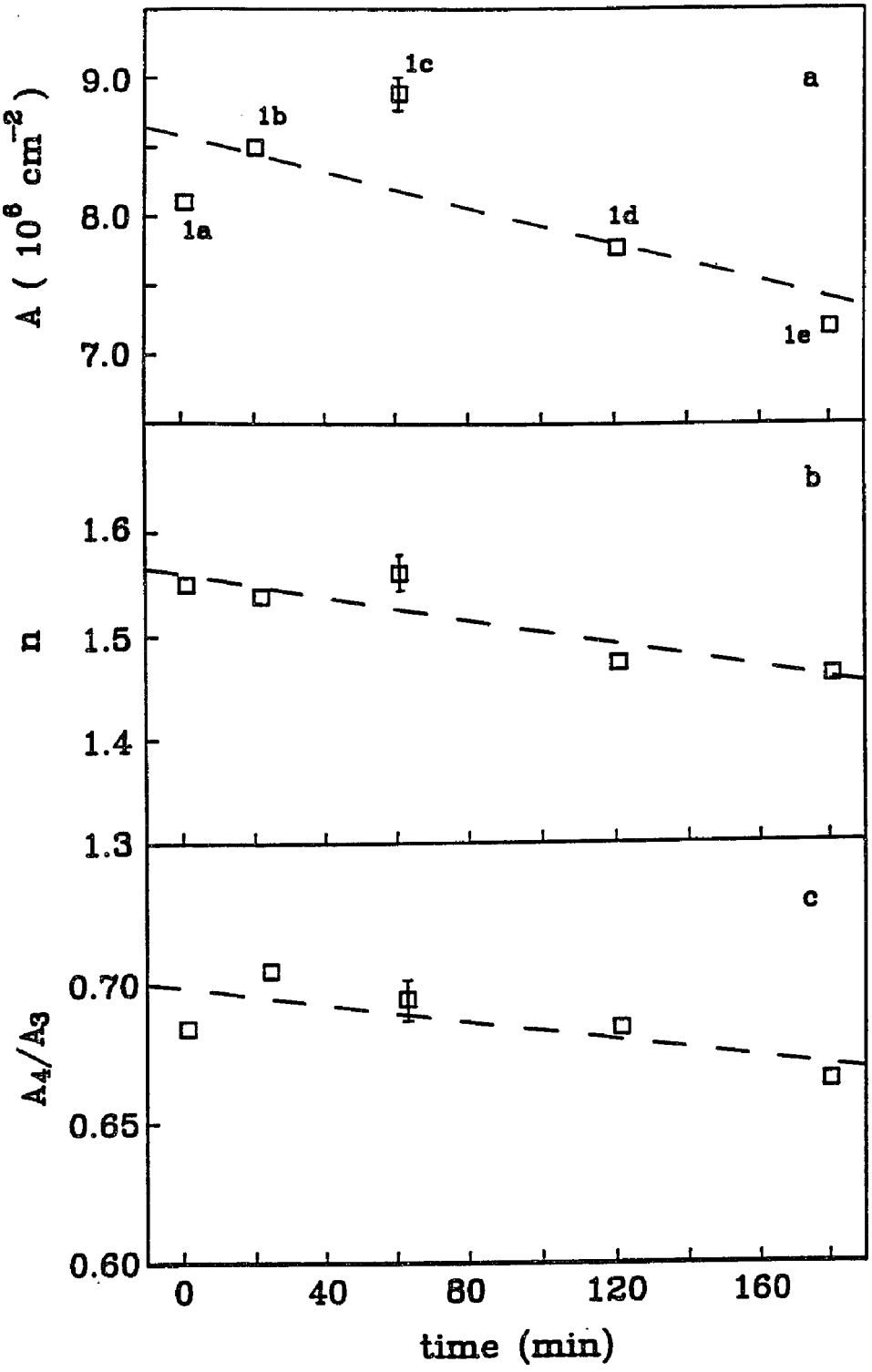

Figure 5.16 (a) Integrated IR absorption in the 0 - 1600 cm^{-1} range, A. (b) Average IR refractive index, n. (c) Relative integrated absorption of B-O tetrahedral, and triangles, A_4/A_3.

While the total IR integrated absorption and the average IR refractive index decrease with annealing time at 850 °C, it is of interest to examine the effect of t on the relative abundance of borate polyhedra forming the glass network. The infrared spectra provide this information, since absorption in the range 800-1150 cm^{-1} is attributed to vibrations of boron-oxygen tetrahedra $B\emptyset_4^-$ (Ø refers to a bridging oxygen), while absorption in the range ~ 1150 - 1600 cm^{-1} originates from vibrations of boron-oxygen triangles $B\emptyset_3$ and $B\emptyset_2O^-$ (O^- refers to a non-bridging oxygen atom) [84]. Thus, we have obtained the integrated absorptions in these spectral ranges, denoted by A_4 and A_3 respectively, and plot the ratio A_4/A_3 vs. annealing time in Fig. 5.16(c). Clearly, A_4/A_3 decreases with t, suggesting the conversion of boron-oxygen tetrahedra $B\emptyset_4^-$ into boron-oxygen triangles and specifically $B\emptyset_2O^-$. We also note that the average value of A_4/A_3 for the present glasses correspond to the value of sodium-borate glass with ~ 25 mol% Na_2O, i.e. of the triborate composition [108].

5.4.4 Density and Molar Volume

The values of density for each glass and quartz series are listed in the corresponding Tables 5.1, 5.2(a), 5.3(a), 5.4(a), 5.5(a) and 5.6(b). Molar volume (V_{mol}) has been determined from the density measurements for the various germanate glass series and its values are shown in the corresponding Tables 5.2(a), 5.3(a), 5.4(a) and 5.5(a). The density data are also used to calculate the "excess volume" per mole of glass ($V_{exc} = V_{mol} - V_{occupied}$), where V_{mol} is the molar volume and $V_{occupied}$ is the volume which is occupied by atoms. The ionic radii of various atoms are taken as R_{K+} = 1.33 Å, R_{Rb+} = 1.47 Å, R_{O2-} = 1.32

Å, $R_{Ge4+\ (CN\ =\ 4)}$ = 0.40 Å, and $R_{Ge4+\ (CN\ =\ 6)}$ = 0.54 Å [109,110] and used for volume calculation assuming each atom as a hard sphere. V_{exc} may be considered as the volume of glass that is not occupied by any atoms, which represents the available space for the diffusion of mobile ions [40]. The values of V_{exc} for the various germanate glasses are also shown in Tables 5.2(a), 5.3(a), 5.4(a) and 5.5(a).

The results of conductivity, density and local structure for each glass and quartz series are listed: Table 5.1: Na_2O-B_2O_3 series, Table 5.2: $xRb_2O•(1-x)GeO_2$ series, Table 5.3: $xK_2O•(1-x)GeO_2$ series, Table 5.4: $0.2(Rb,Ag)_2O•0.8GeO_2$ series, Table 5.5: $0.2(Rb,K)_2O•0.8GeO_2$ series, Table 5.6: high purity quartz series.

5.5 Tables of Results for Each Glass System

5.5.1 Na_2O-B_2O_3 Series

Table 5.1
Room temperature density, the pre-exponential term and activation energy for electrical conductivity of batch 1 and batch 2 sodium-borate glasses.

Batch#-Sample#	Melt treatment	Density (g/cm^3)	σ_o ($\Omega^{-1}cm^{-1}K \times 10^{-4}$)	E_{dc} (KJ/mol, ± 0.1)
1a	1400°C, 2 h; 850°C, 0 min	2.246	6.34	88.0
1a'	1400°C, 2 h; 850°C, 1 min	2.245	7.64	88.3
1b	1400°C, 2 h; 850°C, 20 min	2.250	7.94	88.2
1c	1400°C, 2 h; 850°C, 60 min	2.246	6.69	87.8
1d	1400°C, 2 h; 850°C, 2 h	2.242	6.20	87.4
1e	1400°C, 2 h; 850°C, 3 h	2.240	6.77	86.7
2a	1400°C, 2 h; 850°C, 0 min	2.234	7.28	88.2
2b	1400°C, 2 h; 850°C, 2 min	2.233	5.34	87.0
2c	1400°C, 2 h; 850°C, 10 min	2.232	5.23	87.2
2d	1400°C, 2 h; 850°C, 30 min	2.232	5.00	87.0
2e	1400°C, 2 h; 850°C, 2 h	2.231	4.63	86.3
2f	1400°C, 2 h; 850°C, 3 h	2.231	4.83	86.3

5.5.2 Rb_2O-GeO_2 Series

Table 5.2(a)
Values of Rb-O bond distance (R_{Rb-O}) (from Table 5.2(c)), pre-exponential term (σ_o), activation energy (E_{dc}) for d.c. conductivity, relative dielectric constant (ε_i), density, molar volume (V_{mol}), excess volume (V_{exc}), Coulomb energy between Rb and its charge compensating center ($1/\varepsilon_i R_{Rb-O}$), and Kohlrausch exponent (β) of rubidium germanate glasses.

$xRb_2O \bullet (1-x)GeO_2$	R_{Rb-O} (Å)	σ_o ($\Omega^{-1}cm^{-1}K$)	E_{dc} (eV)	ε_i	Density (g/cm^3)	V_{mol} (cm^3/mole)	V_{exc} (cm^3/mole)	$1/\varepsilon_i R_{Rb-O}$ ($Å^{-1}$)	β
mol% Rb_2O									
1	2.81(2)	5.34×10^6	1.488 ± 0.004	8.0	3.73	28.25	16.39	0.044	0.93
2	2.82(6)	3.55×10^6	1.423 ± 0.002	7.5	3.80	27.95	15.98	0.047	0.93
5	2.82(1)	4.08×10^6	1.455 ± 0.003	9.6	3.94	27.60	15.30	0.037	0.92
10	2.82(4)	2.76×10^6	1.584 ± 0.001	12.5	4.08	27.69	14.90	0.028	0.74
15	2.76(6)	1.31×10^4	1.021 ± 0.001	13.7	4.13	28.30	15.00	0.026	0.55
20	2.73(5)	1.23×10^4	0.817 ± 0.001	14.3	4.12	29.37	15.56	0.026	0.53

Table 5.2(b)
Structural parameters extracted from Ge (1st shell) EXAFS:
Ge-O bond distance, coordination number and disorder (Debye-Waller factor) around Ge atom in rubidium germanate glasses.

$xRb_2O•(1-x)GeO_2$	R_{Ge-O} (Å)	CN_{Ge-O}	$\Delta\sigma^2_{Ge-O}$ ($\times 10^{-4}$ Å^2)
mol% Rb_2O			
2	1.74(0)	4.8	7
5	1.74(1)	4.4	8
10	1.74(6)	4.8	23
15	1.76(1)	4.0	12
20	1.75(5)	4.2	16

Table 5.2(c)
Structural parameters extracted from Rb (1st shell) EXAFS:
Rb-O bond distance, coordination number and disorder (Debye-Waller factor) around Rb atom in rubidium germanate glasses.

$xRb_2O•(1-x)GeO_2$	R_{Rb-O} (Å)	CN_{Rb-O}	$\Delta\sigma^2_{Rb-O}$ ($\times 10^{-4}$ Å^2)
mol% Rb_2O			
1	2.81(2)	5.6	220
2	2.82(6)	6.1	234
5	2.82(1)	5.5	185
10	2.82(4)	7.9	178
15	2.76(6)	5.6	119
20	2.73(5)	5.2	129

Table 5.2(d)
Structural parameters extracted from Rb (2nd shell) EXAFS:
Rb-Ge bond distance, coordination number and disorder (Debye-Waller factor) around Rb atom in rubidium germanate glasses.

$xRb_2O•(1-x)GeO_2$	R_{Rb-Ge} (Å)	CN_{Rb-Ge}	$\Delta\sigma^2_{Rb-Ge}$ ($\times 10^{-4}$ Å^2)
mol% Rb_2O			
1	3.71	6.0	186
2	3.72	6.0	183
5	3.72	6.5	209
10	3.72	4.1	130
15	3.68	8.3	224
20	3.68	7.2	228

Table 5.2(e)

XPS results of O_{1s} parameters for the $xRb_2O\bullet(1-x)GeO_2$ rubidium germanate glasses. N_6 is calculated from the experimental fraction of NBO, A_{NBO}/A_{NBO+BO} (A: area under the peak). E_o is the binding energy of respective BO peaks.

x (mol%)	Peak energy (eV) BO (E_o)	NBO	FWHM (eV) BO	NBO	A_{NBO}/A_{NBO+BO} (%)	N_6 (%)
5	534.0	532.1	1.81	1.55	2.8	2.4
10	534.4	532.3	1.95	1.75	3.8	7.1
15	535.0	533.2	1.93	1.67	5.2	12.0
20	533.8	532.0	1.98	1.45	5.4	18.9
30	529.8	528.2	1.71	1.30	24.3	13.4
40	531.8	530.1	1.43	1.37	43.9	8.1

5.5.3 K_2O-GeO_2 Series

Table 5.3(a)
Values of K-O bond distance (R_{K-O}) (from Table 5.3(c)), pre-exponential term (σ_o), activation energy (E_{dc}) for d.c. conductivity, relative dielectric constant (ε_i), density, molar volume (V_{mol}), excess volume (V_{exc}), Coulomb energy between K and its charge compensating center ($1/\varepsilon_i R_{K-O}$), and Kohlrausch exponent (β) of potassium germanate glasses.

$xK_2O\bullet(1-x)GeO_2$	R_{K-O} (Å)	σ_o ($\Omega^{-1}cm^{-1}K$)	E_{dc} (eV)	ε_i	Density (g/cm^3)	V_{mol} (cm^3/mole)	V_{exc} (cm^3/mole)	$1/\varepsilon_i R_{K-O}$ ($Å^{-1}$)	β
mol% K_2O									
0.23	---	3.00×10^7	1.576 ± 0.002	7.6	3.69	28.37	16.59	---	0.95
2	2.74(6)	4.62×10^6	1.476 ± 0.002	9.5	3.73	27.96	16.10	0.038	0.89
5	2.73(7)	1.26×10^6	1.416 ± 0.003	11.1	3.83	27.15	15.14	0.033	0.88
7.4	2.72(0)	2.62×10^6	1.478 ± 0.002	11.4	3.87	26.82	14.69	0.032	0.85
10	2.72(0)	1.75×10^6	1.491 ± 0.002	12.5	3.89	26.64	14.38	0.029	0.71
15	2.70(8)	3.40×10^4	1.086 ± 0.001	14.3	3.86	26.72	14.21	0.026	0.54
20	2.68(9)	1.63×10^4	0.822 ± 0.002	14.4	3.74	27.24	14.48	0.026	0.52
24.7	2.70(4)	1.59×10^4	0.713 ± 0.002	14.9	3.59	28.41	15.43	0.025	0.53

Table 5.3(b)

Structural parameters extracted from Ge (1st shell) EXAFS:
Ge-O bond distance, coordination number and disorder (Debye-Waller factor) around Ge atom in potassium germanate glasses.

$xK_2O•(1-x)GeO_2$	R_{Ge-O} (Å)	CN_{Ge-O}	$\Delta\sigma^2_{Ge-O}$ ($\times 10^{-4}$ Å^2)
mol% K_2O			
5	1.74(3)	4.6	26
7.4	1.75(1)	4.2	23
10	1.75(0)	4.2	26
15	1.75(4)	3.0	42
20	1.76(4)	4.2	13
24.7	1.76(2)	4.2	14

Table 5.3(c)

Structural parameters extracted from K (1st shell) EXAFS:
K-O bond distance, coordination number and disorder (Debye-Waller factor) around K atom in potassium germanate glasses.

$xK_2O•(1-x)GeO_2$	R_{K-O} (Å)	CN_{K-O}	$\Delta\sigma^2_{K-O}$ ($\times 10^{-4}$ Å^2)
mol% K_2O			
2	2.74(6)	6.3	453
5	2.73(7)	6.0	429
7.4	2.72(0)	5.7	406
10	2.72(0)	6.3	493
15	2.70(8)	5.3	410
20	2.68(9)	4.7	361
24.7	2.70(4)	5.0	346

Table 5.3(d)

XPS results of O_{1s} parameters for the $xK_2O\bullet(1-x)GeO_2$ potassium germanate glasses. N_6 is calculated from the experimental fraction of NBO, A_{NBO}/A_{NBO+BO} (A: area under the peak). E_o is the binding energy of respective BO peaks.

x (mol%)	Peak energy (eV) BO (E_o)	NBO	FWHM (eV) BO	NBO	A_{NBO}/A_{NBO+BO} (%)	N_6 (%)
0.23	532.0	---	1.50	---	0.0	0.2
2.0	532.1	530.5	1.51	1.08	1.5	0.5
5.0	532.2	531.1	1.50	1.27	3.0	2.2
10.0	532.0	530.9	1.75	1.47	4.5	6.4
15.0	532.1	531.0	1.99	1.10	5.9	11.2
20.0	532.1	530.5	1.89	1.02	6.9	17.2
24.7	532.2	530.6	1.80	1.22	11.8	19.1

5.5.4 Mixed $(Rb,Ag)_2O$-GeO_2 Series

Table 5.4(a)
Pre-exponential term (σ_o), activation energy (E_{dc}) for d.c. conductivity, relative dielectric constant (ε_i), and Kohlrausch exponent (β) of mixed rubidium-silver germanate glasses.

$0.2[yAg\bullet(1-y)Rb]_2O \bullet 0.8GeO_2$		σ_o ($\Omega^{-1}cm^{-1}K$)	E_{dc} (eV)	ε_i	Density (g/cm^3)	V_{mol} (cm^3/mol)	V_{exc} (cm^3/mol)	β
y	1-y							
0	1	1.23×10^4	0.817 ± 0.001	14.3	4.127	29.33	15.52	0.53
0.25	0.75	4.56×10^4	1.119 ± 0.001	12.5	4.129	30.59	17.07	0.58
0.5	0.5	7.66×10^3	1.212 ± 0.002	14.3	4.126	31.61	18.39	0.54
0.75	0.25	8.46×10^3	1.279 ± 0.002	12.5	4.133	33.09	20.17	0.60
1	0	1.52×10^4	0.711 ± 0.001	15.4	4.583	30.99	18.36	0.38

Table 5.4(b)

Structural parameters extracted from Ge (1st shell) EXAFS:
Ge-O bond distance, coordination number and disorder (Debye-Waller factor) around Ge atom in rubidium-silver germanate glasses.

$0.2[yAg\bullet(1-y)Rb]_2O \bullet 0.8GeO_2$		R_{Ge-O} (Å)	CN_{Ge-O}	$\Delta\sigma^2_{Ge-O}$ ($\times 10^{-4}$ Å^2)
y	1-y			
0	1	1.75(5)	4.2	16
0.25	0.75	1.75(2)	4.2	14
0.5	0.5	1.75(0)	4.0	19
0.75	0.25	1.74(4)	4.0	7
1	0	1.74(5)	4.0	6

Table 5.4(c)

Structural parameters extracted from Rb (1st shell) EXAFS:
Rb-O bond distance, coordination number and disorder (Debye-Waller factor) around Rb atom in rubidium-silver germanate glasses.

$0.2[yAg\bullet(1-y)Rb]_2O \bullet 0.8GeO_2$		R_{Rb-O} (Å)	CN_{Rb-O}	$\Delta\sigma^2_{Rb-O}$ ($\times 10^{-4}$ Å^2)
y	1-y			
0	1	2.73(5)	5.2	129
0.25	0.75	2.78(3)	4.4	103
0.5	0.5	2.78(9)	6.5	162
0.75	0.25	2.80(9)	6.2	195
1	0			

Table 5.4(d)

Structural parameters extracted from Rb (2nd shell) EXAFS:

Rb-Ge bond distance, coordination number and disorder (Debye-Waller factor) around Rb atom in rubidium-silver germanate glasses.

$0.2[yAg•(1-y)Rb]_2O$ $•0.8GeO_2$		R_{Rb-Ge} (Å)	CN_{Rb-Ge}	$\Delta\sigma^2_{Rb-Ge}$ ($\times 10^{-4}$ Å^2)
y	1-y			
0	1	3.68	7.2	228
0.25	0.75	3.70	5.6	193
0.5	0.5	3.68	7.6	199
0.75	0.25	3.71	6.3	167
1	0			

Table 5.4(e)

Structural parameters extracted from Ag (1st shell) EXAFS:

Ag-O bond distance, coordination number and disorder (Debye-Waller factor) around Ag atom in rubidium-silver germanate glasses.

$0.2[yAg•(1-y)Rb]_2O$ $•0.8GeO_2$		R_{Ag-O} (Å)	CN_{Ag-O}	$\Delta\sigma^2_{Ag-O}$ ($\times 10^{-4}$ Å^2)
y	1-y			
0	1			
0.25	0.75	2.09(6)	1.2	82
0.5	0.5	2.17(4)	1.3	144
0.75	0.25	2.25(0)	2.0	245
1	0	2.24(5)	2.5	273

5.5.5 Mixed $(Rb,K)_2O$-GeO_2 Series

Table 5.5(a)
Pre-exponential term (σ_o), activation energy (E_{dc}) for d.c. conductivity, relative dielectric constant (ε_i), and Kohlrausch exponent (β) of mixed rubidium-potassium germanate glasses.

$0.2[yK\bullet(1-y)Rb]_2O \bullet 0.8GeO_2$		σ_o ($\Omega^{-1}cm^{-1}K$)	E_{dc} (eV)	ε_i	Density (g/cm^3)	V_{mol} (cm^3/mol)	V_{exc} (cm^3/mol)	β
y	1-y							
0	1	1.23×10^4	0.817 ± 0.001	14.3	4.127	29.33	15.52	0.53
0.25	0.75	5.91×10^4	0.955 ± 0.002	14.7	4.046	28.77	15.22	0.54
0.5	0.5	1.93×10^5	1.028 ± 0.002	14.4	3.922	28.50	15.21	0.54
0.75	0.25	1.97×10^5	0.992 ± 0.002	14.3	3.848	27.85	14.82	0.53
1	0	1.63×10^4	0.822 ± 0.002	14.4	3.763	27.24	14.48	0.52

Table 5.5(b)

Structural parameters extracted from Ge (1st shell) EXAFS:
Ge-O bond distance, coordination number and disorder (Debye-Waller factor) around Ge atom in rubidium-potassium germanate glasses.

$0.2[yK•(1-y)Rb]_2O$ $•0.8GeO_2$		R_{Ge-O} (Å)	CN_{Ge-O}	$\Delta\sigma^2_{Ge-O}$ ($\times 10^{-4}$ Å^2)
y	1-y			
0	1	1.76(7)	4.5	37
0.25	0.75	1.76(0)	3.8	26
0.5	0.5	1.76(3)	4.7	40
0.75	0.25	1.76(5)	3.6	42
1	0	1.76(4)	4.2	13

Table 5.5(c)

Structural parameters extracted from Rb (1st shell) EXAFS:
Rb-O bond distance, coordination number and disorder (Debye-Waller factor) around Rb atom in rubidium-potassium germanate glasses.

$0.2[yK•(1-y)Rb]_2O$ $•0.8GeO_2$		R_{Rb-O} (Å)	CN_{Rb-O}	$\Delta\sigma^2_{Rb-O}$ ($\times 10^{-4}$ Å^2)
y	1-y			
0	1	2.84(7)	2.75	122
0.25	0.75	2.85(2)	2.69	309
0.5	0.5	2.85(1)	3.67	129
0.75	0.25	2.85(6)	3.08	144
1	0			

Table 5.5(d)

Structural parameters extracted from K (1st shell) EXAFS:

K-O bond distance, coordination number and disorder (Debye-Waller factor) around K atom in rubidium-potassium germanate glasses.

$0.2[yK\bullet(1-y)Rb]_2O \bullet 0.8GeO_2$		R_{K-O} (Å)	CN_{K-O}	$\Delta\sigma^2_{K-O}$ ($\times 10^{-4}$ Å^2)
y	1-y			
0	1			
0.25	0.75	2.67(5)	6.1	385
0.5	0.5	2.68(0)	5.7	374
0.75	0.25	2.68(1)	5.0	368
1	0	2.68(9)	4.7	361

5.5.6 High Purity Quartz Series

Table 5.6(a)

Activation energy (E_{dc}) and pre-exponential term (σ_o) for d.c. conductivity, and Kohlrausch exponent (β) for as received and annealed Premium Q quartz specimens.

quartz specimen	E_{dc} (eV)	σ_o ($\Omega^{-1}cm^{-1}K$)	β
quartz (as received)	1.78	9.92×10^6	0.70
quartz (after annealing at ~ 500 °C for 5 ~ 10 hr)	1.49	2.72×10^5	0.71
quartz (annealing at 525 °C for 36 hr)	1.33	1.71×10^5	0.85

Table 5.6(b)
Neutron (> 1 MeV) irradiation does, activation energy (E_{dc}) and pre-exponential term (σ_o) for d.c. conductivity, Kohlrausch exponent (β), and density of Premium Q quartz specimens.

	specimen	Neutron dose (n/cm^2)	E_{dc} (eV)	σ_o ($\Omega^{-1}cm^{-1}K$)	β	Density (g/cm^3)
Q6,	before irradiation	---	1.32	7.73×10^4	0.86 ± 0.01	2.654 ± 0.003
	after irradiation and heating	1×10^{18}	1.58	1.69×10^5	0.80 ± 0.01	2.655 ± 0.003
Q4,	before irradiation	---	1.30	1.34×10^5	0.87 ± 0.02	2.629 ± 0.002
	after irradiation and heating	1×10^{19}	2.29	3.50×10^8	---	2.641 ± 0.008
Q2,	before irradiation	---	1.33	1.71×10^5	0.85 ± 0.02	2.624 ± 0.002
	after irradiation and heating	1×10^{20}	1.64	7.93×10^2	---	2.652 ± 0.001

CHAPTER 6 STRUCTURE OF OXIDE GLASSES

In this chapter, we study the local structure of oxide glasses, where the variation of local structure arises from compositional effect. The applicability of the modified random network (MRN) glass structure model is examined for the germanate systems using the structural parameters obtained from EXAFS and XPS. A new structure model which describes the spatial atomic scale inhomogeneity is proposed. The correlation between short-range structure and long-range structure (molar volume) is then discussed.

6.1 Binary Alkali Germanate Glasses

The study of the binary alkali germanate series is to further establish the structure of alkali germanates and also to verify the applicability of MRN model to a glass system which is significantly different from alkali silicates. By contrast with alkali silicate systems, the alkali germanates do not phase-separate readily and, therefore, one would expect them to show less, if any, microheterogeneity (i.e. Rb atoms should be relatively randomly distributed in germanates compared with Rb atoms in silicates). EXAFS is expected to reveal this difference in structural disorder. Further, XPS is used to determine the fraction of NBO and BO, the ratio of which is then used to determine the ratio of sixfold to fourfold Ge coordination. Thus by combining the results of EXAFS and XPS, a more detailed structure of germanate glasses is revealed.

6.1.1 Validity of MRN Structure Model

The concept of MRN structure originated from the observation that the disorder around alkali ions in silicates is primarily of thermal origin [19,20]. To examine the applicability of MRN model to a glass system which is significantly different from alkali silicates, we have studied the structural disorder around Rb and K ions in the above

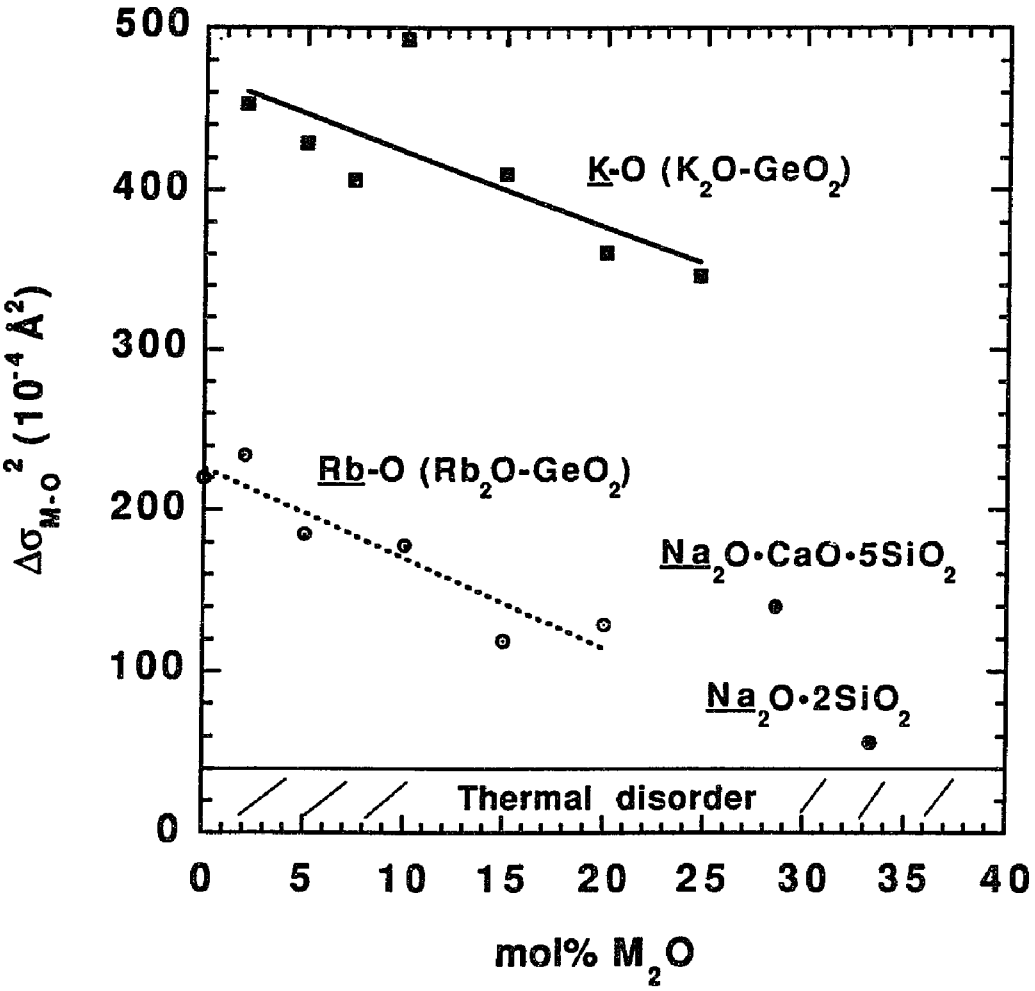

Figure 6.1 $\Delta\sigma^2_{M\text{-}O}$ vs. mol% M_2O (M=Rb, K) in xM2O•(1-x)GeO2 glass series. The disorder for Na-O in Na2O•2SiO2 and Na2O•CaO•5SiO2 glasses at R.T. is also shown for comparison.

mentioned two binary alkali germanate glass series. The results of structural disorder for Rb, $\Delta\sigma^2_{Rb\text{-}O}$, of the $xRb_2O\bullet(1\text{-}x)GeO_2$ series and for K, $\Delta\sigma^2_{K\text{-}O}$, of the $xK_2O\bullet(1\text{-}x)GeO_2$ series are listed in Tables 5.2(c) and 5.3(c) respectively. Fig. 6.1 shows the variations of $\Delta\sigma^2_{Rb\text{-}O}$ and $\Delta\sigma^2_{K\text{-}O}$ with mol% alkali for these two series along with the results for Na, $\Delta\sigma^2_{Na\text{-}O}$, of silicates [19,20]. From Fig. 6.1, we find that the structural disorder around Na ions in the sodium disilicate is very small when the thermal contribution is subtracted. That is, O shell is well defined at a fairly fixed distance from Na (2.3 Å in this case). However, the magnitude of disorder around Rb in our germanate glasses is almost an order of magnitude larger than that of alkali atoms in silicates. The contribution of thermal disorder to the observed disorder was not determined exactly for this case, yet it is evident from the estimated thermal disorder that the structural disorder around Rb is significantly more than for the alkalis in silicates. To establish the generality of these results and to experimentally eliminate the thermal disorder, let us focus on the results of binary potassium germanate series. From this series the disorder around K ions is determined at around liquid helium temperature; thus the thermal contribution to the total disorder has been eliminated. Fig. 6.1 shows that the disorder around K, $\Delta\sigma^2_{K\text{-}O}$, in $K_2O\text{-}GeO_2$ series is even larger than that around Rb, $\Delta\sigma^2_{Rb\text{-}O}$, in $Rb_2O\text{-}GeO_2$ series. One possible reason for this difference could be that smaller alkali ions have a greater freedom to more randomly distribute in the network structure. Notwithstanding, the results for both Rb and K germanate glass series clearly confirm that the structural disorder around alkali ions in alkali germanate glasses is larger than, for example, sodium in a silicate glass. Consequently the segregated channeled structure assumed for alkali migration in MRN

is less meaningful for alkali germanate glasses. Further, the increase in $\Delta\sigma^2_{M\text{-}O}$ with reduction of M_2O content (see Fig. 6.1) implies that the Rb and K environment is less uniform at low concentration. When more Rb_2O (or K_2O) is added, the non-uniformity is averaged out and the environment around Rb/K becomes more homogeneous, resulting in smaller mean square displacement.

6.1.2 Effect of Composition on Local Structure

Key Results

The following figures of the results for glass structure in the Rb_2O-GeO_2 and K_2O-GeO_2 series are plotted using the data obtained in Tables 5.2 and 5.3.

Fig. 6.2 shows the variation of Ge-O bond distance with increasing mol% Rb_2O for the Rb_2O-GeO_2 series. There is an increase of Ge-O bond distance with mol% Rb_2O. The bond distances of Ge-O in quartz-type and rutile-type GeO_2 containing GeO_4 and GeO_6 structures are also shown in the same figure for reference to reveal the existence of GeO_6 structural units in the glass. Similar trend of the variation of Ge-O bond distance with alkali concentration is also found for the K_2O-GeO_2 series (see Table 5.3(b)), suggesting that the conversion of GeO_4 to GeO_6 with the addition of alkali oxide M_2O (M = Rb, K) is perhaps generally true for germanate glasses.

Fig. 6.3 shows the variation of the molar volume (V_{mol}) and Rb-O, Ge-O bond distances as a function of mol% Rb_2O in the Rb_2O-GeO_2 series. The Rb-O distance remains constant within experimental error for $Rb_2O \leq 10$ mol% and then begins to decrease with the further addition of Rb_2O (≥ 15 mol%). V_{mol}, in contrast, clearly shows a minimum at

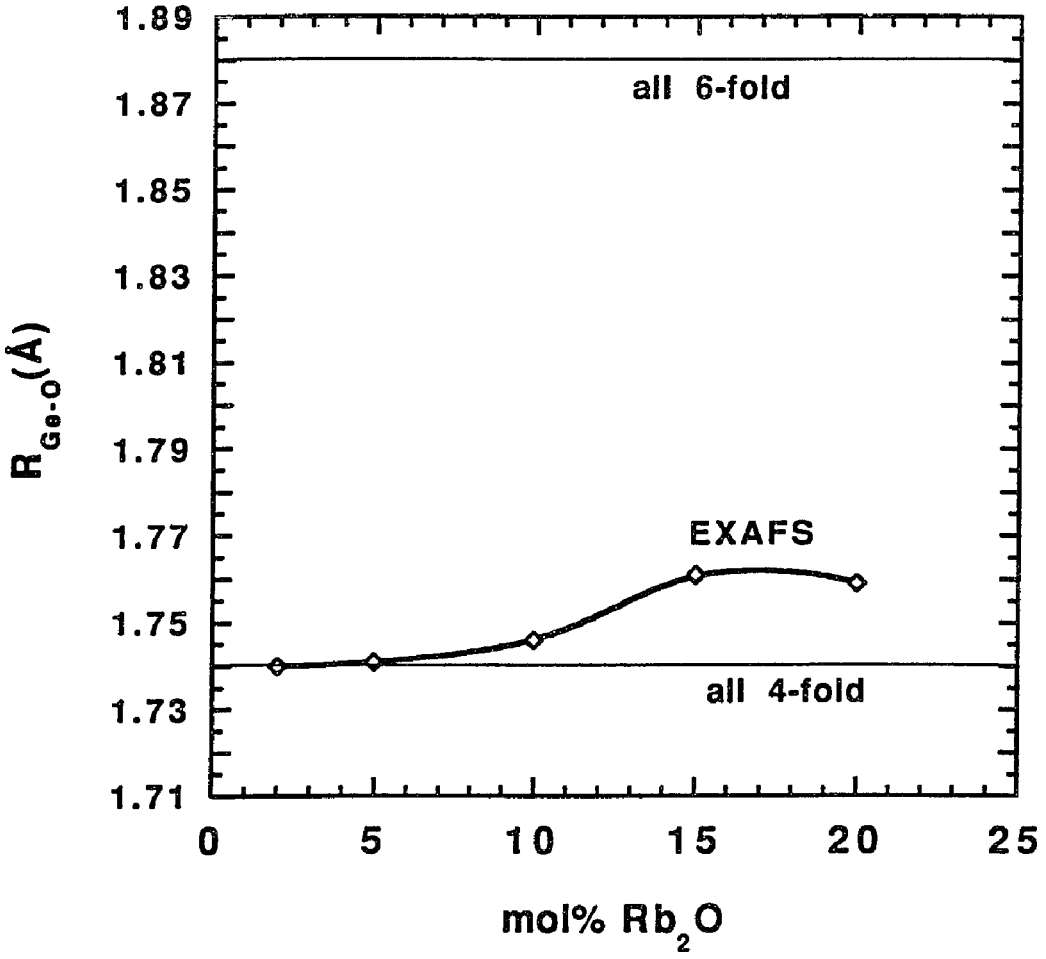

Figure 6.2 Ge-O bond distance, R_{Ge-O}, as a function of mol% Rb_2O. The Ge-O bond distances in quartz-type (fourfold) and rutile-type (sixfold) crystalline GeO_2 are shown for comparison.

Rb_2O concentration between 5 and 10 mol%, but the Rb-O and Ge-O distances monotonically decrease and increase, respectively, with increasing Rb_2O, the relative variation of molar volume being much larger.

Fig. 6.4 shows the variation of the molar volume (V_{mol}) and K-O, Ge-O bond

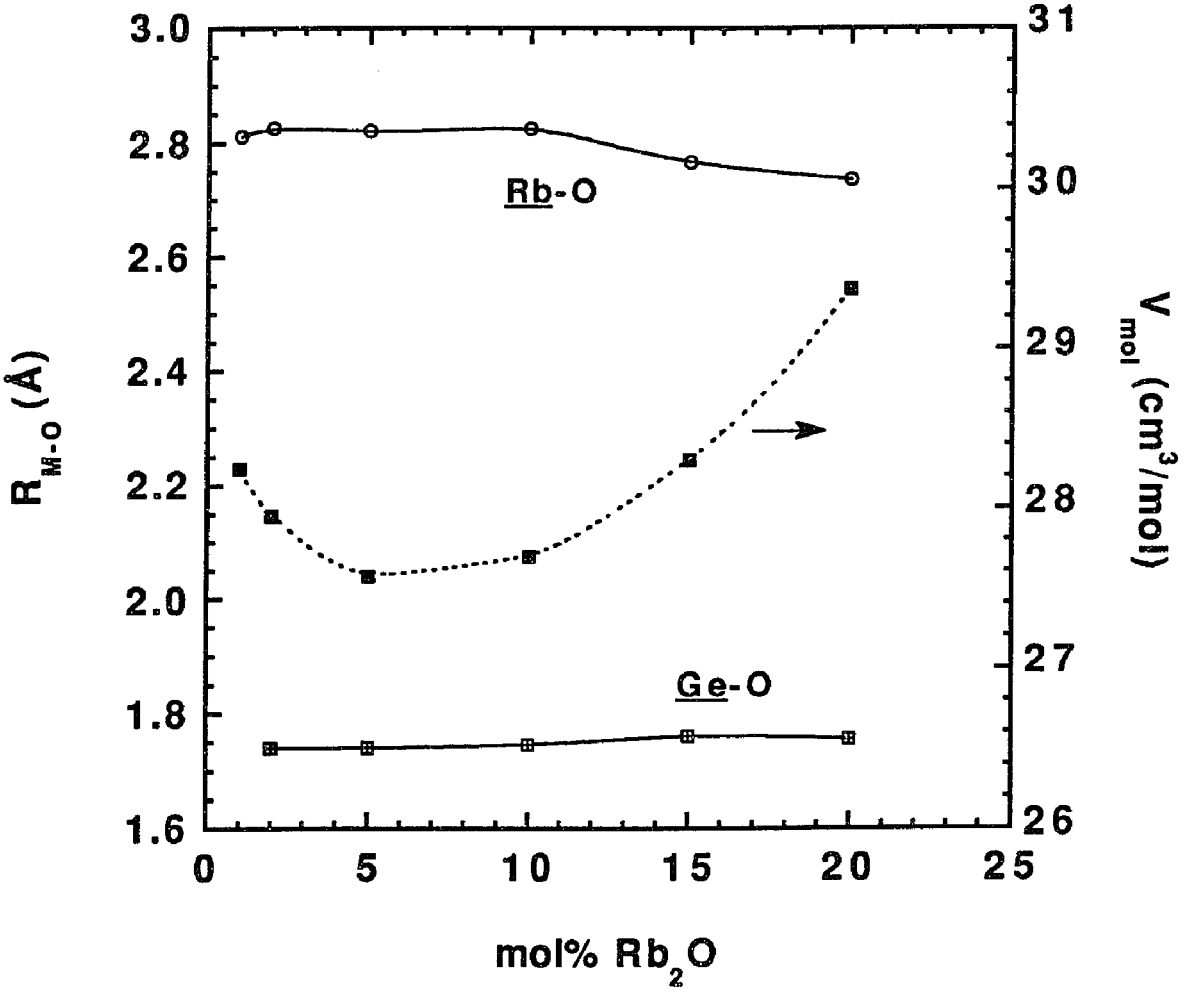

Figure 6.3 Variation of the V_{mol} and Rb-O, Ge-O bond distances as a function of mol% Rb_2O in $xRb_2O•(1-x)GeO_2$ glass series.

distances as a function of mol% K_2O in K_2O-GeO_2 series. The K-O distance slightly decreases with mol% K_2O, and then remains nearly constant as $K_2O \geq 15$ mol%. There is a small increase in Ge-O bond distance from 1.74(3) at 5 mol% K_2O to 1.76(2) at 24.7 mol%. Similar to the Rb_2O-GeO_2 series, V_{mol} in this series shows a minimum at ~ 10 mol% K_2O. The K-O and Ge-O distances monotonically decrease and increase, respectively, with

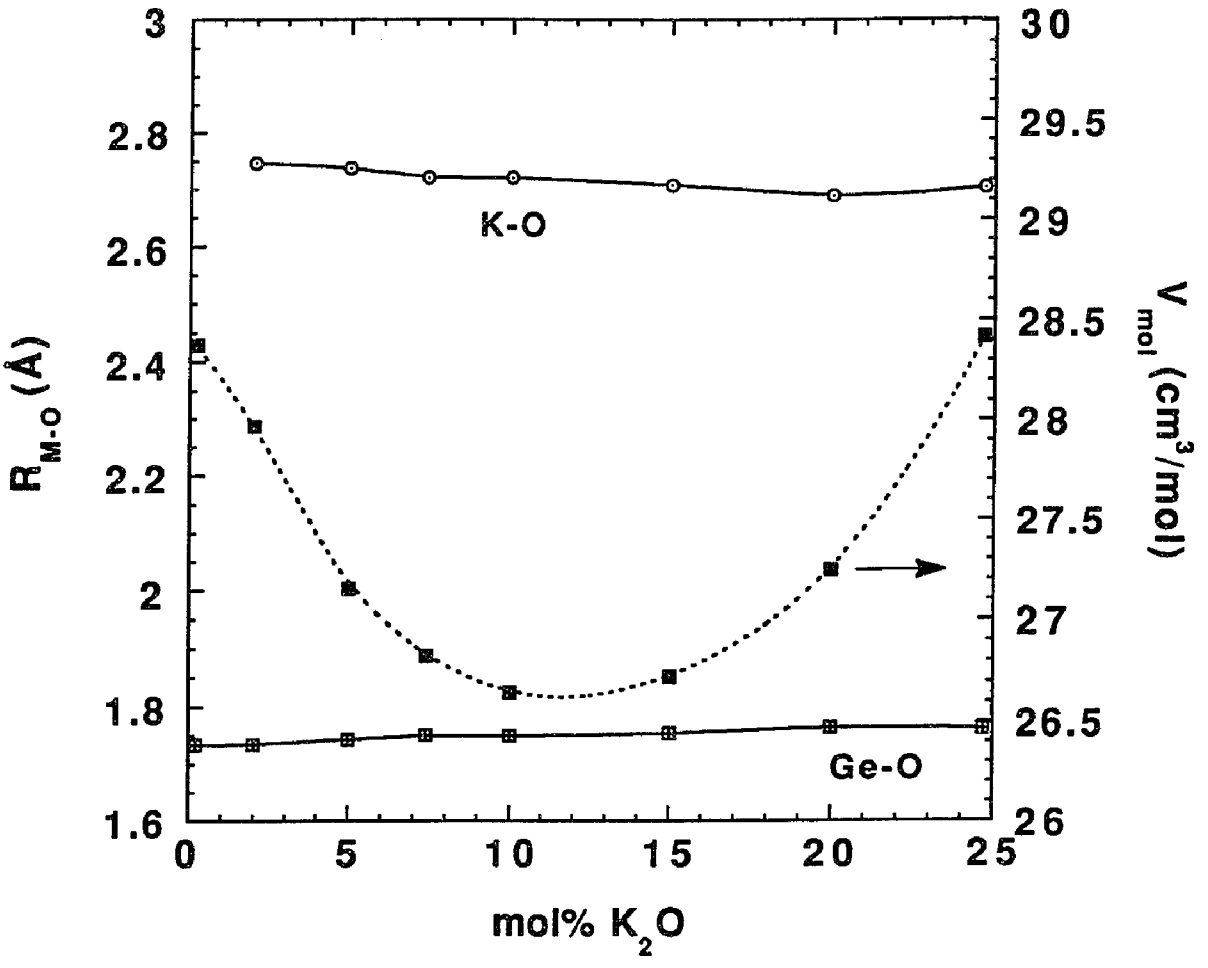

Figure 6.4 Variation of the V_{mol} and K-O, Ge-O bond distances as a function of mol% K_2O in $xK_2O•(1-x)GeO_2$ glass series.

increasing K_2O; the relative variation of V_{mol} being much larger.

From Tables 5.2(e) and 5.3(d), we plot the concentration of NBO as determined from O 1s XPS for both the Rb_2O-GeO_2 and K_2O-GeO_2 series. Fig. 6.5 shows the fraction of NBO concentration in both series. The solid lines show NBO fraction in silicate glasses comprising only SiO_4 units and in a hypothetical germanate glasses where all GeO_4

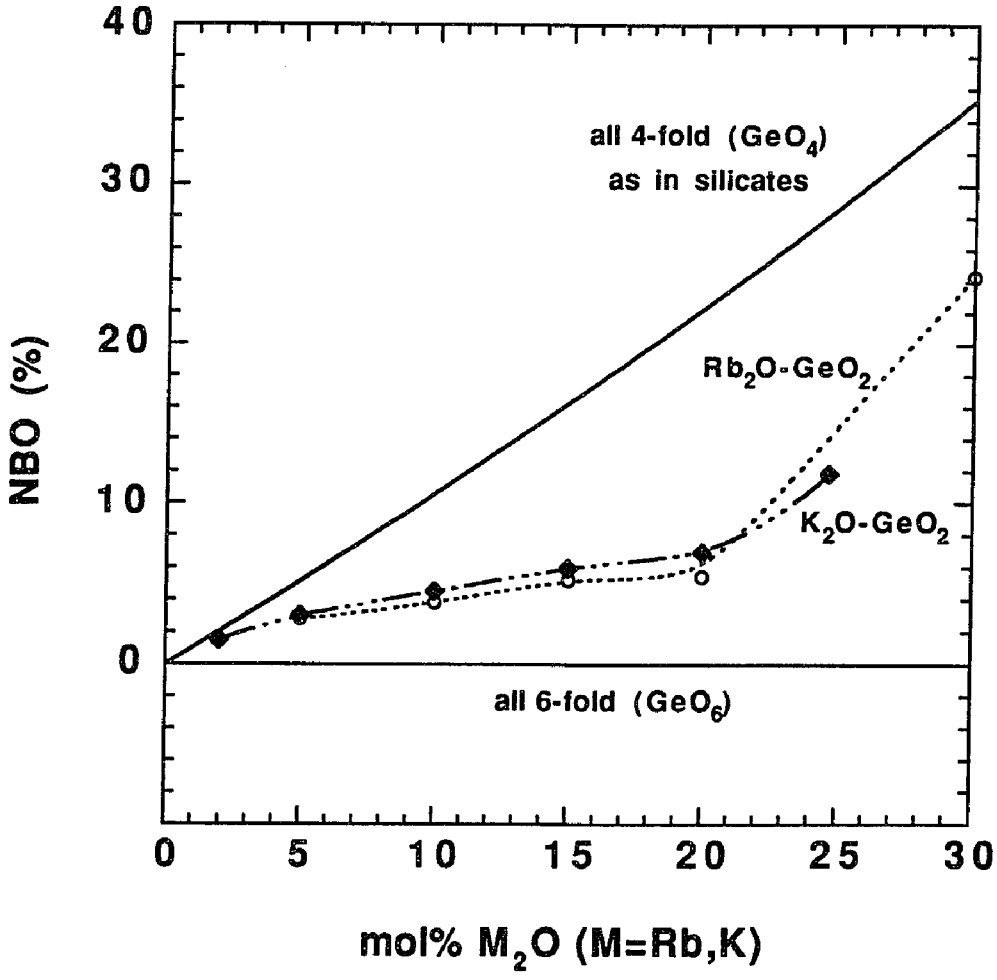

Figure 6.5 Fraction of NBO determined from O 1s XPS of Rb_2O-GeO_2 and K_2O-GeO_2 glass series.

converts into GeO_6 without forming any NBO. Note that the NBOs in germanate glasses are far fewer than in corresponding silicates [24]. Also an appreciable amount of NBOs exists at the lowest M_2O concentration for both series.

Fig. 6.6 shows the fraction of six-coordinated Ge, N_6, as a function of mol% M_2O in both Rb_2O-GeO_2 and K_2O-GeO_2 series (numerical values are listed in Tables 5.2(e) and

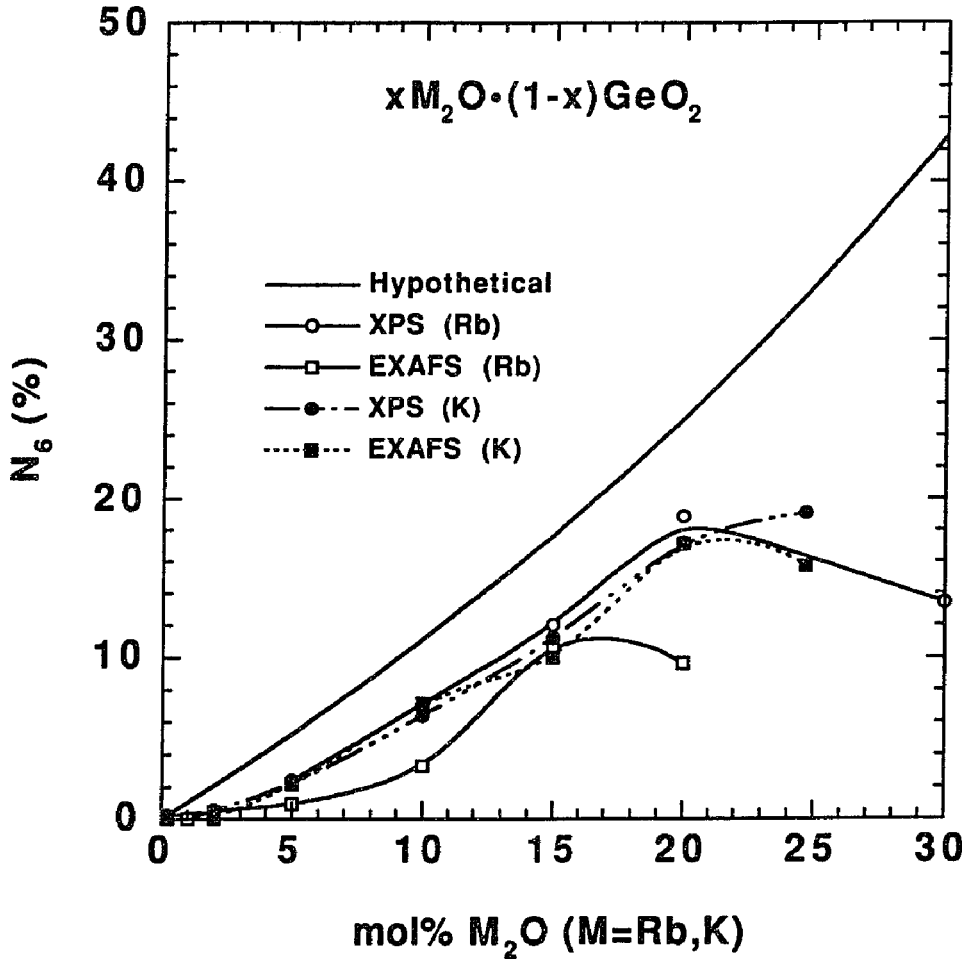

Figure 6.6 The fraction of six-coordinated Ge, N_6, as a function of mol% M_2O (M = Rb, K) in $xM_2O•(1-x)GeO_2$ glass series.

5.3(d)). The XPS results are analyzed using the method described in Sec. 5.4.2. The solid line represents a hypothetical condition in which all the addition of M_2O converts GeO_4 into GeO_6 without producing any NBO. EXAFS results for the fraction of GeO_6, N_6, calculated from the increase in Ge-O bond distances (see Tables 5.2(b) and 5.3(b)) are also shown in this figure for comparison. This figure clearly shows that GeO_4 converts

to GeO_6 with the addition of mol% M_2O; and N_6 reaches a maximum at ~ 20 mol% M_2O. Furthermore, the addition of M_2O not only creates the $GeO_4 \rightarrow GeO_6$ conversion, it also produces some NBOs even at very low alkali concentrations, since the experimental data are always lower than the hypothetical line.

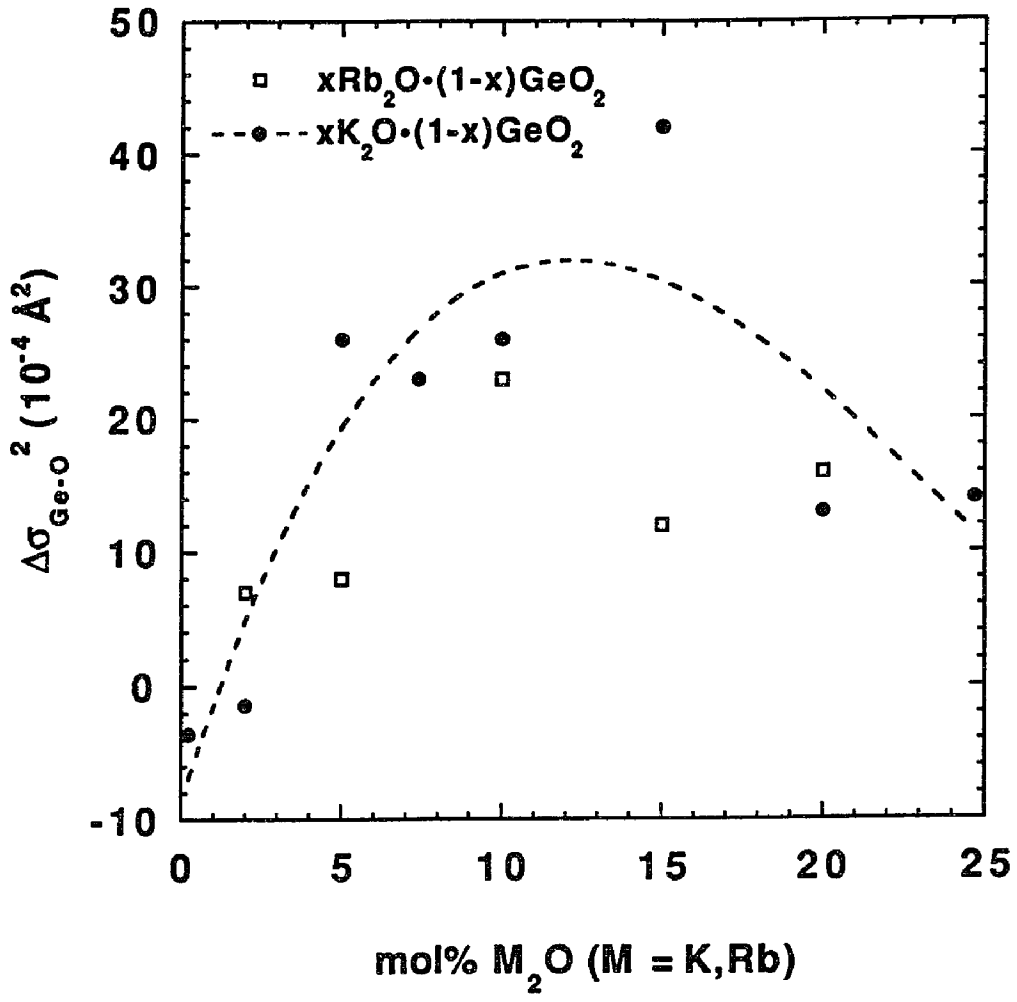

Figure 6.7 Variation of $\Delta\sigma^2_{Ge\text{-}O}$ as a function of mol% M_2O (M = Rb, K) in $xM_2O\bullet(1\text{-}x)GeO_2$ glass series. The broken line is a second order polynomial fit to the data.

Variations of the structural disorder, $\Delta\sigma^2_{Ge\text{-}O}$, with M_2O mol% in both the Rb_2O-

GeO_2 and K_2O-GeO_2 series are shown in Fig. 6.7. Apparently, the disorder is maximum at ~ 10 -15 mol% M_2O.

Discussion

The conversion of GeO_4 to GeO_6 structural units with the addition of alkali oxide in germanate glasses has been suggested from EXAFS [111], IR [112], and X-ray edge shift [113]. In the early studies of Ge EXAFS by Cox et al. [111], only the nearest neighbor oxygen shell could be observed. Their detailed analysis for lithium germanate glasses assumed the splitting of oxygen shell into 2 environments, with Ge-O distances ~ 1.71 Å and ~ 1.85 Å respectively. The bond lengths of the two sites were found to be independent of lithium content and were found very close to 1.74 Å for the α-quartz GeO_2 containing GeO_4 and 1.90 Å for the rutile GeO_2 containing GeO_6, respectively. The CN from these 2 environments was used by the authors to calculate the fractions of GeO_6 and GeO_4. Although this might appear as a direct evidence that the initial addition of alkali oxide simply converts GeO_4 to GeO_6 structural units, the error in CN around Ge is usually shown to be large ~ 30% [100,101]. Furthermore, the S/N (signal to noise) ratio for the larger Ge-O distance was too small to make reliable quantitative evaluation. Hence the fraction of GeO_6 from the CN estimation in their work is not definitive.

Very recently, Greaves and coworkers [114,115] established a fitting index method by constructing matrices for correlation between $\Delta\sigma^2$ and CN to calculate the back Fourier transform fitting error. In their best fit data of 95% accuracy, the precision of CN as well as $\Delta\sigma^2$ was ~ ± 10%. This accuracy is also the best value of precision in CN and $\Delta\sigma^2$ ever

reported [106]. Now let us consider the possible variation of CN for our samples; i.e. the $xRb_2O•(1-x)GeO_2$ and $xK_2O•(1-x)GeO_2$ series. The maximum value of N_6 from XPS is ~ 20% at 20 mole% Rb_2O (~ 15% at ~ 25 mole% K_2O), so that the corresponding maximum average CN of Ge is equal to $6 \times 20\% + 4 \times 80\% = 4.4$ for Rb_2O-GeO_2 series ($6 \times 15\% + 4 \times 85\% = 4.3$ for K_2O-GeO_2 series). Thus the variation of CN with Rb_2O mole% ranges only from 4 to 4.4 for the Rb_2O-GeO_2 series (from 4 to 4.3 for the K_2O-GeO_2 series). This variation of CN $\leq$ 10% is too small to be extracted from EXAFS analysis which has an error of $\pm$ 10% or higher. In other words, CN obtained from the EXAFS analysis is not accurate enough for monitoring the change in coordination of Ge in our germanate glasses.

In subsequent Ge EXAFS studies [112,116] on Li, Na and K germanate glasses, no evidence is given for the presence of Ge-O peak at ~ 1.90 Å. Then the average measured Ge-O bond length has been used to determine the fraction of GeO_6. Here the observed increase of Ge-O distance with increasing alkali content is ascribed to the presence of GeO_6 structural units; it is assumed to be linearly dependent on the conversion of GeO_4 to GeO_6. Hence the increase of Ge-O bond length is indirectly used to calculate N_6. Fig. 6.6 shows that for $xRb_2O•(1-x)GeO_2$ series N_6 calculated from the Ge-O bond lengths (EXAFS) is consistently smaller than that determined from XPS measurement of NBOs. For the $xK_2O•(1-x)GeO_2$ series, N_6 from EXAFS is almost the same as that determined from XPS except for the values at 24.7 mol% K_2O. Fig. 6.8 of the review article by Gurman [106] also shows large scattering of N_6 data points especially when alkali concentration is high, indicating the uncertainty of estimating N_6 from EXAFS. Thus, in

the present study, we may suggest that XPS results are more accurate. In any case, it is reasonable to conclude that the formation of GeO_6 reaches a maximum at ~ 20 mol% M_2O for both the series.

The determination of NBO concentration from XPS has been proven to be precise in silicate glasses [24], and we may expect similar precision for the determination of NBOs in germanates. The XPS results (Fig. 6.6) indicate that at low M_2O concentration the major contribution of M_2O in germanate glasses is to convert GeO_4 to GeO_6 although some NBOs are also observable even at the lowest concentration of M_2O. However, as the concentration of M_2O increases beyond 15 mole%, N_6 starts to deviate from the solid curve and goes through a maximum at ~ 20 mole% M_2O. With further increase of M_2O, in fact, the fraction of six-coordinated Ge decreases. This decrease implies that the conversion of GeO_4 to GeO_6 gradually decreases and, instead, comparatively more NBOs are produced when M_2O is over 20 mole%.

Now, because GeO_6 is a more compact packing of atoms than GeO_4, one would intuitively think that like N_6 the compactness of Ge-O network would also show a maximum at ~ 20 mole% M_2O concentration for both the Rb_2O-GeO_2 and K_2O-GeO_2 glass series. However the molar volume shown both in Fig. 6.3 for the Rb_2O-GeO_2 series and Fig. 6.4 for the K_2O-GeO_2 series does not exactly follow this prediction. Instead, the minimum value of V_{mol}, thus the maximum compactness, for the Rb_2O-GeO_2 series occurs at ~ 7 mole% (it occurs at ~ 10 mol% for the K_2O-GeO_2 series) rather than at 20 mole% M_2O. The reason for this discrepancy is that the structural changes are more complicated than previously suggested [111,112,113,116]. It is true that GeO_4 units are converted to

GeO_6 units with the addition of Rb_2O (Fig. 6.6) but that is not the only change. Fig. 6.5 shows that NBOs are also produced at the same time, although in smaller concentration than in silicates. Even with the initial addition of M_2O, both the GeO_6 units and the NBOs are produced in the structure. As we know, generally the occurrence of NBO upon the addition of alkali oxide leads to the loosening of glass structure [71,117], which is opposite to the effect of GeO_6 formation. So the maximum compactness would occur at an M_2O concentration which is less than the observed concentration of the N_6 maximum (20 mole%). We notice that as the maximum compactness occurs at ~ 10 mol% M_2O, the structural disorder around network forming atoms Ge, $\Delta\sigma^2_{Ge\text{-}O}$, for both glass series also shows a maximum at ~ 10 mol% M_2O (Fig. 6.7). The structural disorder around the network forming atoms can be seen as an indication of the degree of randomness of network matrix. Then it is not surprising to observe a maximum in $\Delta\sigma^2_{Ge\text{-}O}$ when the network structure is mixed with GeO_4, GeO_6 and NBOs. Note that as the Rb-O bond distances in the Rb_2O-GeO_2 series have values comparable to the K-O distances in the K_2O-GeO_2 series, and the Ge-O bond distances in both series are similar, yet we find the overall V_{mol} values in the K_2O-GeO_2 series are significantly smaller than in the Rb_2O-GeO_2 series. This is expected due to the smaller size of the K atoms than that of the Rb atoms, thus resulting in overall greater compactness. The trends of the V_{mol} remain similar for both series.

Next, we ask how does the molar volume correlate with the short range local structure? For Rb_2O-GeO_2 series, since the Rb-O distance remains the same up to 10 mol% Rb_2O and decreases only a little thereafter (Table 5.2(c)), it cannot account for the observed

behavior of minimum in V_{mol}. The average local volume around Ge (i.e. Ge-O distance) increases with increasing Rb_2O by a very small amount (Table 5.2(b)), and its variation with mol% Rb_2O does not correlate at all with that of molar volume (see Fig. 6.3). So, we observe that the change in molar volume does not correlate either with Rb-O or Ge-O interatomic distances. The same is also true for the K_2O-GeO_2 series. For example, the K-O distance decreases a little with increasing mol% K_2O and then remains constant after 10 mol% (Table 5.3(c)). The average local volume around Ge (i.e. Ge-O distance) also increases with increasing K_2O by a very small amount (Table 5.3(b)). Thus, we can conclude that the variation of various bond distances with mol% M_2O does not correlate well with that of molar volume (Figs. 6.3 and 6.4). Then it is possible that the observed variation of molar volume depends more on the CN of network forming atoms viz. Ge and oxygen rather than on the various interatomic distances. A comparison of Figs. 6.3, 6.4 and 6.6 shows that the variation of CN around Ge with composition also does not correlate with that of the molar volume.

From Rb EXAFS we determined second shell Rb-Ge distance (Table 5.2(d)), which varies little with Rb concentration in comparison with the Rb-O and Ge-O distances. (We are unable to determine the second shell K-Ge distance in the K_2O-GeO_2 glass series because of the weak signal to noise ratio. However, we expect it to show similarly little variation with composition). That is, Rb-Ge distance also shows no correlation with the concentration dependence of molar volume. At the same time, one would expect the second shell distances to be more representative of the macroscopic molar volume than the single shell distances. A possible explanation for the lack of correlation between V_{mol} and M-O,

Ge-O or M-Ge distances is that a part of the molar volume is "unoccupied" in the structure which is not affected by the various bond distances. The change in molar volume is mainly from the variation in "unoccupied volume". One can conceive that the unoccupied volume is the preferred pathway for diffusion of alkali atoms in glasses. In the following section, we further discuss the "unoccupied volume" and propose the concept of atomic scale inhomogeneity in glass structure.

6.1.3 Atomic Scale Inhomogeneity in Glass Structure

The homogeneity of glass structure, or the lack of it, has been discussed for many decades, in terms of random network and microcrystallite models, respectively [118]. Until recently common oxide glasses such as sodium silicate have been considered as a continuous random network (CRN) in which the alkali ions are randomly distributed [71]. However, Greaves et al. [19,20], based on EXAFS experiments on several alkali silicate glasses, suggested that the alkali ions are non-randomly distributed, forming clusters. These studies have almost exclusively focused on the distribution of alkali ions. By contrast, from our present EXAFS experiments on both the network former and modifier cations in both Rb_2O-GeO_2 and K_2O-GeO_2 glass series, we have postulated that irrespective of the distribution of alkali ions, there exist inhomogeneously distributed regions which are unoccupied by any of the atoms. In the following paragraphs, we examine the concept of "unoccupied volume" (or "excess volume") in detail.

To obtain the "excess volume" (V_{exc}) per mole of glass for each composition, the values of molar volume are used in the relation: $V_{exc} = V_{mole} - V_{occupied}$, where $V_{occupied}$ is

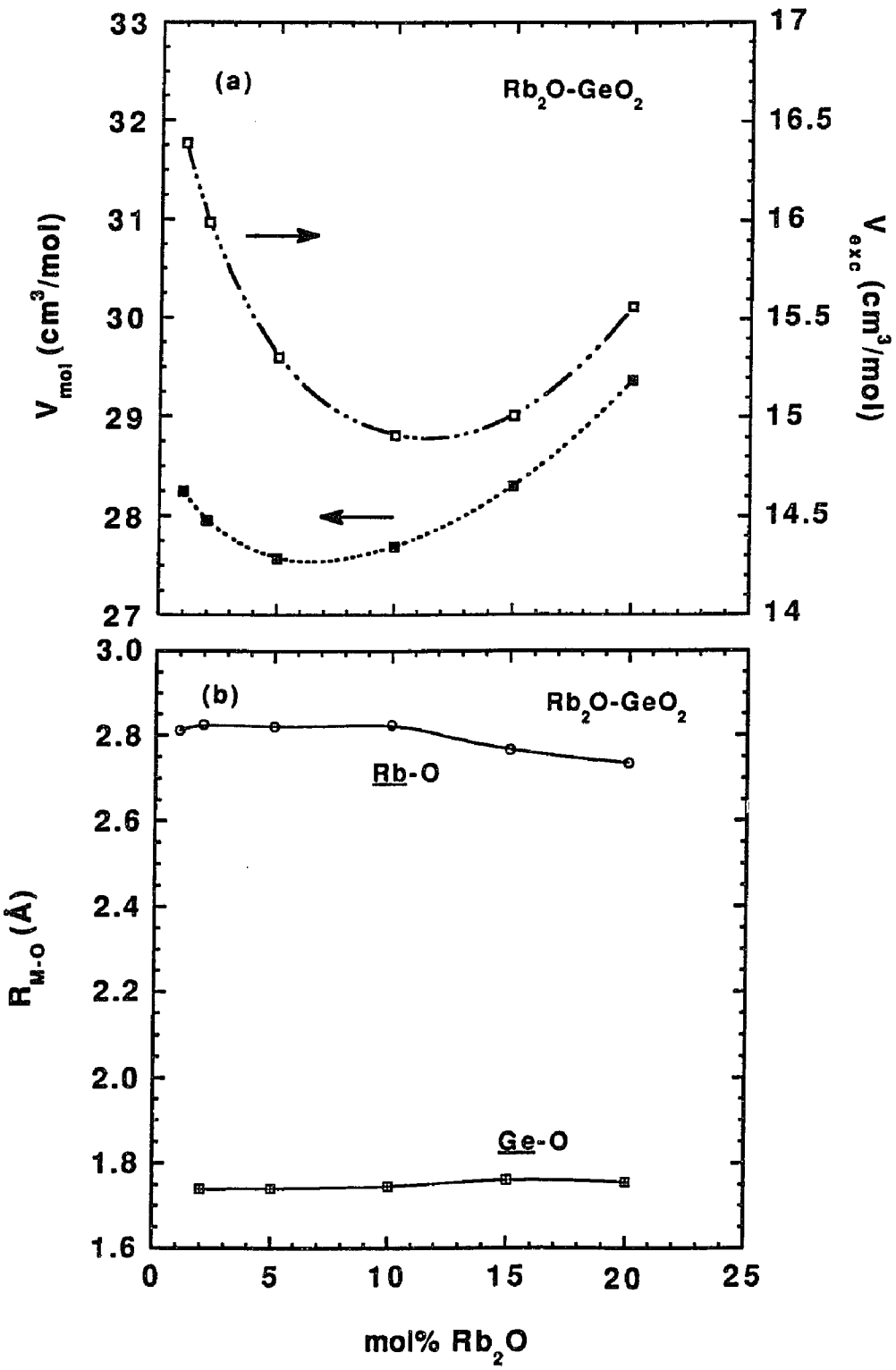

Figure 6.8 (a) Variation of V_{mol} and V_{exc} as a function of Rb_2O mol% in binary Rb_2O-GeO_2 glass series. (b) The corresponding variation of $R_{Rb\text{-}O}$ and $R_{Ge\text{-}O}$.

the volume occupied by individual atoms assumed as hard spheres (for ionic radius information, see section 5.4.4). Fig. 6.8(a) shows the dependence of "excess volume" (V_{exc}) along with molar volume (V_{mol}) per mole of glass as a function of mol% Rb_2O in Rb_2O-GeO_2 series. The variations of various interatomic distances (i.e. Rb-O and Ge-O) in the same series are also shown in Fig. 6.8(b) for comparison. Figs. 6.9(a) and (b) show the corresponding variations as a function of mol% K_2O in K_2O-GeO_2 series. Despite the slight difference in the values of respective structural parameters for the corresponding composition due to the size effect, the overall trends for the variations of V_{exc}, V_{mol} and interatomic distances are similar for both the series. The interatomic distances in these series show rather small variation: there is a small decreasing trend of M-O distance and a small increasing trend of Ge-O distance. However V_{mole} and V_{exc} show large variation, with a minimum in V_{mol} at ~ 5 - 10 mol% and a minimum of V_{exc} at ~ 10 mol% Rb_2O (the minimum in V_{mol} and V_{exc} is at ~ 10 mol% and ~ 15 mol% K_2O, respectively).

In a glass the atoms may not be packed homogeneously, and there are regions unoccupied by any atoms [119]. Structurally, molar volume represents the compactness of the local as well as the extended structure around various atoms. The "unoccupied volume" is a part of the molar volume which is devoid of any atoms in the structure and, hence, unaffected by the variation of various bond distances. However, the unoccupied volume can still vary dramatically with alkali concentration depending on the configurational change of network forming units, such as the conversion of GeO_4 to GeO_6 structural units. Thus the variation of V_{mol} is determined by the variation of "unoccupied volume". The short range local structure has only a relatively small change (within 1 or

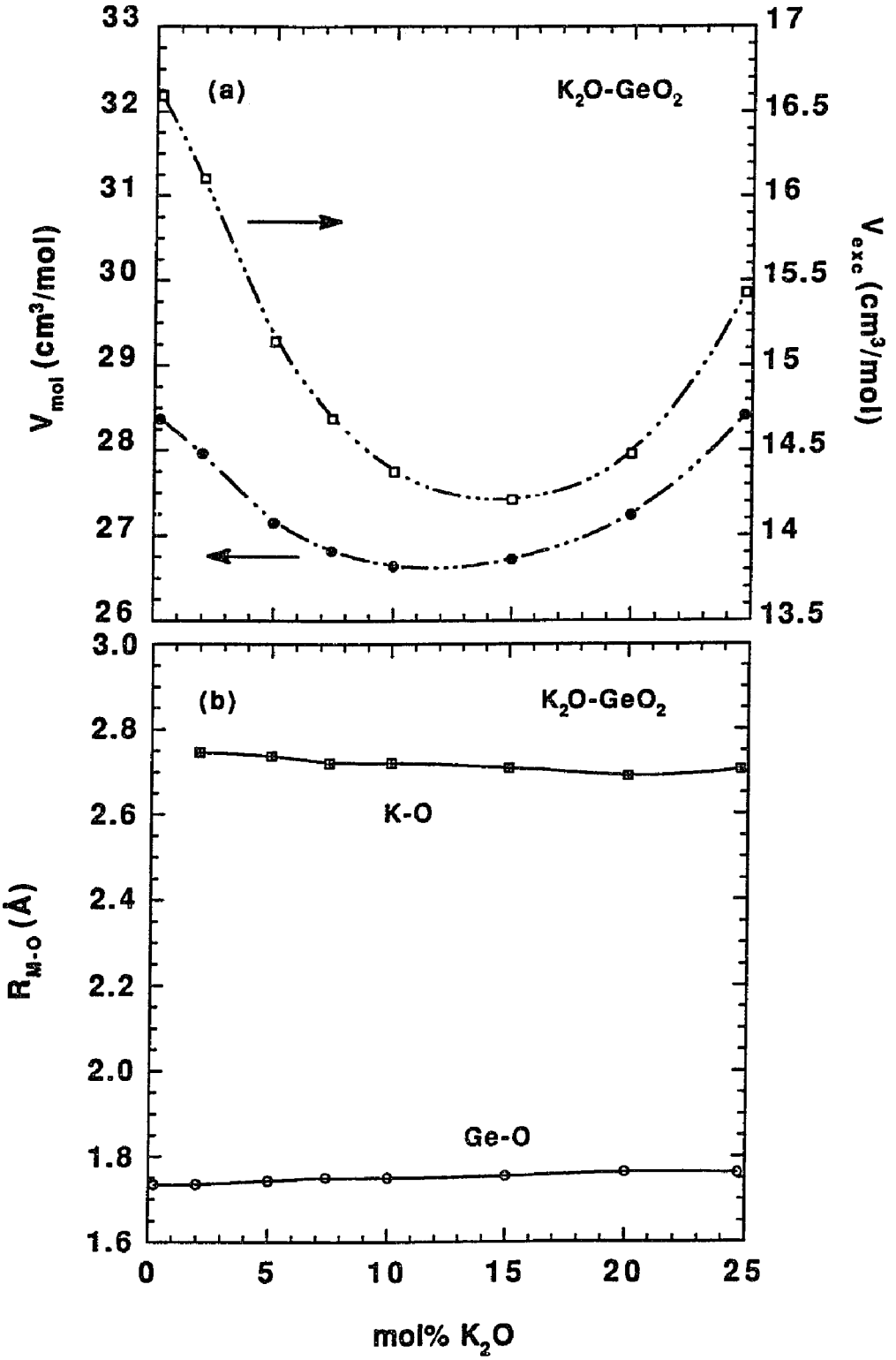

Figure 6.9 (a) Variation of V_{mol} and V_{exc} as a function of K_2O mol% in binary K_2O-GeO_2 glass series. (b) The corresponding variation of R_{K-O} and R_{Ge-O}.

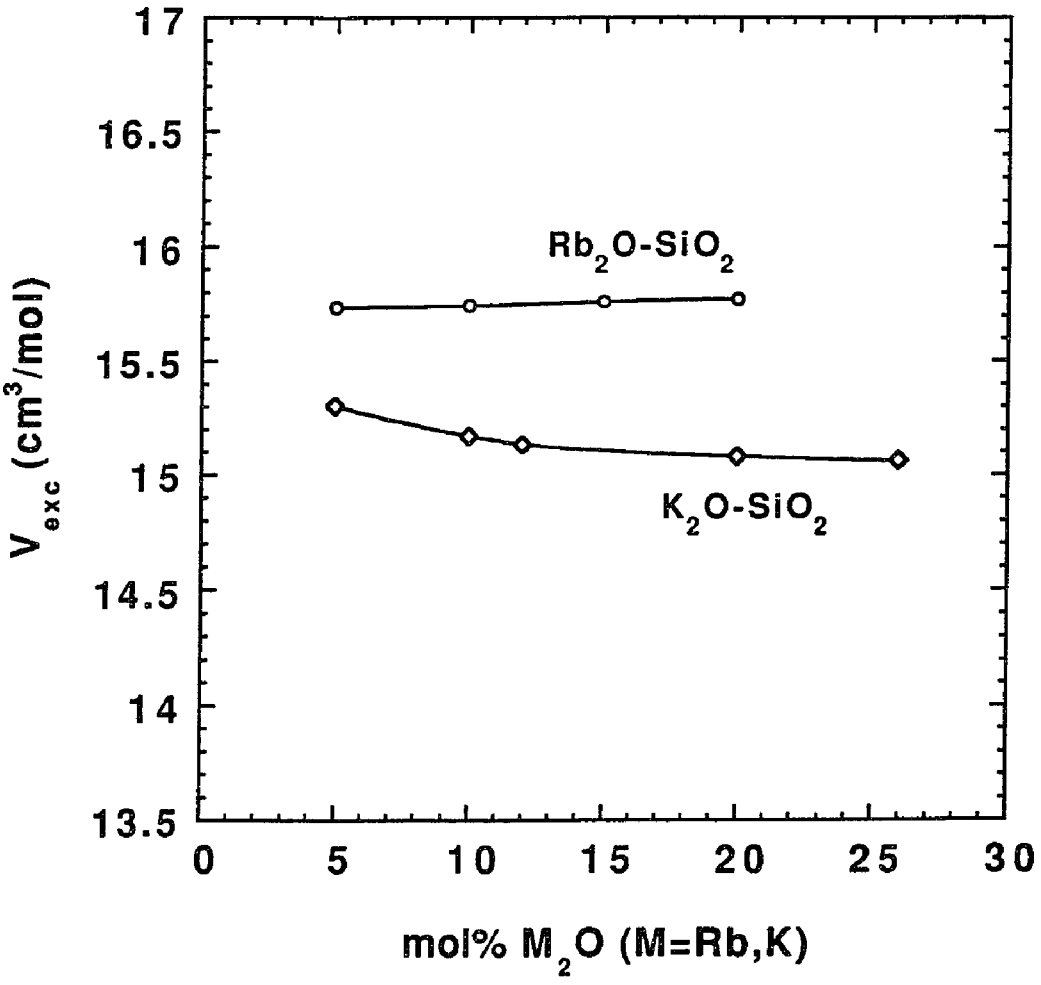

Figure 6.10 Variation of V_{exc} (calculated using the density data from Ref. [120]) as a function of M_2O mol% (M=Rb,K) in binary alkali silicate glasses.

2 % for the bond lengths) when this variation occurs. Then it is not surprising that V_{exc} (Figs. 6.8(a) and 6.9(a)) which can be conceived as the "unoccupied volume" shows a similar trend as does V_{mol}. The unoccupied volume can be considered as the preferred pathway for the diffusion of alkali atoms, and thus determines the strain encountered by these atoms. In the alkali silicates, the variation of excess volume is negligibly small (see

Fig. 6.10), which supports the conclusion by Hsieh and Jain [40] that the dominant energy barrier for alkali movement in silicates is not from the dilation of the network. Note that the atomic scale inhomogeneity discussed here arises from the non-uniform spatial distribution of ions. It is not the chemical heterogeneity such as the segregation of alkali ions in certain channels as proposed in the MRN model by Greaves [19,20].

6.2 Mixed Mobile Ion Germanate Glasses

6.2.1 Glass Structure and Its Implication to the Mixed Mobile Ion Effect

6.2.1.1 $0.2[yAg•(1-y)Rb]_2O•0.8GeO_2$ mixed mobile ion glass series

The results of Ge EXAFS in Table 5.4(b) indicate that Ge-O distance decreases as Rb is replaced by Ag, which is also the trend when Rb_2O concentration is decreased in the binary $xRb_2O•(1-x)GeO_2$ germanate system (see Table 5.2(b)). The results of Rb EXAFS in Table 5.4(c) indicate that Rb-O distance increases as Rb is replaced by Ag, i.e. as y varies from 0 to 1. Again, the same is also observed as x decreases in the binary samples (Table 5.2(c)). Therefore, it appears that the substitution of Ag for Rb produces the same changes in the structure as the reduction of Rb does in the binary $xRb_2O•(1-x)GeO_2$ system. That is, the presence of Ag has little effect on the structure around Ge and Rb. This observation also appears to be true for the disorder around these two species (compare Tables 5.2 and 5.4). Apparently, Ag, being a highly deformable atom, accommodates the influence of composition variation and allows the local environment of more rigid alkali and network former atoms to remain unaffected.

Our mixed Rb-Ag germanate glass series shows a typical mixed mobile ion effect,

in that ionic conductivity (σ) has a minimum and its activation energy (E) has a maximum as Rb is replaced by Ag (see Sec. 7.2). However, Ge-O and Rb-O distances and structural disorder ($\Delta\sigma^2$) vary monotonically with the same composition variation (Tables 5.4(b) and (c)). The fundamental manifestation of the MMI effect is that the diffusivity of a mobile ion (e.g. Rb) decreases but monotonically as it is gradually substituted by another mobile ion (e.g. Ag) [43]; the effect is similar for both the ions. Then it is difficult to understand how the monotonic variation of Ge-O or randomness around Ge can account for the MMI effect in this system. Only those structural parameters can be important which involve the mobile ions. Further, for a structural feature to correlate with the MMI effect, it must vary in a complementary manner as diffusivity does when one cation is replaced by the other [43,121]. That is, we may expect mobile ion-oxygen distance to be important for the MMI effect if the increase of $R_{Rb\text{-}O}$ with decreasing Rb fraction is accompanied by an increase of $R_{Ag\text{-}O}$ with decreasing Ag fraction. Similarly, the disorder around a mobile ion could be relevant for the MMI effect if the increase of $\Delta\sigma^2_{Rb\text{-}O}$ with decreasing Rb is matched by an increase of $\Delta\sigma^2_{Ag\text{-}O}$ with decreasing Ag. However, the Ag K-edge EXAFS results in Table 5.4(e) show that the Ag-O distance, the disorder, and CN around Ag decrease significantly with decreasing Ag_2O content. These relatively larger changes in structural parameters for Ag than for Rb are expected from the large polarizability of Ag ions. The important observation is that the trend of Ag-O distance is qualitatively opposite to that of Rb-O distance as the two ions replace each other. The same is true for disorder around Ag and Rb, respectively. Thus the mobile cation-oxygen distance and the disorder around the mobile cation should not be the key to MMI effect in the present glass system.

From Table 5.4(e), it is not clear if the structural change around Ag atom (viz. the increased Ag-O distance and $\Delta\sigma^2_{Ag\text{-}O}$ with increasing Ag/Rb ratio) is due to the replacement of Rb by Ag or only due to the increase of Ag concentration itself. To answer this question, one must conduct EXAFS experiment for the local structure around Ag atom in $zAg_2O\bullet(1\text{-}z)GeO_2$ binary germanate glass series. Without this information it is difficult to assess whether or not each of the mobile cations (Rb, Ag) stays in its own environment irrespective of Ag/Rb ratio. This assumption is important in a recent theory of MMI effect proposed by Maass et al. [88], which also considers that there are preferred sites for each type of cation. In fact, we have performed preliminary EXAFS experiments on the $zAg_2O\bullet(1\text{-}z)GeO_2$ series with z = 0.02, 0.05, 0.1, 0.15 and 0.2. The results indicate nearly the same Ge Fourier EXAFS spectra for all z values. That is, Ge-O bond distance and structural disorder around Ge atom remain almost unchanged. From Ag EXAFS we note that Ag-O distance also does not seem to change much. Unfortunately the signal to noise ratio for Ag EXAFS is not good and there may be interference from the Ag-Ag correlation presumably coming from Ag microprecipitates. To obtain more accurate structural information it will be necessary to repeat these experiments after eliminating the problem of Ag precipitation. Accordingly, we have also investigated the $0.2[yK\bullet(1\text{-}y)Rb]_2O\bullet0.8GeO_2$ mixed alkali glass series for EXAFS experiments and will discuss its results in the following section. The measurements on this series were performed at around liquid helium temperature where the thermal contribution to structural disorder is eliminated.

6.2.1.2 $0.2[yK\bullet(1-y)Rb]_2O\bullet 0.8GeO_2$ mixed alkali glass series

The results of Ge EXAFS in Table 5.5(b) indicate that Ge-O distance remains nearly constant as Rb is replaced by K, which is not the same as when Rb is replaced by Ag in mixed (Rb,Ag) germanate glass series. The results of Rb EXAFS in Table 5.5(c) indicate that the Rb-O distance also does not vary beyond statistical error. The same is also true for the K-O distance as described in Table 5.5(d). Therefore, it appears that the substitution of K for Rb does not significantly affect the respective environments of Rb and K ions. This confirms that in the $0.2(Ag,Rb)\text{-}0.8GeO_2$ series the change in the structure around Ge and Rb is mainly to accommodate the presence of Ag.

As stated above, for a structural feature to correlate with the MMI effect, it must vary in a complementary manner when one cation is replaced by the other. The variation of bond distances $R_{Rb\text{-}O}$ and $R_{K\text{-}O}$ is shown in Fig. 6.11(a), in which both distances stay nearly constant when Rb is replaced by K ions. The same is also true for the variation of disorder $\Delta\sigma^2_{Rb\text{-}O}$ and $\Delta\sigma^2_{K\text{-}O}$ (Fig. 6.11(b)). That is, neither the variation of bond distance nor the variation of structural disorder correlate with the mixed mobile ion effect. Thus the mobile cation-oxygen distance and the disorder around the mobile cation should not be the key to the MMI effect.

To answer the question in the previous section that whether or not the structural change around Ag atom (viz. the increased Ag-O distance and $\Delta\sigma^2_{Ag\text{-}O}$ with increasing Ag/Rb ratio) is due to the replacement of Rb by Ag or only due to the increase of Ag concentration itself, we examine the EXAFS results for the local structure around K atom in both binary $xK_2O\bullet(1\text{-}x)GeO_2$ (Table 5.3(c)) and mixed alkali $0.2(Rb,K)_2O\bullet 0.8GeO_2$

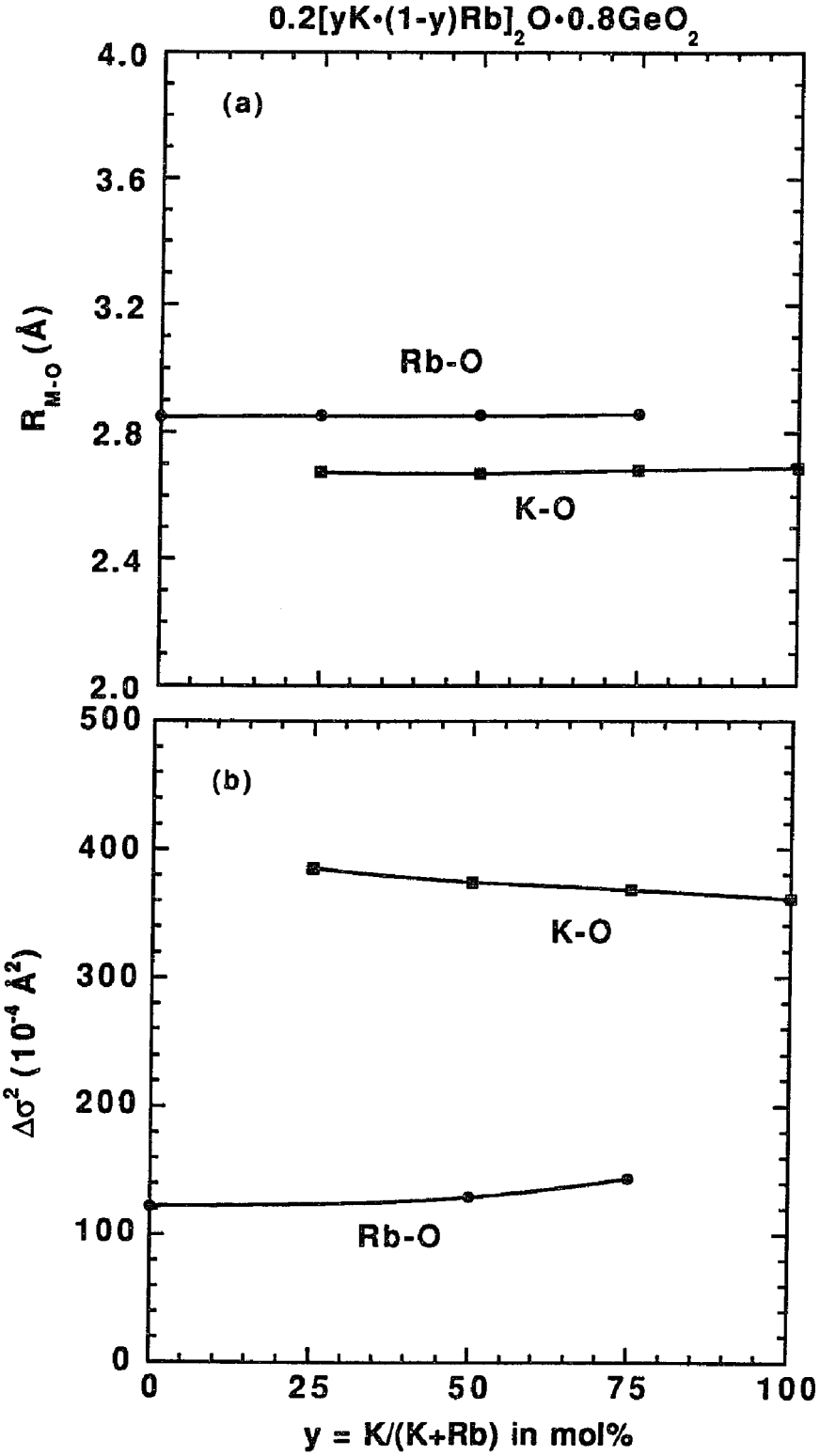

Figure 6.11 Variation of (a) M-O and (b) $\Delta\sigma^2_{M\text{-}O}$ (M = alkali Rb, K) as Rb is replaced by K in $0.2(Rb,K)_2O{\bullet}0.8GeO_2$ mixed alkali glass series.

(Table 5.5(d)) germanate glass series. It is clear that there is a decrease in $R_{K\text{-}O}$ and $\Delta\sigma^2_{K\text{-}O}$ with increasing mol% K_2O in binary system; however, $R_{K\text{-}O}$ and $\Delta\sigma^2_{K\text{-}O}$ in mixed alkali series remain nearly constant. The change around K in the binary series is due to the increasing amount of K_2O, and there is no change around K in mixed alkali glasses when K is replaced by Rb. Thus, we can conclude that the change in Ag environment in the mixed (Rb,Ag) series should be mainly due to the high deformability of Ag atom and, in general, the mobile cations in a MMI series stay in its own environment. This experimental evidence supports the theory of MMI effect proposed by Maass et al. [88] that there are preferred sites for each type of cation. Furthermore, the MMI effect arises from the dynamic interaction between mobile ions and their environments rather than from the static structure variation.

6.2.2 The Relation Between Local Structure and Molar Volume

After examining the variation of local structure in the mixed mobile ion glasses, it is also interesting to study how the local structure correlates with molar volume and excess volume. It is important to determine if the concept of atomic scale inhomogeneity for the binary alkali germanate glasses also holds for the mixed alkali glasses.

The values of molar volume and excess volume per mole of glass for each composition are calculated by the method mentioned in Sec. 6.1.3. and listed in Tables 5.4(a) and 5.5(a). Fig. 6.12(a) shows the variation of V_{exc} along with V_{mol} per mole of glass as Rb is replaced by Ag in the $0.2(Rb,Ag)_2O\text{-}0.8GeO_2$ mixed mobile ion glass series. The variations of various interatomic distances (i.e. Rb-O and Ag-O) in the same series are

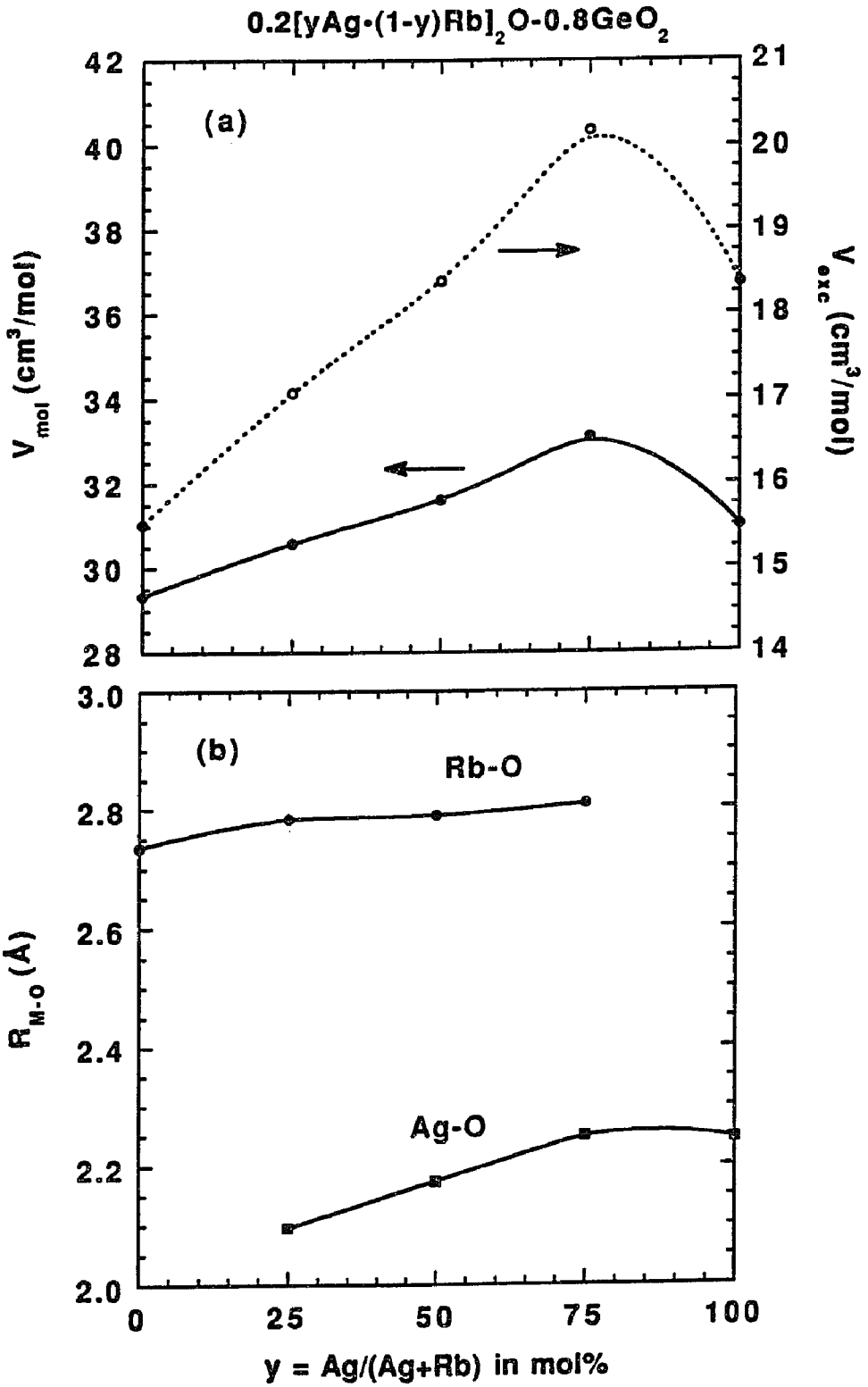

Figure 6.12 (a) Variation of V_{mol} and V_{exc} as Rb is replaced by Ag in mixed $0.2(Ag,Rb)_2O$-$0.8GeO_2$ glass series. (b) The corresponding variation of R_{M-O} (M = Rb, Ag).

also shown for comparison. There is a small increase in Rb-O and Ag-O when Rb is gradually replaced by Ag (i.e. with increasing y), but the increase in V_{exc} and V_{mol} is much larger. The trends are similar for the $0.2(Rb,K)_2O$-$0.8GeO_2$ series. Figs. 6.13(a) and (b) show the corresponding variations as Rb is replaced by K in this series. The interatomic distances show a rather small variation. However V_{mol} and V_{exc} show significant monotonic decrease as Rb is replaced by K. Note that Ag is a very deformable atom and the Ag-O distances are always floppy even in crystalline compounds.

In the $0.2(Rb,Ag)_2O$-$0.8GeO_2$ mixed mobile ion series, the considerable monotonic increase of V_{mol} and V_{exc} (except for a slight decrease in the $0.2Ag_2O \bullet 0.8GeO_2$ glass which may be due to the high deformability of Ag atom or the loss of Ag metals during glass making) does not correlate with the variation of various interatomic distances (Fig. 6.12). However, the Rb-O and Ag-O distances show relatively little increase as Rb is replaced by Ag. The same is also true for the $0.2(Rb,K)_2O$-$0.8GeO_2$ glass series. In this case, the monotonic decrease of V_{mol} and V_{exc} does not correlate with the variation of interatomic distances (Fig. 6.13), e.g. Rb-O and K-O distances stay nearly constant as Rb is replaced by K. So, the lack of correlation between molar volume and various interatomic distances can be explained by the existence of "unoccupied volume" as in binary alkali germanate glasses. As discussed in Sec. 6.1.3, the "unoccupied volume" is a part of molar volume which is devoid of any atoms in the structure and, hence, unaffected by the variation of various bond distances. Thus, it can be concluded that the atomic scale inhomogeneity also exists in mixed alkali glasses. Note that, although this inhomogeneity may affect the long range migration of mobile ions in binary germanate glasses, it cannot account for the MMI

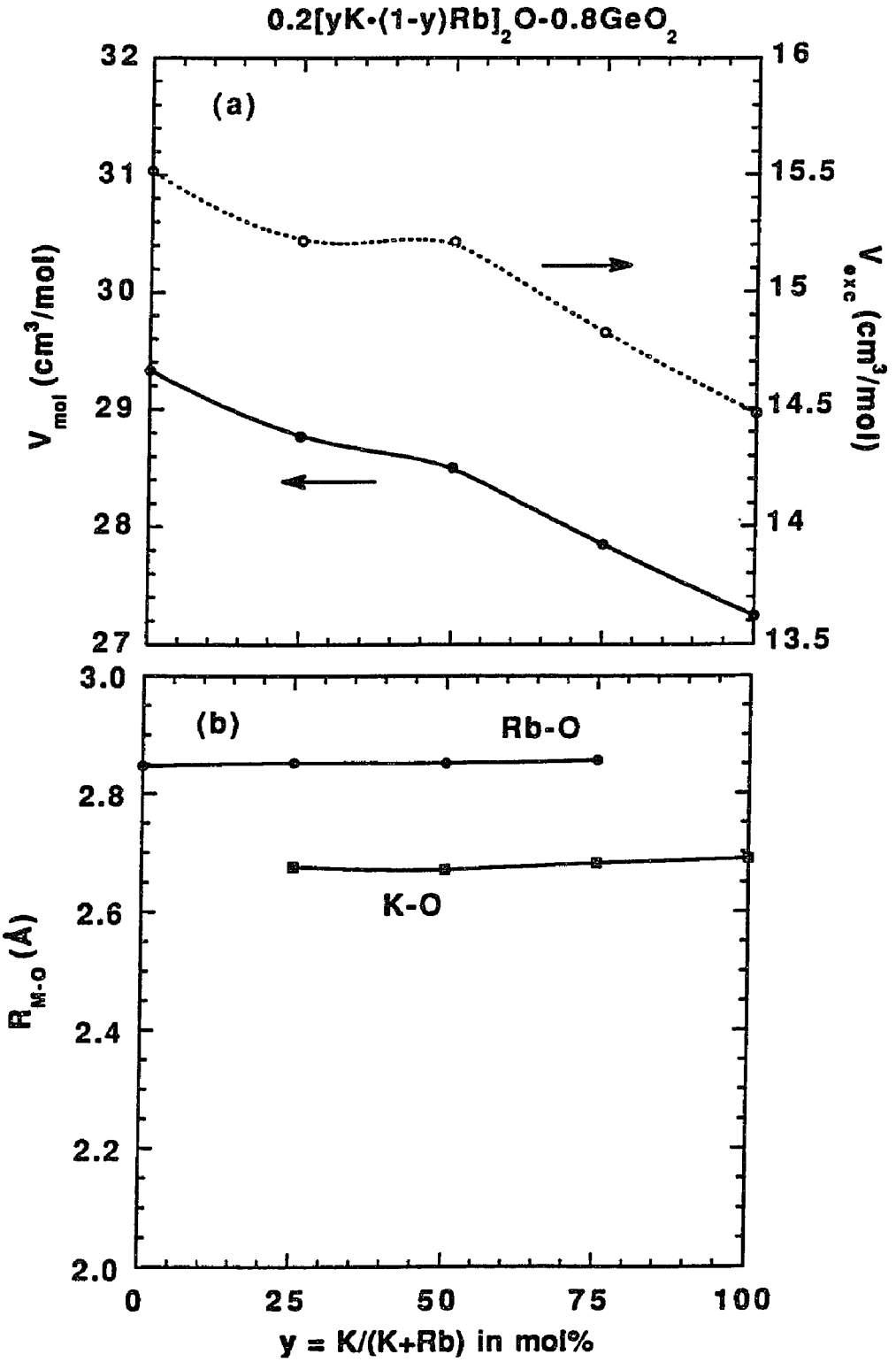

Figure 6.13 (a) Variation of V_{mol} and V_{exc} as Rb is replaced by K in mixed alkali $0.2(Rb,K)_2O$-$0.8GeO_2$ glass series. (b) The corresponding variation of R_{M-O} (M= Rb, K).

effect in mixed mobile ion glasses. The MMI effect should arise from the dynamic behavior of mobile ions rather than static structure.

Note that the increasing trend of V_{mol} and V_{exc} with increasing Ag/Rb ratio (Fig. 6.12) in the $0.2(Rb,Ag)_2O$-$0.8GeO_2$ series is opposite to the decreasing trend of V_{mol} and V_{exc} with increasing K/Rb ratio (Fig. 6.13) in the $0.2(Rb,K)_2O$-$0.8GeO_2$ series. The former trend may due to high Ag deformability and the latter may be attributed to the smaller size of K atom.

6.3 Conclusions

Binary alkali germanate glasses

The presence of GeO_6 structural units besides tetrahedral GeO_4 units is supported by the increase of Ge-O bond distance obtained from Ge EXAFS for both $xRb_2O•(1-x)GeO_2$ and $xK_2O•(1-x)GeO_2$ glass series. However, quantitative evaluation of N_6 from XPS shows that the addition of M_2O (M = Rb, K) introduces GeO_6 as well as NBOs as charge compensating center for all $x \leq 0.2$. For $x > 0.2$, the concentration of NBOs increases at the expense of GeO_6. The variation of molar volume and "excess volume" with composition does not correlate with that of various interatomic distances. We suggest the existence of an "unoccupied volume" in the structure. Its presence indicates that there exists atomic scale inhomogeneity which arises from non-uniform spatial distribution of ions in short range. The spatial inhomogeneity is distinct from the chemical heterogeneity considered in the literature. Relatively large disorder around Rb and K (for K, the thermal disorder has been eliminated) in germanate glass also suggests that the MRN model is less

appropriate for the alkali germanate than for the alkali silicate glasses.

Mixed mobile ion germanate glasses

For the $0.2[yAg•(1-y)Rb]_2O•0.8GeO_2$ glasses, the presence of Ag seems to have little effect on the local structure around Rb and Ge atoms. Replacement of Rb by Ag in these glasses has the same effect on Rb-O distance and disorder around Rb as the reduction of Rb content in binary Rb germanate glasses. The Ag-O distance and disorder around Ag show a trend opposite to that of the Rb-O distance and disorder around Rb when Ag and Rb replace each other. For the $0.2[yK•(1-y)Rb]_2O•0.8GeO_2$ glasses, the replacement of Rb by K does not affect the respective local structure around Rb and K, indicating that there are preferred sites for each type of cation. Therefore, the mobile cation-oxygen distances and structural disorder around them should not be an important component of the MMI effect. In both the mixed mobile ion series, the considerably monotonic change in V_{mol} and V_{exc} does not correlate with the small variation of the interatomic distances. This suggests that the atomic scale spatial inhomogeneity proposed for the binary alkali germanate glasses is also present in the mixed mobile ion germanate glasses.

CHAPTER 7 IMPORTANCE OF STRUCTURE IN D.C. CONDUCTIVITY

In this chapter, we study the effect of composition on d.c. conductivity and its relation to local structure of oxide glasses. The applicability of a cooperative ion movement model is examined for the germanate systems using the structural and conductivity parameters. The roles of different structural parameters (physical factors) in determining d.c. conductivity for the respective glass systems are identified.

7.1 Binary Alkali Germanate Glasses

Over a decade ago, Greaves et al. [19] conducted pioneering EXAFS experiments on a few silicate glasses and determined the local structure around sodium and silicon. The alkali concentration dependence of the structural parameters was then used by Greaves to propose a modified random network (MRN) model of silicate glasses [20] (also see chapter 6), according to which the glass structure is comprised of two-interlacing sublattices: (a) network regions predominantly constructed from the network formers and oxygens and, (b) inter-network regions predominantly made of modifiers. That is, the alkali ions are not distributed randomly and homogeneously through the structure, but segregate in the inter-network regions. More recently, the MRN model was applied by Greaves and Ngai [36,37] to propose a microscopic model for ion transport in silicate glasses, according to which the cooperative ionic motion primarily determines the energy barrier for ion transport. This model was proposed to explain ionic conductivity in silicate glasses only,

but its validity for other oxide glass systems with different structure remains to be established.

Our study of local structure around Rb and K mobile alkali ions as well as network forming Ge in both $xRb_2O•(1-x)GeO_2$ and $xK_2O•(1-x)GeO_2$ binary alkali germanate glass series using EXAFS and XPS (Chapter 6) show that Rb and K are relatively randomly distributed in the structure in comparison to the alkali atoms in silicates and, hence, the MRN model is not as meaningful for the germanate glasses (see Sec. 6.1.1). Then it becomes imperative to examine the applicability of the cooperative ion movement mechanism for the germanate glasses by investigating the correlation between local structure and electrical conductivity. The variation of network structure of germanates with increasing alkali content is also different from that of silicates. For example, in silicates Si is always four-fold coordinated [24] and E_{dc} decreases rapidly with the initial addition of alkali oxide and the decrease is small beyond > 20 mole% M_2O [122]. The concentration dependence of conductivity follows a power law which has been justified by theoretical models [123]. In contrast, in germanates the addition of alkali causes a partial conversion of Ge from four-fold to six-fold coordination (see Sec. 6.1.2). Presumably due to this complex variation of structure with alkali addition, E_{dc} shows little change when an alkali oxide is added to ~ 15 mole% and then decreases rapidly [124,125]. The conductivity does not follow a simple power law dependence on alkali concentration. Thus a comparison of the local structure of the two systems along with their transport behavior should help determine how the local structure around the various species in glasses affects the transport properties.

Key Results

The results of bulk d.c. conductivity, σ, and activation energy, E_{dc}, for the Rb and K germanate glass series were determined in detail in Sec. 5.1 (see Tables 5.2(a) and 5.3(a), Figs. 5.3 and 5.4). The standard deviation of E_{dc} for all the samples is less than 0.04 eV. The dependence of E_{dc} on Rb_2O concentration is plotted in Fig. 7.1(a), and for comparison, the results of Rb_2O-SiO_2 system are also shown on the same figure [120]. The present results are in excellent agreement with the previously published results of Mundy et al. [125] and Ngai et al. [64]; the difference in E_σ from the two investigations is within ± 0.01 eV, which is insignificant considering the variation in glass preparation methods. The dependence of E_σ on K_2O concentration for the $xK_2O\bullet(1\text{-}x)GeO_2$ series is plotted in Fig. 7.2(a), in which E_σ also shows a trend similar to that of the $xRb_2O\bullet(1\text{-}x)GeO_2$ series.

The dependence of V_{mol} and V_{exc} on Rb_2O mol% (Table 5.2(a)), as determined from density data, is shown in Fig. 7.1(b) for the Rb_2O-GeO_2 series. The corresponding variation of V_{mol} and V_{exc} (Table 5.3(a)) is shown in Fig. 7.2(b) for the K_2O-GeO_2 series. Note that both V_{exc} and V_{mole} show a similar trend in each glass series, most strikingly a minimum at ~ 5 - 10 mole% Rb_2O for the Rb_2O-GeO_2 series and a minimum at ~ 10 - 15 mol% K_2O for the K_2O-GeO_2 series.

As described previously in Chapter 6, the relevant structural parameters including interatomic distance ($R_{M\text{-}O}$, M = Ge, Rb, Ag and K), coordination number (CN), and mean square relative displacement ($\Delta\sigma^2_{M\text{-}O}$), are obtained from data processing of the EXAFS spectra. The values of $R_{M\text{-}O}$, $\Delta\sigma^2_{M\text{-}O}$ (M = Rb, Ge) and molar volume for the binary Rb

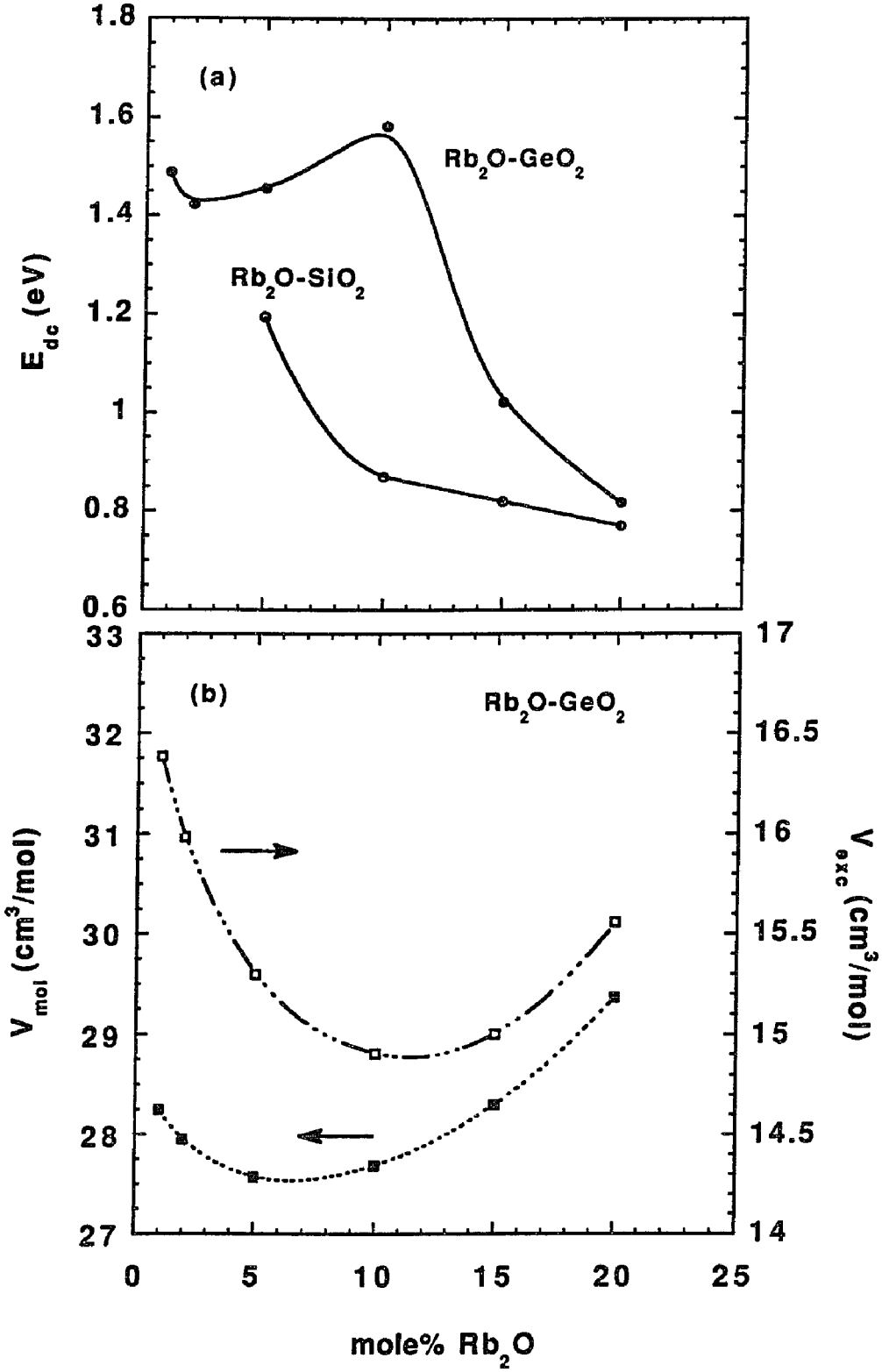

Figure 7.1 (a) variation of E_{dc} as a function of mol% Rb_2O in rubidium germanate and rubidium silicate glass series. (b) Variation of V_{mol} and V_{exc} in rubidium germanate glass series.

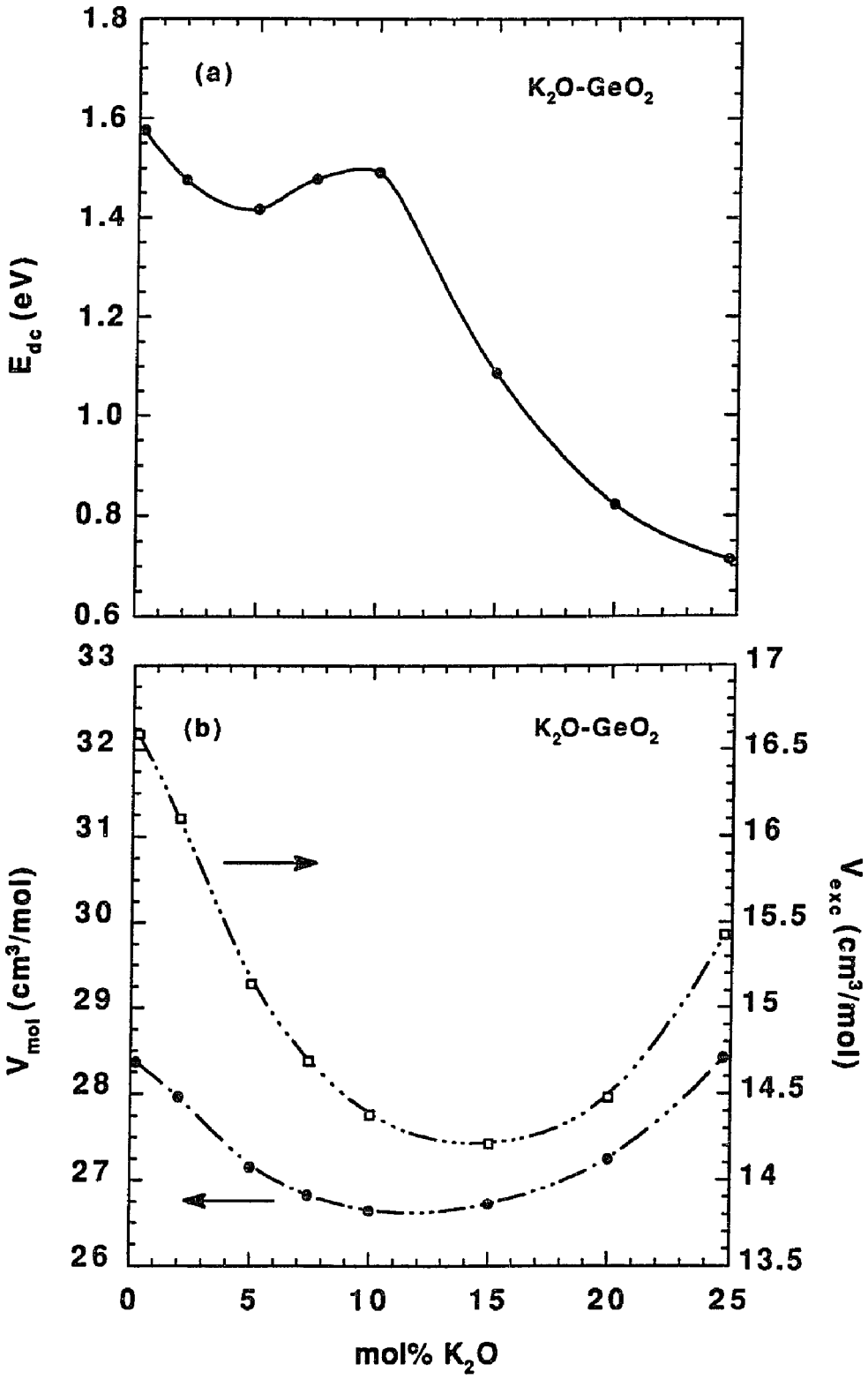

Figure 7.2 (a) variation of E_{dc} as a function of mol% K_2O in potassium germanate glass series. (b) Variation of V_{mol} and V_{exc} in the same series.

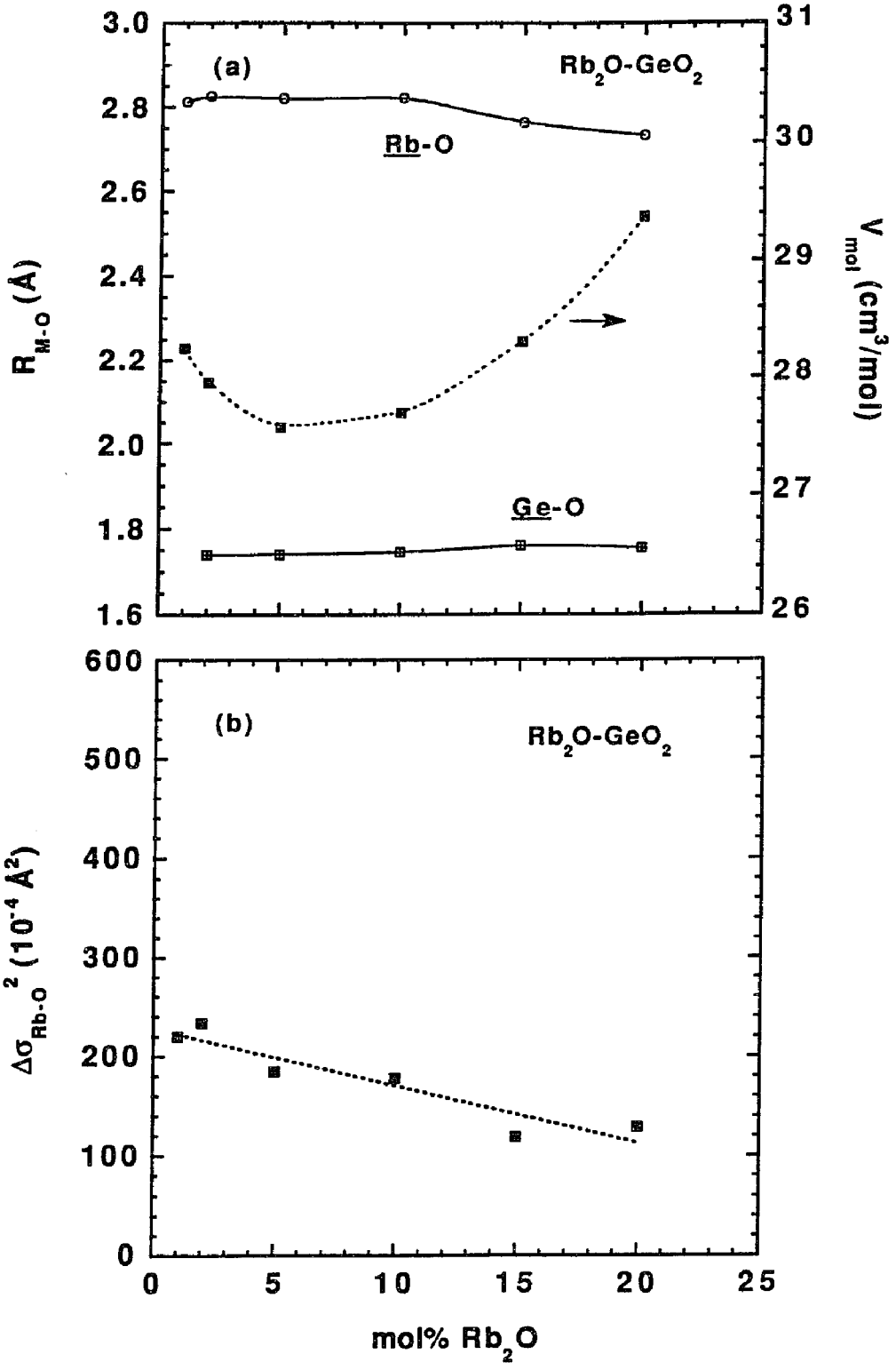

Figure 7.3 (a) Variation of V_{mol}, R_{Rb-O}, R_{Ge-O} and (b) $\Delta\sigma^2_{Rb-O}$ as a function of mol% Rb_2O in $xRb_2O\bullet(1-x)GeO_2$ glass series.

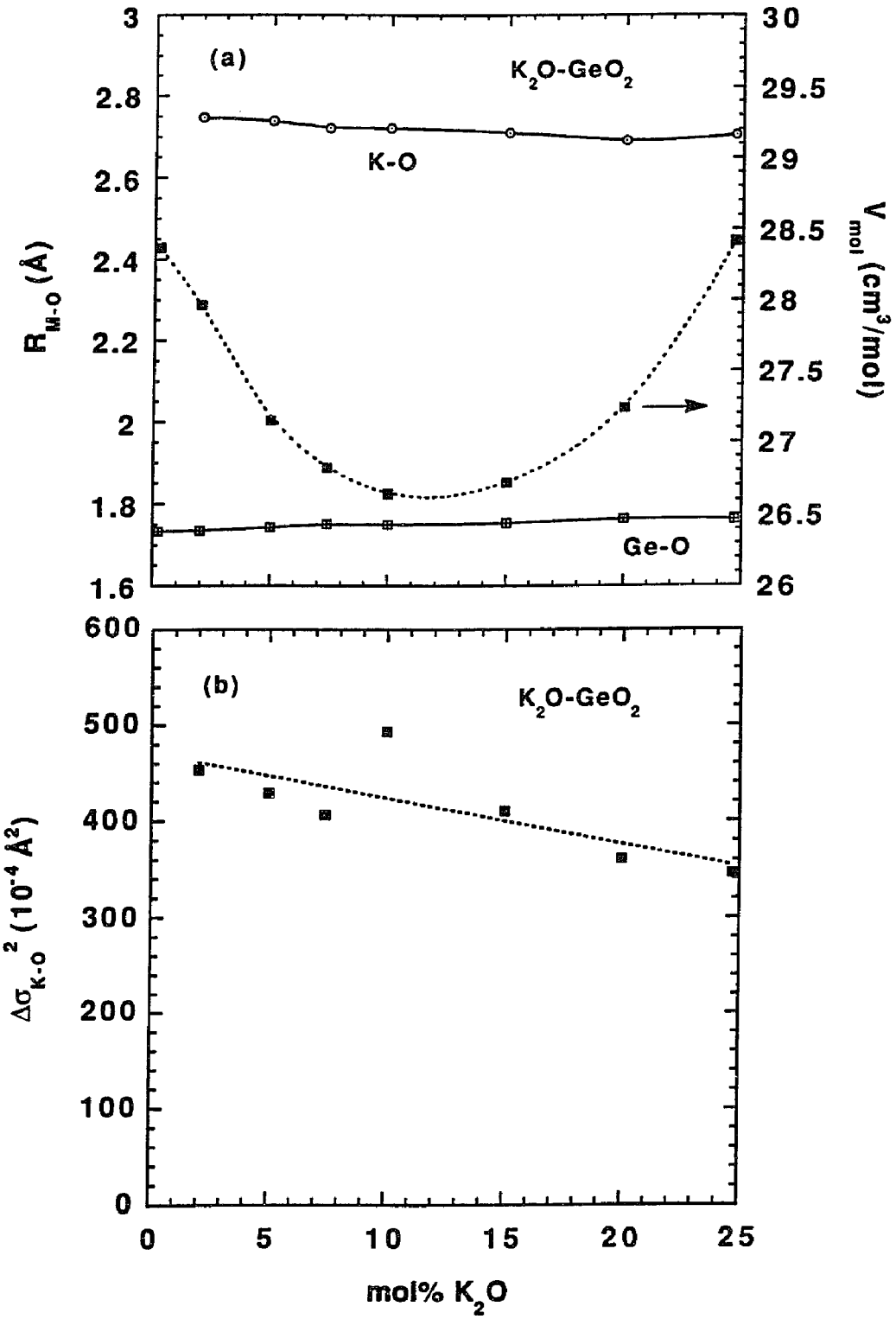

Figure 7.4 (a) Variation of V_{mol}, $R_{K\text{-}O}$, $R_{Ge\text{-}O}$ and (b) $\Delta\sigma^2_{K\text{-}O}$ as a function of mol% K_2O in $xK_2O\bullet(1\text{-}x)GeO_2$ glass series.

germanate glasses are plotted against Rb_2O concentration in Fig. 7.3. The corresponding variations of each structural parameters (M = K, Ge) for the binary K germanate glasses are plotted in Fig. 7.4. Note that although the molar volume shows a minimum at Rb_2O concentration, the Rb-O and Ge-O distances monotonically decrease and increase, respectively with increasing Rb_2O mole%; the relative variation of molar volume being much larger. The same is also true for the variations of respective structural parameters in the binary K germanate glasses.

From the ratio of non-bridging oxygen and bridging oxygen concentration in the Rb germanate glass series and K germanate glass series (Tables 5.2(e) and 5.3(d)), the fraction of 6-coordinated Ge, N_6, is determined assuming that the addition of Rb_2O (or K_2O) to GeO_2 causes either the production of NBO or conversion of GeO_4 to GeO_6 [106]. Fig. 7.5 shows the results of this analysis where the solid line represents a hypothetical condition in which the addition of Rb_2O (or K_2O) converts GeO_4 to GeO_6 without producing any NBOs.

7.1.1 Applicability of Cooperative Ion Movement Model

Greaves and Ngai [37] have attempted to correlate most explicitly the experimentally determined local atomic structure with ionic conductivity. Based on the MRN model, they suggested for the alkali silicate glasses that the cooperative ion movement is crucial for determining the activation energy for d.c. conductivity. Accordingly, the macroscopic activation energy, W, should incorporate a cooperativity factor β, such that

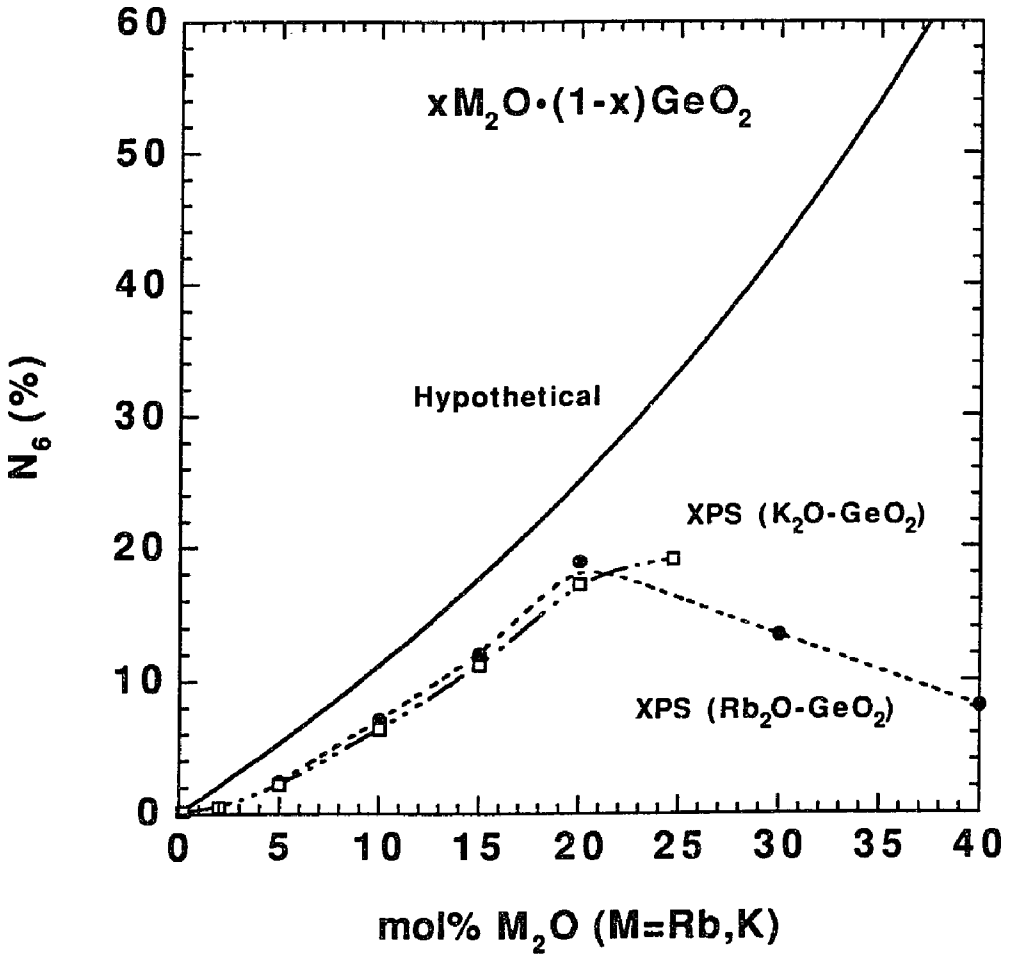

Figure 7.5 The XPS results of N_6 as a function of mol% M_2O (M=Rb,K) in $xM_2O \cdot (1-x)GeO_2$ glass series.

$$W = \frac{E_a}{\beta} + \Delta E \qquad (7.1)$$

where E_a is the "microscopic" activation energy for an isolated alkali and β is the

Kohlrausch exponent (an index for the cooperative ion movement); ΔE is the "disproportionation (or conformational) energy" needed for the change of a structural unit from one configuration to another (e.g. for switching of two Q_n species into a Q_{n-1}-Q_{n+1} pair, where a Q_n represents a SiO_4 tetrahedron with n bridging oxygens). It was suggested that the activation energy for noble gas diffusion could be used as a guide for the conformational energy. Eq. (7.1) assumes that only the first term (Coulombic interaction) is affected by the cooperative ion movements. Subsequently eq. (7.1) has been modified by the same authors [36] to include ΔE in the cooperativity i.e.:

$$W = \frac{E_a + \Delta E}{\beta} \tag{7.2}$$

E_a in eqs. (7.1) or (7.2) was given by

$$E_a = \frac{e^2}{4\pi\varepsilon_0\varepsilon_\infty}\left[1/R_{M\text{-}O} - 1/R_{M\text{-}M}\right] \tag{7.3}$$

where, $R_{M\text{-}O}$ is the distance between an alkali ion and its neighboring O, $R_{M\text{-}M}$ is the distance between two closest ions, ε_∞ is the high frequency dielectric constant, e is the electronic charge and ε_0 is the permittivity of free space.

In the cooperative ion movement model, two different mechanisms are assumed for alkali ion transport in silicate glasses depending on the alkali concentration: (a) the network hopping mechanism. At dilute alkali concentration, there are not enough NBOs to form continuous channels, and ion-ion coupling is small. An alkali is expected to hop

to a similar site without interacting with other alkali ions within the continuous random network structure. Then the alkali hopping correlation function will be Debye-like for which the Kohlrausch exponent β (for details about physical interpretation of β, see [37,49,50]) will equal unity. Further, the second term in eq. (7.3) which reduces W, and ΔE which increases W, have comparably small magnitude at low alkali concentration and tend to cancel each other. Thus the macroscopic activation energy becomes equal to the microscopic energy barrier which is also the Coulombic binding energy of an isolated alkali (E_b), i.e.

$$W \approx E_b = \frac{e^2}{4\pi\varepsilon_o\varepsilon_\infty}[1/R_{M\text{-}O}] \qquad (7.4)$$

(b) the intra-channel hopping mechanism. At high alkali concentration, channels are formed by NBOs and the migration of alkali ions is limited to such channels. The alkali hopping distance ($R_{M\text{-}M}$) is finite and should be taken into consideration for calculating W, because then $1/R_{M\text{-}M}$ becomes large and reduces E_a significantly. In addition, there is cooperativity among the alkali ions as indicated by $\beta < 1$. In this case, the macroscopic activation energy is given by eq. (7.2). The conformational energy ΔE in silicate glasses was estimated by Greaves and Ngai $\approx$ 0.1 to 0.3 eV from the disproportionation energy for switching two Si tetrahedral Q_n species into a Q_{n-1}-Q_{n+1} pair. Presumably, the activation energy for helium diffusion in low alkali silicate glasses (~ 0.17 eV [126]) offers a good guide for the value of conformational energy ΔE).

The validity of MRN-based cooperative ion movement model for rubidium and

Table 7.1
Values of Rb-Rb nominal distance ($R_{Rb\text{-}Rb}$) [124], Kohlrausch parameter (β) [46] (also see Table 5.2(a)), experimental activation energy for d.c. conductivity (E_{dc}) (Table 5.2(a)), Coulomb binding energy for isolated ion (E_b), microscopic activation energy (E_a), conformational energy (ΔE) [127] and calculated macroscopic activation energy ($W = (E_a+\Delta E)/\beta$) for binary rubidium germanate glasses. (for detailed calculations and explanations, see text).

Samples	$R_{Rb\text{-}Rb}$ (Å)	β	E_{dc} (eV)	E_b (eV)	E_a (eV)	ΔE (eV)	W (eV)
1. $xRb_2O\bullet(1\text{-}x)GeO_2$							
$\%Rb_2O$							
1	9.75	0.93	1.488 ± 0.004	0.64	0.46	—	—
2	8.68	0.93	1.423 ± 0.002	0.73	0.49	0.43	0.99
5	6.32	0.92	1.455 ± 0.003	0.53	0.30	0.48	0.85
10	5.18	0.74	1.584 ± 0.001	0.41	0.18	0.52	0.95
15	4.38	0.55	1.021 ± 0.001	0.38	0.14	0.50	1.16
20	3.94	0.53	0.817 ± 0.001	0.37	0.11	0.48	1.11

Table 7.2
Values of K-K nominal distance (R_{K-K}), Kohlrausch parameter (β) (Table 5.3(a)), experimental activation energy for d.c. conductivity (E_{dc}) (Table 5.3(a)), Coulomb binding energy for isolated ion (E_b), microscopic activation energy (E_a), conformational energy (ΔE) [127] and calculated macroscopic activation energy ($W = (E_a+\Delta E)/\beta$) for binary potassium germanate glasses. (for detailed calculations and explanations, see text).

Samples	R_{K-K} (Å)	β	E_{dc} (eV)	E_b (eV)	E_a (eV)	ΔE (eV)	W (eV)
1. $xK_2O•(1-x)GeO_2$							
$\%K_2O$							
0.23	21.72	0.95	1.576 ± 0.002	—	—	—	—
2	10.51	0.89	1.476 ± 0.002	0.55	0.41	0.44	0.96
5	7.67	0.88	1.416 ± 0.003	0.48	0.31	0.51	0.93
7.4	6.70	0.85	1.478 ± 0.002	0.46	0.28	0.54	0.96
10	6.05	0.71	1.491 ± 0.002	0.42	0.23	0.56	1.11
15	5.29	0.54	1.086 ± 0.001	0.38	0.18	0.57	1.39
20	4.84	0.52	0.822 ± 0.002	0.37	0.17	0.56	1.40
24.7	4.57	0.53	0.713 ± 0.002	0.36	0.15	0.53	1.28

potassium germanate glasses can be quantitatively verified by examining the values of W, E_a and E_b in eqs. (7.2), (7.3) and (7.4). For the $xRb_2O•(1-x)GeO_2$ series, the experimental values of ε_∞, R_{Rb-O} and E_{dc} are shown in Table 5.2(a). R_{Rb-Rb} is determined using the unoccupied volume per rubidium ion [124]. The value of β is experimentally determined using imaginary part of the complex electric modulus (see Table 5.2(a)), which is also in good agreement with the published values [64]. The activation energy for helium gas diffusion in rubidium germanate glasses [127] was taken as a guide for the conformational energy, ΔE [36,37]. The calculated values of E_b, E_a and W are listed in Table 7.1 for rubidium germanate glasses. Similarly, the corresponding values of E_b, E_a and W are also calculated for the $xK_2O•(1-x)GeO_2$ series as listed in Table 7.2 (The experimental values of ε_∞, β, R_{K-O} and E_{dc} for this series are listed in Table 5.3(a). ΔE in this case is taken using the activation energy for helium gas diffusion in potassium germanate glasses [127]. R_{K-K} is calculated using the V_{mol} as listed in Table 5.3(a)).

According to the model, at low alkali concentration, where ion-ion cooperativity is negligible, E_b should be approximately equal to the d.c. activation energy. However, for 1 mol% Rb_2O germanate glass, for which β is close to unity (negligible cooperative ionic movement), E_b is only 0.64 eV, whereas the experimental value of activation energy, E_{dc}, is 1.488 eV. A similar discrepancy is also observed for the glasses with 2, 5 and 10 mol% Rb_2O. As the Rb_2O concentration exceeds 10 mol% (a condition at which the intra-channel hopping is expected to dominate [37]), the calculated activation energy (W) is appreciably larger than the experimental E_{dc}. Further, W shows small variation (within ± 0.13 eV) with changing composition whereas E_σ shows a maximum at ~ 10 mole% Rb_2O

and a large decrease for Rb_2O concentration > 10 mole%. The same is also true for the binary potassium germanate glass series. For example, at 2 mol% K_2O concentration, where β is also close to 1 (=0.89), E_b is only 0.55 eV; whereas the experimental E_{dc} is 1.476 eV. The similar discrepancy is also true for K_2O concentration at 2, 5, 7.4 and 10 mol%. As the K_2O concentration exceeds 10 mol%, W is also appreciably larger than the E_{dc}.

Greaves and Ngai's model for alkali silicate glasses considers the cooperativity in ionic movements to arise from Coulombic interaction and conformation of tetrahedral units; the elastic interaction, as envisaged in strain energy by Anderson and Stuart [31] and accounted in noble gas diffusion by Shelby [126], is ignored. This simplification could be acceptable for silicate glasses, for which the elastic strain energy is a small fraction of E_σ [1,40]. The fact that the activation energy (ΔE) for noble gas diffusion in germanates (~ 0.50 eV) [127] is much higher than in silicates (~ 0.17 eV) [126] suggests that the elastic energy associated with the stretching of bonds (not just as disproportionation energy) should be explicitly included in the expression for W. Another possible reason for the above discrepancies is that β does not correctly describe the ion-ion cooperativity for the present glass series (see Sec. 8.1.2). In this regard note, for example, that β is expected to decrease rapidly as ion-ion distance decreases with increasing alkali concentration, but the data show β to decrease appreciably only for > 10 mol% M_2O (M = Rb, K) [46]. This variation of β suggests a far more complex nature of cooperativity in germanates than in silicates [64].

Greaves and co-workers [19,20] conceived the concept of MRN structure from the EXAFS observation that the structural disorder around alkali ions in silicates is very small.

However, the magnitude of disorder around Rb and K in the binary alkali germanate glasses is about an order of magnitude larger (Fig. 6.1) than in silicates. It then follows that alkali ions (Rb or K) are more randomly distributed in germanates than, for example, sodium in sodium silicates. Much larger randomness in the distribution of alkali ions in germanates than for alkali ions in silicates is consistent with the facts that (a) Ge exists in 4 and 6 fold coordination whereas Si exists only in 4 coordination state (see the following discussion), and (b) alkali germanate glasses tend to phase separate much less than the analogous silicates. Consequently the segregated channel structure for alkali migration in MRN is less meaningful for our case. The relationship between the structure and ionic conductivity of germanate glasses should be very different from that of silicates. In conclusion, the present form of the cooperative ion movement model is not appropriate for describing the ionic conductivity of germanate glasses.

7.1.2 The Relation between d.c. Conductivity and Local Structure

The conversion of GeO_4 to GeO_6 structural units with the addition of alkali oxides to GeO_2 has been established from several techniques [106,111,112,113,119] (see Sec. 6.1.2). This 4-fold to 6-fold conversion of germanium coordination was considered by Mundy and Jin [124,125] to affect the molar volume and to explain the occurrence of anomalous minimum in d.c. conductivity in rubidium germanate glass series. They assumed a uniform distribution of the sample volume among various ions. Although the activation energy for the alkali germanate glasses correlates well with the molar volume, our results of interatomic distances [119,128] (also see Sec. 6.1.3) indicate that the local packing

density of the network atoms for both $xRb_2O•(1-x)GeO_2$ and $xK_2O•(1-x)GeO_2$ glass series does not change much with composition. It is shown that the fraction of six-coordinated Ge (N_6) (Fig. 7.5) does not correlate exactly either with the activation energy or with the molar volume (see Fig. 7.1 for the $xRb_2O•(1-x)GeO_2$ series and Fig. 7.2 for the $xK_2O•(1-x)GeO_2$ series). If the replacement of GeO_4 by GeO_6 alone is responsible for the compaction of network, one would predict from Fig. 7.5 the maximum packing to occur at ~ 20 mole% Rb_2O (or K_2O). However neither V_{mol} nor V_{exc} for the rubidium germanate glasses exactly follow this prediction (Fig. 7.1(b)). Instead its minimum value, thus the maximum compactness (determined jointly by network forming cations, mobile ions as well as oxygen atoms), occurs at ~ 5 - 10 mol% in molar volume or at ~ 10 mol% in excess volume. The same non-correlation is also true for the potassium germanate glass series (Fig. 7.2), in which the maximum compactness occurs at ~ 10 mol% K_2O in molar volume or at ~ 10 - 15 mol% in excess volume, whereas its maximum N_6 occurs at ~ 20 mol% K_2O. The reason for this discrepancy is that the structural changes are more complicated than suggested by the early work, which assumed that the conversion of GeO_4 to GeO_6 is the only structural change with the initial addition of M_2O (M = Rb, K) [111,112,113]. Recent data show that some NBO's are also produced at the same time, although in much less concentration than in silicates (see Ref. [119,128,129] and Fig. 6.5). Unlike GeO_6, NBO's are expected to open up the structure. These complex changes lead to the overall maximum compactness at an M_2O concentration which is less than the concentration of N_6 maximum (~ 20 mole%).

If for a moment we ignore the data for extremely low alkali concentration (e.g.

1 mol% Rb_2O in Fig. 7.1(a), (b) and 0.23 mol% K_2O in Fig. 7.2(a), (b)), there appears to be a rather good inverse-correlation between E_{dc} and molar volume or excess volume. Thus, the movement of Rb (or K) ion appears to be predominantly determined by the overall compactness of the structure. So next we would like to ask how the short range local structure affects the molar volume, hence E_{dc}. Let us first focus on the structure around Rb in rubidium germanate glasses as given in Table 5.2(a). We note that within experimental error $R_{Rb\text{-}O}$ remains constant up to 10 mole% Rb_2O and then starts decreasing (Fig. 7.3(a)). If a shorter Rb-O means greater strain energy requirement for Rb movement, E_{dc} should increase rapidly for Rb_2O > 10 mole%, which is in contradiction to the observed behavior of E_{dc}. On the other hand, if this variation of $R_{Rb\text{-}O}$ is combined with that of dielectric constant (ε_∞), we expect to observe a correspondingly decreasing Coulomb binding energy ($\propto 1/\varepsilon_\infty R_{Rb\text{-}O}$) with increasing Rb_2O concentration [31,40] (see E_b in Table 7.1). Obviously the variation of Coulomb energy alone cannot account for the occurrence of small maximum in E_{dc} at 10 mole% Rb_2O (Fig. 7.1(a)). Similar structure-conductivity behavior is also observed for the potassium germanate glasses. For example, the small decrease of $R_{K\text{-}O}$ from 2.74(6) Å to 2.70(4) Å (Table 5.3(a) and Fig. 7.4(a)) cannot explain the observed behavior of E_{dc} in this series. The Coulomb binding energy ($\propto 1/\varepsilon_\infty R_{K\text{-}O}$) shows monotonic decrease (see E_b in Table 7.2), which also cannot account for the maximum of E_{dc}. To sum up, the actual form of E_{dc} vs. mol% R_2O (or K_2O) curve must be determined by both the strain part and the Coulomb part.

Given that for much of the composition range, E_{dc} seems to correlate rather well with the variation of macroscopic molar volume and excess volume (Figs. 7.1 and 7.2),

one may infer that the strain encountered by an alkali ion in moving through the network must be quite important. As we have shown in chapter 6, the variation of molar volume and excess volume does not correlate with the various interatomic distances (Figs. 7.3(a) and 7.4(a)). This lack of correlation has been explained by the existence of "unoccupied volume". This unoccupied volume may vary with alkali concentration depending on the concentration of GeO_6 units and NBOs. The short range local structure seems to have a relatively small change when this variation occurs. Then, it is not surprising that V_{exc} (see Figs. 7.1(b) and 7.2(b)) which may be conceived as the "unoccupied volume" shows a similar trend as molar volume does, i.e. a minimum at ~ 5 - 10 Rb_2O mol% in rubidium germanate glasses and a minimum at ~ 10 -15 K_2O mol% in potassium germanate glasses. One can imagine that the unoccupied volume would be the preferred pathway for the diffusion of alkali atoms and, hence, determines the magnitude of the strain encountered by these atoms. Such pathways are distinct from those formed by NBOs in the Greaves-Ngai model. Thus the maximum of the strain part of E_{dc} would approximately occur at the Rb_2O (K_2O) concentration where the molar volume (unoccupied volume) is minimum.

The variation of disorder parameter for Rb ions, $\Delta\sigma^2_{Rb\text{-}O}$, is shown in Fig. 7.3(b) as a function of Rb_2O mol%. We do not see any simple correlation between $\Delta\sigma^2_{Rb\text{-}O}$ and E_{dc}, the molar volume (compare Figs. 7.1 and 7.3(b)). The same is also true for the potassium germanate glasses as shown in Figs. 7.2 and 7.4(b). This lack of correlation suggests that for the relatively homogeneous germanate glasses, the degree of randomness around alkali ions is not important for ionic diffusion.

7.2 Mixed Mobile Ion Germanate Glasses

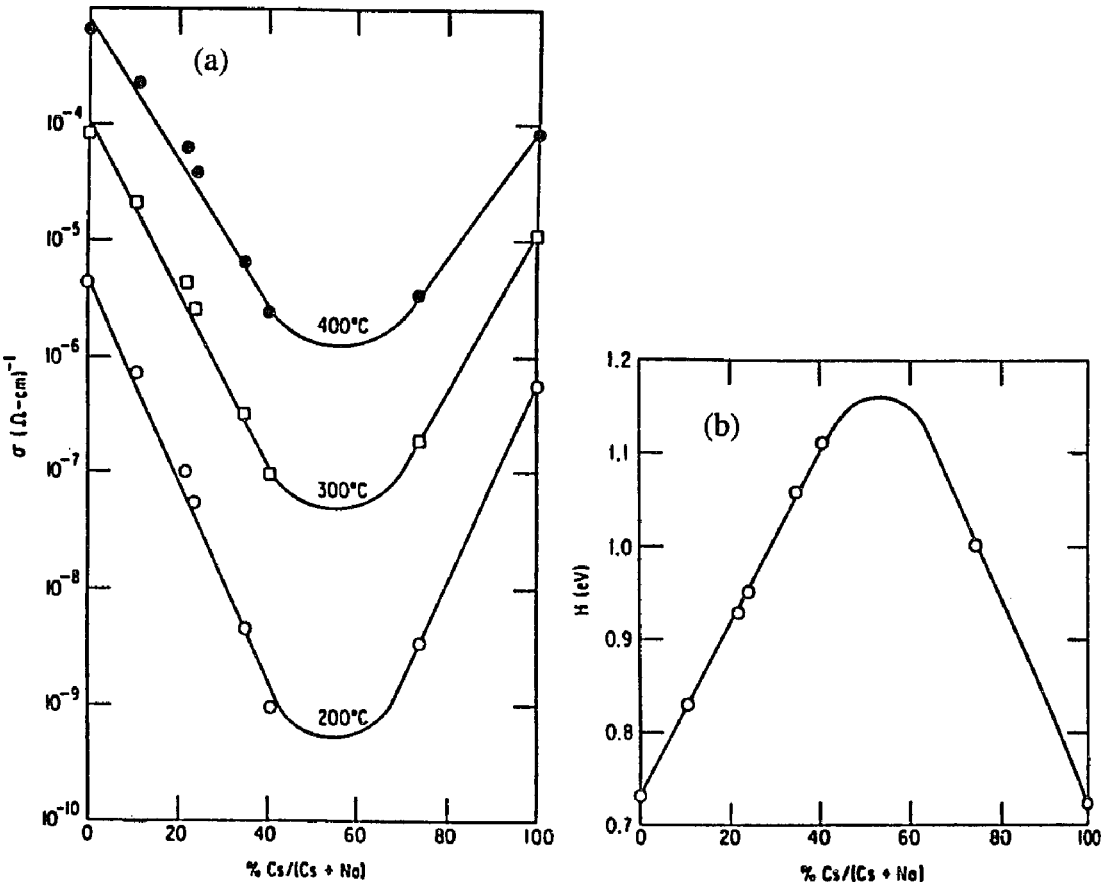

Figure 7.6 (a) Conductivity isotherms as a function of Cs/Na ratio, (b) Composition dependence of the activation enthalpy H for electrical conductivity, for the (Na,Cs) silicate glasses.

The mixed mobile ion (MMI) effect manifests in the maximum/minimum in ion movement related properties [42] when two kinds of mobile ions are mixed (see Fig. 7.6 [43]). A structure based model for the MMI effect has been proposed recently for alkali

silicate glasses [36]. Therefore it will be useful to determine if the local structure plays any role in the development of this effect in germanate glasses. In the present work, we have investigated two mixed mobile ion glass series: i.e. $0.2(Rb,Ag)_2O{\bullet}0.8GeO_2$ and $0.2(Rb,K)_2O{\bullet}0.8GeO_2$, and compared the local structure around mobile ions and Ge cations with the electrical properties. The choice of 20 mole% total nominal mobile ion concentration is to assure a strong MMI effect which becomes pronounced only for MMI concentration > 10 mole% [42].

Key Results

The electrical conductivity of mixed mobile ion $0.2(Rb,Ag)_2O{\bullet}0.8GeO_2$ series shows a strong minimum as Rb is gradually replaced by Ag (Fig. 7.7). The corresponding variation of activation energy for d.c. conductivity shows a pronounced maximum at a mixed mobile ion composition (Fig. 7.8(a), data from Table 5.4(a)), indicating that a mixed mobile ion (MMI) effect is present and effectively Ag behaves as a mobile alkali ion.

The detailed observations and analysis of EXAFS spectra of Ge, Rb and Ag K-absorption edges for the mixed mobile ion (Rb,Ag) germanate glasses have been described in Sec. 6.2. The values of interatomic distance of the mobile ions (Rb,Ag) from oxygen and disorder around them are shown in Fig. 7.8(b). $R_{Rb\text{-}O}$ and $\Delta\sigma^2_{Rb\text{-}O}$ in this series increase monotonically with decreasing Rb content, while $R_{Ag\text{-}O}$ and $\Delta\sigma^2_{Ag\text{-}O}$ decrease with decreasing Ag content.

Similar MMI effect in d.c. conductivity is also observed for the mixed alkali ion $0.2(Rb,K)_2O{\bullet}0.8GeO_2$ glass series. Figs. 7.9 and 7.10(a) show that the electrical

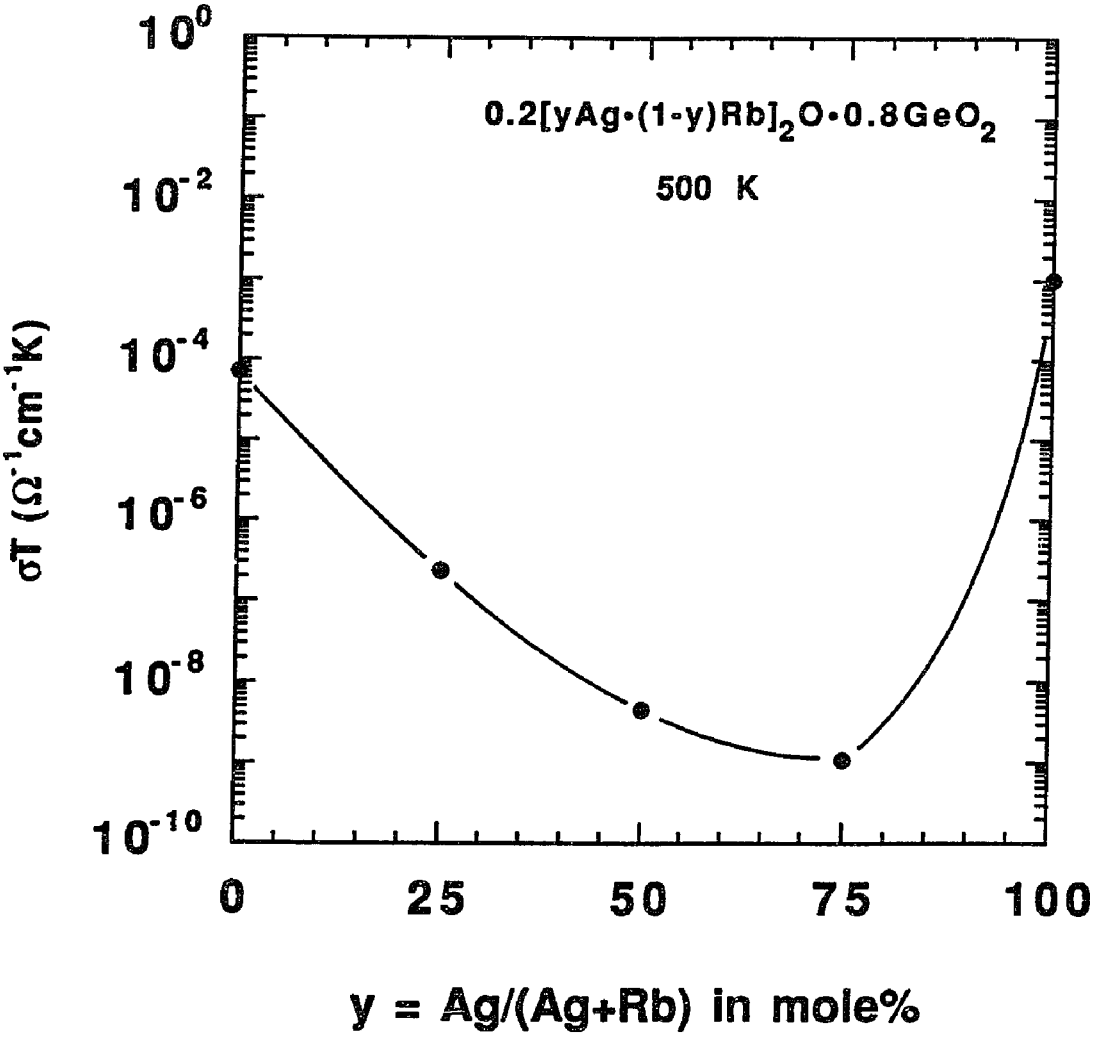

Figure 7.7 Composition dependence of electrical conductivity, σ, at 500 K in the mixed mobile ion glass series, $0.2[yAg\cdot(1-y)Rb]_2O\cdot0.8GeO_2$.

conductivity of this series also has a minimum and the activation energy shows a maximum as Rb is gradually replaced by K; the extrema being not as strong as in the mixed (Rb,Ag) series, indicating that mixed alkali ions with comparable sizes may not have strong mixed alkali effect.

The values of interatomic distance of mobile ions from oxygen and disorder around

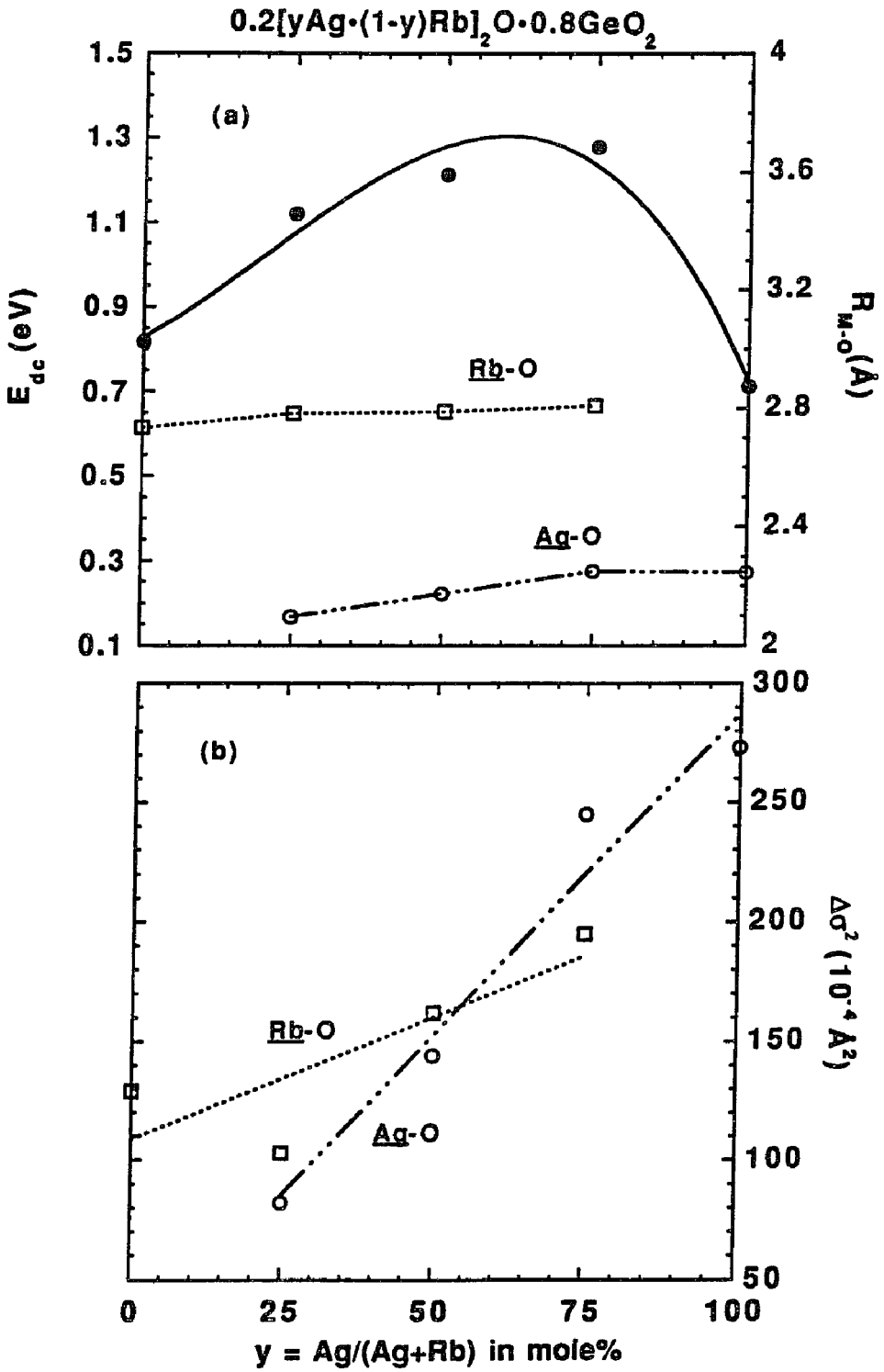

Figure 7.8 (a) Variation of E_{dc} and $R_{M\text{-}O}$ (M=Rb,Ag) as Rb is replaced by Ag in mixed mobile ion (Rb,Ag) germanate glasses. (b) Variation of $\Delta\sigma^2_{M\text{-}O}$ for the same series.

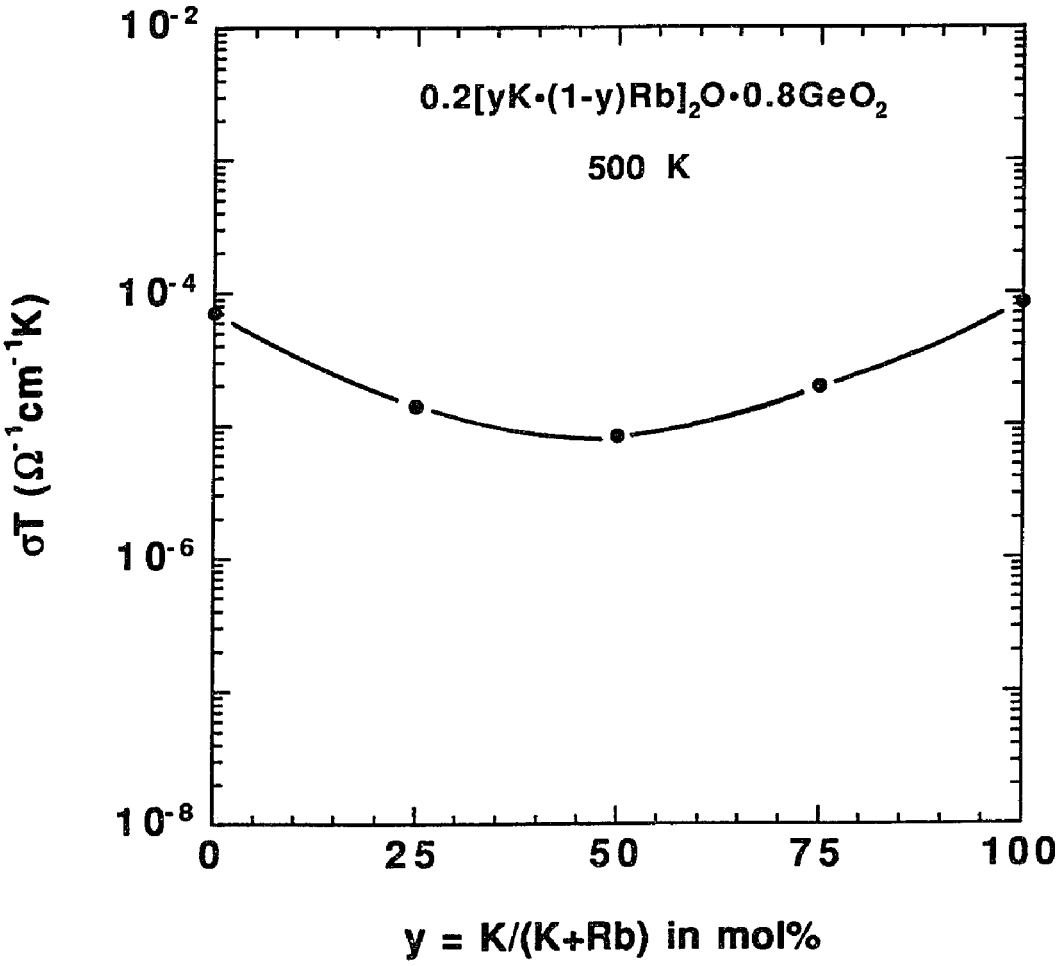

Figure 7.9 Composition dependence of electrical conductivity, σ, at 500 K in the mixed alkali ion glass series, $0.2[yK\cdot(1-y)Rb]_2O\cdot0.8GeO_2$.

them in the Rb-K germanate series are shown in Figs. 7.10 (a) and (b). R_{K-O} and $\Delta\sigma^2_{K-O}$ in this series stay nearly constant as Rb is replaced by K. Also, R_{Rb-O} and $\Delta\sigma^2_{Rb-O}$ do not vary more than the experimental error if not considering the value of $\Delta\sigma^2_{Rb-O}$ (= 309 × 10^{-4} Å^2) at y = 0.25.

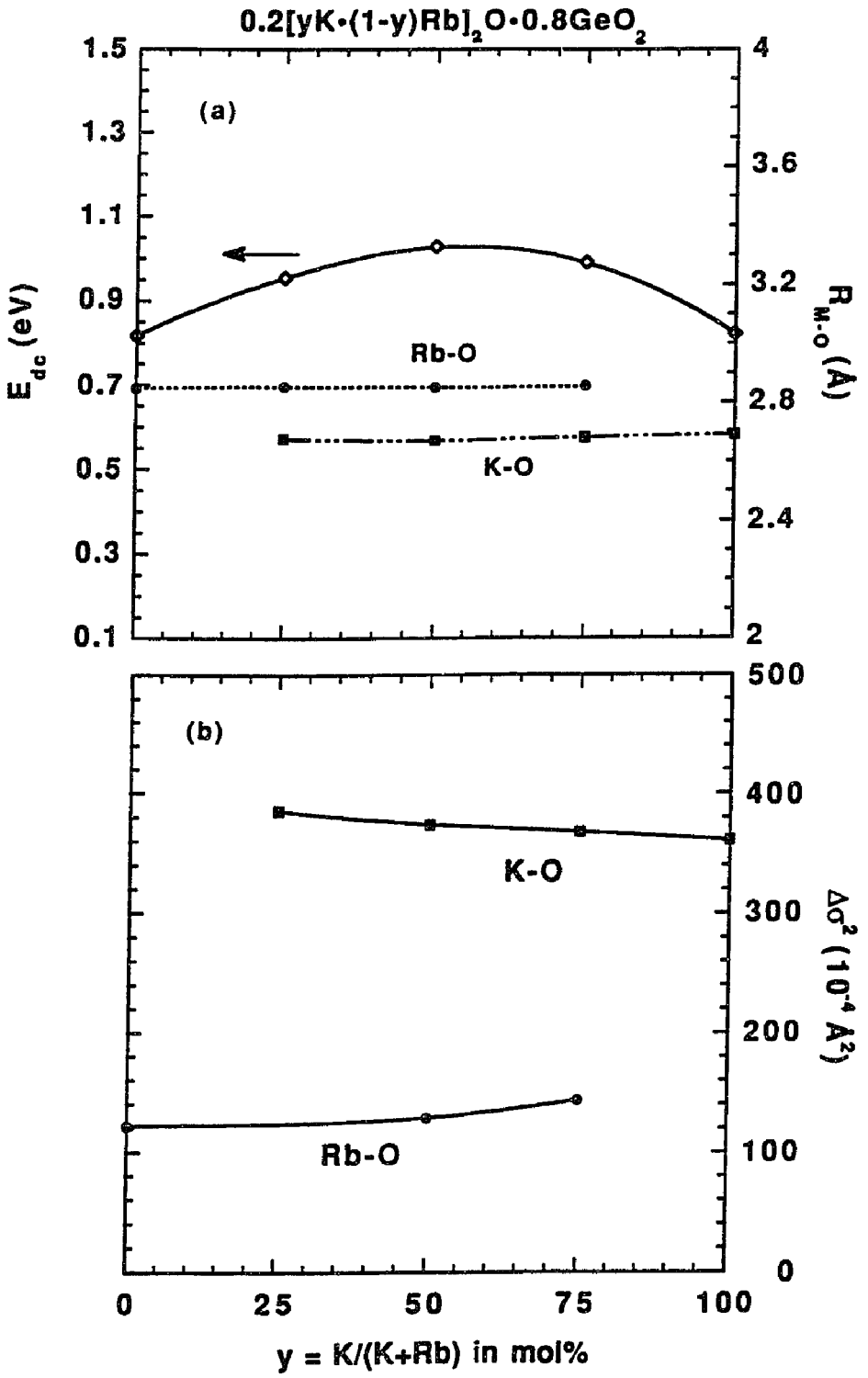

Figure 7.10 (a) Variation of E_{dc} and $R_{M\text{-}O}$ (M=Rb,K) as Rb is replaced by K in mixed mobile ion (Rb,K) germanate glasses. (b) Variation of $\Delta\sigma^2_{M\text{-}O}$ for the same series.

7.2.1 The Mixed Mobile Ion (MMI) Effect and Molar Volume

From Figs. 7.7 and 7.8(a) for the mixed mobile ion (Rb,Ag) germanate glass series and Figs. 7.9 and 7.10(a) for the mixed alkali ion (Rb,K) germanate series, we see that both glass series exhibit a typical mixed mobile ion (MMI) effect, in that σ shows a minimum and E_{dc} shows a maximum as Rb is replaced either by Ag or by K. As discussed in Sec. 7.1, the d.c. conductivity of binary alkali germanate glasses is predominantly determined by the packing density and thus the unoccupied volume (see Fig. 7.1 for the Rb_2O-GeO_2 series, and Fig. 7.2 for the K_2O-GeO_2 series). So one may intuitively consider that d.c. conductivity in mixed mobile ion germanate glasses is also determined by the unoccupied volume. However, by examining the relation between macroscopic volume (V_{mol} or V_{exc}) and activation energy, E_{dc}, for the (Rb,Ag) (Figs. 6.12(a) and 7.8(a)), and for the (Rb,K) germanate series (Figs. 6.13(a) and 7.10(a)), we find that neither the variation of V_{mol} nor the variation of V_{exc} correlates with the variation of E_{dc} for both the glass series. The above observations suggest that the unoccupied volume which plays an important role in d.c. conductivity in binary alkali germanate systems may not be a key factor for developing the mixed mobile ion effect. The decrease in V_{mol} and V_{exc} at y = 1 for the mixed (Rb,Ag) series is probably due to the loss of Ag metal during glass making. The monotonic variation of V_{mol} and V_{exc} as Rb is replaced by K in the mixed (Rb,K) series clearly shows that there is no correlation between E_{dc} and macroscopic volume in the mixed mobile ion glasses.

7.2.2 MMI Effect and Local Structure

Next, we would like to ask if there is any correlation between MMI effect and glass local structure. Fig. 7.8 shows that the local structure around the two mobile cations for the (Rb,Ag) series changes significantly as their relative concentration is varied. A similar observation was reported for potassium-cesium disilicate glass series [130]. The interatomic distance and structural disorder around Rb atoms in the present glass series show the same composition dependence as in the binary Rb germanate system with comparable Rb_2O concentration [119]. This dependence indicates that Ag, being a highly deformable atom, accommodates the influence of composition variation and allows the local environment of more rigid alkali and network former cations to remain unaffected. The relatively larger structural changes around Ag than around Rb as shown in Fig. 7.8(b) support this suggestion. A fundamental manifestation of the MMI effect is that the diffusivity of a mobile ion (e.g. Rb) decreases monotonically as it is gradually replaced by another mobile ion (e.g. Ag) [43]; the effect is qualitatively the same for both ions. So, for a structural feature to correlate with the MMI effect, we expect it to vary in a complementary manner when either cation is replaced by the other. Thus, for example, the increase of $R_{Rb\text{-}O}$ with decreasing Rb fraction should be accompanied by a decrease of $R_{Ag\text{-}O}$. The same should be also true for structural disorder, $\Delta\sigma^2$. However, the trends for respective $R_{M\text{-}O}$ and $\Delta\sigma^2_{M\text{-}O}$ (M = Rb, Ag) in our germanate glasses do not follow this prediction (Figs. 7.8(a) and (b)). $R_{Rb\text{-}O}$ and $\Delta\sigma^2_{Rb\text{-}O}$ increase monotonically with decreasing Rb_2O content, while $R_{Ag\text{-}O}$ and $\Delta\sigma^2_{Ag\text{-}O}$ decrease monotonically with decreasing Ag_2O content. Thus the mobile cation-oxygen distance and the disorder around the mobile ion should not be an important component of the MMI effect.

Recently Maass et al. [88] proposed an explanation for the MMI effect, assuming that the two mobile ions maintain their characteristic environments independent of composition. We note above that although the local structure around Rb depends on Rb/Ag ratio, it remains distinct from that around Ag. Further, the changes in the structure around Rb with decreasing Rb/Ag ratio can be simply interpreted as resulting from decreasing Rb concentration. The highly deformable Ag atoms are only to accommodate the environment change of more rigid Rb atoms (see Sec. 6.2.1). Thus, to further examine the above structural mechanism, we investigate our second mixed mobile ion glass series: $0.2[yK\bullet(1\text{-}y)Rb]_2O\bullet 0.8GeO_2$, where there should be little structural accommodation from the K atoms. From Figs. 7.10(a) and (b), it is clear that the structural change around respective K and Rb atoms (viz. the nearly constant K-O distance and $\Delta\sigma^2_{K\text{-}O}$ and nearly constant Rb-O and $\Delta\sigma^2_{Rb\text{-}O}$ with increasing K/Rb ratio) is not significant within experimental error. This supports Maass's assumption that the two ions in mixed mobile ion glasses remain in their respective characteristic environments. The increase in Rb-O and Ag-O distances and $\Delta\sigma^2_{Rb\text{-}O}$, $\Delta\sigma^2_{Ag\text{-}O}$ in silver containing $0.2[yAg\bullet(1\text{-}y)Rb]_2O\bullet 0.8GeO_2$ glass series should be due to the addition of Ag atoms. Accordingly, it can be concluded that, like macroscopic volume, the local structure of mobile ions does not account for the MMI effect. The origin of the MMI effect is likely to arise from the dynamics of atoms rather than in the static structure of glass.

7.3 Conclusions

Binary alkali germanate glasses

The d.c. conductivity in binary Rb germanate and K germanate glass series has been analyzed in terms of the local structure of these glasses. Unlike for the binary alkali silicate glasses where E_{dc} decreases monotonically with increasing alkali concentration, E_{dc} for binary alkali germanate glasses shows complex behavior with a small maximum at ~ 10 mole% M_2O (M = Rb or K). The occurrence of E_{dc} maximum correlates well with the minimum of molar volume, which is attributed to the conversion of GeO_4 units to GeO_6 and to the formation of NBOs with the addition of M_2O. No correlation is found between the composition dependence of E_{dc} and that of interatomic distance or the disorder parameters. The existence of an "unoccupied volume" in glass, which apparently varies with composition without affecting much the interatomic distances, provides easier path for the transport of alkali ions.

Strain energy component of E_{dc} is relatively more important for the present germanate glass systems than for the analogous silicates. The cooperative ion movement model of Greaves and Ngai, originally proposed for silicates, is not suitable for describing ion conduction in germanates, but a better agreement between the model and data is expected if elastic effects are included explicitly.

Mixed mobile ion germanate glasses

The d.c. conductivity of mixed (Rb,Ag) germanate glass series shows the classical mixed mobile ion (MMI) effect. The presence of Ag seems to have little effect on the local structure around Rb and Ge atoms. The local structure varies in a similar way as in binary Rb germanate glasses. The Ag-O distance and disorder around Ag show trends opposite to that of the Rb-O distance and disorder around Rb when Ag and Rb replace each other.

The d.c. conductivity of mixed (Rb,K) germanate glass series also shows the classical MMI effect. Unlike with the presence of Ag, there is little accommodation of the structural changes by the K atoms in the (Rb,K) germanate series. In this case, the local structure (interatomic distance and structural disorder) remains nearly independent of Rb/K ratio. Therefore the interatomic distance and structural disorder do not seem to be the key for the development of MMI effect in mixed mobile ion glasses. This effect is more likely to arise from the dynamics of atoms rather than from the details of static glass structure.

CHAPTER 8 IMPORTANCE OF STRUCTURE IN ELECTRICAL CONDUCTIVITY RELAXATION

The non-ideality of electrical conductivity relaxation (ECR) behavior has been explained by the distribution of energy barriers or the coupling of charge carriers (chapter 2). Short-range structure is believed to have a significant effect on the non-ideality. In this chapter, we examine the correlation between local structure and ECR behavior in germanate glasses. The significance of local structures, in terms of $R_{M\text{-}O}$ and $\Delta\sigma^2_{M\text{-}O}$ (M = modifier and network forming cations), and the dielectric constant of a glass is discussed. The effects of thermal annealing and neutron irradiation on the ECR behavior of quartz are also examined to establish the importance of amorphousness.

8.1 Conductivity Relaxation in Binary Germanate Glasses

In this section, we investigate the relationships between local structure and ECR behavior in two binary alkali germanate glass series: $xRb_2O\bullet(1\text{-}x)GeO_2$ and $xK_2O\bullet(1\text{-}x)GeO_2$. As discussed in chapter 2, the physical origin of Kohlrausch exponent, β, in vitreous ionic conductors has not been established yet. With the structural information obtained in chapter 6, it becomes possible to seek the microscopic basis of electrical conductivity relaxation. Germanate glasses have several distinct features which make their study appropriate for testing some of the models for ECR response. In the following, we attempt to correlate the special structural features of alkali germanates with their ECR results.

Key Results

The activation energy (E_{dc}) for the d.c. conductivity (σ) for both the $xRb_2O\bullet(1-x)GeO_2$ (Table 5.2(a)) and $xK_2O\bullet(1-x)GeO_2$ (Table 5.3(a)) germanate glass series is plotted in Fig. 8.1 as a function of M_2O (M = Rb,K) concentration. It shows a small maximum

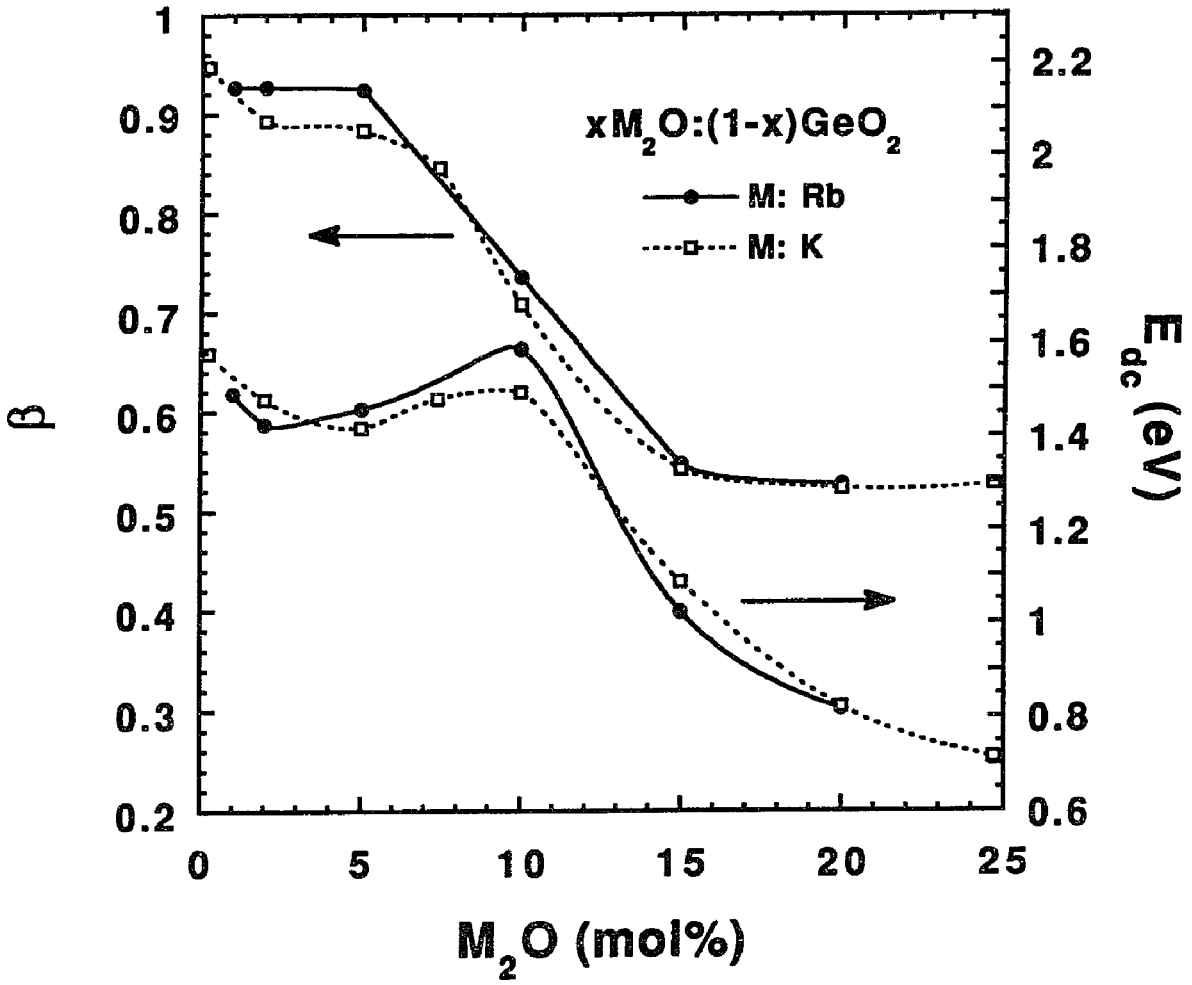

Figure 8.1 Dependence of Kohlrausch exponent, β, and E_{dc} on alkali concentration in $xM_2O\bullet(1-x)GeO_2$ glass series, where M is Rb or K.

at ~ 10 mol% M_2O which does not occur in alkali silicates [120].

The dependence of structural disorder around Rb ($\Delta\sigma^2_{Rb\text{-}O}$) (Table 5.2(c)) and the "excess volume" (V_{exc}) (Table 5.2(a)) on mol% Rb_2O in the Rb_2O-GeO_2 series is shown in Figs. 8.2(a) and 8.2(b) respectively. $\Delta\sigma^2_{Rb\text{-}O}$ shows a monotonic decrease with increasing Rb_2O content, whereas V_{exc} shows a minimum at ~ 10 mol% Rb_2O. Nominal Rb-Rb distance (d*) (Table 7.1) is plotted in Fig. 8.2(c) using the cubic root of the unoccupied volume per rubidium ion [125]. d* decreases rapidly and monotonically for the first few mol% Rb_2O and then decreases slowly as Rb_2O increases. The corresponding values of $\Delta\sigma^2_{K\text{-}O}$ (Table 5.3(c)), V_{exc} (Table 5.3(a)), and d* (Table 7.2) are plotted in Figs. 8.3(a), 8.3(b) and 8.3(c) for the K_2O-GeO_2 series. Both glass series have similar trends for the corresponding structure features.

Relative Coulombic interaction of mobile ions with their charge compensation centers (CCC), $1/\varepsilon_i R_{Rb\text{-}O}$, is plotted in Fig. 8.4 as a function of Rb_2O concentration for the Rb_2O-GeO_2 glass series, where ε_i is the high frequency relative dielectric constant of the samples (Table 5.2(a)) and $R_{Rb\text{-}O}$ is the interatomic bond distance between Rb and O (Table 5.2(c)). The corresponding variation of $1/\varepsilon_i R_{K\text{-}O}$ (Table 5.3(a)) as a function of K_2O concentration in the K_2O-GeO_2 series is shown in Fig. 8.5.

The value of β for a sample is determined from the FWHM of M" peak (see Sec. 5.3). The variation of β as a function of Rb_2O mole% in binary Rb germanate glass series is shown in Fig. 8.1 to compare with that of E_{dc}. Its variation is also shown in Fig. 8.4 for comparison with that of $1/\varepsilon_i R_{Rb\text{-}O}$. The corresponding variation of β as a function of K_2O is shown in Figs. 8.1 and 8.5 for the K_2O-GeO_2 series.

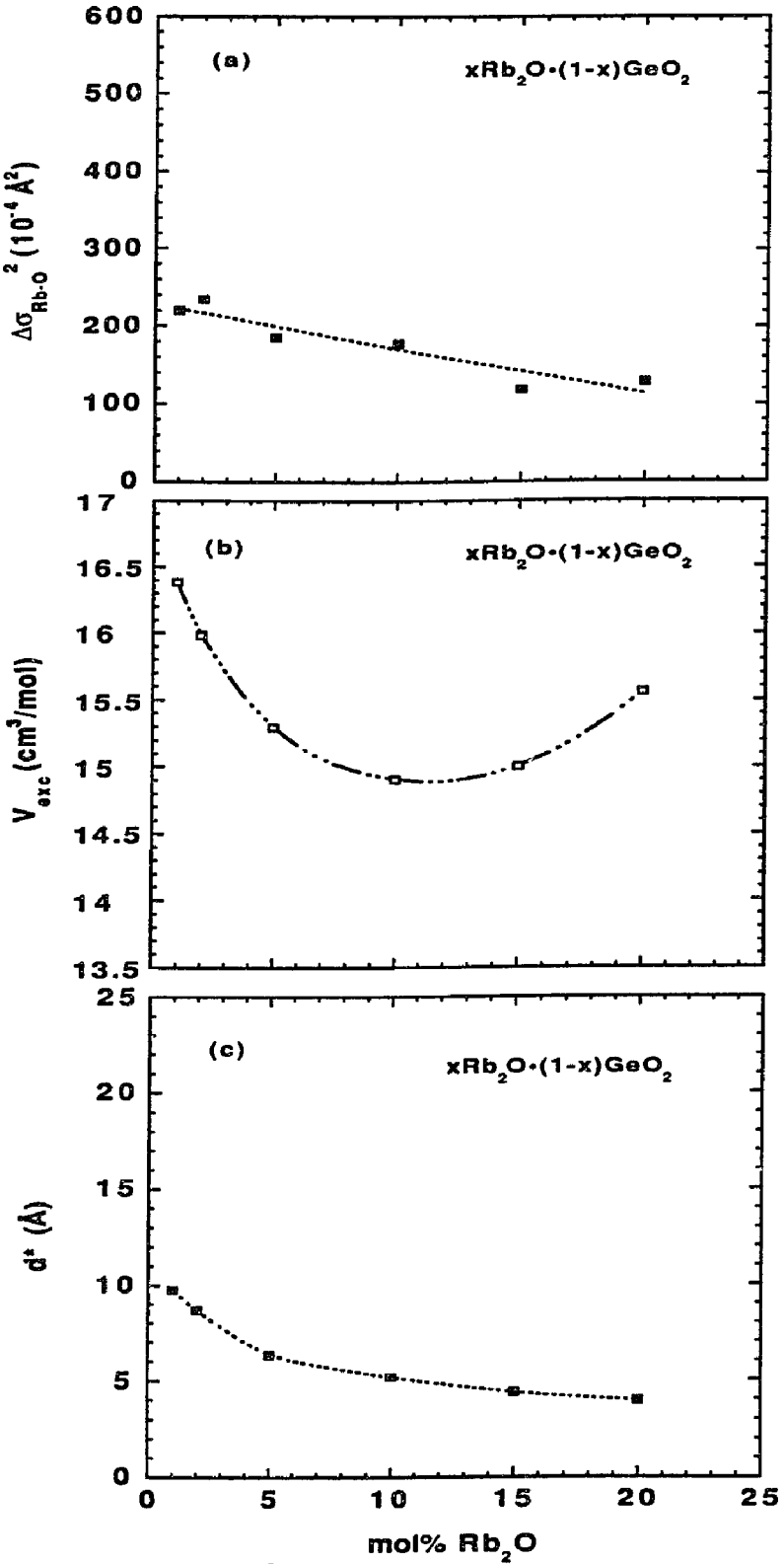

Figure 8.2 Variation of (a) $\Delta\sigma^2_{Rb\text{-}O}$, (b) V_{exc}, and (c) d*, as a function of Rb_2O mol% in $xRb_2O{\cdot}(1\text{-}x)GeO_2$ glass series.

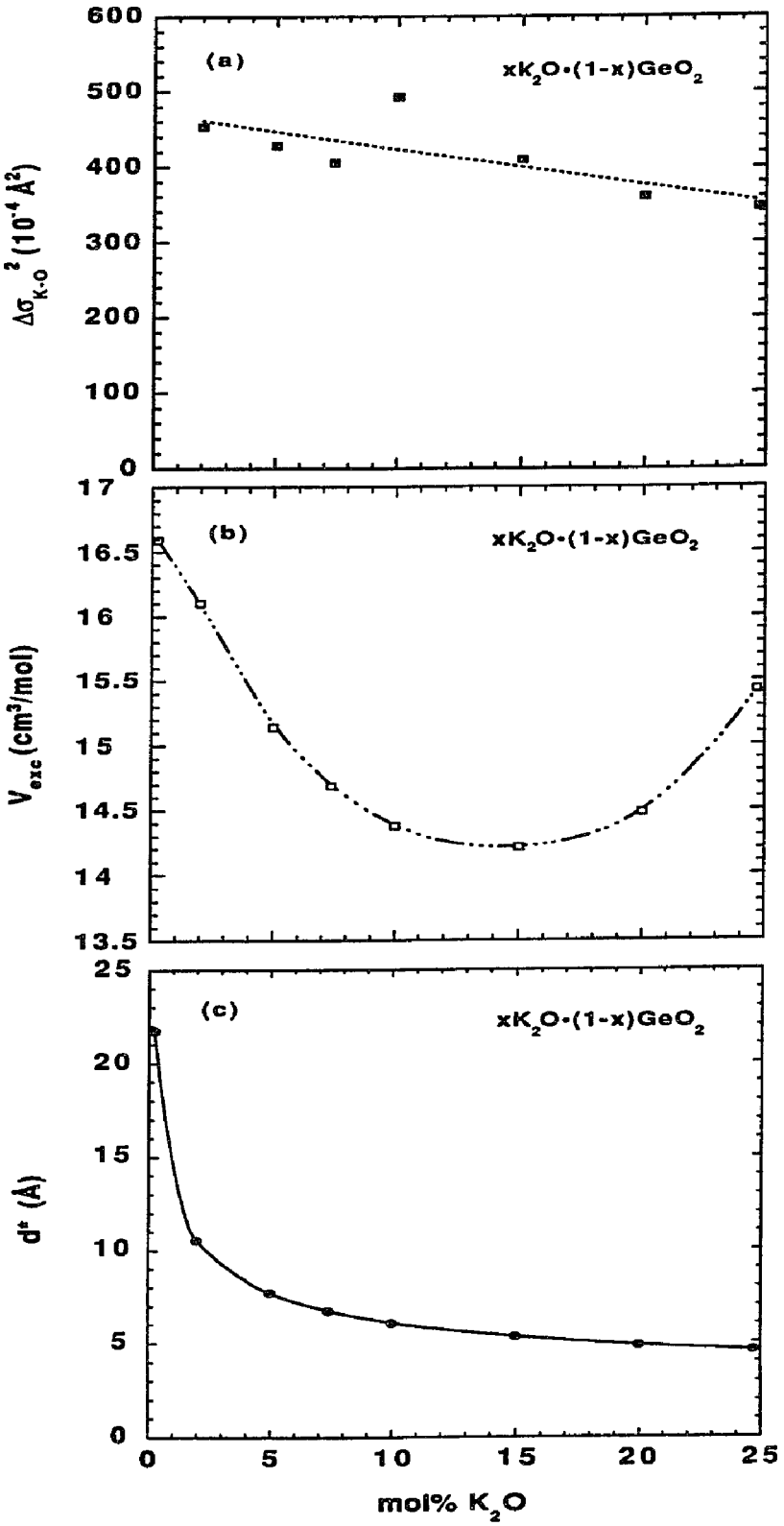

Figure 8.3 Variation of (a) $\Delta\sigma^2_{K\text{-}O}$, (b) V_{exc}, and (c) d*, as a function of K_2O mol% in $xK_2O \cdot (1\text{-}x)GeO_2$ glass series.

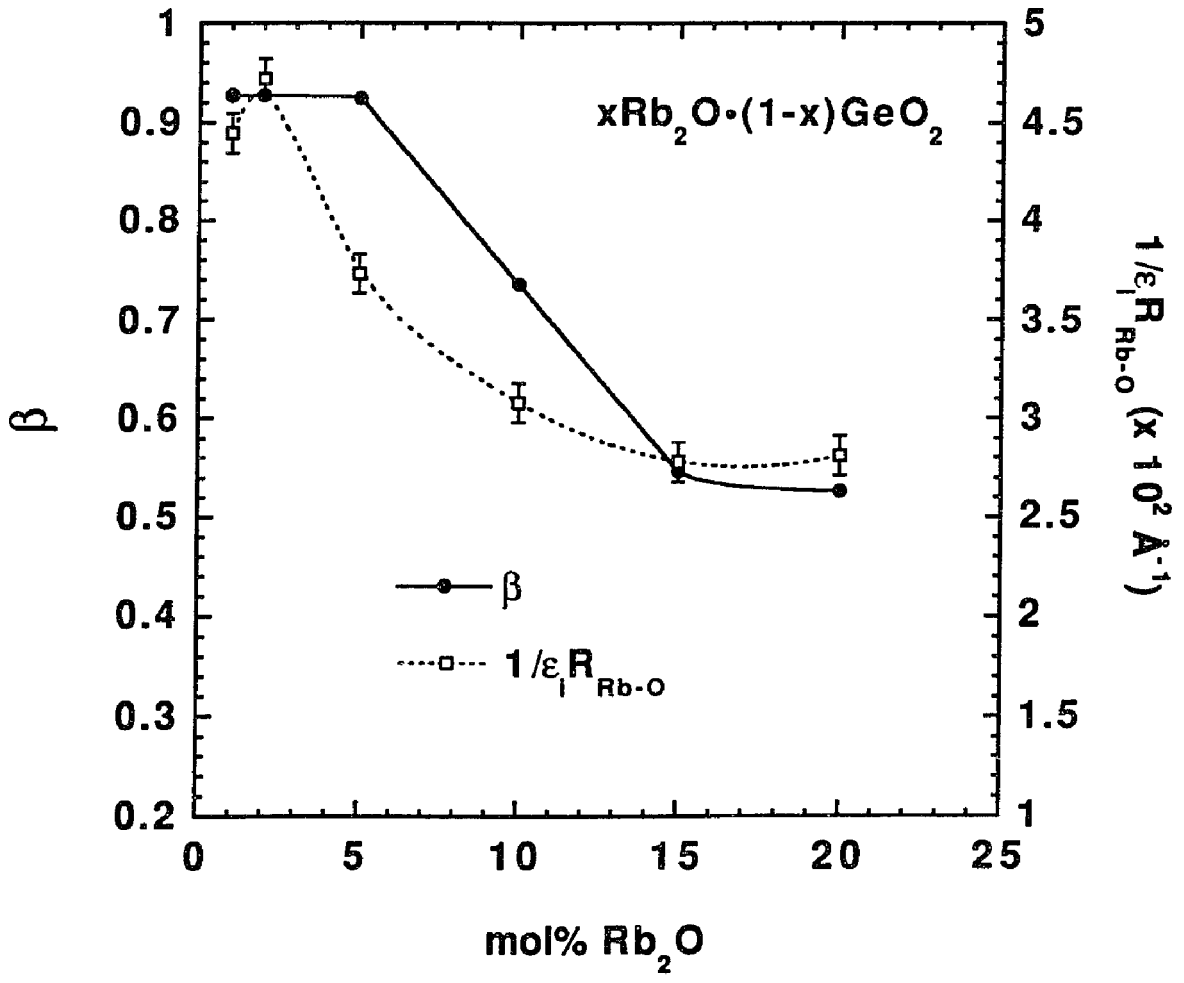

Figure 8.4 Dependence of β and $1/\varepsilon_i R_{Rb\text{-}O}$ on Rb_2O concentration in $xRb_2O\bullet(1\text{-}x)GeO_2$ glass series.

8.1.1 Applicability of Relaxation Time Distribution Models

The ECR behavior is considered here in terms of Kohlrausch exponent β, which represents the sample response on a rather restricted time scale in the vicinity of τ_{dc} [47,60]. A value of $\beta < 1.0$ in Fig. 8.1 represents non-ideal (non-Debye) electrical relaxation. Let

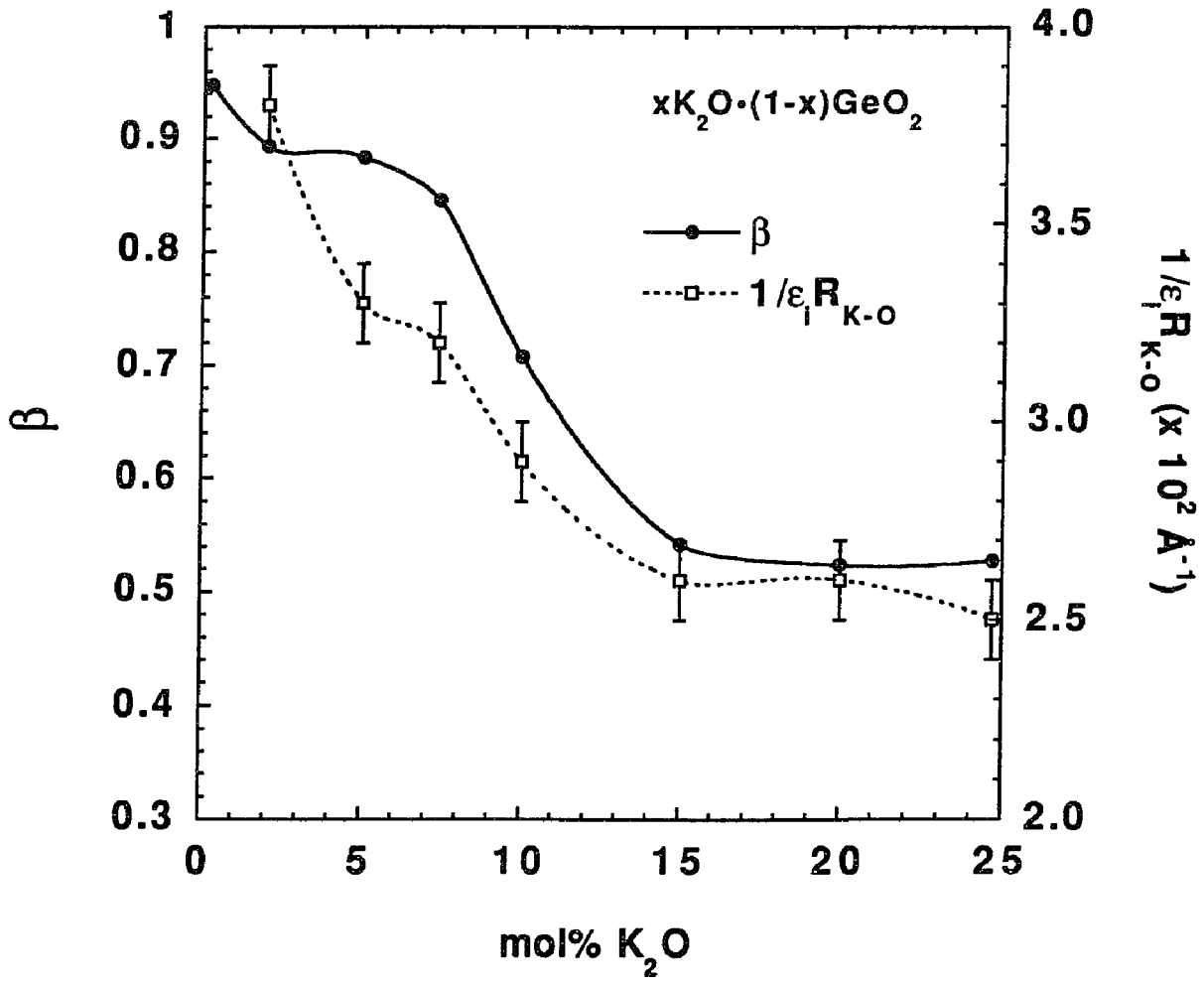

Figure 8.5 Dependence of β and $1/\varepsilon_i R_{K\text{-}O}$ on K_2O concentration in $xK_2O\bullet(1\text{-}x)GeO_2$ glass series.

us examine the local structural information to test the validity of various models for the origin of β.

According to the "distribution of relaxation times" model, the non-Debye relaxation is a consequence of the glass structure which introduces a distribution of activation energy for ion jumps. Because the energy barrier for an ion jump depends on the local structure

around the ion, it is reasonable to assume that the distribution of the activation energy barriers or of the relaxation times in glass is directly related to the structural disorder around the mobile ion: the larger the structural disorder around Rb or K, the broader should be the distribution of relaxation times and consequently smaller the value of β. The decrease of $\Delta\sigma^2_{Rb\text{-}O}$ (Fig. 8.2(a)) and $\Delta\sigma^2_{K\text{-}O}$ (Fig. 8.3(a)) as a function of M_2O (M = Rb or K) mol% indicates that the distribution of relaxation times for alkali germanate glasses becomes narrower with increasing M_2O concentration, which implies that β value should increase with M_2O mol%. However, β value in Fig. 8.1 for both the series shows an opposite trend and so we must conclude that the "distribution of relaxation times" cannot account for the origin of non-ideal ECR behavior in the present germanate glass series.

8.1.2 Applicability of Mobile Ion-Ion Coupling Models

If the source of non-ideal ECR is in "ion-ion coupling" such that the activation energy for ion movement controls the coupling, both β and E_{dc} should show similar composition dependence. Several studies have supported this relationship. For example, Martin and Angell [39] studied lithium phosphate glass series containing rather high concentration of Li_2O varying from 37 to 62.5 mole% and found β to decrease from 0.6 to 0.49. They suggested that β correlates best with the magnitude of conductivity or, alternatively, the decreasing trend of β is correlated with the decreasing activation energy for d.c. conductivity E_{dc}. Ngai and coworkers [64,131] analyzed the data for several different single and mixed alkali germanate and other oxide glass series and further established that in general β increases with E_{dc}. The correlation between β and E_{dc} seems

physically reasonable if the origin of β is from the dynamic correlation among mobile ions [46]. Such correlation of the mobile ion with other ions would become weaker if it must overcome a higher energy barrier for diffusion. However, β for both the Rb_2O-GeO_2 and K_2O-GeO_2 series in Fig. 8.1 does not show one to one correlation with their E_{dc}: E_{dc} shows a maximum at ~ 10 mol% M_2O (M = Rb or K) but β decreases monotonically around this composition. A similarly inexact correlation was reported for the same glass series by Ngai et al. [64]. Also, the variation of β with composition does not correlate well with the variation of local structure characteristics, viz. non-bridging oxygen concentration, fraction of six fold coordinated Ge or $\Delta\sigma^2_{Ge\text{-}O}$ (for the variation of these parameters with composition for both series, see Figs. 6.5, 6.6 and 6.7 in Chapter 6). In addition, the "excess volume", which represents the "unoccupied volume" and can be conceived as the pathway for the long range diffusion of alkali atoms [16], shows a minimum at ~ 10 mol% Rb_2O (Fig. 8.2(b)) (at ~ 10 - 15 mol% K_2O, Fig. 8.3(b)) and does not correlate with β as well. Thus, β, in contrast to E_{dc}, does not appear to be very sensitive to the local configurational changes in the glass network.

Further, if the origin of non-ideal ECR is primarily from the interaction among mobile cations, the closer they get, the interaction between them should become proportionately stronger, giving a smaller β. Patel and Martin [70] noted for their $xNa_2S\bullet(1\text{-}x)B_2S_3$ system that nominal mobile cation-cation distance, d^*, is one property in glasses which shows a rapid decrease, similar to that of β, with initial increase of cation concentration up to several mole% and then changing little with increase in concentration beyond 10 mol%. Therefore they proposed that β is intimately correlated with d^* which

was calculated from density measurements assuming a uniform mobile cation distribution. However, we note that β (Fig. 8.1) for the two present glass series does not decrease rapidly with the addition of the first several mol% of alkali oxide, although a rapid decrease in d^* is found for both the rubidium germanate (Fig. 8.2(c)) and potassium germanate glasses (Fig. 8.3(c)) just like in the thioborate series of Patel and Martin [70] or the lithium germanate series of Kanert et al. [132]. Therefore, in contradiction to the earlier suggestions [70], we conclude that d^* may not be always useful as a parameter for correlating with β. The problem with d^* may be that the origin of β is more complicated than just cation-cation interactions.

In short, we find that the origin of the non-ideal ECR is not exclusively in the "distribution of relaxation times" as reflected in structural disorder around the mobile cation, or in the mobile cation-cation interactions as governed by E_{dc}. It is not determined just by the nominal mobile cation-cation distance, or by the "excess volume" which strongly affects E_{dc}. So, the origin of $\beta < 1$ should be fairly complicated. Unfortunately, so far it has not been possible to independently determine the interaction of a mobile cation with its surroundings. In fact, we do not know even the actual mobile cation-cation distance. Thus the present results do not necessarily undermine the importance of the various factors proposed in the literature as contributors to the non-ideal ECR behavior. At the same time, they illustrate well that any single parameter is unlikely to explain the origin of $\beta < 1$.

8.1.3 Coupling between Mobile Ion and Its Charge Compensating Center

Having made the above disclaimer, we examine the variation of "electrostatic energy" between M^+ (M = Rb, K) and its nearest charge compensating center (CCC) as given by the variation of $1/(\varepsilon_i \bullet R_{M\text{-}O})$, and obtain relatively good correlation with β (for rubidium germanate series, see Fig. 8.4; for potassium germanate series, see Fig. 8.5). The exact expression for the electrostatic force between a mobile cation and its surrounding is expected to be very complicated because of the intricate and poorly characterized distribution of charge. Hence the approximate correlation shown in Figs. 8.4 and 8.5 may be taken to imply that the electrostatic interaction between the mobile ions and their CCCs is perhaps the most important (but not the only) cause of the deviation of ECR from ideal Debye behavior. That is, β depends on the electrostatic interaction between a mobile ion and its CCC as well as the degree of coupling between the mobile ions. A similar observation of the importance of the electrostatic interactions in determining β was also reported for a high purity quartz crystal [46].

A closer examination of Figs. 8.4 and 8.5 shows that although there is a general correlation between β and $1/(\varepsilon_i \bullet R_{M\text{-}O})$, there is a lack of one-to-one correspondence between them especially for the composition between 5 - 15 mol% M_2O. This is the composition region where E_{dc} shows a maximum (Fig. 8.1). As we have mentioned earlier that Coulomb force is not the only, although perhaps the most important, cause for determining β [16]. The other cause such as elastic strain interaction could be also very important, especially for those glasses with large mobile ions and high network compactness such as the present germanate glass systems. The observed increase in β in this composition region than expected from the variation of $1/(\varepsilon_i \bullet R_{M\text{-}O})$ is very likely due to the presence of large

strains, which are also responsible for the E_{dc} maximum [16]. Therefore, we suggest that the cooperativity parameter β depends on at least three factors: the dynamic Coulomb interactions among the mobile ions, the Coulomb interaction between the mobile ions and their CCCs, and the elastic strain interaction between the mobile ions and rest of the glass network. In the present germanate glass series, the second contributor is particularly important.

8.2 Conductivity Relaxation in Mixed Mobile Ion Germanate Glasses

The mixed (alkali) mobile ion (MMI) effect for d.c. conductivity has been known for a long time [42,43], yet the physical basis for ECR behavior in mixed mobile ion glasses has remained just as unclear. Additional complications arise due to the fact that both mobile species might participate in the relaxation process. Ngai et al. [64] pointed out in support of their coupling model that β, just as E_{dc}, shows a maximum in a mixed alkali glass series. However, Tomozawa et al. [133] found this to be true only for high alkali content mixed alkali glasses, such as the $0.33(Li,Na)_2O \bullet 0.67SiO_2$ series. For a low alkali content mixed alkali glass series $0.02(Na,K)_2O \bullet 0.98GeO_2$, β showed a minimum when two kinds of alkali were mixed. Apparently, the β-E_{dc} correlation for mixed alkali series cannot be quantitatively explained by the coupling model. The origin of the non-ideality in electrical relaxation for mixed alkali glasses appears to be as complicated as for binary alkali glasses. A close investigation of the local structure around both types of mobile cations as well as the network forming cation should help to elucidate the complexity.

Key Results

E_{dc} as a function of Ag/Rb ratio for the mixed mobile ion $0.2(Rb,Ag)_2O•0.8GeO_2$ glass series is plotted in Fig. 8.6(a), where it shows a strong maximum as Rb is gradually replaced by Ag, indicating that a mixed mobile ion (MMI) effect is present and effectively Ag behaves as an alkali ion. The corresponding variation of β (with uncertainty ≤ 0.02, see Sec. 5.3) also shows a pronounced MMI effect at the mixed mobile ion composition (Fig. 8.6(b)). The corresponding variation of the high frequency dielectric constant (ε_i) (Fig. 8.6(c)) (with uncertainty ≤ 0.5, see Sec. 5.2), determined from the intersection of complex ε" vs. ε' plot with the ε' axis for eliminating the space charge effects at the electrodes [99], shows a trend approximately opposite to that of β (Fig. 8.6(b)).

E_{dc} as a function of K/Rb ratio for the other mixed alkali $0.2(Rb,K)_2O•0.8GeO_2$ glass series is shown in Fig. 8.7(a), where it also shows a MMI effect as Rb is gradually replaced by K. Nevertheless, the corresponding variations of β (Fig. 8.7(b)) and ε_i (Fig. 8.7(c)) for this series do not show a clear MMI effect as Rb is replaced by K.

The variations of interatomic distances for the mobile ions (Rb, Ag) from oxygen and disorder around them for the mixed mobile Rb-Ag series have been shown in Figs. 7.8(a) and (b). $R_{Rb\text{-}O}$ and $\Delta\sigma^2_{Rb\text{-}O}$ for this series monotonically increase with decreasing Rb content, while $R_{Ag\text{-}O}$ and $\Delta\sigma^2_{Ag\text{-}O}$ decrease with decreasing Ag content. The corresponding variations of $R_{K\text{-}O}$, $\Delta\sigma^2_{K\text{-}O}$ and $R_{Rb\text{-}O}$, $\Delta\sigma^2_{Rb\text{-}O}$ for the mixed alkali Rb-K series have been shown in Figs. 7.10(a) and (b). These structural parameters stay nearly constant as Rb is replaced by K.

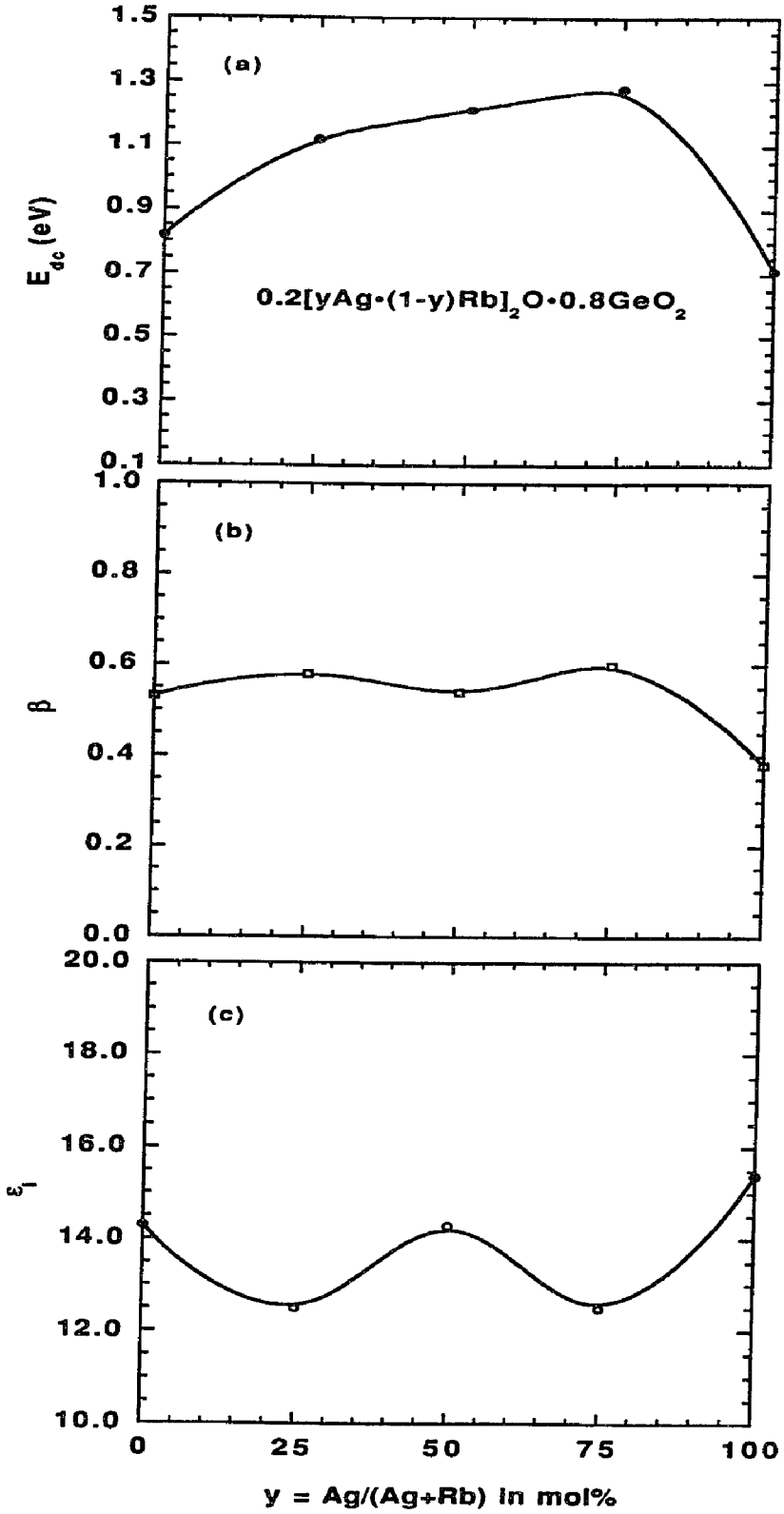

Figure 8.6 Variation of (a) E_{dc} (b) β and (c) ε_i as Rb is replaced by Ag in mixed mobile ion 0.2[yAg•(1-y)Rb]$_2$O•0.8GeO$_2$ glass series.

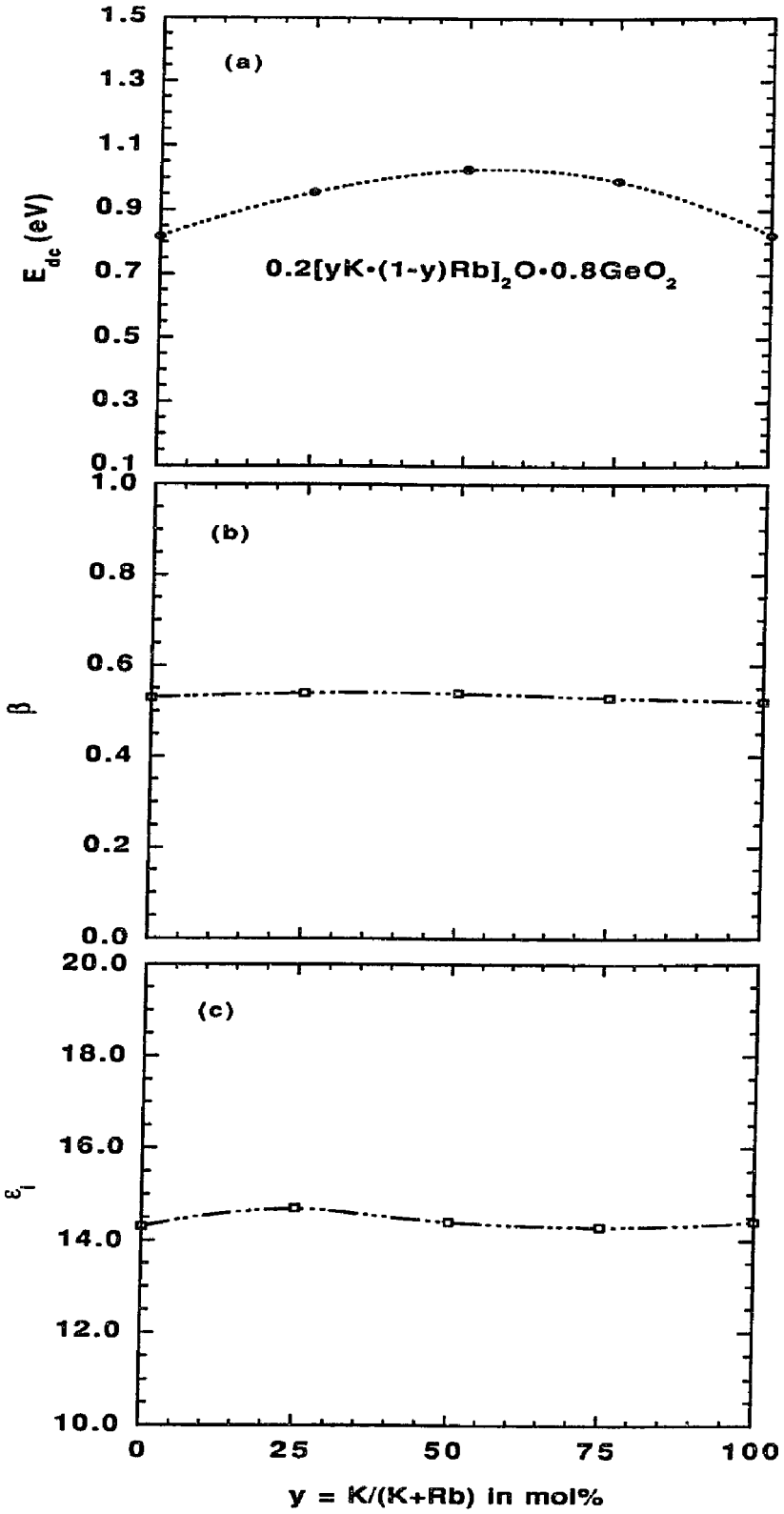

Figure 8.7 Variation of (a) E_{dc} (b) β and (c) ε_i as Rb is replaced by K in mixed alkali $0.2[yK•(1-y)Rb]_2O•0.8GeO_2$ glass series.

8.2.1 Conductivity Relaxation and Glass Structure

The (Rb,Ag) germanate glass series exhibits a typical mixed mobile ion (MMI) effect, in that E_{dc} shows a maximum as Rb is replaced by Ag (Fig. 8.6(a)). β for this series shows a maximum (Fig. 8.6(b)). Thus, we find an overall correlation between β and E_{dc} as suggested by Ngai et al. [49,64,131], although at mixed compositions the correlation is less than perfect. This correlation indicates that there is an effect of the mobile ion coupling on the relaxation behavior for the (Rb,Ag) germanate glasses. However, for our present mixed alkali (Rb,K) germanate glass series, β stays nearly constant (Fig. 8.7(b)) as the two kinds of alkali are mixed, even though the variation of E_{dc} shows an MMI effect (Fig. 8.7(a)). A similar difficulty for correlating β with d.c. conductivity was also noted for a high purity quartz series [46]. Apparently, there lacks a one-to-one correlation between β and E_{dc}, which illustrates well that their physical origins are somewhat (if not totally) different.

As discussed in Sec. 7.2, the fundamental manifestation of the MMI effect is that for a structural feature to correlate with this effect, we expect it to vary in a complementary manner when either cation is replaced by the other. However, neither the trends of respective $R_{M\text{-}O}$ and $\Delta\sigma^2_{M\text{-}O}$ (M = Rb, Ag) for the (Rb,Ag) germanate series (Figs. 7.8(a) and (b)) nor the corresponding trends for the (Rb,K) germanate series (Figs. 7.10(a) and (b)) follow this prediction: For the (Rb,Ag) germanate series, $R_{Rb\text{-}O}$ and $\Delta\sigma^2_{Rb\text{-}O}$ increase monotonically with decreasing Rb_2O content, while $R_{Ag\text{-}O}$ and $\Delta\sigma^2_{Ag\text{-}O}$ decrease monotonically with decreasing Ag_2O content. For the (Rb,K) germanate series, $R_{Rb\text{-}O}$, $\Delta\sigma^2_{Rb\text{-}O}$ and $R_{K\text{-}O}$, $\Delta\sigma^2_{K\text{-}O}$ stay nearly constant. Thus, the mobile cation-oxygen distance and the

disorder around the mobile ion should not be the key to the ECR behavior in MMI glasses. The MMI behavior in β is likely to arise from the dynamics of mobile ions rather than from the static structure of glass.

8.2.2 Conductivity Relaxation and Dielectric Constant

As discussed in Sec. 8.1.3, the cooperativity parameter β depends on at least three factors: the dynamic Coulomb interactions among the mobile ions, the Coulomb interaction between the mobile ions and their CCCs, and the elastic strain interaction between the mobile ions and rest of the glass network. For germanate glasses, the Coulomb interaction between the mobile ions and their CCCs, appears to be the most important contributor. Thus, in principle, a comparison of the respective Coulomb interaction of different mobile ions with their CCCs should help us determine the importance of this contribution in mixed mobile ion germanate glasses. Unfortunately, although EXAFS gives M-O distance for each atom, it is not possible to estimate the relative electrostatic force for each kind of mobile ions. The dielectric constant is an overall electrical response and can not be separated for respective atoms.

Nevertheless, given the fact that the Coulomb interaction between mobile ions and their CCCs is primarily determined by the inverse dielectric constant ($1/\varepsilon_i$) (the interatomic distance between mobile ion and oxygen atom does not vary much), one may anticipate a correlation between β and $1/\varepsilon_i$. In Fig. 8.6 for the (Rb,Ag) germanate series and Fig. 8.7 for the (Rb,K) germanate series, a better correlation is found between β and $1/\varepsilon_i$ than between β and E_{dc}. In fact, for the (Rb,K) germanate series, both β and $1/\varepsilon_i$ do not show

an obvious MMI effect but E_{dc} does. Thus, we may conclude that in germanate glasses the non-ideality in ECR is affected more by ε_i than by E_{dc}. The dielectric constant, ε_i, is a factor determined by the polarizability of ions, which is related to the short range movement of mobile ions. In contrast, E_{dc} is a factor related to the long range movement of mobile ions.

8.3 Conductivity Relaxation in High Purity Quartz

8.3.1 Effect of Annealing on Conductivity Relaxation

It has been generally believed that the non-ideality of ECR behavior results from the complexity of large mobile ion concentration (see Sec. 8.1). Therefore, relatively little attention has been given for determining the frequency dependence of electrical properties of better characterized ionic crystals which have typically very low defect concentration. In fact, none of the theoretical models referenced in Background (Sec. 2.3) was developed for simple single crystals. They were intended for describing ECR in complex materials such as glasses and perhaps highly disordered crystals like β-alumina. One investigation over a decade ago on a nominally pure NaCl gave $\beta = 0.89$ which approaches the ideal behavior [134]. Lee et al. [135] also did not report an independent frequency dispersion between the dc-like and $s = 1$ region for a NaCl crystal doped with 50 ppm zinc or for $KTaO_3$ crystal doped with 30 ppm protons. They, however, found substantial dispersion for CeO_2 ceramic containing much higher defect concentration from doping with 6 mol% Gd_2O_3. These results reinforce the belief stated above. However, to the best of our knowledge, no systematic study has been reported correlating β with the defect/crystal

structure. In the following, we report our results on a high purity quartz crystal, which will hopefully demonstrate clearly the importance of structure and encourage further studies.

Before we discuss the ECR behavior it seems appropriate to first summarize the mechanism of electrical conduction in quartz. It is one of the best understood crystal and the details of the mechanism may be found in Ref. [87]. Typically a synthetic quartz crystal is grown hydrothermally (at 350 °C for our crystal) during which trivalent impurities (predominantly Al but Fe also possible) enter the crystal substitutionally on Si sites. The effective negative charge of Al is compensated by monovalent cations (most important being Na^+ but Li^+ or H^+ may also occur). The concentration of these impurities in a high quality crystal such as used here[$] may range from 1-10 ppm. Oxygen vacancies are other possible source of charge compensation. The electrical conduction in such a crystal is due to highly anisotropic movement of alkali (Na) ions, being much higher along the open channels parallel to c-axis. We have measured conductance and capacitance of our crystal in the c-direction between room temperature and 525 °C. In this temperature range most Na^+ ions are associated with the trivalent impurity with energy E_a. Only a few of them have sufficient thermal energy to break this association and then migrate as free interstitials along the channels with migration energy, E_m. For an ideal crystal containing one kind of trivalent and one kind of monovalent impurities as the only charged point defects the observed activation energy of conductivity $E_{dc} = E_a/2 + E_m$. However, if the distribution of impurities is such that the concentration of unassociated trivalent impurities is relatively

[$] Premium Q sweep grade crystal from the z-growth region - supplied by Sawyer Research Products, Cleveland, Ohio.

large and thus unaffected by the degree of association of monovalent cations, $E_{dc} = E_a + E_m$. Thus in a real crystal E_{dc} may vary between these two extremes depending on the concentration and distribution of various defects.

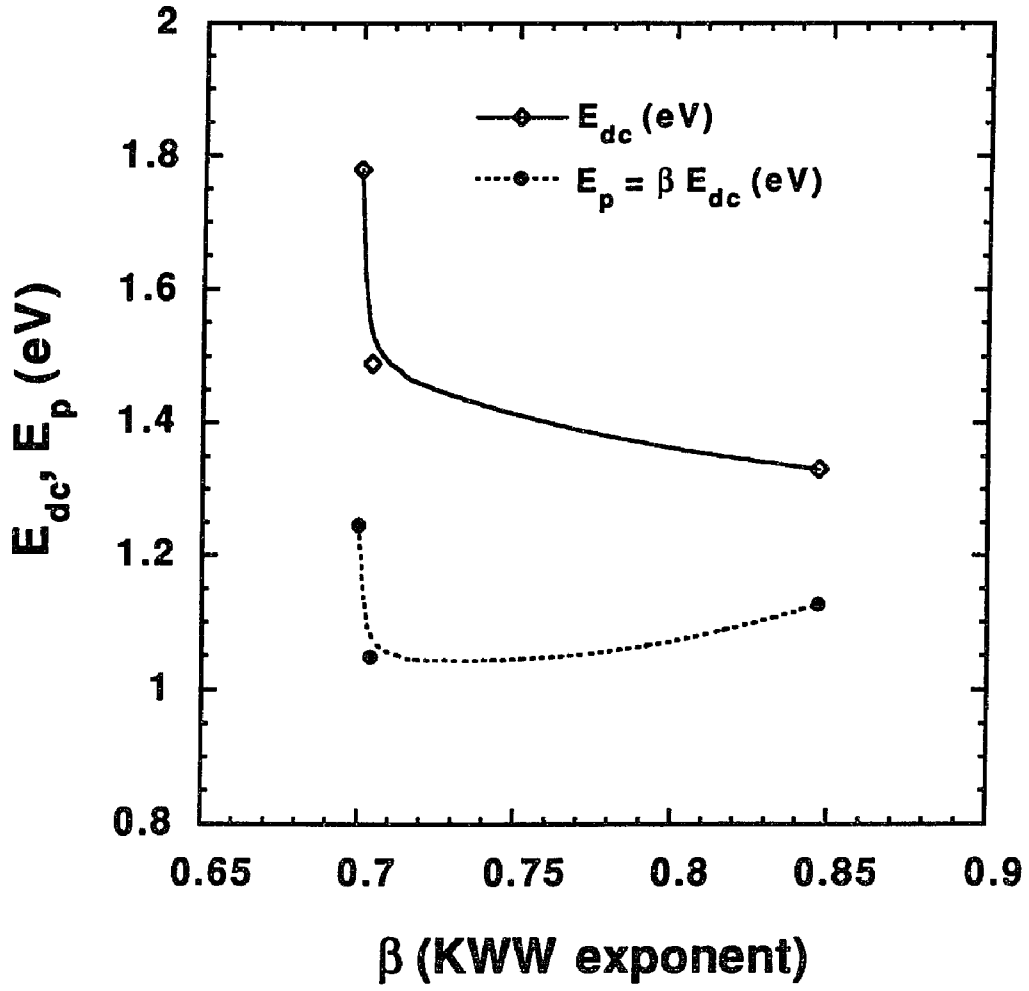

Figure 8.8 Plot of E_{dc} and E_p vs. β for a high purity quartz crystal.

When measuring the temperature dependence of electrical response of our quartz sample we found that d.c. conductivity increases with time when the sample is maintained

at temperature > 350 °C. This is not too surprising considering the general sensitivity of quartz's conductivity to various treatments involving heat and radiation [87]. As our sample is annealed at a higher temperature the conductivity increases further with associated decrease in E_{dc}. This implies that annealing of the sample above the crystal growth temperature homogenizes it and liberates the mobile cations (Na^+) into bulk of the crystal presumably from dislocations or sub-grain boundary regions. The liberated cations form pairs with unassociated trivalent impurities. Accordingly, the observed E_{dc} approaches from high value ($E_a + E_m$) towards lower ($E_a/2 + E_m$). The accompanying variation of β as a result of the annealing treatment is shown in Fig. 8.8 as a function of E_{dc} as well as E_p. First we note that even for very low mobile ion concentration (a few ppm or less), β is significantly lower than 1. Next, β changes for the same sample i.e. for fixed d^*, as a result of heat treatment. So we may conclude that the changes in the defect distribution and structure can not be ignored at least for materials with low ion concentration. Third, we find an unexpected result contrary to general observation that, as the energy barrier for diffusion decreases, the ion-ion correlations responsible for non-ideal ECR also decrease. An indication of similar 'anomalous' behavior is also present in Fig. 8.1 (alkali germanate glasses) for a more complex situation where glass composition is changing.

We now attempt to explain all of our observations on quartz crystal with the schematic of Fig. 8.9. It is based on the low temperature dielectric loss measurements of Park and Nowick [136], and Haven ratio (H_r) results of Jain [137]. To emphasize that our discussion would be applicable also to glasses, this schematic is generalized to the situation where the mobile ion, say Na^+, can move in two dimensions. For actual quartz crystal our

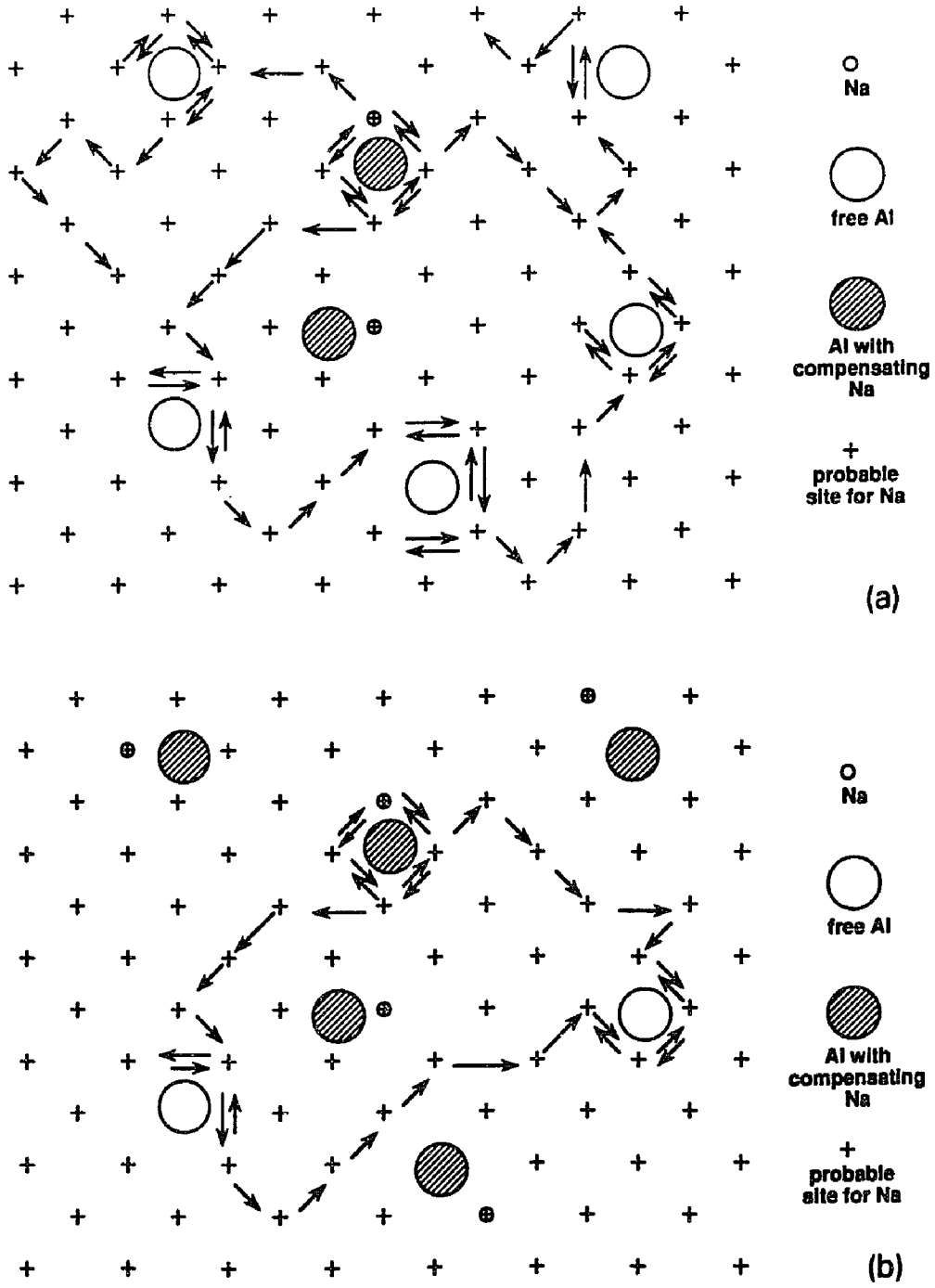

Figure 8.9 The movement of an alkali (Na) ion in a quartz matrix with many more charge compensating centers (Al_{Si}'). (a) As received crystal. (b) The same crystal after high temperature annealing.

discussion would be just as applicable with the constraint of nearly one dimensional conduction. The schematic shows that there are many more sites for sodium to jump than their concentration. Mostly Na^+ remains associated with its charge compensating center (CCC), say the Al_{Si}' defect, but in this condition it can make localized jumps around Al which gives rise to dipolar dielectric relaxation at low temperatures [136]. Occasionally an Na^+ dissociates from its CCC and moves away. Because of coulomb attraction this dissociation step is very likely to be reversed which would make this kind of jump highly non-random leading to a low value of H_r [137]. Once Na^+ has moved away and is not next to a CCC, it may move much like a free interstitial with H_r close to one. It appears reasonable that once a CCC has an Na^+ in its immediate vicinity, it would cease to attract another Na^+ which might be jumping around.

We now assume that the non-randomness in the jumps of a tracer atom averaged over a long time and as manifested in Haven ratio is related to the non-ideality of electric field relaxation which is manifested as the response of the ensemble of all the ions at a particular instant (frequency). A simple but not necessarily the only reason behind this assumption is that the same coulomb forces between the mobile cation and other cations or CCC's would cause a decrease in Haven ratio as well as β parameter. At this point we do not know exactly how the coulomb or other atomic forces affect the two parameters and therefore a quantitative relation between H_r and β can not be predicted. Nonetheless, because of a qualitative correlation between β and H_r we should be able to use the schematic of Fig. 8.9 for understanding the behavior of β in our quartz sample:

The schematic of Fig. 8.9(a) is meant to represent as-received quartz sample

consistent with the relatively high value of E_{dc}. In this case there is a large number of unassociated Al_{Si}' centers. Therefore, a freed Na^+ will have high probability of being trapped by one of them. This would lead to large non-randomness in its jumps as well as lower value of β. As the sample is annealed at a temperature above 350 °C, E_{dc} decreases meaning that additional Na^+ are liberated from dislocations etc. and fewer Al_{Si}' centers are now uncompensated, as shown in Fig. 8.9(b). That is, now for a moving Na^+ there are fewer trapping sites which tend to decrease H_r and β. So the annealing treatment should enhance β, exactly as found experimentally (Fig. 8.8). Thus, the apparently anomalous relation between E_{dc} and β in Fig. 8.8 is a simple consequence of the change in ion distribution. So, in summary, we note that the behavior of β in our quartz crystal provides a beautiful example for illustrating how the distribution of ions/defects can significantly affect ECR. Obviously to see the effect of structure on ECR, one must work with the materials of rather low ion concentration for which β is large to start with and likely to show large changes. Further, at very low ion concentrations mobile cation-cation distances are expected to be very large. At least in such cases the interaction between a cation and its CCC's may be far more important than with other cations, for determining the value of β.

In closing we may ask: can one ever find a solid for which β is exactly unity considering that even for a highly pure quartz crystal with mobile ion concentration less than a few ppm or a pure NaCl, β approaches but does not equal 1.0? We believe that the answer is: unlikely! Our reason is that as long as we are working with non-metallic systems, there will always be significant Coulomb interaction among charges which would

not permit the system to behave as an ideal ECR dielectric around τ_{dc}.

8.3.2 Effect of Neutron Irradiation on Conductivity Relaxation

In general, at a fixed temperature the frequency ($\omega = 2\pi f$) dependence of ionic conductivity (σ) of glasses consists of two regions [29,55,60] (see Sec. 2.3): (i) A d.c. plateau region at sufficiently low frequencies where σ does not depend on frequency and, (ii) An a.c. region above the d.c. plateau frequency where σ increases strongly with frequency ($\sigma_{ac} \propto \omega^s$, see eq. (2.15)). The frequency where the transition occurs from d.c. plateau region to the a.c. region is a function of temperature so that at a given temperature it is possible that one does not observe both the regions in an experimentally accessible frequency window. The frequency dependent conductivity or the resulting electrical relaxation is the subject of this section.

Most of the investigations of a.c. ionic conductivity have been confined to measurements at or above room temperature and in 2 to 3 decades of frequency above the d.c. plateau region, the so-called Jonscher-Ngai region. For an ideal ionic conductor one does not anticipate the conductivity to depend on frequency (except at very high frequencies approaching vibration frequency of the mobile ions), and s (the Jonscher power law exponent, see eq. (2.15)) and β (the Kohlrausch exponent) should be 0 and 1.0, respectively. However, in reality for most glasses containing significant concentration of mobile ions (say > 1.0 mol%), both s and β approach ~ 0.5 [64]. Numerous models [44,45,138,139,140] have explained this non-Debye nature in the Jonscher-Ngai region, explicitly or implicitly, by the inherent disorder in glass. This disorder introduces

randomness of structure and/or chemical, coulomb and elastic interactions among atoms. The complex nature of the atomic interactions leads to a time dependent component in the relaxation of electric field. Intuitively, these explanations appear physically quite reasonable, but there is little experimental evidence which establishes the significance of the disorder. Wittels and Sherrill [141,142] were the pioneers to study the effect of neutron irradiation on the structural disorder of quartz. They applied X-ray diffraction and density measurement to examine the structural change of quartz subjected to progressive neutron irradiation, e.g. with doses from less than 1×10^{19} to 1.2×10^{20} neutron/cm^2. These extensive studies on the effect of various neutron doses on structural disorder in quartz provide a basis for the present work. Accordingly, we investigate the electrical conductivity relaxation of a single crystal quartz as its crystallinity is gradually destroyed by neutron irradiation. Previously β for an unirradiated quartz single crystal was shown to be between 0.7 and 0.85 which is higher than for typical alkali oxide glasses [46], thus indicating that the electrical relaxation of the former is closer to the ideal behavior than that of the latter. By measuring the effect of neutron irradiation on β, we attempt to delineate the importance and necessity of a disordered structure for producing non-ideal electrical conductivity relaxation.

Key Results

Typical variation of conductivity against frequency is shown in Figs. 8.10 and 8.11 for the Q4 specimen after homogenizing it at 525 °C for 36 hr. and then after subjecting it to a total dose of 1×10^{19} n/cm^2, respectively. The irradiation produces transient defects

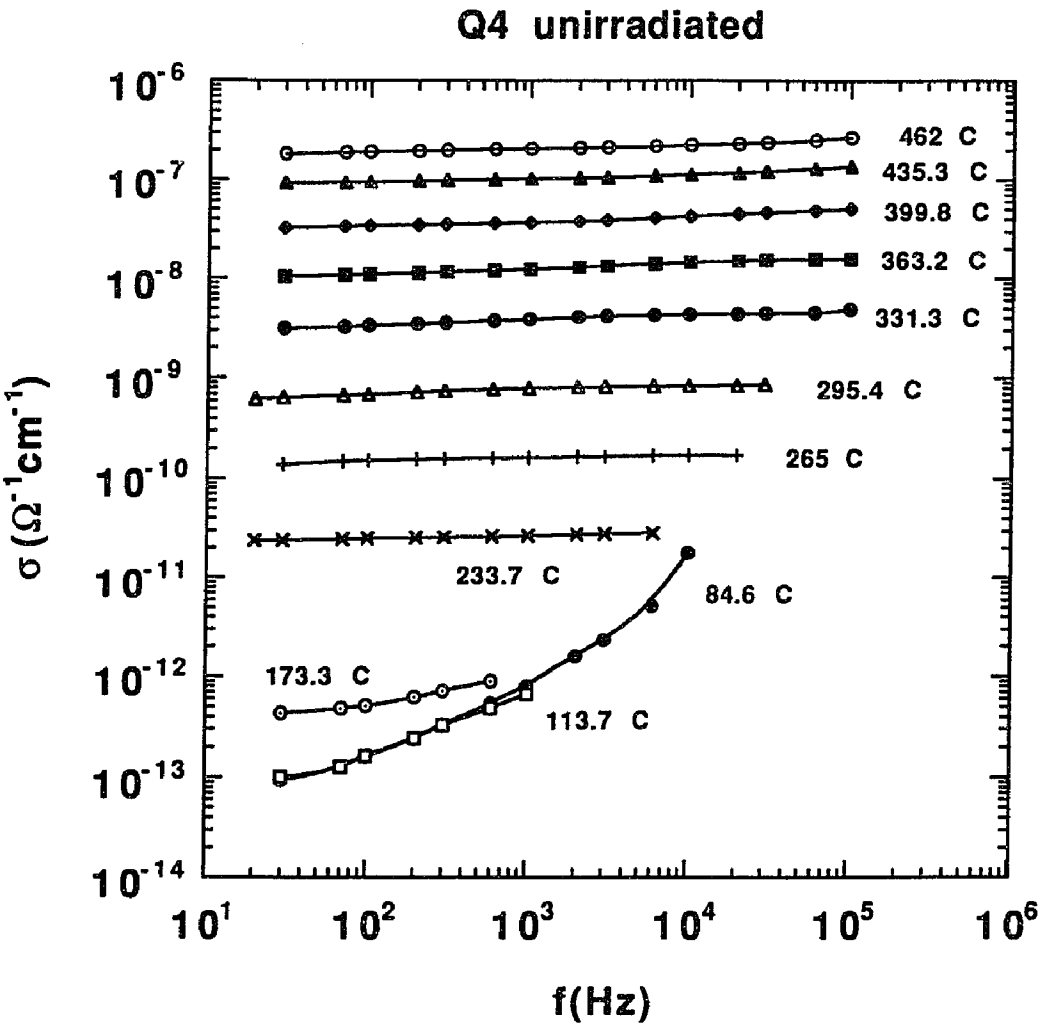

Figure 8.10 Electrical conductivity vs. log frequency for Q4 quartz specimen at various temperatures before neutron irradiation. Lines are drawn as guides for the eyes.

as well as permanent change in the structure [143]. However, the electronic transient defects are eliminated upon heating to ~ 350 °C so that the observed conductivity reflects changes in the atomic structure and defects [90,144]. Thus, the values of conductivity obtained above 350 °C are appropriate for comparing with those of the reference state

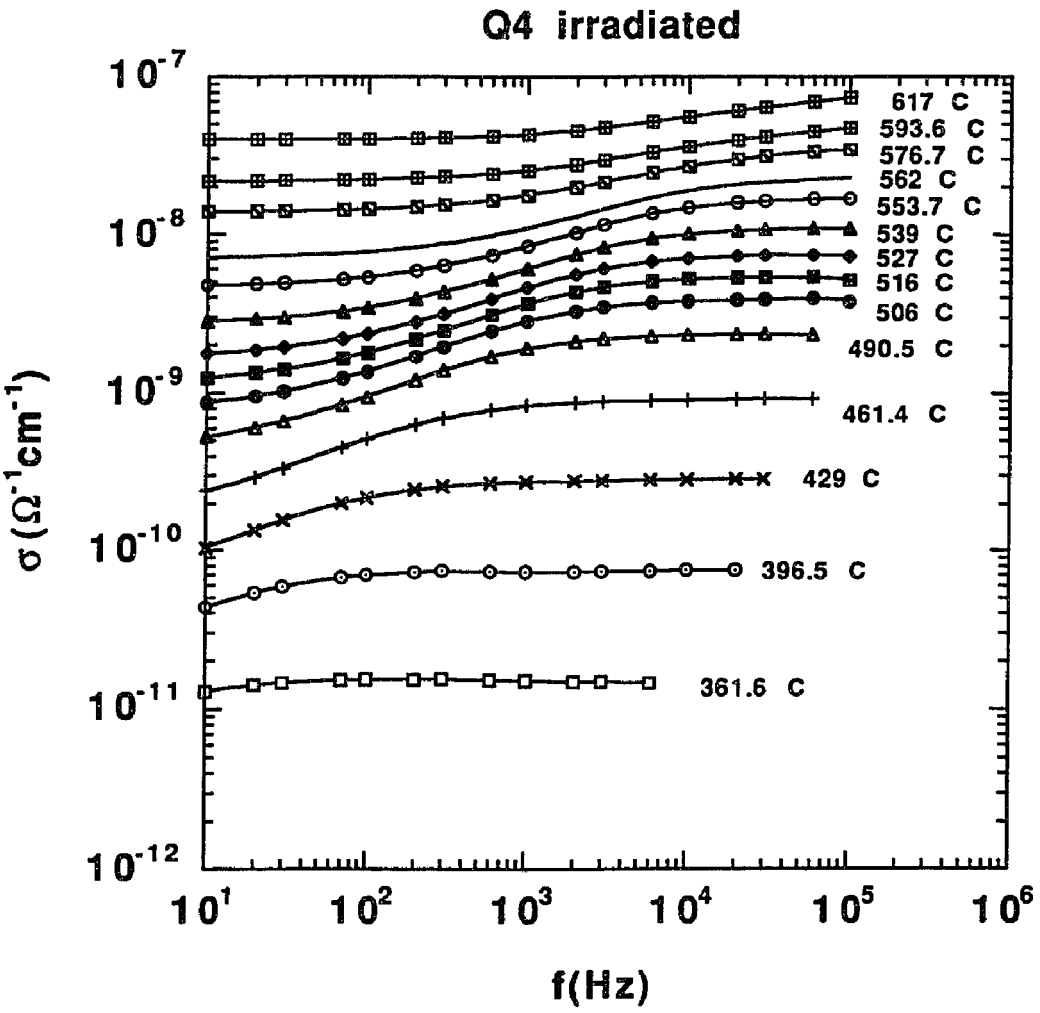

Figure 8.11 Electrical conductivity vs. log frequency for Q4 quartz after neutron irradiation (dose = 1×10^{19} n/cm^2). Lines are drawn as guides for the eyes.

before irradiation.

The electrical relaxation is determined in the vicinity of d.c. relaxation time (τ_{dc}) (Chapter 2). Accordingly, G(ω) and C(ω) values have been analyzed in the M" formalism. Fig. 8.12 shows the peak in M" vs. frequency plot for the Q6 specimen before and after neutron irradiation. Note that because of large increase in τ_{dc} due to irradiation, the M"

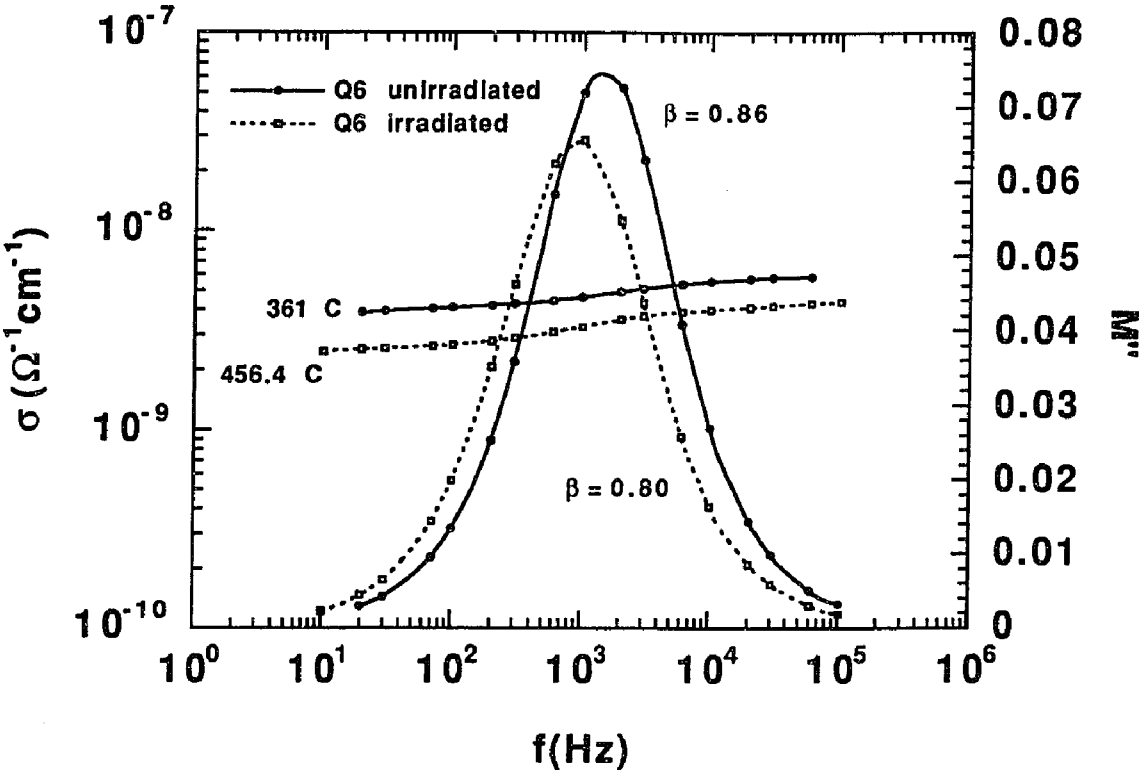

Figure 8.12 M" vs. log frequency for the Q6 quartz sample before and after neutron irradiation (see Table 5.6(b)). The figure also shows frequency dependence of conductivity corresponding to the M" plot.

peak for the irradiated specimen is observed at a higher temperature than that for the same specimen before irradiation. The best fit values of the Kohlrausch parameter (β) have been obtained following Ref. [45]. β has a small variation (within ± 0.02) with temperature. Its average value together with the range of variation with temperature is given in Table

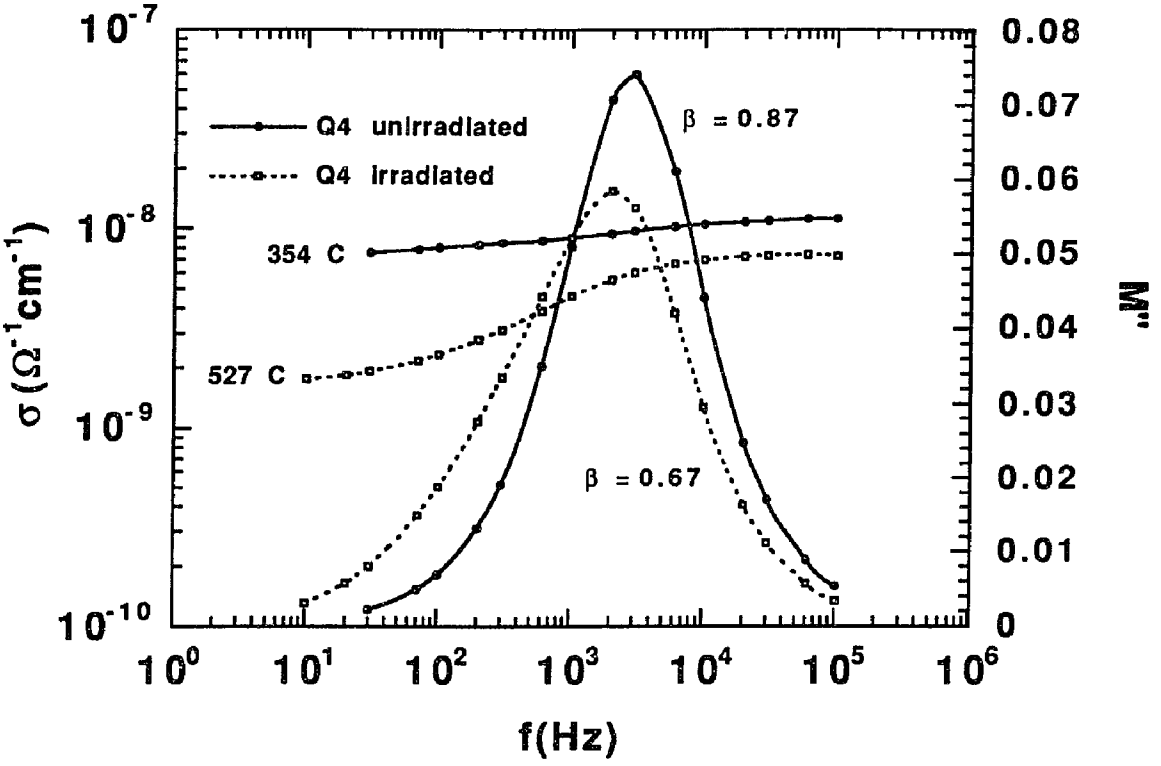

Figure 8.13 M" vs. log frequency for the Q4 quartz sample before and after neutron irradiation (see Table 5.6(b)). The figure also shows frequency dependence of conductivity corresponding to the M" plot.

5.6(b). Figs. 8.13 and 8.14 show results parallel to those in Fig. 8.12 for the Q4 and Q2 quartz specimens which were subjected to much higher neutron doses (1×10^{19} neutron/cm^2 for the Q4 specimen and 1×10^{20} for the Q2 specimen). Although the magnitude of electrical conductivity is different for the homogenized, unirradiated Q6, Q4 and Q2

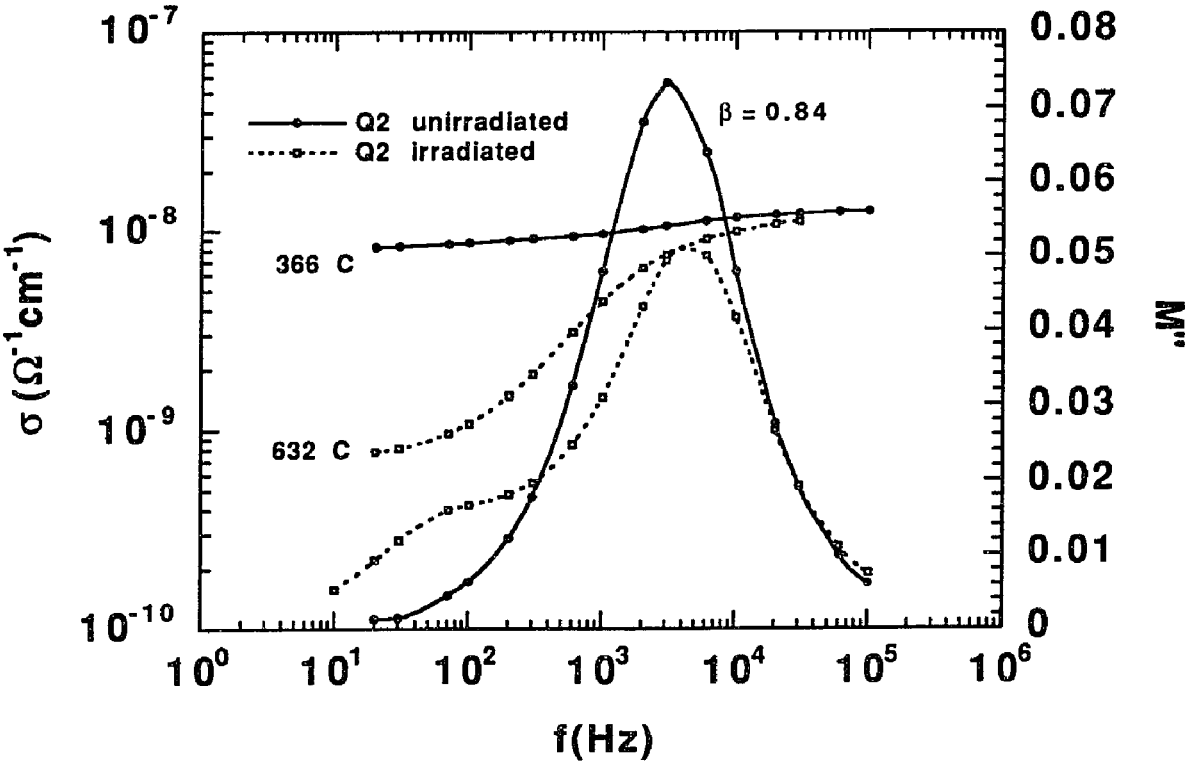

Figure 8.14 M" vs. log frequency for the Q2 quartz sample before and after neutron irradiation (see Table 5.6(b)). The figure also shows frequency dependence of conductivity corresponding to the M" plot.

specimens, E_{dc} and β values are considered the same within experimental uncertainty for these specimens. Note that the shape of the M" peak for the Q4 and Q2 specimens after irradiation shows broadening at low frequencies (the M" peak for Q2 being broader and showing a lower shoulder at low frequencies), which is not expected from the Kohlrausch

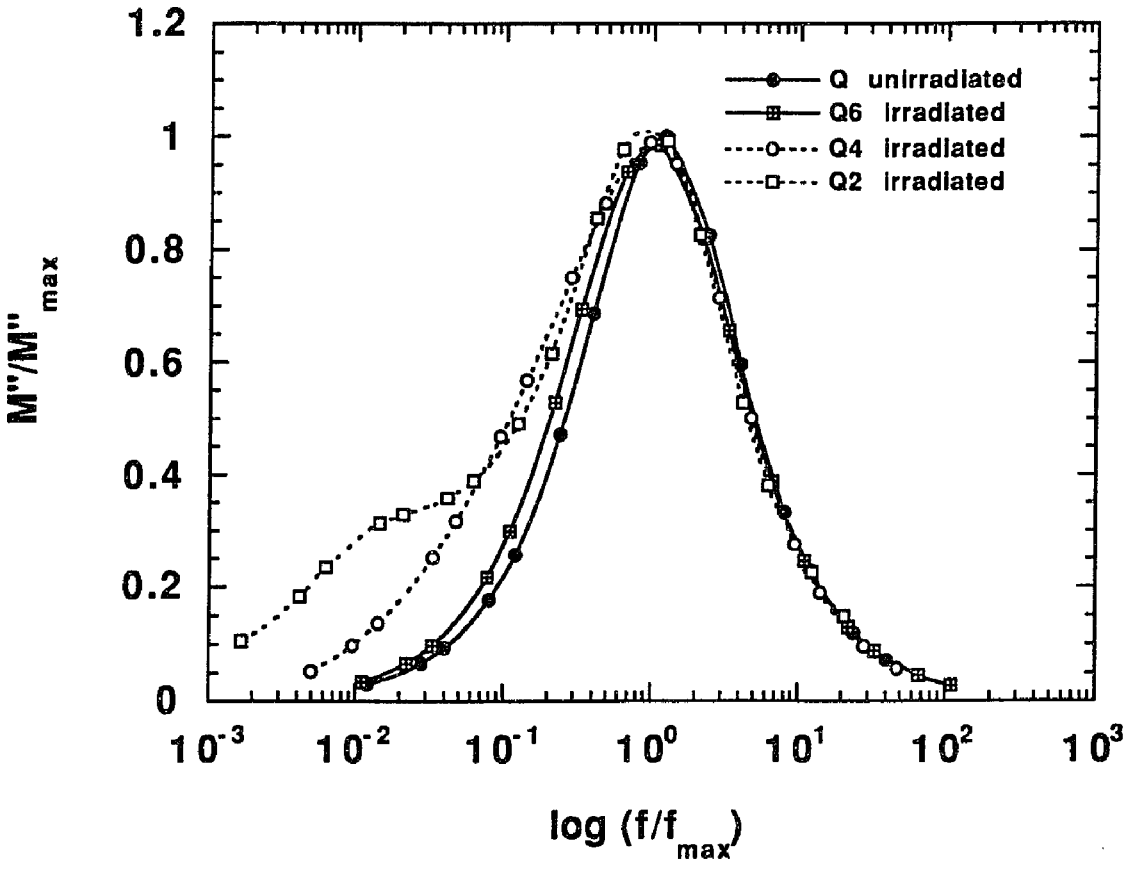

Figure 8.15 M" vs. log frequency for the quartz sample before neutron irradiation and for the Q6, Q4 and Q2 samples after irradiation. (see Table 5.6(b)).

form of the decay function. Therefore, no β value has been determined for the Q4 and Q2 samples. The increase in the M" peak broadening at low frequencies with increasing neutron dose is shown in Fig. 8.15, indicating that there is a strong effect of neutron irradiation on the electrical relaxation. Fig. 8.16 describes the temperature dependence of d.c. conductivity in the form of Arrhenius plots as obtained from complex impedance

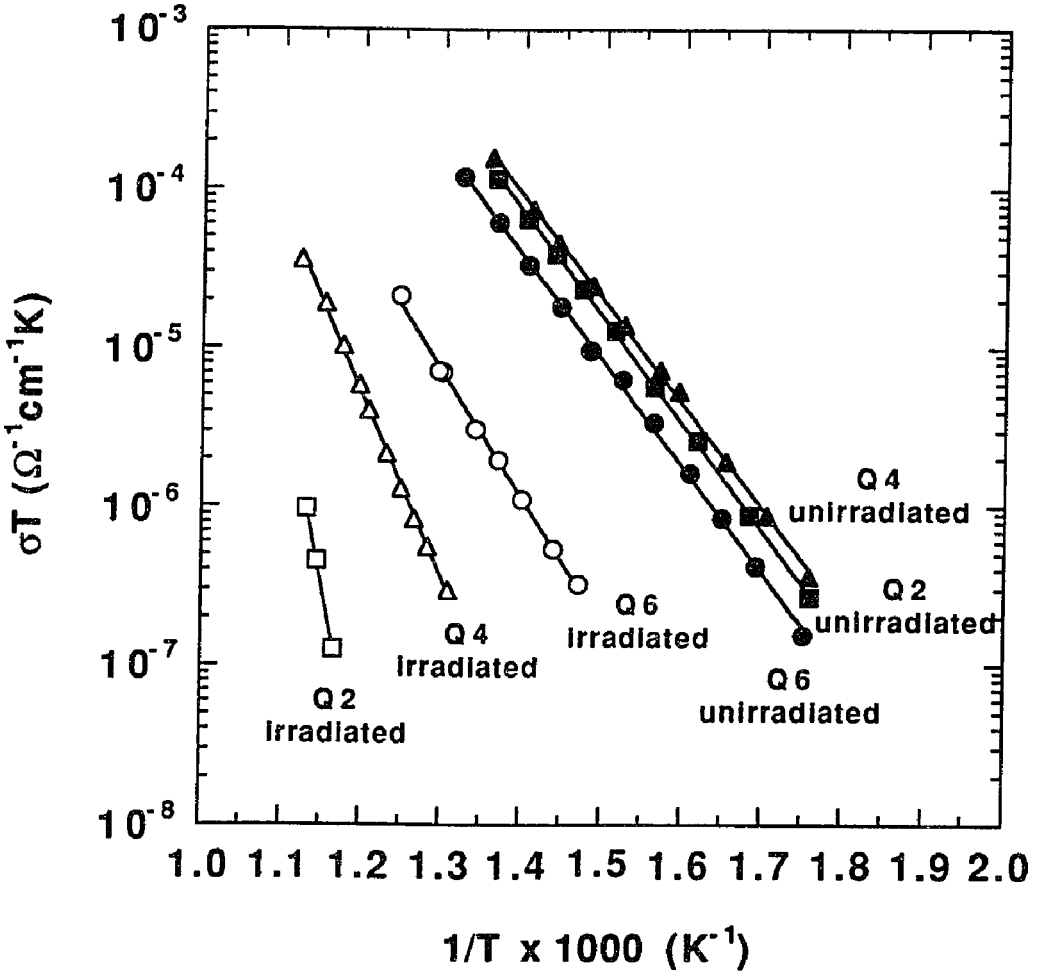

Figure 8.16 Arrhenius plots for d.c. conductivity of Q6, Q4 and Q2 quartz specimens before and after neutron irradiation. The curves represent the function $\ln(\sigma_{dc}T) = \ln\sigma_o - E_{dc}/kT$ (see Table 5.6(b)).

analysis [91]. The slope of the curves to which the data was fitted by a root mean square method (R = 0.9963 - 0.9999) gives activation energy for d.c. conductivity (E_{dc}) - see Table 5.6(b), which also lists the pre-exponential factor for Arrhenius law, the neutron dose, and density for the three specimens.

The small difference between the density of Q2, Q4 and Q6 specimens before irradiation is well within the variations reported in the literature [145]. Generally neutron irradiation of quartz should produce a detectable decrease in density for doses greater than a few times 10^{19} n/cm^2 [145]. The irradiation dose for the Q6 specimen is too small for any observable change in density. The dose for the Q4 and Q2 specimens could have shown a decrease in density, but the results show a small increase, if any. The reason for this observation is that the density values reported in Table 5.6(b) for the Q4 and Q2 specimens were obtained after the samples were heated to ~ 620 °C following irradiation. Such an annealing is known to increase the density towards the value before irradiation [145], making the difference between the density of the specimen (Q4 and Q2 samples) before and after irradiation within the experimental scatter of the data.

Discussion

Since the electrical properties of quartz are in part dependent on the concentration and distribution of impurities which may vary from one specimen to the next (see the discussion in Sec. 8.3.1), different specimens from the same crystal growth region of our crystal may have somewhat different distribution of the impurities, hence slightly different values of E_{dc}, if any (Table 5.6(b)). Therefore, it is important to compare the electrical properties of the same specimen before and after neutron irradiation.

From the inspection of Figs. 8.10 to 8.14 for Q2, Q4 and Q6 quartz samples, we find that electrical relaxation in quartz has three features which are distinct from those observed for common alkali oxide glasses:

(a) Above the d.c. plateau the electrical conductivity of common glasses continues to increase rapidly with increasing frequency (the Jonscher's power law) up to the far infrared region where absorption peak due to local alkali vibration is observed [99]. There are a couple of exceptions reported for fast ion conductors where a.c. conductivity shows a second plateau at frequencies between the microwave and far infrared regions [139]. Fig. 8.11 shows a clear second plateau for quartz after irradiation but at much lower frequencies than those for the exceptional fast ion conductors [70,139]. The second plateau for the fast ion conductors is considered a crucial prediction of a number of models of electrical relaxation (e.g. see refs. [49,139,140,146]). The capacitance of the present samples is less than a few pF for the whole range of frequency and temperature, thus suggesting that electrode processes are not present under the present conditions.

(b) The M" peak in Figs. 8.12, 8.13 and 8.14 is observed at a frequency which is just above the end of the low frequency plateau of d.c. conductivity - this is generally true for common alkali oxide glasses also [1]. However, for the latter case the conductivity shows a strong power law ($s \sim 0.5$), but for quartz the strong power law is not present in the experimental frequency range and appears to have been terminated by the high frequency plateau for the cases of irradiated Q4 and Q2 specimens.

(c) The broadening of the M" peak for quartz after neutron irradiation (Figs. 8.12, 8.13 and 8.14) is on the low frequency side, which is different from the common glasses where the broadening of M" peak is in the high frequency region.

In spite of the differences noted above, the increase in conductivity, σ, with frequency just above the d.c. plateau seems to be qualitatively the same for quartz and

common glasses - the difference being quantitative in that the increase of σ with frequency is slower for quartz which also has a larger value of β. Therefore, it appears reasonable that the electrical relaxation around τ_{dc}, as expressed in the broadening of the M" peak through Kohlrausch parameter $\beta < 1.0$, is a phenomenon basically common to alkali oxide glasses as well as the quartz specimens of this study. In other words, the observed changes in M" peak due to the disorder should be qualitatively valid for assessing the importance of amorphousness for electrical relaxation in oxide glasses.

The small neutron irradiation dose and consequently no change in density for the Q6 specimen is sufficient only, if any, to displace a small number of atoms without significantly affecting the long range order of the crystal [141,142,145]. Neutron irradiation of this specimen increases E_{dc} and decreases β slightly. Such an inverse correlation between E_{dc} and β is opposite to the observations for numerous glasses [64]. A similar inverse correlation between E_{dc} and β was also found for the annealed quartz [46] (see Sec. 8.3.1). It is against the conventional picture that a higher energy barrier for ion diffusion should reduce the correlation of its movement with the surroundings, where a diminished correlation means the atom can jump more independently and therefore relax the field exponentially with $\beta \rightarrow 1.0$. In any case, the increase in E_{dc} and decrease in β due to neutron irradiation of this specimen should be at least partly due to the redistribution of impurities such that the relative concentration of *unassociated* trivalent impurities increases with respect to the sodium concentration [87] (Sec. 8.3.1). Previous investigation of quartz irradiation by x-rays and γ-rays, where photons do not produce atomic defects, also have caused a similarly small increase of E_{dc} [87]. Thus, the change in d.c. conductivity of the

Q6 specimen is too small to clearly demonstrate the importance of the amorphous state to electrical relaxation.

The increase in E_{dc} of the Q4 specimen from 1.30 eV to 2.29 eV due to irradiation is too large to have happened due to the redistribution of impurities [87]. It is due to the structural changes in the sample (the smaller increase in E_{dc} of the Q2 specimen than of the Q4 specimen from 1.33 eV to 1.64 eV may be due to the effect of high temperature annealing during the electrical measurement). The total dose received by the Q4 specimen (1×10^{19} n/cm^2) and consequent change in density is at a stage where the crystal begins to be disordered permanently [145]. The total dose received by the Q2 specimen (1×10^{20} n/cm^2) is at a stage where the change in disorder is nearly complete [145]. Therefore, if disorder in a specimen enhances departure from ideal Debye electrical relaxation, β should decrease (resulting in a broadening M" peak) for these specimens as a result of neutron irradiation. On the other hand, if the amorphous state or disorder of the matrix has no influence on the electrical relaxation process, β should increase according to its generally observed positive correlation with E_{dc}. Unfortunately, because the M" plot for the Q4 and Q2 specimens after irradiation shows a very unusual broadening at low frequencies, we have refrained from obtaining a value for β. Nevertheless, it is clear that the M" peak has become broader as a result of increasing irradiation: the degree of broadening for the M" peak being Q2 > Q4 > Q6 (Fig. 8.15). Such a broadening of the M" peak, or the observation of the second plateau, is an indication of electrical inhomogeneity in the specimen [147]. So the irradiation induced disorder does move the electrical relaxation process farther from the ideal Debye relaxation behavior - in fact it moves to a form which

is too complicated to be described by the Kohlrausch decay function.

8.4 Conclusions

Binary alkali germanate glasses

Unlike for the alkali silicates, β does not decrease rapidly with the addition of the first several mol% of potassium or rubidium oxide. Both the increasing E_{dc} and nominal cation-cation distance tend to enhance β, but a simple relation may not always exist among these parameters. No correlation has been found between β and the "unoccupied volume", the local structure disorder or other structural parameters such as various interatomic distances, and the fraction of NBOs or GeO_6 units. Unlike for d.c. conductivity where E_{dc} is determined predominantly by the strains associated with ion jumps, β is mainly determined by the electrostatic interactions among the mobile ions and with their charge compensation centers.

Mixed mobile ion germanate glasses

The mixed (Rb,Ag) germanate glass series shows the classical mixed mobile ion (MMI) effect in d.c. conductivity and a.c. electrical conductivity relaxation. However, the mixed (Rb,K) germanate glass series shows the MMI effect only in d.c. conductivity. β for this series remains nearly unchanged when Rb and K replace each other. The origin of β is more likely to arise from the dynamics of mobile ion rather than from the static structure of glass. Among the various parameters affecting β, dielectric constant (or Coulomb interactions between mobile ions and their CCCs) appears to best correlate with it when composition is varied for both glass series.

High purity quartz (annealing effect)

β is significantly lower than 1 for high purity quartz with extremely low alkali concentration (~ ppm Na^+), where there should be little mobile ion-ion interaction. However, β increases with high temperature annealing even for the fixed alkali concentration. It shows opposite trend to E_{dc} which decreases with annealing. The model in Fig. 8.9 which explains the above behaviors illustrates the importance of the following factors for determining β: the distribution of ions, and the interaction between mobile cation and its ccc rather than just among the cations. For the understanding of the origin of $\beta < 1$, it is specially important to investigate crystalline solids with low ion concentrations.

High purity quartz (irradiation effect)

The electrical conductivity of a high purity quartz crystal, both before and after neutron irradiation, exhibits a low frequency d.c. plateau and a weakly small frequency dependent conductivity region. After irradiation a second plateau is observed at high frequencies. The irradiation of a specimen by a dose of 1×10^{18} fast n/cm^2 produces too little change in the structure to significantly affect the electrical relaxation in the vicinity of d.c. relaxation time. However, as a result of a 10 to 100 times greater irradiation, (a) the M" peak becomes increasingly more asymmetric (and broader) at low frequencies, and (b) the conductivity approaches a second plateau at high frequencies which does not appear in alkali oxide glasses. Both observations can not be described by the Kohlrausch decay function.

CHAPTER 9 EFFECT OF MELT CONDITIONS ON GLASS STRUCTURE AND IONIC CONDUCTIVITY

In this chapter, we study the effect of melt conditions on glass structure and its relation to d.c. conductivity for sodium triborate glasses. To study the effect of melt conditions, the glasses are prepared at a constant cooling rate. The evolution of the melt structure and its effect on d.c. conductivity of glassy state are discussed.

9.1 Introduction

The purpose of this study is to determine whether the melt temperature (and hence melt structure) has any effect on the structure and, thus, the properties of glass. Traditionally, it was believed that only the thermal treatment in the vicinity of glass transition temperature, T_g, can affect the structure or properties of the glassy state [61,148,149,150]. Treatment much above T_g will be 'washed out' because at such high temperature the structural relaxation rate is much larger than the cooling rate. However, the above picture has been recently challenged by a few observations [151,152,153,154] that different melt temperature, T_ϕ, also affects the final structure and properties of glass. This new picture has raised some questions. For example: could the observed difference in the properties of glasses with varying T_ϕ be due to the difference in cooling rates in the region of T_g. This is very likely to happen considering that heat content of the melt varies with T_ϕ and, therefore, heat flow rate (cooling rate) would also vary with T_ϕ, unless special steps are taken to prevent it (see Fig. 9.1). To study the effect of melt conditions,

we have prepared glasses from the melt at identical cooling rate by keeping the melt at 1400 °C ($T_{\phi 1}$) for 2 h and maintaining it at 850 °C ($T_{\phi 2}$) for varying times before it was casted. Fig. 9.1 shows the schematic diagram of the procedure for glass forming with varying thermal history of the melt but with the identical cooling rate. We have selected a sodium borate composition which shows large fluidity in the molten state, forms glass easily and for which a large amount of reference data is available. A large mole fraction of Na_2O has been chosen to minimize the effect of any inadvertent impurities.

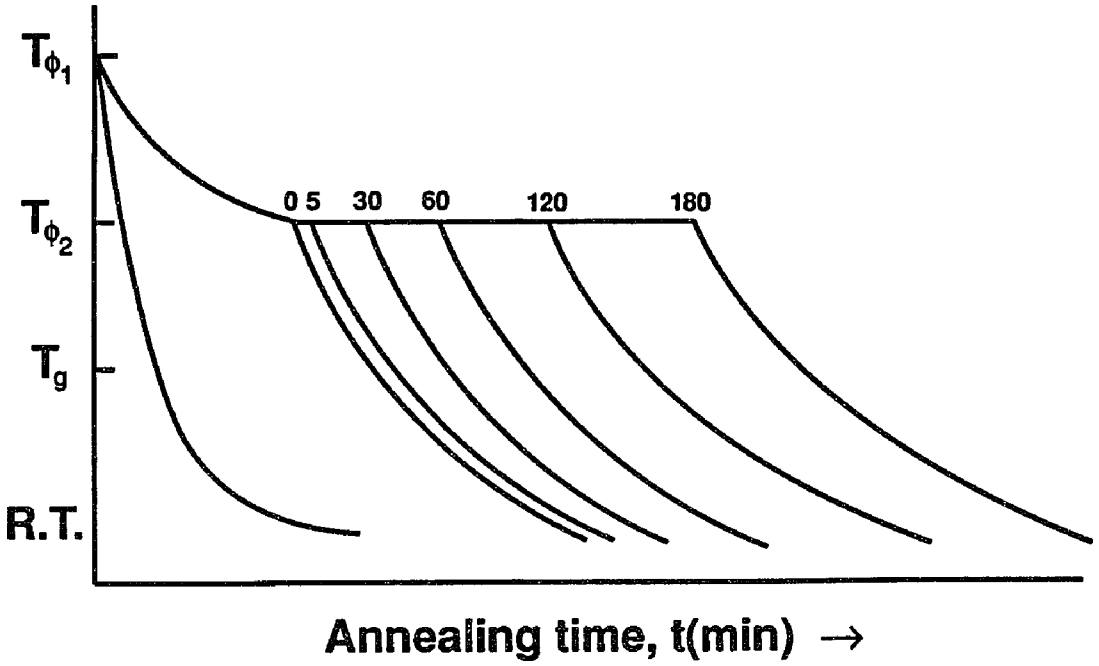

Figure 9.1 Schematic of the procedure for glass forming with varying thermal history of the melt but at the identical cooling rate. The numbers at temperature $T_{\phi 2}$ represent the annealing time before glass forming.

9.2 Experimental Design for Constant Cooling Rate

To determine the effect of melt temperature (and hence structure) on the structure and properties of glass, we investigate glasses prepared with melt temperatures as the only variable parameter; cooling rate in the glass transformation range, composition, etc. must remain constant. Unfortunately it is rather difficult to ensure experimentally that the cooling rate, ξ, is not affected at all by the melt temperature. That is, it is difficult to isolate the effect of $T\phi$ from the effect of ξ on glass structure and properties. To circumvent this problem the following experimental plan was adopted [155]. It is similar to the procedure commonly used in relaxation studies around T_g [156] - for the present we are interested in relaxation in liquid state.

We begin with the following assumption and then attempt to verify it: "The structure of melt varies with temperature and also it affects the structure and properties of glass." Then as we cool a melt from temperature $T\phi_1$ to $T\phi_2$ at time $t = 0$, its structure will change with time, t, to reflect the change of temperature. The important question related to our objective is: what is the time scale for such structural change? Our conventional understanding of structural relaxation in liquid would suggest that this change will be instantaneous on the laboratory time scale (some seconds or longer). In contrast, according to our assumption the change in structure should be sufficiently slow that a memory of melt structure is carried into the glassy state at ambient temperature. Likewise evolution of melt structure determined by $T\phi_1$ to that determined by $T\phi_2$ must also be observable on laboratory time scale. So we test our assumption by monitoring this evolution of melt structure at $T\phi_2$. It is done by characterizing glass samples all of which are prepared by

quenching the melt from $T\phi_2$ but with varying values of t. Since the samples are prepared from the same batch and melt temperature in an identical fashion, they should have the same composition (assuming no preferred evaporation at $T\phi_2$) and thermal history subsequent to quenching (See Fig. 9.1). They will differ only with regard to the extent of melt structure relaxation from that of $T\phi_1$ to that of $T\phi_2$.

If the structure and properties of glasses with varying t are found to be the same, we should conclude that the structure of melt relaxes from that at $T\phi_1$ to that at $T\phi_2$ in a time much shorter than the laboratory time scale. Then it is unlikely that a memory of melt structure can be retained into the glassy state and our initial assumption should be incorrect. On the contrary, a systematic variation in the structure and properties with t will support the assumption.

9.3 Anomalous Expansion of the Glass Melt and Its Effect on Glass Properties

Key Results

The room temperature density (ρ) of the samples from two starting batches is given in Table 5.1, and plotted in Fig. 9.2 as a function of melt annealing time, t, at 850°C. We note that the average density of the present glasses is significantly lower than the values for our batch composition published in literature [157,158,159,160]. It corresponds approximately to the density of sodium triborate composition, which appears to be reasonable assuming the well known preferential loss of soda from the melt at 1400°C.

For electrical conductivity, the values of σ_o and E_{dc} for sodium borate glasses of the two batches are listed in Table 5.1. When electrical measurements were repeated on

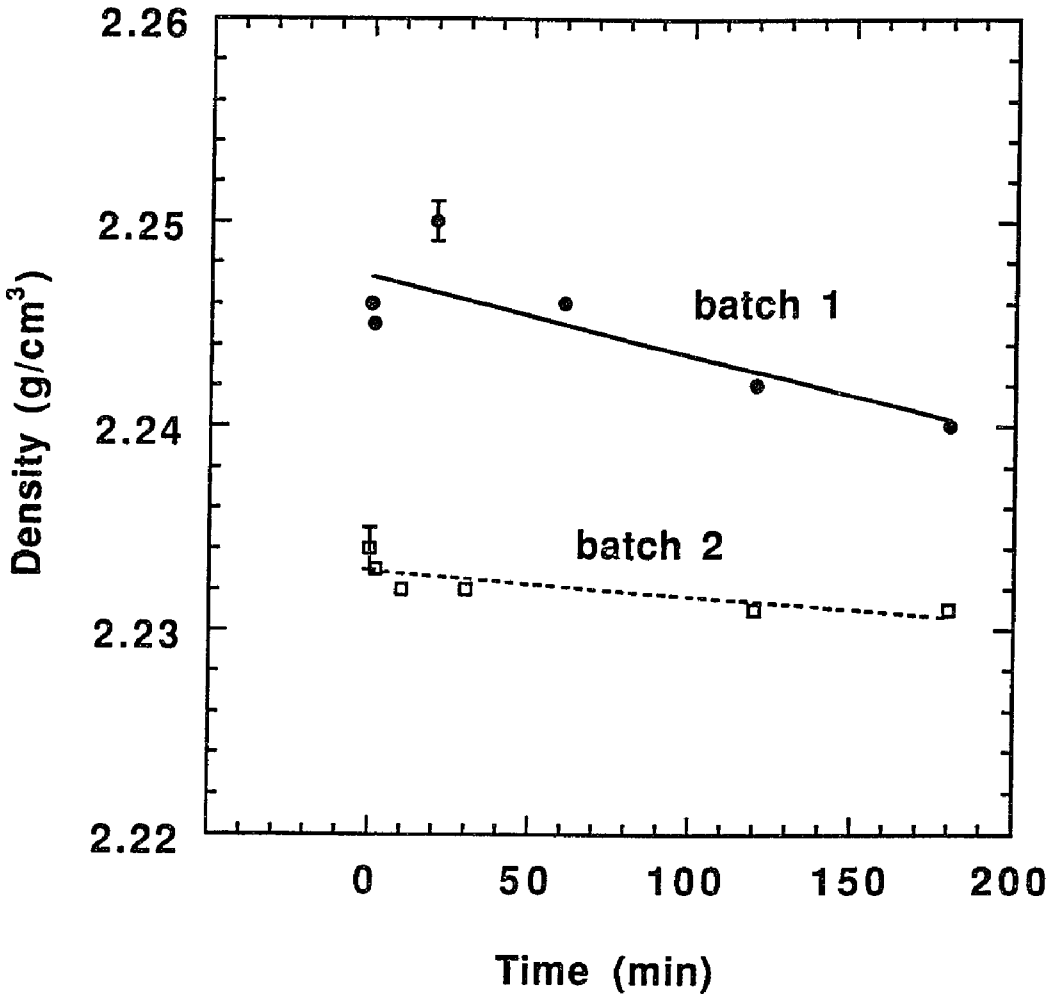

Figure 9.2 Decrease in room temperature density of glass with melt annealing time at 850°C for batch 1 and batch 2 samples.

one sample with new electrodes, the value of E_{dc} was reproduced to be within 0.078 kJ/mol. Note that such small error in E_{dc} has been reported for other glasses as well [121,124]. The dependence of E_{dc} on the melt annealing time at 850°C is shown in Fig. 9.3. It follows from this figure that the melt structure is relaxing on the time scale of annealing.

Fig. 9.4 shows the total integrated infrared absorption in the 0-1600 cm^{-1} region,

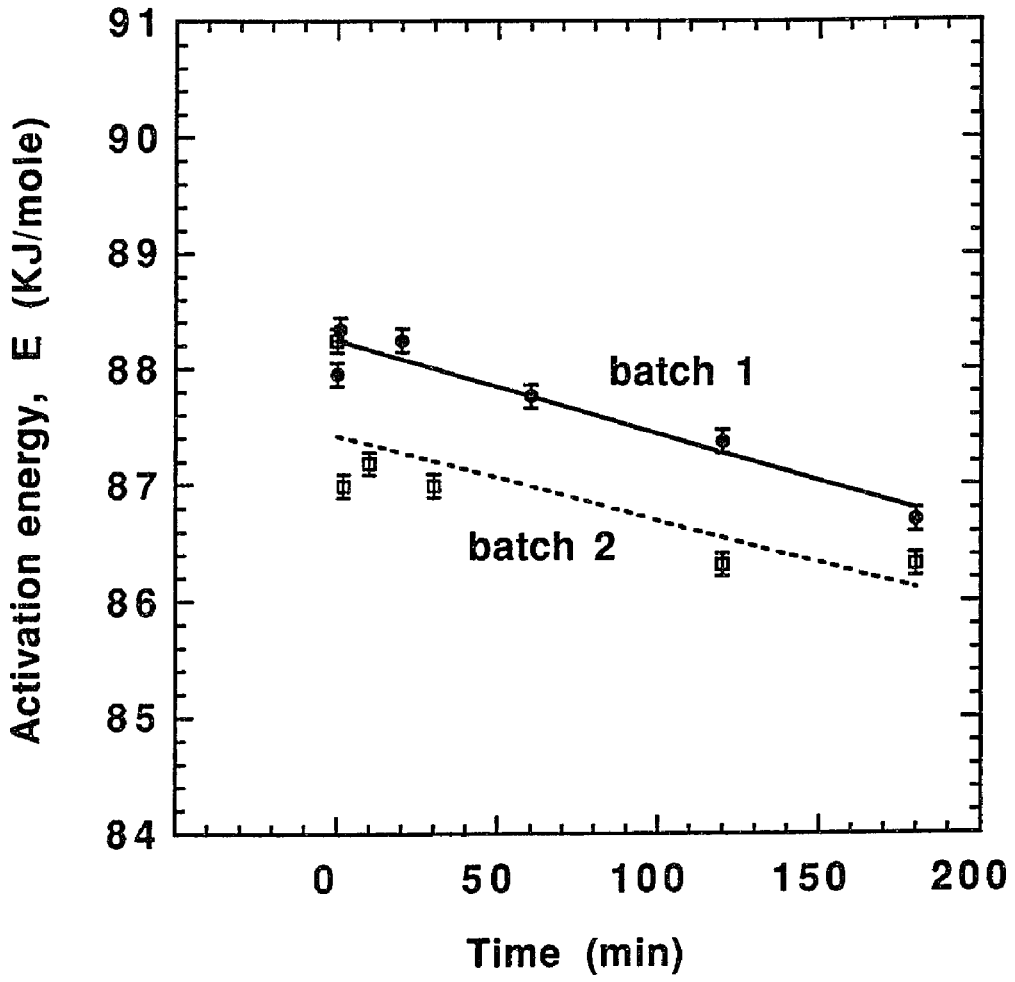

Figure 9.3 Decrease in activation energy, E, for d.c. conductivity with melt annealing time at 850°C for batch 1 and 2 samples.

the average value of the refractive index n (obtained at frequencies 2500, 3300 and 3,900 cm^{-1}), and the ratio A_4/A_3 vs. annealing time (A_4 represents the vibrations of boron-oxygen tetrahedra $B\emptyset_4^-$; and A_3 represents the vibrations of boron-oxygen triangles $B\emptyset_3$ and $B\emptyset_2O^-$) as replotted from Fig. 5.16. The total IR area appears decreasing with annealing time. The same trend is followed by the average value of the refractive index n. Also, A_4/A_3 decreases

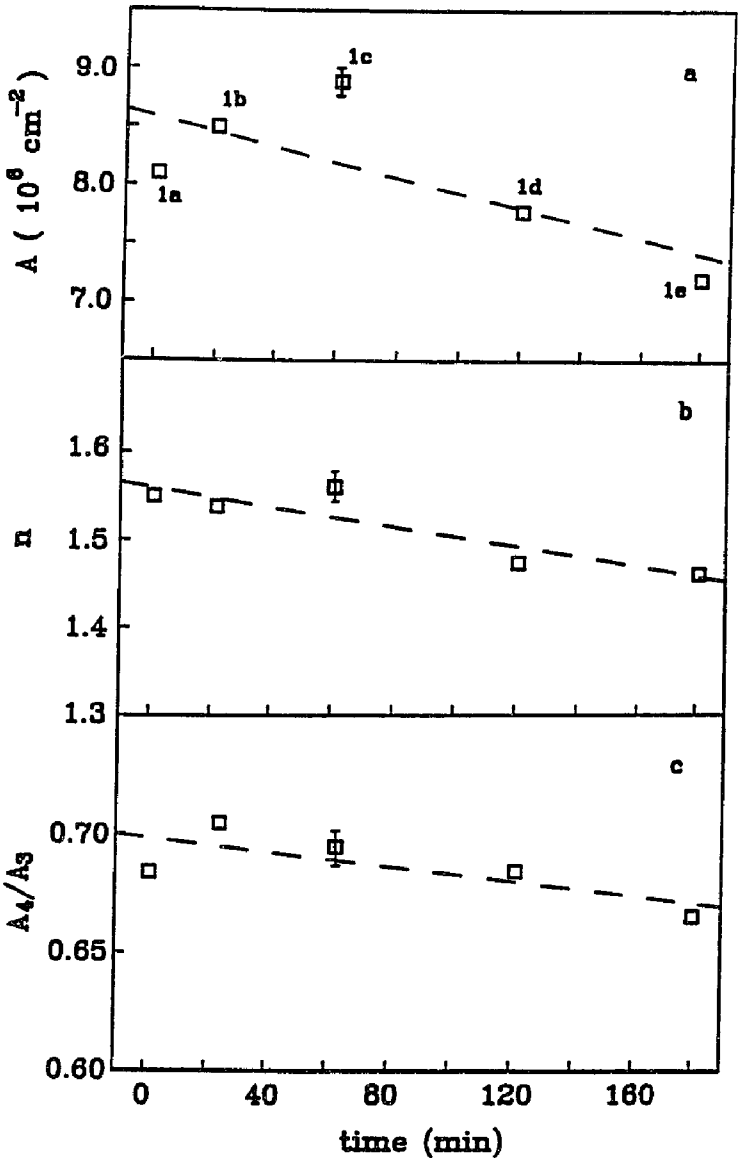

Figure 9.4 (a) Integrated IR absorption in the 0 - 1600 cm^{-1} range, A. (b) Average IR refractive index, n. (c) Relative integrated absorption of B-O tetrahedral, and triangles, A_4/A_3.

with t, suggesting the conversion of boron-oxygen tetrahedra $B\emptyset_4^-$ into boron-oxygen triangles and specifically $B\emptyset_2O^-$. We note that the average value of A_4/A_3 for the present

glasses correspond to the value of sodium-borate glass with ~ 25 mol% Na_2O, i.e. of the triborate composition [108]. This is in agreement with the density data presented above.

Discussion

The average relaxation time, which describes structural changes in a liquid or glass is given by [161]

$$\tau_S = \frac{N_S}{G_\infty} \tag{9.1}$$

where N_S is shear viscosity and G_∞ is the infinite frequency or "solid like" shear modulus. We have not measured N_S or G_∞ for our melts but we can obtain an order of magnitude estimate of τ_S using $N_S \approx 27$ poise at 850°C from [162] and $G_\infty \sim 10^{10}$ dynes\cm^2 which does not vary drastically with composition [163]. Thus $\tau_S \sim 2.7 \times 10^{-9}$ sec. That is, as our melt is cooled from 1400°C to 850°C, it will take only ~ 10^{-9} second to reach equilibrium structure of 850°C. Arguments may be given that N_S is not the appropriate viscosity for describing structural relaxation but the corrections can not change τ_S by more than one or two orders of magnitude [164]. In short, the structure of melt should reach equilibrium almost instantaneously at 850°C and, therefore, the structure and properties of the samples within either batch must be identical. This statement is equivalent to saying that a glass can have no memory of melt structure. The structure of supercooled liquid becomes important only around T_g where τ_S ~ seconds. Note that the present melt temperatures are much above the liquidus temperature which should be ~ 777°C for our glass composition [165]. T_g for sodium triborate glass is around 477 °C [166]. The present results described

in the previous sub-section seem to contradict our above understanding of structural relaxation in liquids. Before we conclude that we have observed the effects of some unusually slow relaxation or transformation in the liquid state, let us ensure that our observations are beyond experimental error and uncertainty. The following arguments show that indeed our conclusion and the initial assumption given above are correct.

(a) The activation energy of electrical conductivity, E, clearly shows a decreasing trend with increasing annealing of the melt at 850°C (Fig. 9.3). We have chosen to focus on E rather than conductivity itself because the former excludes any errors arising from the measurements of sample and electrode dimensions. When we repeated the conductivity measurement of a sample after repolishing and applying new electrodes, E was determined to be identical within 0.1 kJ/mol. Since the conductivity of all the samples was measured in an identical fashion, the uncertainty in E from electrical measurements is determined to be less than $\pm$ 0.1 kJ/mol. The decreasing trend of E with increasing t is well beyond this uncertainty.

(b) The trend of E vs. t in Fig. 9.3 correlates directly with the variation of density vs. t in Fig. 9.2, total IR integrated absorption in Fig. 9.4(a), and average IR refractive index in Fig. 9.4(b). Such consistent correlations prove that the observed trends in various properties are beyond the error in anyone of the measurements.

(c) Perhaps the greatest uncertainty and source of error in the present work remain in the sample preparation itself. In this regard, we note that the average trend of E vs t for batch 1 is reproduced by the data for batch 2. Therefore, the trend is not due to some random error in sample preparation. Because of uncertainty in determining t = 0 (when

the melt has just reached 850°C) as well as temperature gradients within the melt, the scatter of various data is relatively large for t < 5 minutes. If we allow for this source of scatter, the observed trends of properties become even more convincing.

The fact that E for batch 2 is systematically lower than for batch 1 reflects the fact that it is almost impossible to replicate glass composition exactly. The difference in E is, in fact, very small (<1 kJ/mole), which could be due to a number of reasons including the difference in starting batch composition, etc. For the purpose of present discussion it is important that both the batches show nearly parallel trends; the systematic difference between E of the two batches is of little significance.

(d) What about any systematic errors in sample preparation which can lead to the observed trends of properties as a function of t? Based on our knowledge of borate glass preparation, change in composition due to selective evaporation of constituents at 850°C appears to be the only possibility for introducing systematic error. Actually 850°C is too low a temperature for any such evaporation but for the sake of argument let us consider its consequences. We have found the actual Na_2O content of the glass to be significantly lower than the starting batch composition which should have occurred when the melt was held at 1400°C for two hours. Therefore, if there is any selective evaporation at 850°C, it is likely to be of Na_2O. Then at the composition of the present glass a decreasing Na_2O content with t should be manifested as an increasing E with t [167]. However, the observed variation of E vs. t in Fig. 9.3 is just the opposite and, therefore, we conclude that it can not be due to systematic error from the loss of Na_2O.

(e) Next, let us consider the unlikely possibility of selective evaporation of B_2O_3

at 850°C. This will explain the observed trend of E vs t. However, the work of Karki et al. [160] predicts that with decreasing mol% of B_2O_3 the density of Na_2O-B_2O_3 system should increase, which is the opposite of the density trend shown in Fig. 9.2.

(f) Finally, we consider the unlikely variation of the amount of H_2O and CO_2 content during annealing at 850°C, which could affect our glass structure and properties. Hydration of Sodium-borate glasses and compounds is manifested by the appearance of a broad infrared envelope centered at ca. 3450 cm^{-1} and a sharper feature at ca. 1640 cm^{-1}, due to -OH groups [168,169]. The infrared spectra of our polished specimens show practically negligible absorption at these frequencies, which has any correlation with the annealing time. This suggests that under the preparation conditions employed in our work an influence of hydration can not explain the trend of Figs. 9.2 and 9.3. This is also consistent with the high stability regarding water of sodium triborate composition, which approaches the maximum value of N_4, i.e. the fraction of four-coordinated boron atoms [170].

Previous studies by Martin et al. [171] and Karki et al. [160] have shown that CO_2 is retained in high Na borate glasses (Na_2O content greater than 65 mole%), when they are prepared from Na_2CO_3 compound. In such cases, it was shown that carbonate species (CO_3^{2-}) are present and easily detectable by their sharp bands at 1062 cm^{-1} (Raman) and 880 cm^{-1} (infrared) [172]. The sodium triborate compositions investigated here give no spectroscopic evidence for the presence of CO_2 in these glasses.

Thus, we can safely conclude that the observed trends of E, ρ, and IR absorption vs. t of our glasses are real and beyond any experimental error (Figs. 9.2, 9.3 and 9.4).

Having concluded that after cooling from 1400°C to 850°C the properties and structure of sodium triborate melt continue to change on the laboratory scale, it is natural to ask the origin of such extremely slow changes. In this connection we again emphasize excellent correlation among our different observations. That is, decreasing E with t results simply from the decreasing density of the glass. As the structure becomes less dense, it becomes easier for a sodium ion to make the diffusive jump and E decreases. In parallel, the bulk properties like refractive index (IR) and integrated IR absorption which depend on density show a corresponding decrease with increasing t. Therefore, one expects a common explanation for our various observations.

We noted above that the average viscosity relaxation time is several orders of magnitude shorter than t in the present study. However, the relaxation time is believed to have a broad distribution in glasses [173] and it is possible that we are observing the long "tail" of a distribution function. A characteristic of such structural relaxation, which is commonly observed around the glass transformation range, is that the structure approaches equilibrium volume or density with time. For sodium triborate melt the equilibrium density increases with decreasing temperature in a classical manner [159,174]. That is, as we cool the melt from 1400°C to 850°C and maintain there, the density at 850°C must vary from ρ(1400°C) to a higher ρ(850°C), however slowly. For the same reasons, the glasses prepared from 850°C should show a decreasing conductivity or increasing E, as reported previously for other systems by several groups [148,149,150]. The trend of present results showing volume expansion with annealing time is just the opposite and, therefore, should be considered anomalous.

The present observation of expansion of sodium triborate melt is unusual because the equilibrium density shows normal temperature dependence, yet anomalous behavior is shown by the transient relaxation. We can understand it better with the help of schematic

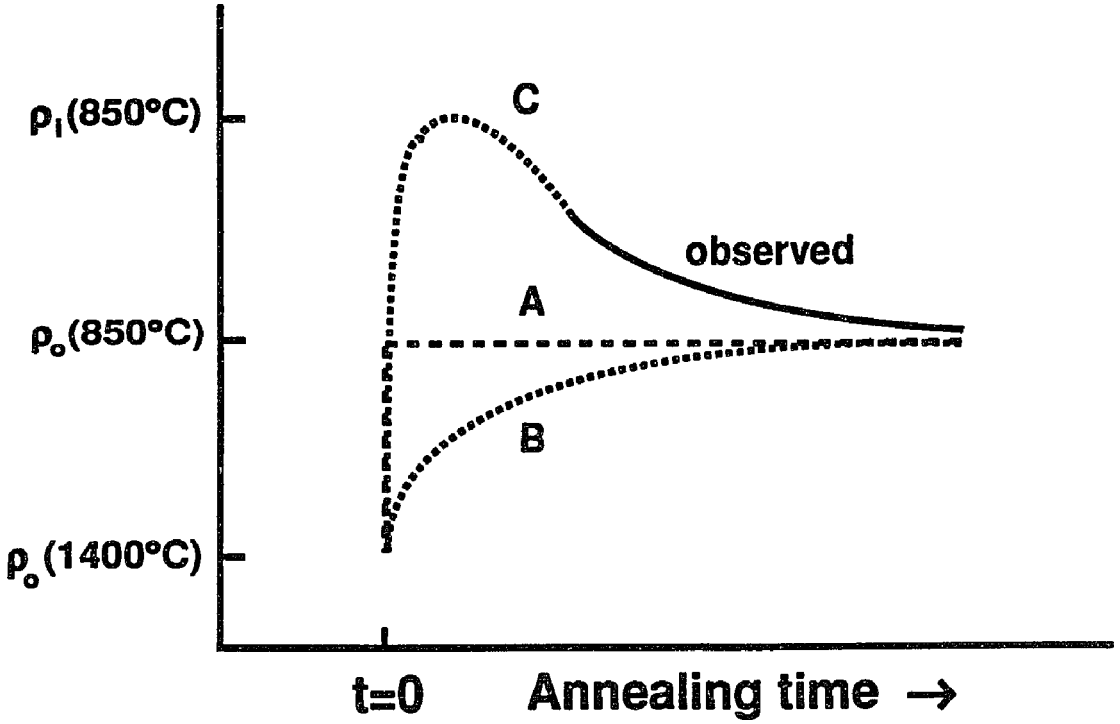

Figure 9.5 Schematic variation of density with annealing time for various possibilities. (A) Normal relaxation process (B) Extremely slow relaxation with normal density (C) Extremely slow relaxation with anomalous density.

Figure 9.5 (not to the scale). If the sodium triborate melt behaved in a normal fashion, its density will increase from ρ_o (1400°C) to ρ_o (850°C) almost instantaneously on the time scale of the present experiments following dotted curve A (subscript o on ρ refers to equilibrium conditions). If it showed only unusually slow relaxation, the density will vary as shown by the broken curve B. The experimentally observed variation of ρ with t resembles the solid curve which is qualitatively different from curve A or B, thus showing an anomalous and unusually slow relaxation. We infer that the solid curve is a part of the more complete curve C. As soon as the melt temperature is reduced from 1400°C to 850°C, instantaneously the amplitude of atomic vibrations decreases and interatomic distances shrink according to the shape of the potential wells of the atoms. This represents normal contraction of the melt giving instantaneously density ρ_i (850°C) before any structural changes can occur in the glass structure. As time passes at 850°C, the structure starts rearranging, a component of which is slow enough to be observable in the present experiments (solid part of curve C).

As far as extremely slow nature of relaxation at 850°C and its manifestation in glass properties is concerned, we recall observations of similar nature in GeO_2 for which the melt temperature has been shown to affect physical properties in the glassy state [151,152,153]. It is not clear how accurately the cooling rate was kept constant in these studies. Nonetheless, the observation of varying absorptivity (λ = 245 nm) along the thickness of a sample [152,153] which was prepared from melt initially kept at 1550°C and then annealed at 1350°C for 185 hours, must be due to a very slow change in the melt. This slow change has been attributed to an oxygen related defect whose concentration at

a given pressure depends on temperature. The equilibration of defect concentration requires diffusion of oxygen which is relatively very slow compared to normal structural relaxation. At present, we do not have evidence to believe that a similar diffusion process is responsible for the slow nature of expansion of sodium triborate melt but it is an attractive possibility which needs to be investigated.

As far as the anomalous expansion of the sodium triborate melt is concerned, we note that the similar behavior in liquid H_2O, SiO_2, etc. has been attributed to their tendency for forming an expanded tetrahedral network structure with decreasing temperature [175]. A tendency of structural transformation involving ligand exchange in the liquid state has also been suggested for $CrCl_3$ aqueous solution [176]. The existence of BO_4 tetrahedra and BO_3 triangles in sodium borate melt at high temperature has been inferred by Riebling [177] from density measurements. With this in mind, we carefully analyzed the part of IR spectrum which characterizes the network structure, in particular the tetrahedrally and triangularly coordinated boron units viz. $B\emptyset_4^-$ and $B\emptyset_2O^-/B\emptyset_3$ units. The relative IR peak area corresponding to these units, A_4/A_3, is shown in Figure 9.4(c). Because error from some sources like sample surface condition is eliminated when taking the ratio A_4/A_3, the data in Fig. 9.4(c) should be more accurate than in Fig. 9.4(a). Interestingly, A_4/A_3 also changes with t suggesting that structure of melt at 850°C changes on the laboratory time scale. Specifically, $B\emptyset_4^-$ units are slowly converted into $B\emptyset_2O^-$ units with increasing t. The isomerization process $B\emptyset_4^- \rightleftharpoons B\emptyset_2O^-$ has been shown to be of special importance in borate glass of relatively low alkali content [107]. It is quite remarkable that Karki et al. [160] have concluded that $B\emptyset_2O^-$ units occupy 1.70 times more volume than the $B\emptyset_4^-$ units in

sodium borate glass system. That is, the observed anomalous expansion in our glass can be traced to the conversion of $B\emptyset_4^-$ to $B\emptyset_2O^-$ units. This mechanism is slightly different from that proposed for SiO_2 or H_2O, but essentially the origin of anomalous expansion remains in structural rearrangement in either case.

In the end we wish to remark that the cooling time to reach glassy state from melt in laboratory is likely to be less than some minutes. Therefore, the effect of melt temperature on the properties of glass should be stronger in normally prepared glass than demonstrated by the present data. An advantage of the present scheme of experiment, however, remains that it eliminates the effects arising from the variation of cooling rate.

9.4 Conclusions

We employed a special scheme of heat treating the sodium triborate melt for investigating the influence of melt structure on the properties of glass. It allowed the preparation of glasses with identical cooling rate but differing in the starting melt structure. The results indicate the presence of extremely slowly occurring changes in the melt at 850°C by comparison with viscosity relaxation time, which affect activation energy for electrical conductivity, density, and IR reflectance/absorption in the glassy state below T_g.

An anomalous expansion of the melt at 850°C occurs with time after it is cooled from 1400°C. Accordingly, the activation energy for conductivity, density, and total IR absorption of glass at ambient decrease with time for which the melt is kept at 850°C. A detailed analysis of IR spectrum suggests that this anomalous trend in properties with time is due to the very slow transformation of more compact tetrahedrally coordinated

boron units to less compact triangularly coordinated boron units.

CHAPTER 10 CONCLUSIONS

The ion conduction (d.c. conductivity and electrical relaxation) has been analyzed in terms of the structure for four oxide glass systems: (1) binary alkali germanate glasses, (2) mixed mobile ion germanate glasses, (3) high purity quartz and (4) sodium triborate glasses.

It is found that besides tetrahedral GeO_4 units, both NBOs and GeO_6 structural units exist in germanate glasses. Molar volume and excess volume vary with composition without affecting various interatomic distances, suggesting that there exists an 'unoccupied volume' in the structure which is not directly determined by the local structure. The presence of the 'unoccupied volume' indicates the existence of atomic scale inhomogeneity in the structure which arises from a locally non-uniform spatial distribution of ions. The structural disorder around alkali ions in germanate glasses is much larger than that around alkali ions in silicates, suggesting that if at all the MRN model is less appropriate for the germanate than for the silicate glasses.

For the (Rb,Ag) mixed mobile ion germanate glasses, the presence of Ag seems to have little effect on the local structure around Rb and Ge atoms. Replacement of Rb by Ag in mixed mobile ion glasses has the same effect on the Rb-O distance and disorder around Rb as the reduction of the Rb content in binary Rb germanate glasses. This negligible effect of Ag on glass structure is consistent with the high deformability of Ag atoms. For the (Rb,K) mixed mobile ion germanate glasses, replacement of Rb by K does not seem to affect the respective local environments around the Rb, K and Ge atoms. In

both series, the monotonic change in molar volume or excess volume with composition does not appreciably affect the various interatomic distances, supporting that the 'unoccupied volume' in the glass structure is not directly determined by the local structure.

Unlike for the binary alkali silicate glasses where the activation energy for d.c. conductivity decreases monotonically with alkali concentration, the activation energy for the binary alkali germanate glasses shows complex variation with a small maximum at ~ 10 mol% alkali oxide concentration. This complex variation of activation energy correlates well with that of molar volume or excess volume but not with that of the various interatomic distances or disorder. This suggests that the 'unoccupied volume' which can be conceived as the pathway for long range ion movement is the most important factor for determining the d.c. conductivity in germanate glasses. The cooperative ion movement model recently proposed for silicate glasses is not suitable for describing ion conduction in germanates, presumably because the strain energy, which is particularly important in germanate glasses, is excluded in the current version of this model. The d.c. conductivity of the (Rb,Ag) and (Rb,K) germanate glasses shows classical mixed mobile ion effect. The various interatomic distances and structural disorder, which show little variation, do not seem to be the key for the development of MMI effect. The effect is more likely to arise from the dynamics of atoms rather than from the details of static glass structure.

The melt conditions are observed to affect the structure and properties of sodium triborate glass. An anomalous expansion of the glass melt at 850 °C occurs with annealing time after it is cooled from 1400 °C. The activation energy for d.c. conductivity, density and IR absorptivity of the glass decrease with annealing time of the melt at above the

equilibrium melting temperature due to the anomalous expansion of the melt. The origin of this expansion is in the transformation of tetrahedrally coordinated boron to less compact triangularly coordinated boron structural units.

The decreasing E_{dc} and nominal cation-cation distance tend to enhance non-ideality of electrical relaxation, but a simple relation does not always exist among these parameters. No one-to-one correlation has been found between Kohlrausch parameter β and the 'unoccupied volume', the local structure or the inherent disorder in glass. Unlike for d.c. conductivity of the present germanate glasses where E_{dc} is determined predominantly by the strains associated with ion jumps, β is mainly determined by the electrostatic force among the mobile ions and with their charge compensation centers. The structure based model which illustrates the importance of the distribution of ions and the interaction between a mobile cation and its charge compensating center describes well the electrical relaxation behaviors for both the germanate glasses and quartz crystal.

Neutron irradiation with a dose of greater than 1×10^{19} fast n/cm^2 produces structural disorder in quartz. As a result, (a) the M'' peak becomes considerably more asymmetric (and broader) at low frequencies, being broader with greater irradiation dose, and (b) the conductivity approaches a second plateau at high frequencies which does not appear in alkali oxide glasses. Both observations cannot be described by the Kohlrausch decay function.

REFERENCES

[1] M.D. Ingram, "Ionic conductivity in glass", *Phys. Chem. Glasses* **28(6)** (1987) 215.

[2] K. Itoh, K. Miura and I. Masuda, "Low-loss fluorozirco-aluminate glass fiber", *J. Non-Cryst. Solids* **167(1/2)** (1994) 112.

[3] G. Partridge, "Glass-ceramics with unusual electrical properties", *Adv. Mat.* **4(10)** (1992) 668.

[4] K. Keller, J. Antonenko and K.H. Weber, "High-temperature insulations", *Esa Bull.* **80** (1994) 50.

[5] B. Pang and K.E. Windom, "Nuclear waste into glass: viscosities of molten analogs of radioactive waste disposal media", *J. Iowa Acad. Sci.* **101(2)** (1994) 49.

[6] K.S. Matlack and T. Labuda, "Fluorine analysis of nuclear waste glasses", *J. Chem. Tech. Biotech.* **62** (1995) 91.

[7] F.A. Fusco and H.L. Tuller, "Fast ion transport in glasses", in Superionic Solids and Solid Electrolytes, Recent Trends: eds. A.L. Laskav and S. Chandra, Academic Press, Inc., (1989), pp. 43-110.

[8] P. Huang and E.A. Secco, "Fast Na^+ ionic conductivity in glass and crystalline solids of Na_2MoO_4-UO_2SO_4 system", *Solid St. Ionics* **72** (1994) 289.

[9] I. Svare, F. Borsa, D.R. Torgeson, S.W. Martin and H. Patel, "Use of the modulus formalism in the analysis of ac conductivity data for fast ion conductors", *J. Non-Cryst. Solids* **185(3)** (1995) 297.

[10] B. Vaidhyanathan, K.J. Rao and S. Asokan, "Electrical switching in AgI based fast ion conducting glasses: possibility for newer applications", *J. Appl. Phys.* **78(2)** (1995) 1358.

[11] T. Takahashi, "Recent trends in high conductivity solid electrolytes and their applications: an overview", in Superionic Solids and Solid Electrolytes, Recent Trends: eds. A.L. Laskav and S. Chandra, Academic Press, Inc., (1989), pp. 1-41.

[12] M.S. Meikhail, I.A. Gohar and A.A. Megahed, "Lithium borosilicate glasses as electrolyte for solid state batteries", *J. Phys. d. Appl. Phys.* **26(7)** (1993) 1125.

[13] I. Bloom and M.C. Hash, "Ceramic/glass electrolytes for sodium-ion-condcuting applications", *J. Electrochem. Soc.* **139(4)** (1992) 1115.

[14] A.C. Khandkar and A.V. Joshi, "Solid electrolytes: emerging applications and technologies", *Electrochem. Soc. Interface* **2(2)** (1993) 26.

[15] H. Jain, "Dynamics of ions in oxide glasses", *Rev. Solid St. Sci.* **3(3-4)** (1989) 223.

[16] W.C. Huang and H. Jain, "Correlation between local structure and electrical response of Rb and (Rb,Ag) germanate glasses: dc conductivity", *J. Non-Cryst. Solids* **188** (1995) 254.

[17] M.B. Salamon, Physics of Superionic Conductors, Springer-Verlar, 1979.

[18] S. Chandra, Superionic Solids: Principles and Application, North-Holland, 1981.

[19] G.N. Greaves, A. Fontaine, P. Logarde, D. Raoux and S.J. Gurman, "Local structure of silicate glasses", *Nature* **293** (1981) 611.

[20] G.N. Greaves, "EXAFS and the structure of glass", *J. Non-Cryst. Solids* **71** (1985) 203.

[21] G.S. Henderson, "A Si K-edge EXAFS/XANES study of sodium silicate glasses", *J. Non-Cryst. Soli*ds **183** (1995) 43.

[22] E.I. Kamitsos, "Infrared reflectance studies of ionic conductive glasses: network structures and cation dynamics", *Journal de Physique iv, colloque* **2(2)** (1992) C2-87.

[23] E.I. Kamitsos, J.A. Kapoutsis and H. Jain, "Vibrational study of the role of trivalent ions in sodium trisilicate glass", *J. Non-Cryst. Solids* **171** (1994) 31.

[24] D.S. Goldman, "Evaluation of the ratios of bridging to nonbridging oxygens in simple silicate glasses by electron spectroscopy for chemical analysis", *Phys. Chem. Glasses* **27(3)** (1986) 128.

[25] C.H. Hsieh, H. Jain, A.C. Miller and E.I. Kamitsos, "X-ray photoelectron spectroscopy of Al- and B-substituted sodium trisilicate glasses", *J. Non-Cryst. Solids* **168** (1994) 247.

[26] W.D. Kingery, H.K. Bowen and D.R. Uhlmann, in Introduction to Ceramics, 2nd ed., John Wiley & Sons, Inc., New York, (1976), ch. 17.

[27] L.L. Hench and J.K. West, in Principles of Electronic Ceramics, John Wiley & Sons, NY, (1990), ch. 4.

[28] D.P. Almond, A.R. West and R.J. Grant, "Temperature dependence of the a.c. conductivity of Na β-Alumina", *Solid St. Communications* **44** (1982) 1277.

[29] D.P. Almond, G.K. Duncan and A.R. West, "The determination of hopping rates and carrier concentrations in ionic conductors by a new analysis of ac conductivity", *Solid St. Ionics* **8** (1983) 159.

[30] S.R. Elliott, in Physics of Amorphous Materials, 2nd ed., Longman Sci. & Tech, co-published with John Wiley & Sons, Inc., New York, (1990), ch. 4.

[31] O.L. Anderson and D.A. Stuart, "Calculation of activation energy of ionic conductivity in silica glasses by classical methods", *J. Am. Ceram. Soc.* **37** (1954) 573.

[32] D. Ravaine and J.L. Souquet, "A thermodynamic approach to ionic conductivity in oxide glasses. Part 1. Correlation of the ionic conductivity with the chemical potential of alkali oxide in oxide glasses", *Phys. Chem. Glasses* **18(2)** (1977) 27.

[33] D. Ravaine and J.L. Souquet, "A thermodynamic approach to ionic conductivity in oxide glasses. Part 2. A statistical model for the variations of the chemical potential of the constituents in binary alkali oxide glasses", *Phys. Chem. Glasses* **19(5)** (1978) 115.

[34] A.B. Lidiard, in: Handbuch der Physik, vol. 20, ed. S. Flugge, Springer, Berlin, (1957), p. 246.

[35] Y. Haven and B. Verkerk, "Diffusion and electrical conductivity of sodium ions in sodium silicate glasses", *Phys. Chem. Glasses* **6(2)** (1965) 38.

[36] G.N. Greaves and K.L. Ngai, "Ionic transport properties in oxide glasses derived from atomic structure", *J. Non-Cryst. Solids* **172-174** (1994) 1378.

[37] G.N. Greaves and K.L. Ngai, "Modelling ionic transport from the structure of silicate glasses", in Defects in Insulating Materials, eds. O. Kanert and J.-M. Spaeth, World Scientific, Singapore, (1993), p. 53.

[38] J.O. Isard, M. Jagla and K.K. Mallick, "Simple models for the ionic conduction mechanism in glasses", *J. Physique* **43** (1982) C9-387.

[39] S.W. Martin and C.A. Angell, "Dc and ac conductivity in wide composition range Li_2O-P_2O_5 glasses", *J. Non-Cryst. Solids* **83** (1986) 185.

[40] C.H. Hsieh and H. Jain, "Influence of network forming cations on ionic conduction in sodium silicate glasses", *J. Non-Cryst. Solids* **183** (1995) 1.

[41] J.O. Isard, "The mixed alkali effect in glass", *J. Non-Cryst. Solids* **1** (1969) 235.

[42] D.E. Day, "Mixed alkali glasses-their properties and uses", *J. Non-Cryst. Solids* **21** (1976) 343.

[43] H. Jain, N.L. Peterson and H.L. Downing, "Tracer diffusion and electrical conductivity in sodium-cesium silicate glasses", *J. Non-Cryst. Solids* **55** (1983) 283.

[44] P.B. Macedo, C.T. Moynihan and R. Bose, "The role of ionic diffusion in polarisation in vitreous ionic conductors", *Phys. Chem. Glasses* **13(6)** (1972) 171.

[45] C.T. Moynihan, L.P. Boesch and N.L. Laberge, "Decay function for the electric field relaxation in vitreous ionic conductors", *Phys. Chem. Glasses* **14(6)** (1973) 122.

[46] H. Jain and W.C. Huang, "Importance of structure in electrical conductivity relaxation", *J. Non-Cryst. Solids* **172-174** (1994) 1334.

[47] H. Jain and O. Kanert, "Ionic motion in inorganic glasses", in Defects in Insulating Materials, eds. O. Kanert and J.-M. Spaeth, World Scientific, (1993), p. 274.

[48] H. Jain, "Ion movement relaxation in inorganic glasses-salient features", *J. Non-Cryst. Solids* **131-133** (1991) 961.

[49] K.L. Ngai, "Universality of low-frequency fluctuation, dissipation and relaxation properties of condensed matter, I", *Comments Solid St. Phys.* **9** (1979) 127; "Universality of low-frequency fluctuation, dissipation and relaxation properties of condensed matter, II", *Comments Solid St. Phys.* **9** (1980) 141.

[50] K.L. Ngai, R.W. Rendell and H. Jain, "Anomalous isotope-mass effect in lithium borate glasses: comparison with a unified relaxation model", *Phys. Rev. B* **30(4)** (1984) 2133.

[51] R. Kohlrausch, *Pogg. Ann.* **12(3)** (1847) 393.

[52] G. Williams and D.C. Watts, "Non-symmetrical dielectric relaxation behavior arising from a simple empirical decay function", *Trans. Faraday Soc.* **66** (1970) 80.

[53] G. Balzer-Jöllenbeck, O. Kanert, H. Jain and K.L. Ngai, "New interpretation of activation enthalpies for electrical conductivity and nuclear spin relaxation in glassy ionic conductors", *Phys. Rev. B* **39(9)** (1989) 6071.

[54] I.M. Hodge, M.D. Ingram and A.R. West, "Impedance and modulus spectroscopy of polycrystalline solid electrolytes", *J. Electroanal. Chem.* **74** (1976) 125.

[55] A.K. Jonscher, "Review article: the 'universal' dielectric response", *Nature* **267** (1977) 673.

[56] X. Lu, H. Jain, O. Kanert, R. Küchler and J. Dieckhöfer, "Low-temperature dynamics of inorganic glasses-electrical conductivity against nuclear spin relaxation", *Philo. Mag. B* **70** (1994) 1045.

[57] J.C. Dyre, "Some remarks on ac conduction in disordered solids", *J. Non-Cryst. Solids* **135** (1991) 219.

[58] S.R. Elliott, "Use of the modulus formalism in the analysis of ac conductivity data for ionic glasses", *J. Non-Cryst. Solids* **170** (1994) 97.

[59] A.S. Nowick, B.S. Lim and A.V. Vaysleyb, "Nature of the ac conductivity of ionically conducting crystals and glasses", *J. Non-Cryst. Solids* **172-174** (1994) 1243.

[60] H. Jain and C.H. Hsieh, "'Window' effect in the analysis of frequency dependence of ionic conductivity", *J. Non-Cryst. Solids* **172-174** (1994) 1408.

[61] L.P. Boesch and C.T. Moynihan, "Effect of thermal history and electrical relaxation in alkali silicate glasses", *J. Non-Cryst. Solids* **17** (1975) 44.

[62] P. Abelard and J.F. Baumard, "Dielectric relaxation in alkali silicate glasses: a new interpretation", *Solids St. Ionics* **14** (1984) 81.

[63] K.L. Ngai and R.W. Rendell, "Explanation of mechanical and electrical relaxation due to mobile ions in a superionic glass over the range 1 Hz - 20 GHz by the coupling theory", *Phys. Rev. B* **38(14)** (1988) 9987.

[64] K.L. Ngai, J.N. Mundy, H. Jain, O. Kanert and G. Balzer-Jollenbeck, "Correlation between the activation enthalpy and Kohlrausch exponent for ionic conductivity in alkali aluminogermanate glasses", *Phys. Rev. B* **39(9)** (1989) 6169.

[65] U. Strom, K.L. Ngai and O. Kanert, "Nature of the linear frequency-dependent ac conductivity in glassy ionic conductors", *J. Non-Cryst. Solids* **131-133** (1991) 1011.

[66] S.R. Elliott and A.P. Owens, "The diffusion-controlled relaxation model for ionic transport in glasses", *Philo. Mag. B* **60(6)** (1989) 777.

[67] S.R. Elliott and A.P. Owens, "Non-exponential relaxation in ionically conducting glasses: the diffusion-controlled relaxation model", *J. Non-Cryst. Solids* **131-133** (1991) 1036.

[68] K. Funke, "Is there a 'universal' explanation for the 'universal' dynamic response?", *Ber. Bunsenges. Phys. Chem.* **95** (1991) 955.

[69] K. Funke, "Jump relaxation model and coupling model - a comparison", *J. Non-Cryst. Solids* **172-174** (1994) 1215.

[70] H.K. Patel and S.W. Martin, "Fast ionic conduction in $Na_2S + B_2S_3$ glasses: compositional contributions to nonexponentiality in conductivity relaxation in the extreme low-alkali-metal limit", *Phys. Rev. B* **45(18)** (1992) 10292.

[71] W.H. Zachariasen, "The atomic arrangement in glass", *J. Am. Chem. Soc.* **54** (1932) 3841.

[72] C. Huang and A.N. Cormack, "The structure of sodium silicate glass", *J. Chem. Phys.* **93(11)** (1990) 8180.

[73] B. Vessal, G.N. Greaves, P.T. Marten, A.V. Chadwick, R. Mole and S. Houde-Walter, "Cation microsegregation and ionic mobility in mixed alkali glasses", *Nature* **356** (1992) 504.

[74] G.N. Greaves, S.J. Gurman, C.R.A. Catlow, A.V. Chadwick, S. Houde-Walter, C.M.B. Henderson and B.R. Dobson, "A structural basis for ionic diffusion in oxide glasses", *Phil. Mag. A* **64(5)** (1991) 1059.

[75] S.R. Elliott, in Physics of Amorphous Materials, 2nd ed., Longman Sci. & Tech, co-published with John Wiley & Sons, Inc., New York, (1990), ch. 3.

[76] D.E. Sayers, E.A. Stern and F.W. Lytle, "New method to measure structural disorder: application to GeO_2 glasses", *Phys. Rev. Lett.* **35** (1975) 584.

[77] B.M.J. Smets and T.P.A. Lommen, "The structure of germanosilicate glasses, studied by x-ray photoelectron spectroscopy", *J. Non-Cryst. Solids* **46** (1981) 21.

[78] P.I.K. Onorato, M.N. Alexander and C.W. Struck, "Bridging and nonbridging oxygen atoms in alkali aluminosilicate glasses", *J. Am. Ceram. Soc.* **68(6)** (1985) C-148.

[79] R. Gresh, W. Muller-Warmuth and H. Dutz, "X-ray photoelectron spectroscopy of sodium phosphate glasses", *J. Non-Cryst. Solids* **34** (1979) 127.

[80] J.F. Watts, in An Introduction to Surface Analysis by Electron Spectroscopy, Oxford University Press, 1990, ch. 1.

[81] J.F. Watts, in An Introduction to Surface Analysis by Electron Spectroscopy, Oxford University Press, 1990, ch. 5.

[82] E.I. Kamitsos, M.A. Karakassides and G.D. Chryssikos, "A vibrational study of lithium borate glasses with high Li_2O content", *Phys. Chem. Glasses* **28(5)** (1987) 203.

[83] E.I. Kamitsos and M.A. Karakassides, "Structural studies of binary and pseudo binary sodium borate glasses of high sodium content", *Phys. Chem. Glasses* **30(1)** (1989) 19.

[84] E.I. Kamitsos, A.P. Patsis, M.A. Karakassides and G.D. Chryssikos, "Infrared reflectance spectra of lithium borate glasses", *J. Non-Cryst. Solids* **126** (1990) 52.

[85] W.G. Spitzer, R.C. Miller, D.A. Kleinman and L.E. Howarth, "Far infrared dielectric dispersion in $BaTiO_3$, $SrTiO_3$ and TiO_2", *Phys. Rev.* **126** (1962) 1710.

[86] G. Lucovsky and T.M. Hayes, in Amorphous Semiconductors, M.H. Brodsky ed., (Topics in Applied Physics, vol. 36), Springer-Verlag, p. 215.

[87] H. Jain and A.S. Nowick, "Electrical conductivity of synthetic and natural quartz crystals", *J. Appl. Phys.* **53(1)** (1982) 477.

[88] P. Maass, A. Bunde and M.D. Ingram, "Ion transport anomalies in glasses", *Phys. Rev. Lett.* **68(20)** (1992) 3064.

[89] E.F. Riebling, "Preparation and structure of thallium and silver germanate glasses", *J. Chem. Phys.* **35** (1971) 804.

[90] H. Jain and A.S. Nowick, "Radiation-induced conductivity in quartz crystals", *J. Appl. Phys.* **53(1)** (1982) 485.

[91] H. Jain, in Experimental Techniques of Glass Science, Ch. 12, eds. C. Simmons and O. El-Bayoumi, American Ceramic Society, Westerville, OH, 1993, pp. 433-461.

[92] M.C.R. Shastry and K.J. Rao, "A chemical approach to an understanding of the fast ion conduction in silver iodide-silver oxysalt glasses", *Solid St. Ionics* **37** (1989) 17.

[93] M.A. Marcus and W. Flood, "A procedure for the manufacture of EXAFS samples of concentrated materials", *Rev. Sci. Instr.* **62** (1991) 839.

[94] S.M. Heald, in X-ray Absorption: Principles, Applications, Techniques of EXAFS, SEXAFS and XANES, eds. D.C. Koningsberger and R. Prins, John Wiley & Sons, Inc., (1988) pp. 119-161.

[95] D.C. Koningsberger, in X-ray Absorption: Principles, Applications, Techniques of EXAFS, SEXAFS and XANES, eds. D.C. Koningsberger and R. Prins, John Wiley & Sons, Inc., (1988) pp. 163-210.

[96] D.H. Wilkinson, Ionization Chambers and Counters, Cambridge University Press, 1950.

[97] D.A. Shirley, "High resolution x-ray photoemission spectrum of the valence bands of gold", *Phys. Rev. B* **5** (1972) 4709.

[98] H. Jain, H.L. Downing and N.L. Peterson, "The mixed alkali effect in lithium-sodium borate glasses", *J. Non-Cryst. Solids* **64** (1984) 335.

[99] R.H. Cole and E. Tombari, "Analysis of electric relaxation in sodium trisilicate and lithium fluoroborate glasses from 10^2 to 10^9 Hz and 25 to 300 °C", *J. Non-Cryst. Solids* **131-133** (1991) 969.

[100] B.K.Teo, EXAFS: Basic Principles and Data Analysis, Springer, Berlin (1986).

[101] D.E. Sayers and B.A. Bunker, in X-ray Absorption: Principles, Applications, Techniques of EXAFS, SEXAFS and XANES, eds. D.C. Koningsberger and R. Prins, John Wiley & Sons, Inc., (1988) pp. 211-253.

[102] P.A. Lee, P.H. Citrin, P. Eisenberger and B.M. Kincaid, "Extended X-ray absorption fine structure - its strengths and limitations as a structural tool", *Rev. Mod. Phys.* **53** (1981) 769.

[103] B. Rupp, B. Smith and J. Wong, "SEXIE - a microcomputer program for the calculation of coordination shells and geometries", *Comp. Phys. Commum.* **67** (1992) 543.

[104] G. Meitzner, G.H. Via, F.W. Lytle and J.H. Sinfelt, "Structure of bimetallic clusters. Extended x-ray absorption fine structure (EXAFS) studies of Re-Cu, Ir-Cu, and Pt-Cu clusters", *J. Chem. Phys.* **83** (1985) 353.

[105] J.J. Rehr, J. Mustre de Leon, S.I. Zabinsky and R.C. Albers,"Theoretical x-ray absorption fine structure standards", *J. Am. Chem. Soc.* **113** (1991) 5135.

[106] S.J. Gurman, "EXAFS and structural studies of glasses", in Applications of Synchrotron Radiation, eds. C.R.A. Catlow and G.N. Greaves, Blackie: Glasgow, UK, (1990), p. 141.

[107] E.I. Kamitsos, M.A. Karakassides and G.D. Chryssikos, "Cation-network interactions in binary alkali metal borate glasses. A far-infrared study", *J. Phys. Chem.* **91** (1987) 5807.

[108] M.A. Karakassides, PhD thesis, University of Athens, (1990).

[109] W.D. Kingery, H.K. Bowen and D.R. Uhlmann, Introduction to Ceramics, 2nd ed., John Wiley & Sons, New York, (1976), p. 58.

[110] CRC Handbook of Chemistry and Physics, **71**st ed, ed. D.R. Lide, CRC Press, Inc., (1991), p. **12**-1.

[111] A.D. Cox and P.W. McMillan, "An EXAFS study of the structure of lithium germanate glasses", *J. Non-Cryst. Solids* **44** (1981) 257.

[112] S. Sakka and K. Kamiya, "Structure of alkali germanate glasses studied by spectroscopic techniques", *J. Non-Cryst. Solids* **49** (1982) 103.

[113] C.D. Yin, K. Morikawa, F. Marumo, Y. Gohshi, Y.Z. Bai and S. Fukashima, "Coordination number of Ge atoms in Na_2O-GeO_2 glasses studied by chemical shift measurements", *J. Non-Cryst. Solids* **69** (1984) 97.

[114] G.N Greaves, A.J. Dent, B.R. Dobson, S. Kalbitzer, S. Pizzini and G. Muller, "Environments of ion-implanted As and Ga impurities in amorphous silicon", *Phys. Rev. B* **45** (1992) 6517.

[115] S.N. Houde-Walter, J.M. Inman, A.J. Dent and G.N. Greaves, "Sodium and silver environments and ion exchange processes in silicate and aluminosilicate glasses", *J. Phys. Chem.* (1993).

[116] C. Lapeyre, J. Petiau and G. Calas, in The Structure of Non-Crystalline Materials, ed P.H. Gaskell, Taylor & Francis, London (1982).

[117] B.E. Warren, "The X-ray diffraction of vitreous silica", *Z. Kristallogr. Mineralog. Petrogr.*, **86** (1933) 349.

[118] E.A. Porai-Koshits, in Glass Science and Technology, vol. 4, eds. D.R. Uhlmann and N.J. Kreidl, Academic Press, 1990, p. 1.

[119] W.C. Huang, H. Jain and M.A. Marcus, "Structural study of Rb and (Rb,Ag) germanate glasses by EXAFS and XPS", *J. Non-Cryst. Solids* **180** (1994) 40.

[120] K.K. Evstrop'ev and V.K. Pavlovskii, "Ionic diffudion and electroconductivity of single-alkaline glasses", *Izve. Akad. Nauk SSSR, Neorg. Mater.* **3(4)** (1967) 673.

[121] H.L. Downing, N.L. Peterson and H. Jain, "Mixed isotope electrical conductivity in lithium borate glasses", *J. Non-Cryst. Solids* **50** (1982) 203.

[122] R.M. Hakim and D.R. Uhlmann, "Electrical conductivity of alkali silicate glasses", *Phys. Chem. Glasses* **12** (1971) 132.

[123] A. Hunt, "Statistical and percolation effects on ionic conduction in amorphous systems", *J. Non-Cryst. Solids* **175** (1994) 59.

[124] J.N. Mundy and G.L. Jin, "Ionic transport in sodium aluminogermanate glasses", *Solid St. Ionics* **21** (1986) 305.

[125] J.N. Mundy and G.L. Jin, "Ionic transport in rubidium aluminogermanate glasses", *Solid St. Ionics* **24** (1987) 263.

[126] J.E. Shelby, in Treatise on Materials Science and Technology, **vol. 17**, eds. M. Tomozawa and R.H. Doremus, Academic Press, New York, (1979), pp. 1-40.

[127] J.E. Shelby, "Helium migration in alkali germanate glasses", *J. Appl. Phys.* **50** (1979) 276.

[128] W.C. Huang, H. Jain and G. Meitzner, "EXAFS study of local structure of K and (K,Rb) germanate glasses", to be published.

[129] E.I. Kamitsos, Y.D. Yiannopoulos, M.A. Karakassides, G.D. Chryssikos and H. Jain, "Raman and infrared structural investigation of $xRb_2O\bullet(1-x)GeO_2$ glasses", to be published in *J. Phys. Chem.*

[130] G.N. Greaves, in Glass Science and Technology, **vol. 4B**, eds. D.R. Uhlmann and N.J. Kreidl, Academic Press, New York, (1990), pp. 1-76.

[131] K.L. Ngai and S.W. Martin, "Correlation between the activation enthalpy and Kohlrausch exponent for ionic conductivity", *Phys. Rev.* **B40** (1989) 10550.

[132] O. Kanert, M. Kloke, R. Kuchler, S. Ruckstein and H. Jain, "Nuclear spin relaxation and electrical conductivity in lithium germanate glasses", *Ber. Bunsenges. Phys. Chem.* **95** (1991) 1061.

[133] M. Tomozawa, J.M. Hyde, J.F. Cordaro and M. Yoshiyagawa, "Decay function Kohlrausch exponent for the electric modulus of mixed alkali glasses", *Phys. Chem. Glasses* **33** (1992) 69.

[134] H.L. Downing and H. Jain, unpublished work (1982).

[135] W. Lee, J. Liu and A.S. Nowick, "Limiting behavior of ac conductivity in ionically conducting crystals and glasses: a new universality", *Phys. Rev. Lett.* **67** (1991) 1559.

[136] D.S. Park and A.S. Nowick, "Dielectric relaxation of point defects in α-quartz", *Phys. Status Solidi* **A26** (1974) 617.

[137] H. Jain, "Haven ratio for sodium in synthetic α-quartz", *Phys. Status Solidi* **A80** (1983) K15.

[138] C.T. Moynihan, "Analysis of electrical relaxation in glasses and melts with large concentrations of mobile ions", *J. Non-Cryst. Solids* **172-174** (1994) 1395.

[139] K. Funke, "Jump relaxation in solid electrolytes", *Prog. Solid St. Chem.* 22 (1993) 111.

[140] D. Knödler, W. Dietrich and J. Petersen, "Coulombic traps and ion conduction in glassy electrolytes", *Solid St. Ionics* **53-56** (1992) 1135.

[141] M.C. Wittels, "Structural behaviour of neutron irradiated quartz", *Phil. Mag.* **8** (1957) 1445.

[142] M.C. Wittels and F.A. Sherrill, "Radiation damage in SiO_2 structures", *Phys. Rev.* **93** (1954) 1117.

[143] R.A. Weeks, "The many varieties of E' centers: a review", *J. Non-Cryst. Solids* **179** (1994) 1.

[144] D.L. Griscom, in Materials Research Society Symposia Proceedings, vol. 61: Defects in Glasses, eds. F.L. Galeener, D.L. Griscom and M.J. Weber, 1986, p. 213.

[145] W. Primak, "Fast-neutron-induced changes in quartz and vitreous silica", *Phys. Rev.* **110** (1958) 1240.

[146] P. Maass and M. Meyer, "Conductivity vs. Spin-Lattice relaxation: Contrasting Behavior in a Correlated Disordered Structure", submitted to *J. Chem. Phys.*

[147] B. Munro, B. Wang and M. Greenblatt, *J. Non-Cryst. Solids*, to be published.

[148] R.H. Magruder, D.L. Kinser and R.A. Weeks, "Fusion temperature effects on the annealing behavior of GeO2 glasses as measured by the d.c. resistivity", *J. Non-Cryst. Solids* **71** (1985) 95.

[149] J. Kawamura and M. Shimoji, "Ionic conductivity and glass transition in superionic conducting glasses $(AgI)_{1-x}(Ag_2MoO_4)_x$, (x = 0.25, 0.3, 0.35)", *J. Non-Cryst. Solids* **88** (1986) 295.

[150] K. Papadopoulos, D.M. Mattox and T.T. Meek, "Effect of heat treatment on the Na+ resistivity of viterous silica", *J. Am. Ceram. Soc.* **66** (1983) 120.

[151] R.H. Magruder, D.L. Kinser, R.A. Weeks and J.M. Jackson, "Effect of melt temperature on the d.c. conductivity of GeO2 glasses", *J. Appl. Phys.* **57** (1985) 345.

[152] J.M. Jackson, M.E. Wells, G. Kordas, D.L. Kinser, R.A. Weeks and R.H. Magruder, "Preparation effects on the UV optical properties of GeO_2 glasses", *J. Appl. Phys.* **58** (1985) 2308.

[153] R.A. Weeks and D.L. Kinser, "Effects of liquid equilibration temperature T_ϕ on the properties of germania glass: a review", *Diff. Defect Data* **53&54** (1987) 117.

[154] E.I. Kamitsos and M.A. Karakassides, "Effect of melt temperature on glass structure", *Phys. Chem. Glasses* **30** (1989) 235.

[155] H. Jain and W.C. Huang, in: Int. Conf. on Defects and Diffusion in Materials, DD-91, Moscow, 1991, Abstracts, vol. 1, p. 70.

[156] S. Brawer, Relaxation in Viscous Liquids and Glasses, Amer. Ceram. Soc., Colombus, OH, 1985, p. 58.

[157] E.J. Gooding and W.E.S. Turner, "Study of the series of glasses containing sodium oxide, boric oxide and silica", *J. Soc. Glass. Technol.* **18** (1934) 69.

[158] S. Takeuchi, T. Yamate and M. Kunugi, "Density of borate glass melts", *J. Soc. Mater. Sci. Jpn.* **14** (1965) 255.

[159] M. Kunugi, A. Konishi, S. Takeuchi and T. Yamate, "Density of alkali borate glasses", *J. Soc. Mater. Sci. Jpn.* **21** (1972) 978.

[160] A. Karki, S. Feller, H.P. Lim, J. Stark, C. Sanchez and M. Shibata, "The density of sodium borate glasses related to atomic arrangements", *J. Non-Cryst. Solids* **92** (1987) 11.

[161] T.A. Litovitz and C.M. Davis, in: Physical Acoustics, Vol. 2A, ed. W.P., Mason (Academic Press, New York, 1965), p. 288.

[162] E. Eipeltauer and K. Schaden, "Interrelation between viscosity and composition of binary Na borate glasses", *Glastech. Ber.* **35** (1962) 505.

[163] T.A. Litovitz and C.M. Davis, in: Physical Acoustics, Vol. 2A, ed. W.P., Mason (Academic Press, New York, 1965), p. 320.

[164] P.K. Gupta, in: Current Trends in the Science and Technology of Glass, ed. H. Jain, A.R. Cooper, K.J. Rao and D. Chakravorty, World Scientific, Singapore, 1989, p. 5.

[165] T. Milman and R. Bouaziz, "Sodium borates", *Ann. Chim.* (Paris) **3** (1968) 311.

[166] J.E. Shelby, "Thermal expansion of alkali borate glasses", *J. Am. Ceram. Soc.* **66** (1983) 225.

[167] S.W. Martin, "Conductivity activation energy relations in high-sodium-content borate and aluminoborate glasses", *J. Am. Ceram. Soc.* **71** (1988) 438.

[168] S. Anderson, R.L. Bohon and D.D. Kimpton, "Infrared specta and atomic arrangement in fused boron oxide and soda borate glasses", *J. Am. Ceram. Soc.* **38** (1955) 370.

[169] K. Frey and E. Funck, "Vibrational spectra of complex borates, I. pentaborates", *Z. Naturforsch.* **27B** (1972) 101.

[170] J. Zhong and P.J. Bray, "Change in boron coordination in alkali borate glasses, and mixed alkali effects, as elucidated by NMR", *J. Non-Cryst. Solids* **111** (1989) 67.

[171] S.W. Martin, E.I. Cooper and C.A. Angell, "CO_2 retention in high-alkali borate glasses", *J. Am. Ceram. Soc.* **66** (1983) C153.

[172] E.I. Kamitsos, M.A. Karakassides and A.P. Patsis, "Spectroscopic study of carbonate retention in high-basicity borate glasses", *J. Non-Cryst. Solids* **111** (1989) 252.

[173] J. Tauke, T.A. Litovitz and P.B. Macedo, "Viscous relaxation and non-Arrhenius behavior in B_2O_3", *J. Am. Ceram. Soc.* **51** (1968) 158.

[174] L. Shartsis, W. capps and S. Spinner, "Density and expansivity of alkali-borates and density characteristics of some other binary glasses", *J. Am. Ceram. Soc.* **36** (1953) 2, 35.

[175] C.A. Angell and H. Kanno, "Density maxima in high-pressure supercooled water and liquid silicon dioxides", *Science* **193** (1976) 1121.

[176] C.A. Angell, J. Green, D. List, Z. Qing and H. Senapati, "New modes of glass formation using negative pressure quenching and superstructureing principles", *Diff. Defect Data* **53&54** (1987) 77.

[177] E.F. Riebling, "Volume relations in Na_2O-B_2O_3 and $Na_2O{\bullet}SiO_2{\bullet}B_2O_3$ melts at 1300 °C", *J. Am. Ceram. Soc.* **50** (1967) 46.

APPENDIX DISSERTATION RESEARCH PUBLICATIONS

1. W.C. Huang, H. Jain, E.I. Kamitsos and A.P. Patsis, "Anomalous expansion of sodium triborate melt and its effect on glass properties", **J. Non-Cryst. Solids 162 (1993) 107-117**.

2. H. Jain and W.C. Huang, "Importance of structure in electrical conductivity relaxation", **J. Non-Cryst. Solids 172-174 (1994) 1334-1342**.

3. W.C. Huang, H. Jain and M.A. Marcus, "Structural study of Rb and (Rb,Ag) germanate glasses by EXAFS and XPS", **J. Non-Cryst. Solids 180 (1994) 40-50**.

4. W.C. Huang and H. Jain, "Correlation between local structure and electrical response of Rb and (Rb,Ag) germanate glasses: DC conductivity", **J. Non-Cryst. Solids 188 (1995) 254-265**.

5. W.C. Huang, H. Jain and G. Meitzner, "The structure of potassium germanate glasses by EXAFS", **J. Non-Cryst. Solids (1996), in press**.

6. H. Jain and W.C. Huang, "Significance of the disorder induced by neutron irradiation for electrical relaxation in SiO_2", **J. Non-Cryst. Solids (1996), in press**.

7. W.C. Huang and H. Jain, "Local structure and electrical response of Rb and (Rb,Ag) germanate glasses: AC conductivity", submitted to **J. Non-Cryst. Solids (1996)**.

8. W.C. Huang, H. Jain and G. Meitzner, "The local structure of mixed alkali germanate glasses by EXAFS", **Phys. Chem. Glasses (1996)**, to be submitted.

9. W.C. Huang and H. Jain, "Relationship between local structure and ionic conductivity of potassium germanate glasses", in preparation.

10. W.C. Huang and H. Jain, "Structural implications for the mixed alkali effect in germanate glasses", in preparation.

11. W.C. Huang and H. Jain, "Effect of neutron irradiation on ionic conduction in quartz crystal", in preparation.

12. E.I. Kamitsos, Y. Yiannopoulos, H, Jain and W.C. Huang, "Correlation between far infrared absorption and electrical conductivity of rubidium germanate glasses", **J. Non-Cryst. Solids (1996)**, in press.

13. H. Jain, E.I. Kamitsos, Y. Yiannopoulos, G.D. Chryssikos, W.C. Huang, O. Kanert and R. Kuchler, "A comprehensive view of the local structure around Rb in rubidium germanate glasses", **J. Non-Cryst. Solids (1996)**, in press.

14. X. Lu, H. Jain and W.C. Huang, "Structure of potassium and rubidium germanate glasses by X-ray photoelectron spectroscopy", **J. Non-Cryst. Solids (1996)**, in press.

VITA

Wei-Che Huang received his high school diploma from the Taipei Municipal Chan-Kuo High School in 1983. After entering the highly competitive National College Entrance Examination, he was admitted to the National Tsing Hua University, one of the best Universities in Taiwan. He obtained his B.S. degree from the Department of Materials Science and Engineering at National Tsing Hua University in 1987. After that, he served in the Taiwan Military as a junior lieutenant for two years. He was admitted as a graduate student to the Department of Materials Science and Engineering, Lehigh University in 1990. Since then, he has been working in the program 'ionic conduction in glass' for his Ph.D degree under the guidance of professor H. Jain. Mr. Huang is a productive author and co-author of more than 10 papers in the field of glass science.